Electronic properties of doped carbon-based nanostructures

James Lawlor

A thesis submitted for the degree of

Doctor of Philosophy

School of Physics

Trinity College Dublin

2016

Declaration

I, James Andrew Lawlor, declare that thesis has not been submitted as an exercise for a degree at this or any other university; That it comprises work done entirely by myself during the course of my PhD studies at Trinity College Dublin; That I was involved in a number of collaborations, and where it is appropriate my collaborators are acknowledged for their contributions.

A copy of this thesis may be lent or copied by the Trinity College Library upon request by a third party provided it spans single copies made for study purposes only, subject to normal conditions of acknowledgement.

James Andrew Lawlor

June 24, 2016

Dedication

Dedicated to my grandparents Irene & Paddy Lawlor and Irene & Eddie Banks.

Summary

Carbon-based nanostructures have been at the forefront of scientific research for the last couple of decades due to their unique properties, giving rise to many potential applications especially for electronics. Their simple structure and the ease with which many of their electronic properties can be studied makes them particularly interesting from a theoretical perspective. These electronic properties can be modified by altering the atomic structure, for example through the introduction of dopants to the system. In this thesis a thorough investigation of several topics related to doping in bulk graphene, narrow strips of graphene (nanoribbons) and carbon nanotubes is be undertaken.

A tight-binding Green function formalism is developed and then employed in the study of impurity modelling, Friedel oscillations, impurity scattering and sublattice segregation of impurities. The distinct advantage of using such a mathematically transparent approach is that it better reveals the underlying physical mechanisms than a purely numerical simulation. The first demonstration of this is to the case of impurity modelling. A self-consistent method is demonstrated for obtaining the tight-binding parameters that characterise the impurity, e.g. energy levels and overlap integrals. This requires only a handful of inputs from density functional theory and presents a computationally effi-

cient alternative to the commonly used method of band structure matching. Tight-binding parameters for substitutional nitrogen, substitutional boron and adsorbed hydrogen are calculated for a host graphene system.

The focus is then moved to the phenomenon of Friedel oscillations in graphene and carbon nanotubes, spatial modulations in the density of states and the carrier density, caused by symmetry breaking of the system due to the presence of an impurity. The differences between substitutional impurities, vacancies and several kinds of adsorbates will be studied. Closed-form analytic expressions describing the Friedel oscillations will be derived and compared to numerical calculations.

The role of the bonding symmetry of adsorbed impurities on scattering and electronic transport properties in graphene is then studied. It is shown that scattering is heavily suppressed for particular bonding symmetries, making these impurity types quite poor for use with conventional graphene chemical sensors. This suppression is explained from the viewpoint of interference between the propagators describing electron propagation. By breaking the underlying system symmetry via uniaxial strain this scattering suppression can be mitigated, suggesting impurities exhibiting this quality would be ideal candidates for high-sensitivity strain sensors.

The mathematical model is then used to investigate the recently observed experimental phenomenon of sublattice segregation, where under conditions large numbers of nitrogen dopants in graphene exhibit an overwhelming preference to occupy one of graphene's two sublattices. It is proposed that inter-impurity interactions are driving this effect and that, moreover, this is not particular to nitrogen or graphene and is a consequence of symmetry breaking in the lattice. Alternative scenarios are then discussed where the same sublattice ordering

behaviour should arise: in carbon nanotubes where their reduced dimensionality is predicted to enhance the effect; and Gaussian strain 'bubbles' in bulk graphene created in such a way that destroys the underlying sublattice symmetry and makes one more preferential for adsorption.

Acknowledgements

While working in academia can sometimes feel like a solitary endeavour, the successful completion of a PhD rarely comes about solely through the efforts of the person whose name is on the thesis cover. During the past four years I have been fortunate enough to receive a huge amount of support from many people, without whom this thesis would not have been possible.

First and foremost I would like to thank Mauro for his supervision throughout my PhD and for the incredible level of patience, enthusiasm and guidance that he has shown me since day one. Finding a PhD supervisor is very much like casting a die, I'm glad to say I rolled a figurative six.

I would also like to thank the many people I've had the opportunity to collaborate with and who have helped me develop professionally. In no particular order I'd like to say a great big thank you to Claudia Rocha, Stephen Power, Paul Gorman, John Duffy, Ana Claudia Carvalho, Claudionor Bezerra, Andrea Latgé, Filipe Guimarães, Vanessa Torres and Caio Lewenkopf. I would also like to acknowledge the financial support this project received from the Irish Research Council for Science, Engineering and Technology, the School of Physics, Trinity College Dublin and the TCHPC group for the computational

resources provided.

Perhaps the most important factor in being content with your job is having great people to work alongside. I would like to thank Eric, Pankaj, Glenn, Karaca, Shane and Sofia and the many others who shared Lloyd Institute Room 2.22 with me over the last four years. Whether it was sharing funny things we found online or lending an ear when having troubles with something, they made the office feel like a second home.

I could have never arrived at this point in life without the loving support of my parents Jack and Susan and my brother Richard. Finally, I would like to thank my girlfriend Katie for her love and friendship over the past couple of years. Fortunately for everyone I was a physicist rather than a poet, so you are all safe from further embarrassment. For now.

Publications

List of publications resulting, partially or wholly, from this work.

- Impurity invisibility in graphene: Symmetry guidelines for the design of efficient sensors,
  J Duffy, J A Lawlor, M S Ferreira, C Lewenkopf,
  Accepted for publication, Physical Review B, June 2016.

- The influence of Gaussian strain on sublattice selectivity of adsorbates in graphene,
  J A Lawlor, V Torres, A Latgé, M S Ferreira,
  Journal of Physics: Condensed Matter 28 (23), 235001, May 2016.

- Sublattice segregation of hydrogen adsorbates in carbon nanotubes,
  J A Lawlor, M S Ferreira,
  Physical Review B 92 (11), 115405, September 2015.

- Green functions of graphene: An analytic approach,
  J A Lawlor, M S Ferreira,
  Physica B: Condensed Matter 463, 48-53, April 2015.

- Sublattice asymmetry of impurity doping in graphene: A review,
  J A Lawlor, M S Ferreira,
  Beilstein journal of nanotechnology 5 (1), 1210-1217, August 2014.

- Sublattice imbalance of substitutionally doped nitrogen in graphene,
  J A Lawlor, P D Gorman, S R Power, C G Bezerra, M S Ferreira,
  Carbon 77, 645-650, June 2014.

- Density of states of helically symmetric boron carbon nitride nanotubes,
  A C M Carvalho, C G Bezerra, J A Lawlor, M S Ferreira,
  Journal of Physics: Condensed Matter 26 (1), 015303, November 2013.

- Friedel oscillations in graphene: Sublattice asymmetry in doping,
  J A Lawlor, S R Power, M S Ferreira,
  Physical Review B 88 (20), 205416, November 2013.

Research Trips, Conferences and Seminars

Topic: Electronic structure of impurity doped graphene: an inverse modelling approach

- Mar. 2015, Poster Presentation - Graphene 2015, Bilbao, Spain.

Topic: Sublattice asymmetry of substitutional dopants in graphene

- Dec. 2014, Oral Presentation - PRTLI Meeting, University College Dublin, Ireland.
- Oct. 2014, Seminar - Let's Talk About Nano, CRANN Seminar Series, Trinity College Dublin, Ireland.
- Aug. 2014, Research Trip - Universidade Federal Fluminense, Brazil.
- Jul. 2014, Poster - Flatlands: Beyond Graphene, Trinity College Dublin, Ireland.

- May 2014, Oral Presentation - Graphene 2014, Toulouse, France.
- May 2014, Oral Presentation - Irish Atomistic Simulators Meeting 2014, Queen's University Belfast, U.K.
- Feb. 2014, Oral Presentation - NanoTP Meeting, University of Nantes, France.
- Feb. 2014, Oral Presentation - Towards Reality in Nanoscale Materials VII, Levi, Finland.

Topic: Friedel oscillations in graphene

- May 2013, Oral Presentation & Poster - Synthetic Nanocarbon Materials Symposium, Trinity College Dublin, Ireland.

Table of Contents

Declaration iii

Dedication v

Summary vii

Acknowledgements xi

Publications xiii

Research trips, conferences and seminars xv

Table of Contents xvii

Common Acroynms xxiii

1 Introduction 1

1.1 Carbon-based nanomaterials 4

1.2 Friedel oscillations and scattering 8

1.3 Band gap engineering through doping 10

1.4 Thesis layout 13

2 Mathematical tools **19**

2.1 Introduction to Green functions 20

2.2 Dyson equation 23

2.2.1 Substitutional impurities and vacancies 26

2.2.2 Adsorbed impurities 28

2.3 Density of states and occupation 31

2.3.1 Local density of states and occupation 32

2.4 Lloyd equations 34

2.4.1 The Lloyd formula 35

2.4.2 Equation for global charge 36

2.4.3 Equation for total electronic energy change of a system due to perturbations 40

2.5 Recursive methods 42

2.5.1 Standard recursive method 43

2.5.2 The Rubio-Sancho method 47

2.5.3 Kubo formula 51

2.6 Chapter summary 53

3 Green functions of graphene and carbon nanotubes **55**

3.1 Graphene 58

3.1.1 Mathematical description of the graphene lattice 58

3.1.2 Eigenvalues and eigenvectors of the diagonalised Hamiltonian 62

3.1.3 Electronic dispersion 64

3.1.4 Derivation of lattice Green functions 66

3.1.5 Single integral expression for the lattice Green functions 69

3.1.6 First nearest neighbour Green functions 74
3.2 Stationary phase approximation 77
3.2.1 Second nearest-neighbour approximations 79
3.2.2 First nearest neighbour; no overlap 81
3.3 Carbon nanotubes 84
3.3.1 Via bulk graphene Green functions 85
3.3.2 Via recursive methods 86
3.3.3 Band gap comparisons between different methods . . . 89
3.3.4 Stoichiometry of boron carbon nitride nanotubes 90
3.4 Chapter summary 95

4 An inverse modelling scheme for dopants in graphene 99
4.1 Substitutional impurities 101
4.2 Adsorbed impurities 105
4.3 Chapter summary 110

5 Friedel oscillations 111
5.1 Graphene 112
5.1.1 Weak substitutional impurities 112
5.1.2 Multiple weak substitutional impurities 124
5.1.3 Vacancies 129
5.1.4 Adsorbates 135
5.2 Carbon nanotubes 140
5.2.1 Substitutional impurities 141
5.2.2 Effect of increasing diameter 144
5.3 Chapter summary 145

6 Scattering suppression and symmetry breaking **149**

6.1 Quantifying scattering 151

6.1.1 Green function component behaviour 154

6.2 Uniaxial strain 159

6.3 Electrical conductance 168

6.4 Chapter summary 173

7 Sublattice segregation of impurities in carbon nanomaterials **177**

7.1 Inter-impurity interaction energy 181

7.1.1 Pairs of impurities 187

7.1.2 Alternate method using the SPA 190

7.2 Nitrogen doped graphene 191

7.2.1 Critical concentration of impurities 196

7.3 Carbon nanotubes with hydrogen 200

7.3.1 Tight-binding and Monte Carlo model 202

7.3.2 Two hydrogen impurities 207

7.3.3 Finite concentration of hydrogen 209

7.4 Gaussian strain 218

7.4.1 Patched Green functions method 219

7.4.2 Segregation and Gaussian strain calculations 226

7.5 Chapter summary 233

8 Summary and future work **235**

8.1 Summary of thesis 236

8.2 Possible extensions and future work 241

8.2.1 Impurity scattering and Friedel oscillations 242

8.2.2 Inverse modelling 245
8.2.3 Sublattice segregation 246

A Change of variable for computation of integrals **249**
A.1 Onsite occupation variations 249
A.2 Energy variations 253

B Low energy approximations in the nearest-neighbour regime **255**
B.1 Dispersion relation 255
B.2 Pristine Green functions of graphene 256

Bibliography **259**

Common Acronyms

ACNT Armchair carbon nanotube

BCNT Boron carbonitride nanotube

BNNT Boron nitride nanotube

CNT Carbon nanotube

CVD Chemical vapour deposition

DFT Density functional theory

FN First nearest-neighbour tight-binding approximation

FOs Friedel oscillations

GF Green function

LDOS Local density of states

SN Second nearest-neighbour tight-binding approximation

SNO Second nearest-neighbour with wavefunction overlap tight-binding approximation

SPA Stationary phase approximation

ZZNT Zigzag carbon nanotube

Chapter 1

Introduction

"So let's have a round of applause for... this inanimate carbon rod!"

- Mr. Burns, *The Simpsons* [1].

Carbon is a non-metallic element with atomic number 6, the fourth most abundant element in the Universe [2] and essential to the existence of all known biological systems. Humankind owes many facets of its technological and cultural advancement to this simple element and its allotropes. In antiquity, carbon-based materials were used as fuel in the form of charcoal [3] and for cutting and aesthetic purposes in the form of diamond [4]. In modern times it plays an important role in an ever growing number of technologies, from hypothetical space elevators to the humble pencil lead. It is thus quite fitting, as will soon be shown, that it finds itself playing a central role in the field of nanotechnology, the control and manipulation of matter on the atomic scale

and one of the most exciting and quickest developing scientific fields of the twenty-first century.

Nanotechnology has found use in many fields, one research area being the development of nanoscale components for future electronic devices. To understand this application, an overview of current electronics technology is now presented. Over the past few decades there has been an explosion in the availability and computational power of commercial electronics. Their ubiquity has been directly responsible for much of the economic growth over this time period. Growing consumer demand for smaller and more powerful electronics has created the need for smaller and faster electrical components. This is where the application of nanotechnology aims to improve on the limitations of current technology. Transistors are one such component, integral to the functioning of all electronic devices, used as signal amplifiers or low-power logic switches. Billions of them are packed into each and every one of the two billion smartphones in usage around the world at the time of writing [5]. For logic uses, a single transistor exists in either an "on" or an "off" state - either passing or blocking current passing through - which is controlled externally, for example by an applied electric field (field effect transistors).

For decades the vast majority of transistors used in commercial devices have been made from silicon. Microchips, sometimes called integrated circuits, are thumbnail-sized arrays of billions of transistors which are combined with other electronic components in order to store information and perform computations. One factor determining the operational speed of these chips is the physical size of the transistors. As techniques have evolved to make transistors smaller, more can fit inside the typical microchip area, which has the effect of making them both cheaper and more energy efficient. This rate of transistor

down-sizing has been fairly consistent for decades - the number of them that can fit in a given area doubles approximately every two years, a famous observation called Moore's Law. This trend cannot continue indefinitely however, as these increasingly smaller physical dimensions of the transistors lead to issues such as overheating and current leakage. Some experts have suggested the trend of Moore's Law may end within the next couple of decades or sooner [6]. Consequentially there has been much attention directed towards finding suitable alternatives and there are many nascent fields of research showing potential for tackling this problem, for example optical transistors (photonics) [7]. Nanoscience is another obvious candidate, and the recent development of materials exhibiting quantum mechanical effects is a testament to that fact. Fabrication of transistors using these novel materials and incorporating new designs can exploit the quantum mechanical phenomena inherent to these materials. The hope is that a new paradigm could be produced which circumvents the limitations of the current silicon technology. This is the area where carbon-based nanomaterials like graphene and carbon nanotubes (CNTs) show great promise due to their remarkable electronic properties, and they are the primary materials investigated in this work.

Since the advent of solid-state physics it is well known that the electronics of a material are determined by its atomic structure and symmetries e.g. crystallinity and doping. The usage of materials as electronic components relies on the control of the electronic band gap, which can be affected by the location and species of chemical dopants. The role of these dopants is particularly important in the case of graphene which in its native state lacks a band gap. The size of the gap when induced can further be tuned by altering the dopant concentration. Therefore if graphene is to be used in future electronics technology a thorough understanding of the physics of doping and the subsequent alter-

ation to the system electronics is very important, and this is the central topic of this thesis. With this as motivation, the goal of this work is to formulate a mathematical framework for the physics of doped carbon-based nanomaterials. In doing this it can be shown that the system's distinct underlying symmetries and how these are broken by doping can explain several observed experimental phenomena. Of particular interest are Friedel oscillations and sublattice segregation of impurities, and these will be explained in this introductory chapter. This chapter now begins with a broad overview of carbon-based nanomaterials followed by general discussion of the role of dopants and how they are used in tailoring the electronics of these systems. After, Friedel oscillations and sublattice segregation are introduced and an outline of the thesis is presented.

1.1 Carbon-based nanomaterials

Great interest in the field nanotechnology began in the 1980s with advancements in atomic-level microscopy which made direct images of atoms possible [9]. Around the same time, there was the experimental discovery of nanoparticles called C_{60} fullerenes, nanometer sized spherical cages of 60 carbon atoms bonded together in pentagonal and hexagonal rings as shown in Fig. 1.1 [10]. This was soon followed in 1991 by the discovery of CNTs [11], another kind of fullerene, which have a long cylindrical structure with the same hexagonal bonding as C_{60} (see Fig. 1.1 middle). Among their properties are unparalleled tensile strength [12] and very high electron mobility [13]. Curiously the electronic structure was found to be influenced entirely by the chirality of the nanotube structure, where different widths and wrapping symmetries result

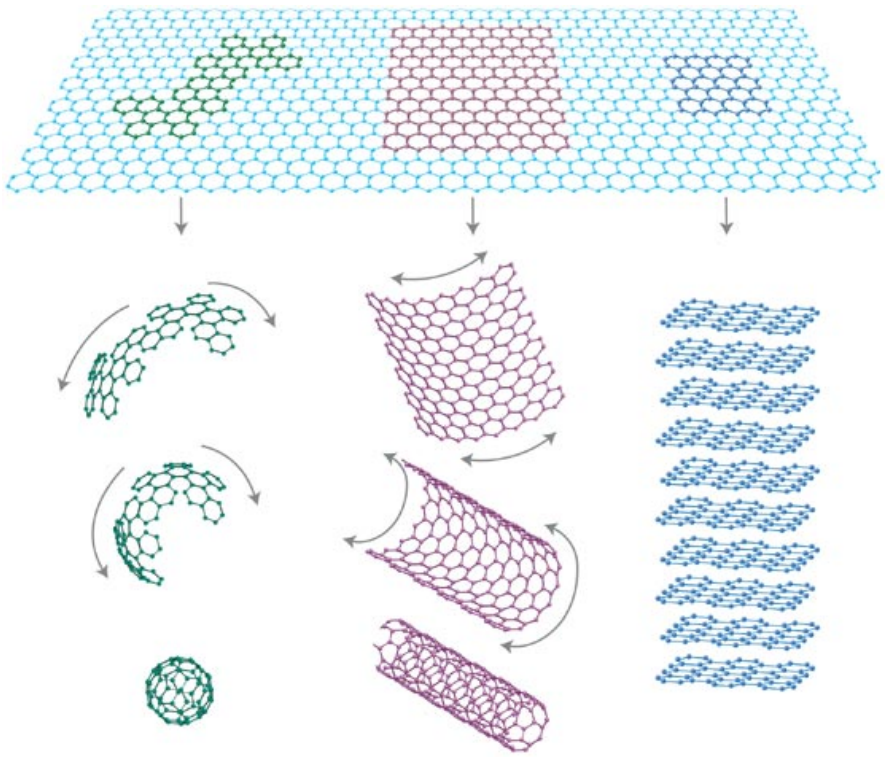

Figure 1.1: Graphene is the basic building block from which many other carbon-based nanomaterials can be derived. Shown from left to right are the relation between graphene and zero-dimensional fullerenes called buckyballs, one-dimensional carbon nanotubes, and three dimensional graphite. Reproduced with permission from [8].

in different energy spectra. Further investigation of their unique mechanical and electronic properties has subsequently lead to a wide range of applications such as energy storage in the form of lithium-ion batteries and electrochemical capacitors [14–16], composites [17, 18] and electronics [19–21].

It was known that this growing family of carbon-based nanomaterials should, in theory, be linked by a common building block - a single atom thick layer of graphite called graphene. This is shown in Fig. 1.1 where the relationship and symmetries between fullerenes, CNTs, graphene and graphite can

be understood. Graphite is the most stable form of carbon and is composed of stacks of crystalline graphene layers weakly bound together by van der Waals forces. These layers can be separated easily by application of a small force, which is the mechanism by which a pencil traces. Despite the abundance of graphite found naturally, for a long time the scientific consensus was that a single graphene layer, and indeed any other two-dimensional crystal, could not exist in a free-standing state. Arguments were put forward around 1950 that such materials would be thermodynamically unstable and would collapse at finite temperatures due to vibrations, as argued by Peierls [22] and Landau [23] and backed up by experimental studies of thin films. As a result they were regarded for some time as a mere theoretical curiosity by the general scientific community. Fortunately this viewpoint did not deter some researchers, and over decades it was eventually shown that graphene layers could exist as the surface part of a three-dimensional bulk system [24] or eventually in free-standing stacks of only a few layers. The breakthrough came relatively recently in 2004 when a team led by Geim and Novoselov at the University of Manchester were able to extract graphene monolayers from bulk graphite using sticky tape (euphemistically known as mechanical exfoliation) [25]. Interestingly, this method is still used widely in labs around the world as it is still the cheapest and most reliable way to make small high-quality samples for study, despite the availability of myriad other production methods. Since the discovery of free-standing graphene, for which Geim and Novoselov were awarded the 2010 Nobel Prize in Physics, many other two-dimensional crystals have been fabricated using other materials. Examples include silicon (silicene) [26] and MoS_2 [27], each with a variety of distinct and useful properties which directly link to their atomic chemistry. Further investigations with graphene have shown it to have many interesting properties and phenomena

owing entirely to its unique structure. The electronic properties are the most important properties to understand for this thesis. Of primary importance is that graphene is a zero-gap semiconductor, the conduction and valence bands meeting at two inequivalent points of zero density of states in the Brillouin zone, referred to as the Dirac points. Around these points in momentum space the dispersion relation is linear and the carriers behave relativistically as massless Dirac fermions, giving rise to mobilities in excess of 250,000 cm^2/Vs [25, 28] and excellent thermal conductivity as high as 5000 $W\,m^{-1}K^{-1}$ [29]. Graphene also exhibits superior mechanical properties with a Young's modulus of 1 TPa [30].

As discussed previously, the ability to tune and control the electronic properties of nanomaterials is key to their use in electronics, and this can be done by altering their structure or by introducing dopants. This engineering is particularly important for graphene. Initially it seems like an ideal material for use in transistors due to the high carrier mobility, which is higher than both Indium antimonide and semi-conducting CNTs, two of the highest mobility semiconductors currently in existence [31]. However, the lack of band gap means any field effect transistors made in the conventional way using the material would be unable to be switched off, rendering it useless as a logic device. Therefore a band gap must be induced in order to allow current to be switched on and off, which would allow graphene to be used in a commercial environment as ultra high-speed transistors, integrated circuits and other novel devices [8, 31, 32]. This is, however, difficult to achieve [33]. The prospects for using graphene as a substitution for silicon have gradually faded in recent years as a result of poor on/off current ratios evidenced in graphene transistors [34–36]. One of the goals of this thesis is to investigate and model possible band gap engineering scenarios with dopants in graphene and other carbon nanostructures. As

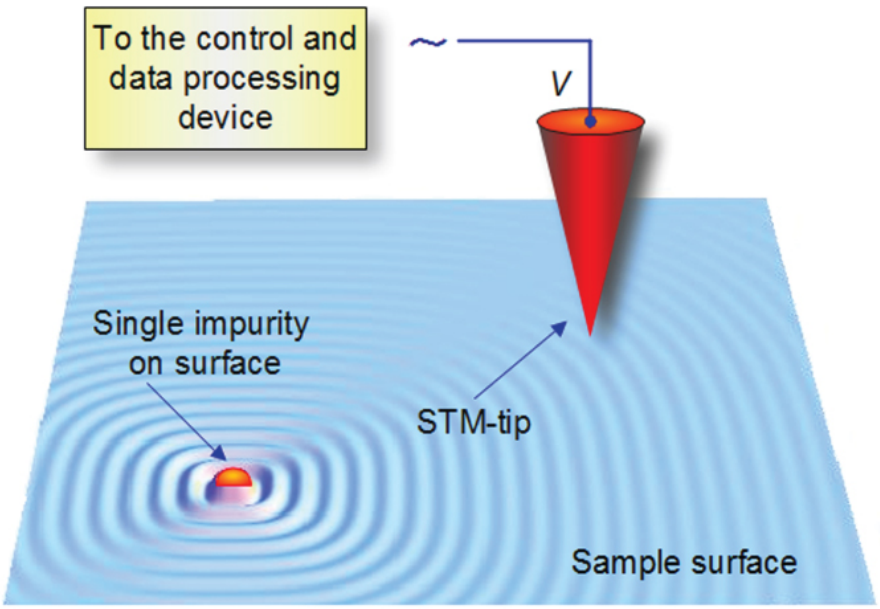

Figure 1.2: Probing density of states oscillations using a scanning tunnel microscope (STM). An impurity embedded at the surface of a material modulates the electron density and thus the density of states in the region nearby, resulting in spatial oscillations that can be mapped using the STM. Adapted under creative commons license from [37].

a consequence one must understand how dopants behave in these systems.

1.2 Friedel oscillations and scattering

Symmetry breaking produced by defects in an otherwise pristine system, for example in a Fermi gas, induces perturbations in the electronic environment of the gas via scattering of electrons. This results in spatial oscillations called Friedel oscillations (FOs) [38] which manifest themselves in many electronic quantities such as the local density of states (LDOS) and the electron density. Oscillations in the density of states can be experimentally observed directly

using scanning tunnel microscopy, a schematic of this is shown in Fig. 1.2. Generally these spatial oscillations radiate away from the location of the symmetry breaking perturbation and decay at a rate of $\sim D^{-d}$ with the distance D from the perturbation and dimensionality d of the system. As graphene is a two-dimensional system one would therefore expect this decay to go as D^{-2}.

There has been a lot of attention focused recently on Friedel oscillations caused by symmetry breaking in graphene [39–48]. Of particular interest is the behaviour of the oscillations in the electron density when the Fermi energy of the system lies around the Dirac point. Here, the vanishing of the density of states has been shown to change both the decay rate and the character of the electron density oscillations. It has been shown that not only does the decay rate change from D^{-2} to a faster D^{-3} rate for ungated/undoped graphene, but that the oscillations themselves disappear due to their commensurability with the lattice spacing resulting in a smooth non-oscillatory decay profile [39, 41, 45]. One should be reminded that the aim of this project is to understand the physics of dopants in carbon nanostructures and hence Friedel oscillations and related phenomena will play an important role in determining the subsequent electronic properties. While the spatial oscillation in the electron distribution is an interesting quantum mechanical effect in its own right, in the next section a more useful effect for graphene's use as an electrical component that arises from these oscillations will be discussed. The main mathematical tools for investigating electron behaviour in condensed matter physics are Green functions, which are introduced in Chap. 3 and used throughout this work. They will play a major role in Chap. 5 where a mathematical model for Friedel oscillations in graphene and CNTs will be developed, and in Chap. 6 where the bonding symmetry of impurities is discussed in relation to the impact on scattering.

1.3 Band gap engineering through doping

To meet or exceed the limits of silicon semiconductor technology, graphene would need to match a current on/off ratio of roughly 10^4-10^7 along with a band gap of at least 340 meV whilst maintaining high carrier mobility [49–51]. Several methods to do this exist currently, for example one-dimensional quantum confinement by construction of thin strips of graphene (called nanoribbons and abbreviated GNR) [52], stacking of graphene monolayers and applying perpendicular electric fields (GFETs) [53, 54], strain [55] and mounting on a substrate [56–58], however the alteration of the crystal structure through the introduction of dopants is one of the more realistic and scalable solutions. There are problems with this approach, mainly that achieving large band gaps relies on high dopant concentrations which leads to a lot of scattering of electrons, thus degrading the transport quality of the device. Using nitrogen dopants can yield band gaps up to 200meV [59] and by inclusion of boron this can be expanded to around 600meV with 6% total dopant concentration [58]. Although these gaps are quite sizeable, the effect of scattering would lead to a detrimental impact on the transport characteristics.

Recent experimental and theoretical research has shown however that this scattering can be mitigated by placing impurities on only one of graphene's two sublattices with electrons travelling relatively freely on the undoped sublattice, preserving the excellent electronic properties intrinsic to pristine graphene [60–65]. The situation where dopants situate on the same sublattice is referred to as *sublattice asymmetry* or *sublattice segregation*. These terms are equivalent and will be used interchangeably throughout this work. The effect was first seen with groups nearby nitrogen impurities in graphene, although there is

some observational evidence of it occurring with other dopant types [66, 67]. It was not until 2011 that a viable experimental approach for producing large-scale sublattice segregation of nitrogen was found by Zhao et al. [60]. It was found that graphene grown via Chemical Vapour Deposition (CVD) in the presence of ammonia (NH_3) naturally incorporates nitrogen atoms as substitutional so-called 'graphitic' dopants into the crystal, and with a distinct sublattice segregation of dopants. Further theoretical work confirmed that a tunable band gap would be obtainable using this method [63], sparking further interest into this phenomenon.

Subsequent investigations undertaken by Lv et al. [61] and Zabet-Khosousi et al. [62] were able to replicate the findings of Zhao et al. and large areas of sublattice segregated nitrogen doped graphene were synthesised. Results from the Zabet-Khosousi group are shown in Fig. 1.3, demonstrating a striking STM image of a large area of nitrogen doped graphene with two clearly defined domains of different sublattice preference. The sharp borders are thought to arise from terracing of the substrate which acts to disrupt the segregation effect.

Similar studies with boron dopants have found no segregation [68], the reason for this is thought to be due to a strong interaction between the Cu (111) substrate and the boron impurity, in contrast to a very weak interaction with the substrate for nitrogen impurities [68].

Despite extensive literature on the segregation effect, the physical mechanism responsible is not understood. It was originally suggested in one report that it may be occurring during the growth phase - that is as the CVD grown 'islands' of graphene flakes grow larger there exist preferential edge configurations that lead to the segregation of the system [62, 69]. There are problems with this explanation as naturally one would expect that the clearly defined

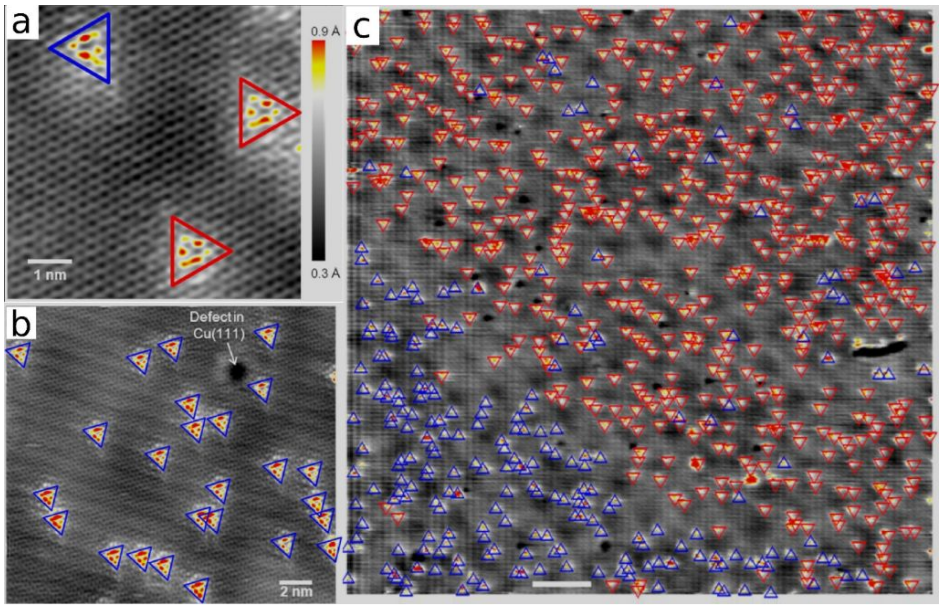

Figure 1.3: STM images of nitrogen doped graphene on (a) 7 nm^2, (b) 20 nm^2 and (c) 100 nm^2 scales, adapted with permission from Zabet-Khosousi et al. [62]. Copyright 2014 American Chemical Society. Dopants locations are identified by finding bright spots on the STM image caused by slight perturbations in the positions of neighbouring carbon atoms. The dopant sublattice can be found through the orientation of the bright triangle features. The red and blue triangles in each subfigure correspond to impurities on different sublattices. Panel (c) best demonstrates that while the distribution of dopants appears random two large domains exist with opposite sublattice segregation. Shown at the bottom off-centre left of (c) is a white 10 nm scale bar.

segregation domains seen experimentally (e.g. Fig. 1.3) would naturally fall in with the graphene grain boundaries, but this has not been observed. There are also a number of reports of impurity correlation in other graphene-based systems, e.g. molybdenum impurities [66] and high-coverage hydrogenated graphene [67]. Most interestingly there is some experimental evidence of segregation being induced post-synthesis by doping by direct ion implantation followed by heat treatment [70]. This suggests both that the segregation phe-

nomenon is not unique to CVD grown nitrogen doped graphene and that the physical mechanism may not be solely growth based. In Chap. 7 it is proposed that it arises from inter-impurity interactions mediated by the conduction electrons. This mechanism is closely related to Friedel oscillations, and it is argued that it should also occur in other carbon-based nanomaterials and with other dopants, and that it is not unique to graphene and nitrogen. It is also shown that impurity segregation could similarly be induced in CNTs with hydrogen impurities and in graphene using Gaussian strain to break the sublattice symmetry in place of an impurity.

1.4 Thesis layout

This thesis is comprised of eight chapters including this introduction. In Chap. 2 a general introduction to Green functions is given. These are the essential mathematical tools used throughout this work, and their uses in condensed matter physics and their calculation will be explained in detail. It is shown how these can be used in conjunction with the Dyson equation to quantify how the properties of the system respond to doping. Examples are given of these perturbations for the most commonly found dopant types. The Lloyd equation is also introduced which is used to calculate the change in the total charge and the total energy of a system due to the introduction of impurities. Recursive methods are introduced in the final part of the chapter, which are a set of computational methods for the calculation of the Green functions of one-dimensional channels. The Kubo formula for electrical conductance is also stated and explained within the context of the recursive approach.

Starting from a mathematical description of the graphene lattice which in-

corporates first and second nearest neighbour interactions and wavefunction overlap, the Green functions for graphene and CNTs are derived in Chap. 3, along with the electronic dispersion relations and density of states. For comparison, equivalent expressions for a simpler first nearest neighbour model are shown which neglects the overlap term, and it is found that this is sufficient for the purpose of this thesis. To simplify the computation of the Green functions it is demonstrated how their initial double integral form can be solved exactly to give an equivalent single integral expression. Furthermore it is shown how, over long distances, the Green functions can be approximated using a stationary phase approximation, a technique which allows an analytic 'pen and paper' solution to be found for quantum phenomena such as Friedel oscillations arising in these materials. It is then shown how the regular graphene Green functions can be extended to the case of CNTs through a quantisation of momentum condition. The advantage of requiring such a high degree of mathematical transparency throughout this work is that it can allow for insights into the underlying features of the studied phenomena. Beyond this approach an alternate method to obtain the CNT Green functions using the recursive algorithms is described in detail. These various approaches for computing the electronic structure of a CNT are then compared through comparison of the band gaps between the different tight-binding models and methods. Recursive methods are then applied to a case study of boron carbonitride nanotubes, investigating how their stoichiometry affects the electronic band gap.

Chapter 4 introduces and discusses the problem of finding suitable tight-binding parameters to describe impurities. Current techniques involve matching band structures between tight-binding and density functional theory (DFT), and the parameters are tweaked until a match is found. It will be argued that this is inefficient and sometimes inaccurate, and a more quantitative and simpler

method is presented that uses the Lloyd equations from Chap. 2 in combination with DFT results. The problem is recast as an inverse process, where the initially unknown parameters are associated with the set of Lloyd equations whose solution is known. It is then possible to find the unique set of tight-binding parameters that correspond to the solutions. This process will hereafter be referred to as *inverse modelling*. The work in this chapter builds on previous research which applied the same formalism to doped nanotubes [71–73]. The inverse modelling procedure is used to produce a tight-binding description of substitutional nitrogen and boron, and adsorbed hydrogen impurities in graphene.

In Chap. 5 the phenomenon of Friedel oscillations in graphene and CNTs with armchair and zigzag geometry will be described within the overarching mathematical framework. Their behaviour for substitutional, vacancy and adsorbate type impurities are discussed in detail. It is shown how the stationary phase approximation of the Green functions can be used to obtain closed-form mathematical expressions for the Friedel oscillations in the LDOS and charge density. The benefit of this is that not only does it deepen the physical understanding of the phenomenon in a mathematically transparent manner, but it can be used when investigating similar behaviour arising from the presence of impurities.

In Chap. 6 the role of the bonding symmetry of adsorbed impurities in determining electron scattering is discussed in the context of gas sensor technology. In simple terms gas sensing works by detecting the change in electrical properties of a device upon an increasing concentration of adsorbed chemical species. Common chemical dopants exhibit either a top, bridge or central adsorbed configuration and these are described in Chap. 2. Using the math-

ematical methods derived in previous chapters, the different effects of these impurities on the electron scattering for low energies where most sensing experiments take place is examined. It is shown using both numerical and analytic approaches that the scattering resulting from central adsorbed impurities is greatly diminished in comparison to top and bridge adsorbates, with the exception of rare cases which are identified. This suggests that graphene sensors for gases which prefer a central adsorbed position will not be very effective. The proposed mechanism is the destructive interference of the long-range Green function propagators arising from the particular bonding symmetry of central adsorbates. This is further supported by modelling the effect of uniaxial strain on the system - it is shown that the interference effect can be mitigated and the scattering becomes greatly enhanced with increasing strain. This demonstrates that graphene hosting central bonded impurities can function instead as efficient and highly-sensitive strain sensors.

In Chap. 7 the model derived previously for Friedel oscillations to investigate inter-impurity interactions of dopants in graphene and CNTs is used as a foundation to provide an explanation for the experimentally observed sublattice segregation of nitrogen. It is argued that the inter-impurity interactions give rise to the segregation effect via symmetry breaking and that the effect should not be unique to nitrogen doped graphene. Two alternative scenarios are presented where the effect should also be observed - firstly the case of consider hydrogen impurities in CNTs where the one-dimensional nature causes the interactions to be enhanced, and secondly with Gaussian strain applied so as to break the symmetry between the graphene sublattices causes an energetic preference for adsorbates for one sublattice over the other. Ultimately these findings suggest that Friedel oscillations are directly linked to the segregation effect.

A summarised discussion of this work is presented in Chap. 8 along with ideas for possible extensions. A chapter introducing Green functions and their uses in condensed matter physics will now follow.

Chapter 2

Mathematical tools

This chapter will introduce the main mathematical methods to be used throughout the thesis, specifically single-particle Green functions and their associated quantities. Throughout this work endeavours will be made to give the maximum amount of mathematical transparency as possible to the investigations. Such an emphasis allows for greater insight into the underlying physics which a more computational approach by its very nature cannot provide. When used in conjunction with a tight-binding model describing the periodic arrangement and bonding of atoms in the lattice, Green functions allow one to model the electronic behaviour of such quantum mechanical systems and subsequent related phenomena. A general introduction to them is provided in Sec. 2.1. In the context of condensed matter theory, Green functions are particularly useful due to their direct relationship with several electronic quantities both local and global. Their direct link to the properties of local density of states and electron occupation (Sec. 2.3), total system charge and energy variations (Sec. 2.4) and

electron transport measurements (Sec. 2.5) will be shown in this chapter. Another key strength is the ability for Green functions to accommodate defects and disorder in an otherwise crystalline structure without loss of generality. This is done using perturbation theory resulting in the so-called Dyson equation (Sec. 2.2), a concise expression for the change in the system Green functions resulting from the introduction of a localised impurity. Several examples are provided for the most common dopant types found in carbon-based nanomaterials - substitutional, vacancies and a variety of adsorbates - but without reference to any specific host system, i.e. the same formalism could be applied to a square lattice as to graphene. The Dyson equation allows for a thorough mathematically transparent treatment of electronic phenomena in disordered carbon-based nanoscale systems, the focus of this thesis. Finally, methods to calculate the Green functions of large or even infinite systems through recursive application of the Dyson equation is demonstrated (Sec. 2.5). The Kubo formula for the DC conductance in these systems is then introduced (Sec. 2.5.3). The mathematical tools introduced in this chapter will be used for investigations of the effects of disorder in bulk graphene, carbon nanotubes and graphene nanoribbons throughout this work.

2.1 Introduction to Green functions

Green functions are used to find solutions to differential equations and are encountered in many areas of physics, from electromagnetism to quantum physics. Green functions represent the impulse response of a system to a singular input, specifically in condensed matter physics, they are used as an efficient method to investigate the behaviour and response of many-body sys-

tems. Once calculated they contain a great deal of information about a system, for example the density of states and transport properties, and are linked to the propagation of an electron through the system [74].

In a broad mathematical sense the Green function for a time-independent, hermitian, linear differential operator $\mathcal{L}(r)$ with a complete set of eigenfunctions $\{\phi_n(r)\}$ is defined as the solution to the equation

$$[z - \mathcal{L}(r)]g(r, r'; z) = \delta(r - r') \tag{2.1}$$

where r, r' are the coordinates of two physical locations in the system and the variable $z = \lambda \pm i\eta$ where λ_n are the eigenvalues of $\mathcal{L}(r)$ according to $\mathcal{L}(r)\phi_n(r) = \lambda_n\phi_n(r)$. An infinitesimal imaginary part $\eta \to 0^+$ is added to z to prevent poles (or branch cuts in the case of a continuous spectrum of eigenvalues) occurring when z coincides with the spectrum of eigenvalues λ_n.

Eq. 2.1 can be rewritten to give the Green function in matrix form as

$$\hat{g} = \sum_n \frac{|\phi_n\rangle \langle\phi_n|}{z - \lambda_n}.$$

The choice of the sign of $\pm i\eta$ determines the causality of whether electron propagation is from r to r' ($+$ive sign) or the opposite ($-$ive sign). The resulting functions are called the *retarded* and *advanced* Green functions respectively and correspond to perturbations acting forward (causal) or backwards in time. The retarded Green functions are chosen by convention when time-reversal symmetry exists for a problem - their use reflects the natural intuition for cause-and-effect. For the remainder of this work any reference to Green functions in a general sense refers to this type, except for a few specific cases

which will be noted explicitly.

The description of Green functions up to this point is extremely general and can be applied to many areas of physics for example electrodynamics, quantum field theory and aerodynamics. In the case of condensed matter theory, the single-particle Green function for a system with Hamiltonian $\mathcal{H}$ can be derived by assuming a linear combinations of atomic orbitals (LCAO). This is the assumption that the molecular orbitals of the system can be expressed as a linear sum of each of the atomic orbitals by analogy to the operator $\mathcal{L}$. This Hamiltonian must also satisfy the time-independent Schrödinger equation

$$\mathcal{H}\psi_n(r) = E_n\psi_n(r)$$

where the energies E_n are the eigenvalues of this quantum mechanical system. Using the definition of the Green function (Eq. 2.1) it follows that the Green function $\mathcal{G}$ describing the electron propagation in this particular system is defined as

$$\hat{\mathcal{G}} = \lim_{\eta\to 0}[(E + i\eta)\hat{I} - \hat{\mathcal{H}}]^{-1}. \tag{2.2}$$

It should be clarified that this result is valid for any many-body system where a suitable tight-binding Hamiltonian can be found. While in principle the above form of $\mathcal{G}$ readily allows calculation of all the system Green functions via matrix inversion, their calculation for extremely large or infinite systems becomes unwieldy or impossible. The matrix $\mathcal{H}$ contains all the necessary information of the system's n orbitals, so as the system increases in size the computational complexity of calculating $\mathcal{G}$ directly through matrix inversion becomes difficult or impossible, scaling as $\sim \mathcal{O}(n^{2.3})$ or higher [75]. For large systems the Green functions can be calculated recursively by piecewise connection of small

regions of the entire system using the Dyson equation (Sec. 2.2). For infinite systems a solution can be approximately computed, this is demonstrated and explained for a carbon nanotube in Sec. 2.5. An exact solution for infinite systems can be found by exploiting the periodicity and homogeneity of the system allowing for determination of individual matrix elements of $\mathcal{G}$. This will constitute the main discussions of Chap. 3 where the Green functions for bulk graphene and carbon nanotubes will be calculated using Bloch functions. It will frequently be required to specify elements of the Hamiltonian and Green function matrices which will be done using the notation X_{ij} to denote the matrix elements of $\hat{X}$ which correspond to the orbitals indexed by i and j. This can be obtained by projecting the matrix onto the states $\langle i|$ and $|j\rangle$ describing the atomic orbitals so that the Green function between i and j is

$$g_{ij} = \langle i| \hat{g} |j\rangle = \sum_n \frac{\langle i|\phi_n\rangle \langle \phi_n|j\rangle}{z - \lambda_n} \tag{2.3}$$

and the states $\langle i|$ and $|j\rangle$ need not be orthogonal. In Chap. 3 the Green functions of graphene and carbon nanotubes will be calculated both with and without the orthogonality condition.

2.2 Dyson equation

This work aims to model disorder in graphene and nanotubes and investigate the subsequent effects on the electronic behaviour of these systems. The Green function formalism detailed in the previous section however requires a translation-invariant (i.e. periodic) system, which is at odds with inhomogeneous disorder. The Dyson equation [76] is a way to bypass this issue by

treating the disorder as a localised perturbation applied to the regular crystal lattice. It allows for the Green function $\hat{G}$ of the now disordered system to be described entirely in terms of the pristine system Green function $\hat{g}$ and a matrix $\hat{V}$ describing the perturbation. The usage of G and g to designate Green functions of the perturbed and unperturbed systems respectively will be used throughout this work. By perturbation theory if the disordered system Hamiltonian

$$\hat{H}' = \hat{H} + \hat{V},$$

where $\hat{H}$ is the pristine crystal Hamiltonian, then by Eq. 2.2 it can be seen that $\hat{G}$ can be written in a recursive format as

$$\begin{aligned} \hat{G} &= [(E + i\eta)\hat{I} - (\hat{H} + \hat{V})]^{-1} \\ &= [\hat{g}^{-1} - \hat{V}]^{-1} \\ &= [\hat{I} - \hat{g}\hat{V}]^{-1}\hat{g} \\ &= \hat{g} + \hat{g}\hat{V}\hat{G}. \end{aligned} \tag{2.4}$$

It is useful to define the so-called T-matrix

$$\hat{T} = \hat{V}[\hat{I} - \hat{g}\hat{V}]^{-1}$$

which contains all the perturbation terms. $\hat{G}$ can be written in a more convenient form

$$\hat{G} = \hat{g} + \hat{g}\hat{T}\hat{g}, \tag{2.5}$$

this is known as the *Dyson equation*. It is now demonstrated how this can be used to study the response of a host system when subjected to doping. The impurities considered in this thesis can all be modelled through a shift in on-

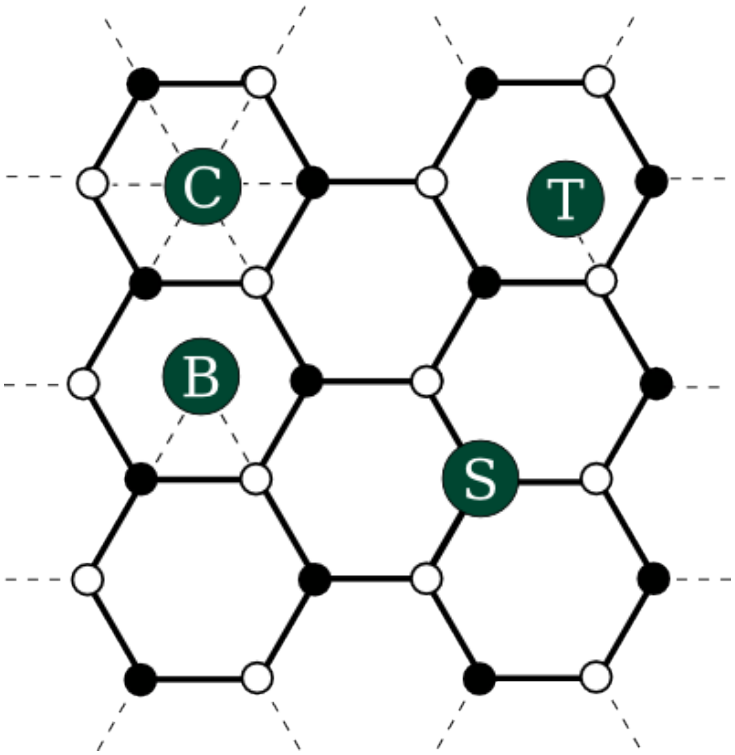

Figure 2.1: Schematic of common impurity types found in hexagonally-bonded carbon-based nanomaterials, indicated by the green atoms with bonds shown by dashed lines. Shown are substitutional (S), and top (T), bridge (B) and central (C) adsorbed atoms which bond to 1, 2 and 6 lattice sites respectively.

site energy and/or the connection of a foreign atom or molecule to the host system. Two general species of impurities will be looked at, substitutional (Sec. 2.2.1) and adsorbed (Sec. 2.2.2). Examples of these impurities occurring in a hexagonal lattice are shown in Fig. 2.1.

2.2.1 Substitutional impurities and vacancies

In condensed matter physics the most common and simplest impurity found in many systems is the substitutional type, where an atom in the crystal lattice is replaced by the dopant. To a first approximation this is simulated by shifting the existing onsite energy terms that describe the affected orbitals. If a single orbital model is assumed, then the energy of the one affected orbital is shifted by a potential λ, typically of the order of several eV. Because the intended effect of adding this potential is to produce scattering of the electrons in the system, care must be taken in choosing its parameters when attempting to model realistic systems. There are several ways that this can be done and they will be discussed in Chap. 4. The derivation of $\hat{G}$ for a single orbital system with one substitutional impurity added begins by considering a general orbital/atomic site labelled u in the undoped lattice. If the atom at this site is replaced with a single orbital dopant as shown by the impurity labelled "S" in Fig. 2.1, then using the above prescription the perturbation to the system is described by

$$\hat{V} = |u\rangle \, \lambda \, \langle u| \, .$$

Applying the Dyson equation (Eq. 2.5) the effect of this perturbation on the pristine system Green function g_{ij} is

$$\begin{aligned} \Delta G_{ij} &= G_{ij} - g_{ij} \\ &= \frac{g_{iu}\lambda g_{uj}}{1 - g_{uu}\lambda} \\ &= g_{iu}\lambda g_{uj} + g_{iu}\lambda g_{uu}\lambda g_{uj} + \dots \\ &= g_{iu}T_{uu}g_{uj}. \end{aligned} \tag{2.6}$$

ΔG_{ij} quantifies the change in system response between the perturbed and unperturbed states. Written in this form it is clearer to see how the perturbation affects propagation between i and j. In the trivial case of an absence of a potential at u (i.e. $\lambda = 0$), $\Delta G_{ij} = 0$ which corresponds to electrons propagating without scattering between sites i and j. Finite λ values produce an infinite number of indirect scattering paths (with diminishing cross-sections) that electrons in the lattice can take, all of which are contained within the matrix $\hat{T}$. This concept can be represented diagrammatically with Feynman diagrams [74] and is particularly useful in the case of two or more scatterers. Additionally from the form of ΔG_{ij} one can deduce that there exists a system resonance manifesting whenever $g_{uu}(E) = \lambda^{-1}$ is satisfied. The effect of this will be discussed in Chap. 5 and a more thorough investigation of impurity scattering is given in Chap. 6.

The above treatment applies only to the simplest impurity cases where the perturbation can be reliably modelled with a single potential. It can be necessary to expand this presumption to include effects on neighbouring atomic sites and changes to the overlap integral between orbitals. For example, one can consider shifting the energy levels of neighbouring orbitals by an energy λ' and modifying the overlap integral from itself to these sites by an energy τ. This extended perturbation is

$$\hat{V} = |u\rangle \, \lambda \, \langle u| + \sum_i \Big(|i\rangle \, \lambda' \, \langle i| + |i\rangle \, \tau \, \langle u| + |u\rangle \, \tau^* \, \langle i| \Big)$$

where i is a sum over the nearest lattice sites to u. Like the single parameter case, the Dyson equation can be used to obtain $\hat{G}$ for this system.

This formalism for substitutional impurities can be applied to the case of va-

cancies in the lattice. These occur naturally in the growth process and can also be induced by ion bombardment [77]. Using the parametrisation $\lambda \to \infty$ shifts the potential of the vacancy site so as to make it completely inaccessible to the system's electrons, simulating the effect of a vacancy.

2.2.2 Adsorbed impurities

Adsorbed impurities are atoms or molecules bound to the surface of the host system, bonding to one or more sites in the lattice. There are two processes by which an impurity may adsorb: physisorption, which occurs through van der Waals forces; or chemisorption, which involves the formation of chemical bonds and is therefore a stronger interaction. In this work only chemisorption is treated, so for conciseness all mentions of adsorption refer to this kind only. The simplest type to consider is a single atom with one s-orbital, which initially (i.e. prior to any perturbation) exists independently of the host system. This isolated dopant has a single energy level with an energy of ϵ_a and has the Green function

$$g_{aa} = \frac{1}{E - \epsilon_a}.$$

Unlike the case of substitutional impurities where the perturbation matrix $\hat{V}$ effectively creates the impurity, in the case of adsorbates it acts to connect the host system to the impurity via the creation of a single chemical bond quantified by the overlap energy τ. A schematic representation of this single bonded impurity is shown in Fig. 2.1 labelled "T" and hereafter referred to as the top adsorbate. Also shown are the so-called bridge and central adsorbates (la-

belled "B" and "C") which have the same parameters and onsite Green function, but which bond to two and six host sites respectively and therefore are bound to the host system by a different $\hat{V}$ matrix. To aid the understanding of the act of connection through $\hat{V}$, the unperturbed Green function matrix of the initial disconnected bulk-adatom system can be written

$$\hat{g} = \begin{pmatrix} g_{aa} & 0 & 0 & \dots & 0 & \dots \\ 0 & g_{11} & g_{12} & \dots & g_{1v} & \dots \\ 0 & g_{21} & g_{22} & \dots & g_{2v} & \dots \\ \vdots & \vdots & \vdots & \vdots & \vdots & \vdots \\ 0 & g_{v1} & g_{v2} & \dots & g_{vv} & \vdots \\ \vdots & \vdots & \vdots & \vdots & \vdots & \ddots \end{pmatrix}.$$

It is clear that initially there exists no Green function matrix element connecting the adsorbate to the host. The physical meaning of this is that no carrier propagation is possible and the adsorbate is initially completely disconnected from the host. In a single orbital system, a top adsorbed impurity attaches to the system at a single orbital / lattice site v, and this is described by the perturbation

$$\hat{V} = |v\rangle \, \tau \, \langle a| + \text{c.c.}$$

and is equivalent to the sparse matrix

$$\hat{V} = \begin{pmatrix} 0 & 0 & 0 & \dots & \tau^* & \dots \\ 0 & 0 & 0 & \dots & 0 & \dots \\ 0 & 0 & 0 & \dots & 0 & \dots \\ \vdots & \vdots & \vdots & \vdots & \vdots & \vdots \\ \tau & 0 & 0 & \dots & 0 & \vdots \\ \vdots & \vdots & \vdots & \vdots & \vdots & \ddots \end{pmatrix}.$$

It should be noted that this is analagous to the Anderson impurity Hamiltonian [78]. The resulting Green function G_{ij} of the perturbed system can be found through the Dyson equation as

$$G_{ij} = g_{ij} + \frac{g_{iv}\tau g_{aa}\tau^* g_{vj}}{1 - g_{vv}g_{aa}\left|\tau\right|^2}$$

and so the corresponding T-matrix is

$$T_{vv} = \frac{g_{aa}\left|\tau\right|^2}{1 - g_{vv}g_{aa}\left|\tau\right|^2}.$$

By comparison with Eq. 2.6 it can be seen that the effect of the adsorbed impurity on the system is an energy dependent perturbation potential that is applied to site v in the host system on which it makes contact. This potential is called the *self-energy* and is denoted

$$\Sigma_{vv}(E) = g_{aa}(E)\left|\tau\right|^2,$$

and is analogous to the perturbation by a substitutional impurity, however this self-energy term is energy dependent instead of being a constant. The effect of this is the potential experienced by electrons with energies close to that of ϵ_a is

divergent but becomes much smaller as the difference in energies increases.

As was shown for substitutional impurities, the perturbation matrix can be expanded to account for extra parameters to describe the interaction in more detail, for example the connection to two or more host sites for the cases of bridge and central adsorbates. The process is straightforward and will be shown later where appropriate. This concludes the discussion on how impurities and doped systems can be treated in a Green functions regime. In the following sections the various condensed matter quantities directly associated with Green functions will be introduced and their uses outlined. The combination of these quantities and the above methods for modelling dopants forms the foundation for this thesis - to investigate the effect of impurities on the electronics of nanoscale carbon-based materials and how they can be controlled.

2.3 Density of states and occupation

The density of states (DOS) is a key quantity in the study of many-body systems, describing the number of states per energy level that electrons are able to occupy in the system. In many crystalline materials the DOS is a continuous spectrum and contains information about the electronic behaviour, such as band gaps and dispersion. It is also possible to determine a local density of states spectrum, denoted $\rho_j(E)$ and abbreviated LDOS. This is the spatially-resolved density of states, a function of both energy and the orbital indexed j. The electron occupation on any atomic orbital can be found simply by taking the integral of the LDOS up to the Fermi energy E_F. The advantage of using a Green functions approach is their direct relation to these quantities, and this correspondence will now be derived. The eventual aim is to show that

by using the expressions for these quantities in conjunction with the Dyson equation, the effects of introducing disorder can be understood. This will be particularly advantageous in Chap. 5 where Friedel oscillations, the spatial modulations in quantities like the LDOS which arise from disorder, are investigated in the context of carbon nanostructures.

2.3.1 Local density of states and occupation

The derivation of the LDOS at some atomic orbital j ($\rho_j(E)$) begins with a Hamiltonian $\hat{H}$ which is assumed to be diagonalised and has eigenvalues ϵ_n, such that $\hat{H} = \sum_n |\Phi_n\rangle \, \epsilon_n \, \langle\Phi_n|$. From Eq. 2.3 it is known that a general Green function g_{jl} for this system can be written

$$g_{jl} = \lim_{\eta \to 0} \sum_n \frac{\langle j|\Phi_n\rangle \, \langle\Phi_n|l\rangle}{E + i\eta - \epsilon}.$$

By multiplying the right-hand side by $\frac{E-i\eta-\epsilon}{E-i\eta-\epsilon} = 1$ and choosing $l = j$ for a diagonal element, it can be seen that the imaginary part of g_{jj} is

$$\mathrm{Im}\, g_{jj} = \lim_{\eta \to 0} \sum_n |\langle j|\Phi_n\rangle|^2 \, \frac{-\eta}{(E-\epsilon)^2 - \eta^2}. \tag{2.7}$$

This is analogous to the well-known Poisson kernel

$$\nu_y(x) = \frac{1}{\pi} \frac{y}{y^2 + x^2}$$

which in the limit of $y \to 0^+$ becomes equivalent to the Dirac delta function

$$\lim_{y \to 0^+} \nu = \delta(x).$$

Applying this to Eq. 2.7 for $\operatorname{Im} g_{jj}$ yields

$$-\frac{1}{\pi} \operatorname{Im} g_{jj} = \sum_n |\langle j|\Phi_n\rangle|^2 \, \delta(E - \epsilon).$$

This produces delta-function peaks at the specific eigenenergies ϵ, the definition of the LDOS, hence it can be written that

$$\rho_{jj} = -\frac{1}{\pi} \operatorname{Im} G_{jj}. \tag{2.8}$$

This is a natural point to note that in this chapter so far the existence of spin degeneracy has been ignored, and it has been implicitly assumed that only one electron can occupy one energy level. When applying the methods of this chapter to real systems later on the spin degeneracy will be accommodated for.

It follows that the global DOS (ρ_{global}) can be obtained by the summation of the LDOS over all orbitals. This is equivalent to the operation

$$\Delta\rho_{\text{global}} = -\frac{1}{\pi} \operatorname{Im} \operatorname{Tr}\Big(\hat{G}(E)\Big).$$

Both expressions for the DOS and the LDOS are extremely powerful and are used in the computation of many physical properties. Their use is demonstrated shortly in the derivation of the Lloyd equations - a set of equations quantifying the change of global energy and occupation as a result of a perturbation to the system.

Directly related to the concept of the density of states is the electron occupation of lattice orbital j which is denoted n_j. It can be obtained by integrating Eq. 2.8 to the Fermi energy E_F

$$n_j = -\frac{1}{\pi} \operatorname{Im} \int_{-\infty}^{E_F} dE G_{jj}. \tag{2.9}$$

This expression can be used to quantify how charge is spatially redistributed in a system when an impurity is introduced. Frequently it is found that the integral here is difficult to evaluate numerically. Integrals involving Green functions, especially when in the context of low-dimensional systems, present numerous problems. This can be resolved using techniques explained in Appendix A. Nevertheless, when n_j is used in conjunction with the expression for ρ_j given in Eq. 2.8, this gives a complete description of the spatial behaviour of electrons in the host system.

2.4 Lloyd equations

The Lloyd equations are a set of equations that express the changes in the global quantities of charge (ΔN) and total energy (ΔE) as a result of some local perturbation $\hat{V}$ applied to the system. This pair of equations are of particular importance as they allow global system changes to be expressed through local perturbations. In this section they will be derived from the expressions for global density of states and the Dyson equation. ΔN is typically used in a modelling context as a self-consistent check condition. Its value can be ascertained in a variety of circumstance without any calculation - in the case of an adsorbate, for example, $\Delta N = 0$ is required because the perturbation

$\hat{V}$, by definition, acts only to connect the adatom and the host system. This act of connection cannot increase or decrease the number of electrons in the whole system, hence the total change must be zero. The value of ΔE, however, always requires computation. In this work it will be used in the inverse modelling procedure (Chap. 4) and impurity segregation (Chap. 7).

2.4.1 The Lloyd formula

The Lloyd formula is an expression describing the change in global DOS ($\Delta\rho_{\text{global}}$) due to the local perturbation $\hat{V}$ [79, 80]. From the previous section it is known that this quantity can be written as the trace

$$\Delta\rho_{global} = -\frac{1}{\pi}\,\mathrm{Im}\,\mathrm{Tr}\Big(\Delta\hat{G}\Big) = -\frac{1}{\pi}\,\mathrm{Im}\,\mathrm{Tr}\Big(\hat{g}\hat{T}\hat{g}\Big). \tag{2.10}$$

By using the cyclic property of the trace operator

$$\mathrm{Tr}\Big(\hat{g}\hat{T}\hat{g}\Big) = Tr(\hat{g}\hat{g}\hat{T}) = Tr(\hat{g}^2T) = Tr(\hat{T}\hat{g}^2)$$

and identifying that $\hat{g}^2 = (E\hat{I} - \hat{H})^{-2} = -\frac{d}{dE}\hat{g}$ it can be written that

$$\Delta\rho_{\text{global}} = \frac{1}{\pi}\,\mathrm{Im}\,\mathrm{Tr}\left(\frac{\hat{V}}{\hat{I} - \hat{g}\hat{V}}\frac{d}{dE}\hat{g}\right), \tag{2.11}$$

which can be seen by substitution into Eq. 2.10. The reader should be reminded that $\hat{g}$ here is dependent on energy, but that the perturbation $\hat{V}$ is not, even for the case of adsorbed impurities. Recalling the following identity for the natural logarithm function

$$\frac{d}{dE}\ln(f(E)) = \frac{f'(E)}{f(E)}$$

and making the substitution $f(E) = \hat{I} - \hat{g}\hat{V}$ and $f'(E) = \hat{V}\frac{d\hat{g}}{dE}$ it follows from Eq. 2.11 that

$$\Delta\rho_{\text{global}} = -\frac{1}{\pi}\,\text{Im}\,\text{Tr}\left(\frac{d}{dE}\ln\left(\hat{I} - \hat{g}\hat{V}\right)\right).$$

Applying the identity $\text{Tr}\ln\hat{X} = \ln\det\hat{X}$ gives

$$\Delta\rho_{\text{global}} = -\frac{1}{\pi}\,\text{Im}\,\frac{d}{dE}\ln\det\left(\hat{I} - \hat{g}\hat{V}\right). \tag{2.12}$$

This is the Lloyd formula, expressing change in global density of states due to a perturbation of the system. In the following two subsections it will be shown how the formula can be used to obtain equations for the global change in charge ΔN and energy ΔE due to $\hat{V}$.

2.4.2 Equation for global charge

The power of the Lloyd formula is that it expresses the change in the global density of states, a property of the entire system, as a first order differential equation involving only local quantities which describe the perturbation. This is useful because, as will soon be shown, the calculation of ΔN and ΔE are found directly via integration of the global density of states. The Lloyd formula thus vastly simplifies the mathematical steps needed. The expression for ΔN is now derived.

It initially seems trivial to define ΔN as

$$\Delta N = N_{\text{after}} - N_{\text{before}}, \tag{2.13}$$

where N is the total charge in the system and the subscript denotes either before or after the perturbation. The reason for stating this will soon become evident. There exist subtle but important differences between the cases of a substitutional and adsorbed impurities, they will be treated in separate subsections.

2.4.2.1 Substitutional

It is physically intuitive to see that the total amount of charge either before or after the doping is found through the integration of the global density of states. Mathematically speaking this corresponds to the expressions

$$N_{\text{after}} = \int_{-\infty}^{E_F} \rho_{after}$$

and similarly

$$N_{\text{before}} = \int_{-\infty}^{E_F} \rho_{before}.$$

Substitution into Eq. 2.13 gives

$$\begin{aligned} \Delta N &= \int_{-\infty}^{E_F} \Delta\rho \\ &= -\frac{1}{\pi} \operatorname{Im} \int_{-\infty}^{E_F} \operatorname{Tr} \hat{g}\hat{T}\hat{g}, \end{aligned}$$

the step from the first to second line having been given in section 2.3. Applying the Lloyd formula (Eq. 2.12) along with the fundamental theorem of calculus allows the above equation to be recast as

$$\Delta N = -\frac{1}{\pi} \operatorname{Im} \ln \det\left(\hat{I} - \hat{g}\hat{V}\right). \tag{2.14}$$

This is essentially a charge conservation equation. As stated previously, ΔN can be used as a self-consistent condition for inverse modelling as its value is known without any calculation required. Depending on whether the substitutional impurity has more or less charge than the atom it replaces, the value of ΔN is simply the difference in net charge of the system.

2.4.2.2 Adsorbates

Care must be taken when applying the same methods to the calculation of ΔN for an adsorbed impurity. The key difference is that the perturbation $\hat{V}$ acts not to create the impurity, as in the previous case, but merely to connect it to the host system, it must be required that $\Delta N = 0$ always. An additional subtlety is that the disconnected impurity has an energy level which may or may not be occupied by electrons, but must be considered in the integration step. Below it will be shown how this can be taken into account to give an equivalent expression for ΔN for adsorbates.

Consider a single orbital host system and an isolated atom denoted by the index a with energy level ϵ_a occupied by C_0 electrons. The total charge in the system before the connection is

$$N_{\text{before}} = C_0 + \int_{-\infty}^{E_F} dE \rho_{\text{host}},$$

where ρ_{host} is the global DOS of the host system without the impurity.

If $\epsilon_a < E_F$ then the isolated energy level is occupied, so one can deduce that

$$\int_{-\infty}^{E_F} dE \rho_a = \Theta(E_F - \epsilon_a).$$

Here, Θ is the Heaviside step function. By manipulating the algebra it can be seen that

$$\int_{-\infty}^{E_F} dE\rho_a - C_0 = \Theta(E_F - \epsilon_a) - C_0$$

$$\therefore C_0 = -(\Theta(E_F - \epsilon_a) - C_0) + \int_{-\infty}^{E_F} dE\rho_a$$

and

$$N_{\text{before}} = -(\Theta(E_F - \epsilon_a) - C_0) + \int_{-\infty}^{E_F} dE(\rho_a + \rho_{\text{host}}).$$

Now defining

$$N_{\text{after}} = \int_{-\infty}^{E_F} dE\rho_{\text{after}}$$

where ρ_{after} is the global DOS for the connected adsorbate and host found through the Dyson equation, it can be seen that because

$$\Delta\rho = \rho_{\text{after}} - \rho_a - \rho_{\text{host}}$$

then using the Lloyd equation

$$\Delta N = (\Theta(E_F - \epsilon_a) - C_0) - \frac{1}{\pi} \operatorname{Im} \ln \det\left(\hat{I} - \hat{g}\hat{V}\right). \tag{2.15}$$

As the connection via $\hat{V}$ never changes the amount of charge in the system it must be required that $\Delta N = 0$ always for this type of perturbation.

2.4.3 Equation for total electronic energy change of a system due to perturbations

Conventionally the change in the total electronic energy of a system due to a perturbation by $\hat{V}$ is expressed as

$$\Delta E = E_{\text{after}} - E_{\text{before}}.$$

Here E_{after} is the total electronic energy of the perturbed system and E_{before} the pristine system. Problems in calculating E directly in this manner arise as for large or infinite systems the numerical values of E_{after} and E_{before} are naturally very big, but ΔE is typically several orders of magnitude smaller. This presents an obvious challenge for numerical calculation and doing this reliably is extremely difficult. However, it will now be shown that using the definition of $\Delta\rho$ in the Lloyd formula (Eq. 2.12) one can arrive at an alternate expression for ΔE with only knowledge of the local perturbation $\hat{V}$. This allows for its direct calculation much like was shown for ΔN in the previous section. As with the determination of ΔN there are subtleties between the substitutional and adsorbed cases which must be accounted for. The derivation for both cases follows from the definition of the total electronic energy in a system, either before or after perturbation, being defined as

$$E_{TOTAL} = \int_{-\infty}^{E_F} dE E\rho(E), \tag{2.16}$$

that is the integral over the occupied energy spectrum of the product of the DOS and the energy.

2.4.3.1 Substitutional

The substitutional impurity is the simplest dopant with which to calculate ΔE. The Lloyd formula (Eq. 2.12) can be combined with the definition of total energy in Eq. 2.16 to give the result

$$\Delta E = -\frac{1}{\pi}\,\mathrm{Im}\int_{-\infty}^{E_F} dE E \frac{d}{dE}\ln\det\left(\hat{I}-\hat{g}\hat{V}\right).$$

If one then integrates by parts and uses the expression derived previously for ΔN it can be shown that

$$\Delta E = E_F\Delta N + \frac{1}{\pi}\,\mathrm{Im}\int_{-\infty}^{E_F} dE \ln\det\left(\hat{I}-\hat{g}\hat{V}\right). \tag{2.17}$$

It should be noted that this quantity accounts for the electronic energy only and does *not* describe energy gained or lost through other means such as changing of bonds or structural warping, quantities which are routinely included when calculating total energies in DFT. It is possible to extract this directly from the calculation result, however.

2.4.3.2 Adsorbates

A similar procedure can be done to find ΔE for an adsorbate. The caveat here is that the electronic energy of the isolated adatom must be equal to $C_0\epsilon_a$. With this extra accommodation and the requirement $\Delta N = 0$ for adsorbates it is straightforward to show

$$\Delta E = (\Theta(E_F - \epsilon_a) - C_0)\epsilon_a + \frac{1}{\pi}\,\mathrm{Im}\int_{-\infty}^{E_F} dE \ln\det\left(\hat{I} - \hat{g}\hat{V}\right). \tag{2.18}$$

While the solution is complete the integrand is often irregular over the integration range, hence for numerical calculations it is necessary to undertake further steps to transform it into a more readily computable form. This is covered in Appendix A. The discussion of the calculation of physical quantities from Green functions is now concluded.

2.5 Recursive methods

Determining G directly by matrix inversion scales poorly with system size, becoming prohibitively expensive from a computational standpoint rather quickly. Even with the most efficient algorithms, such a calculation scales as $\mathcal{O}(n^{2.3})$ or higher for a system with n atomic orbitals, becoming impossible for infinite bulk crystals. For some systems such as pristine graphene, there exist ways to find specific matrix elements of G analytically using Bloch functions, instead of calculating the entire matrix. This process is generally sufficient for most purposes and the method will be demonstrated in Chap. 3. However, systems that are characterised by long-range random disorder, large scattering regions or irregular geometries cannot be treated effectively with such methods and a different set of techniques, called recursive methods, must instead be employed. These recursive methods are numerical implementations for calculating the Green functions of such systems using a piecewise approach [81–83]. Small sections of the system (called cells) - which can be designed to include scatterers, deformations or novel kinds of geometry - are connected to-

gether via connection matrices using the Dyson equation and the system Green function is updated. The act of connection is conceptually similar to how adsorbed impurities were connected to the host system in Sec. 2.2.2. In this section two different approaches are presented, each with their own strengths and weaknesses - the so-called standard recursive method and the Rubio-Sancho method. These are shown in Sec. 2.5.1 and Sec. 2.5.2 respectively. The former, the less efficient of the two, constructs the system in a cell-by-cell fashion. As each cell can be constructed differently, this is ideal for modelling systems with random disorder. The latter is much faster and works by doubling the size of the system on every iteration. While much more efficient from a computational standpoint, the drawback is that it is only suitable for producing an homogeneous system. The strength of recursive methods is that these two different approaches can be used in conjunction with one another - it enables one to model a finite scattering region (built with the standard method) embedded in an infinite one-dimensional channel (two semi-infinite leads built via Rubio-Sancho). This process is described in Sec. 2.5.3 along with the statement of the Kubo formula, which gives the DC conductance in recursively-built systems and is based on standard linear response theory. In the following chapter recursive techniques will be applied to the phenomenon of band gap variations in boron carbonitride nanotube (BCNT) stoichiometry (Sec. 3.3.4), and in a later chapter used with the Kubo formula to study the effects of impurity scattering in graphene nanoribbons (Chap. 6).

2.5.1 Standard recursive method

To provide a thorough understanding of each recursive method, both will be used to calculate the Green functions of a single cell embedded in an infinite

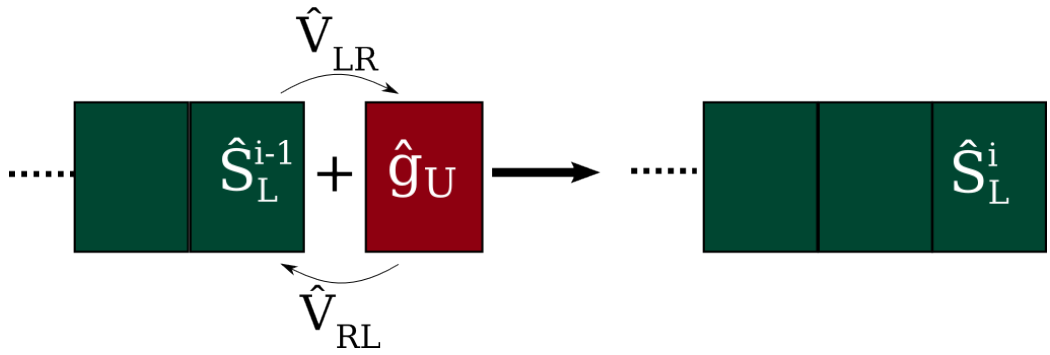

Figure 2.2: An illustration of the standard recursive technique. A unit cell (g_U, red) is connected to the left lead (surface Green function S_L^{i-1}, green) via the equation (2.22), producing a new lead. Upon connection the surface Green function of the new left lead is updated to S_L^i.

one-dimensional channel. The first step using either technique is the construction of two semi-infinite leads which the cell of interest is then connected between. The advantage of these methods becomes quickly apparent as it can be seen that only a handful of Green functions are required to be calculated at each stage of the process, namely the *surface Green functions* (denoted $\hat{S}$) of the leads, vastly simplifying the computation. In the standard recursive approach, the surface Green function of a *left-hand* lead ($\hat{S}_L$) is first calculated. The process begins by considering a single disconnected unit cell, described by the Hamiltonian $\hat{H}_U$ which has the associated Green function

$$\hat{g}_U(E) = (E\hat{I} - \hat{H})^{-1}. \tag{2.19}$$

Additional cells are then connected one-by-one to the right-hand side via the Dyson equation, using the matrix $\hat{V}_{RL}$ describing the connections between two neighbouring cells in the direction right to left. The exact form of the matrices $\hat{H}_U$ and $\hat{V}$ will be given in Sec. 3.3.2 for a nanotube, but for now a general

approach is used without reference to any particular system. Suppose a system of $i-1$ connected cells already exist, the notation $\hat{S}_L^{i-1}$ denoting the surface Green function of the right-most cell. A schematic of this is shown in Fig. 2.2. If one wishes to connect an extra cell to the right of this system this will result in a new surface Green function $\hat{S}_L^i$. Using the Dyson equation it is straightforward to describe this as

$$\hat{S}_L^i = \hat{g}_U + \hat{g}_U \hat{V}_{RL} \hat{G}_{i-1,i} \tag{2.20}$$

where $\hat{V}_{RL}$ connects the cells i and $i-1$. The Green function $\hat{G}_{i-1,i}$ above, which is the propagator between the old surface cell $i-1$ and the new one i in the connected system, can also be expressed through the Dyson equation as

$$\hat{G}_{i-1,i} = \hat{g}_{i-1,i-1} \hat{V}_{i-1,i} \hat{G}_{i,i}. \tag{2.21}$$

It is straightforward to see that

$$\hat{g}_{i-1,i-1} = \hat{S}_L^{i-1}$$

and

$$\hat{G}_{i,i} = \hat{S}_L^i$$

so by substitution into Eq. 2.20 and rearranging

$$\hat{S}_L^i = (\hat{I} - \hat{g}_U \hat{V}_{LR} \hat{S}_L^{i-1} \hat{V}_{RL})^{-1} \hat{g}_U. \tag{2.22}$$

Using this iterative procedure a system of any desirable length can be constructed in a piecewise fashion. It should be emphasised that $\hat{g}_U$ need not be the same for each iteration and can be tailored to include dopants or irregular geometry, for instance. Written in the form of Eq. 2.22 it is easy to see that if

the system was originally consisting of only a single unit cell then

$$\hat{S}_L^0 = \hat{g_U}$$

and so

$$\hat{S}_L^1 = (\hat{I} - \hat{g}_U \hat{V}_{LR} \hat{g}_U \hat{V}_{RL})^{-1} \hat{g}_U$$

will be the surface Green function of a lead, composed of just two unit cells. This prescription allows one to start with a single unit cell and from there the system can be constructed. It was explained previously that this method is ideal for modelling short scattering regions, but it can be used for semi-infinite or infinite systems by defining a convergence criteria. For a semi-infinite lead, it is assumed that there is a surface Green function of a lead with length N that is sufficiently similar to that of a lead of length $N-1$ that convergence is considered achieved. A good metric is the convergence of the absolute value of the trace of the surface Green function. The surface Green function for a right-handed lead $\hat{S}_R^i$ can be calculated in a similar fashion to the left-hand lead above, yielding

$$\hat{S}_R^i = (\hat{I} - \hat{g}_U \hat{V}_{RL} \hat{S}_R^{i-1} \hat{V}_{LR})^{-1} \hat{g}_U.$$

An infinite one-dimensional channel can be formed by connecting the two semi-infinite left and right-hand leads. The Green functions for any cell in this system, the goal of this short section on the standard recursive method, can be obtained using the Dyson equation. For example, the cell that was originally the surface cell of the left-hand lead prior to the connection has the Green function

$$\hat{G}_C = (\hat{I} - \hat{S}_R \hat{V}_{RL} \hat{S}_L \hat{V}_{LR})^{-1} \hat{S}_R \tag{2.23}$$

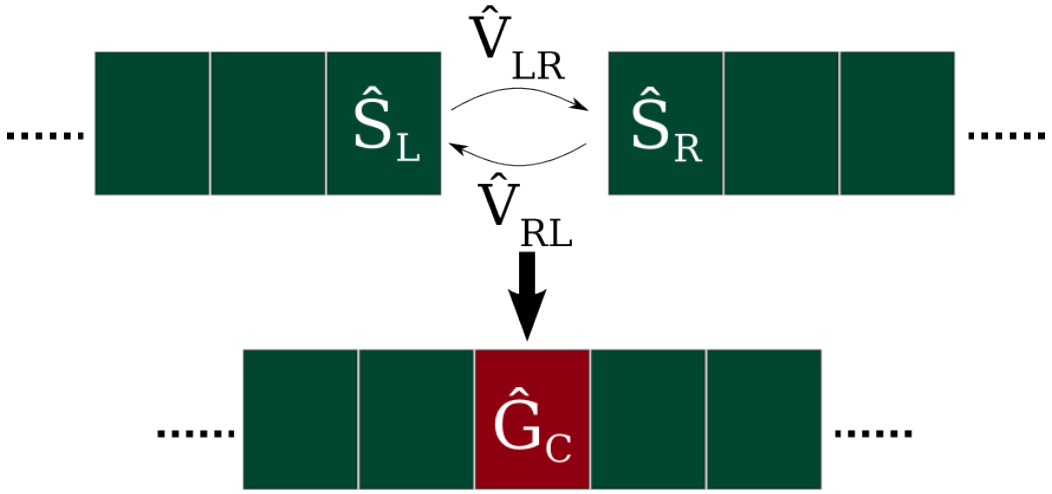

Figure 2.3: The connection of two semi-infinite leads (S_L and S_R) resulting in an infinite system is illustrated here. The Green functions for a unit cell embedded in the infinite system are denoted G_C and its derivation explained in the text, given as Eq. 2.23.

in the connected system. If the leads are homogeneous this corresponds to an arbitrary unit cell in an infinite one-dimensional channel, hence the subscript notation C ($\hat{g}_C$ was used for an isolated arbitrary cell). The procedure of connecting the two semi-infinite leads is illustrated schematically in Fig. 2.3.

Knowledge of the system Green functions can be used directly in determining the physics of the system, for example transport properties and density of states spectra. For the former, this is derived shortly in Sec. 2.5.3. For the latter, the equation derived for the LDOS previously in Eq. 2.8 remains valid.

2.5.2 The Rubio-Sancho method

As mentioned in the section introduction, the Rubio-Sancho method [84, 85] works by effectively doubling the size of the system on each iteration. It ex-

ploits the fact that as the lead is built, it can be connected to a clone of itself and hence doubling the size, as opposed to the piecewise standard recursive method. While this is not suited to disordered systems, one clear advantage is that pristine semi-infinite leads for a wide variety of different systems can be generated quickly. Clearly, achieving the desired convergence of a semi-infinite lead using the standard approach would be a very time-consuming task. Instead, if the leads are constructed quickly via Rubio-Sancho the shorter disordered region of the system can then be attached to the leads using the standard recursive method.

The derivation of the Rubio-Sancho method begins by supposing there exists a left-hand semi-infinite lead, for example like that in Fig. 2.2 extending to infinity to the left of the page, terminating at cell 0 and the other cells numbered 1, 2, 3 etc. It is known from Eq. 2.21 and Eq. 2.22 that the surface Green function of the system is

$$\hat{G}_{00} = [\hat{I} - \hat{g}_U \hat{V}_{LR} \hat{g}_{11} \hat{V}_{RL}]^{-1} \hat{g}_U$$

and the Green function between cells 1 and 0 is

$$\hat{G}_{10} = \hat{g}_{11} \hat{V}_{RL} \hat{G}_{00}.$$

Using the fact that $\hat{G}_{00} = \hat{g}_{11}$, as they are both equivalent to the surface Green function in a semi-infinite system, and defining a transfer matrix $\hat{T} = \hat{G}_{00} \hat{V}_{RL}$, the above system of equations can be recast as

$$\hat{G}_{00} = [\hat{I} - \hat{g}_U \hat{V}_{LR} \hat{T}]^{-1} \hat{g}_U \tag{2.24}$$

and

$$\hat{G}_{10} = \hat{T} \hat{G}_{00}. \tag{2.25}$$

Consider now a general Green function $\hat{G}_{N0}$ between cell 0 on the surface and cell N within the lead. The action of disconnecting this cell and then reconnecting it using the Dyson equation gives

$$\hat{G}_{N0} = \hat{g}_U \hat{V}_{RL} \hat{G}_{N-1,0} + \hat{g}_U \hat{V}_{LR} \hat{G}_{N+1,0}. \tag{2.26}$$

To simplify the mathematics the substitutions $\hat{t}_0 = \hat{g}_U \hat{V}_{RL}$ and $\hat{s}_0 = \hat{g}_U \hat{V}_{LR}$ will be used. The Green function $\hat{G}_{N0}$ works for any choice of cell index N, so it is natural to apply it to the cases $N \to N-1$ and $N \to N+1$ in Eq. 2.26. This results in the pair of equations

$$\hat{G}_{N-1,0} = \hat{t}_0 \hat{G}_{N-2,0} + \hat{s}_0 \hat{G}_{N0}$$

$$\hat{G}_{N+1,0} = \hat{t}_0 \hat{G}_{N0} + \hat{s}_0 \hat{G}_{N+2,0}$$

which when substituted back into Eq. 2.26 gives

$$\hat{G}_{N0} = \hat{t}_0^2 \hat{G}_{N-2,0} + \hat{s}_0^2 \hat{G}_{N+2,0} + \hat{t}_0 \hat{s}_0 \hat{G}_{N0} + \hat{s}_0 \hat{t}_0 \hat{G}_{N0} + .$$

It should be noted that commas have been used in the matrix indices here for clarity where appropriate. Rearranging leads to

$$\hat{G}_{N0} = \hat{t}_1 \hat{G}_{N-2,0} + \hat{s}_1 \hat{G}_{N+2,0}$$

where

$$\hat{s}_1 = (\hat{I} - \hat{t}_0 \hat{s}_0 - \hat{s}_0 \hat{t}_0)^{-1} \hat{s}_0^2$$

$$\hat{t}_1 = (\hat{I} - \hat{t}_0 \hat{s}_0 - \hat{s}_0 \hat{t}_0)^{-1} \hat{t}_0^2.$$

This process can be repeated for a large number of iterations such that $N \geq 2^i$,

giving the general equation

$$\hat{G}_{N0} = \hat{t}_i \hat{G}_{N-2^i,0} + \hat{s}_i \hat{G}_{N+2^i,0}$$

where

$$\hat{s}_i = (\hat{I} - \hat{t}_{i-1}\hat{s}_{i-1} - \hat{s}_{i-1}\hat{t}_{i-1})^{-1}\hat{s}_{i-1}^2$$

$$\hat{t}_i = (\hat{I} - \hat{t}_{i-1}\hat{s}_{i-1} - \hat{s}_{i-1}\hat{t}_{i-1})^{-1}\hat{t}_{i-1}^2.$$

If $N = 2^i$ this general equation becomes

$$\hat{G}_{2^i,0} = \hat{t}_i \hat{G}_{00} + \hat{s}_i \hat{G}_{2^{i+1},0}$$

which is the i^{th} iteration of the pattern

$$\hat{G}_{10} = \hat{t}_0 \hat{G}_{00} + \hat{s}_0 \hat{G}_{2,0}$$

$$\hat{G}_{20} = \hat{t}_1 \hat{G}_{00} + \hat{s}_1 \hat{G}_{4,0}$$

$$\vdots$$

$$\hat{G}_{2^i,0} = \hat{t}_i \hat{G}_{00} + \hat{s}_i \hat{G}_{2^{i+1},0}.$$

Back-substitution of the equations starting at the i^{th} into the $(i-1)^{\text{th}}$ and so forth gives $\hat{G}_{10}$ in expanded form

$$\hat{G}_{10} = (\hat{t}_0 + \hat{s}_0\hat{t}_1 + \hat{s}_0\hat{s}_1\hat{t}_2 + \ldots + \hat{s}_0\hat{s}_1 \ldots \hat{s}_{i-1}\hat{t}_i)\hat{G}_{00} + \hat{s}_i \hat{G}_{2^{i+1},0}.$$

Iterating this function until the matrix $\hat{G}_{2^{i+1}0}$ becomes a propagator over such a large range in the system that it is effectively zero means the equation for $\hat{G}_{10}$

above is then equal to Eq. 2.25. Hence the transfer matrix $\hat{T}$ must be

$$\hat{T} = \hat{t}_0 + \hat{s}_0\hat{t}_1 + \hat{s}_0\hat{s}_1\hat{t}_2 + \ldots + \hat{s}_0\hat{s}_1 \ldots \hat{s}_{i-1}\hat{t}_i$$

which, using the iterative set of equations for $\hat{s}_i$ and $\hat{t}_i$, allow calculation of $\hat{G}_{00}$ defined in Eq. 2.24. $\hat{T}$ is calculated iteratively until it reaches sufficient convergence, similar to the convergence procedure for a semi-infinite lead in the standard recursive method. When the desired convergence criteria is met, $\hat{T}$ is substituted into Eq. 2.24 which gives the required surface Green function of the lead. This procedure is clearly much more computationally efficient than the standard recursive method for generating semi-infinite leads. As with the more rudimentary standard recursive method, the only required matrices are $\hat{H}_U$ (and thus $\hat{g}_U$ directly), $\hat{V}_{LR}$ and $\hat{V}_{RL}$, which minimises the computational requirements of the calculation.

2.5.3 Kubo formula

The electrical conductance Γ of a system can be calculated using the Kubo formula [86]. Using linear response theory the DC conductance can be expressed in terms of the recursive system Green functions as

$$\Gamma(E_F) = \frac{4e^2}{h} \,\mathrm{Tr}\left(\tilde{G}_{ii}(E_F)\hat{V}_{ij}\tilde{G}_{jj}(E_F)\hat{V}_{ji} - \hat{V}_{ij}\tilde{G}_{ji}(E_F)\hat{V}_{ij}\tilde{G}_{ji}(E_F)\right) \qquad (2.27)$$

where $\tilde{G}_{ab} = \frac{1}{2i}(\hat{G}^R_{ab} - \hat{G}^A_{ab})$ and $\hat{G}^R$ ($\hat{G}^A$) denotes a retarded (advanced) Green function [87]. The subscripted indices denote neighbouring cells i and j in the recursive scheme. The Kubo formula is equivalent to the Landauer-Buttiker formalism for ballistic conductance, and this can be seen by writing the trans-

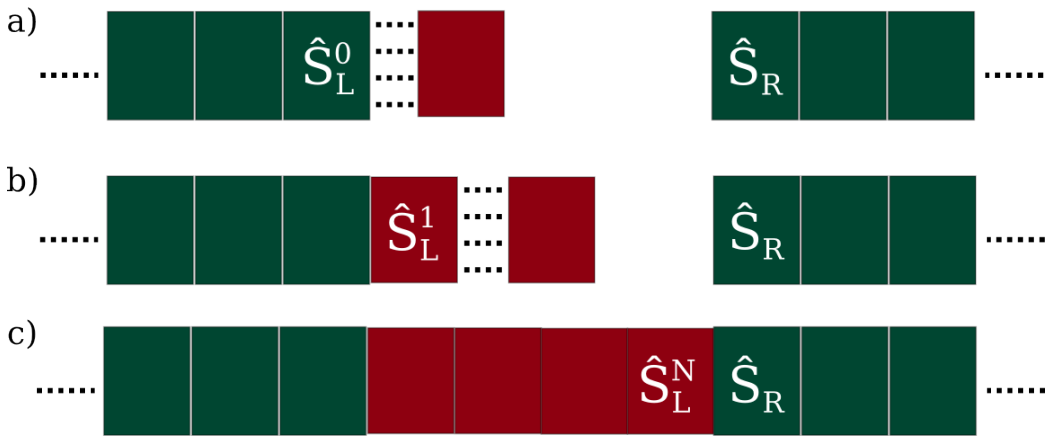

Figure 2.4: Two pristine leads (green) are constructed via the Rubio-Sancho method, with surface Green functions $\hat{S}_L^0$ and $\hat{S}_R$. The doped cells (red) are connected one-by-one to the left-hand lead using the standard recursive method and this updates the surface Green function $\hat{S}_L$ as demonstrated in steps a) and b). When the desired scattering region length of N cells is reached, the two leads are connected as shown in panel c) and the DC conductance is computed via the Kubo formula as described in the main text.

mission matrix in the latter in terms of Green functions. Kubo formalism is particularly useful for investigating the electrical response of a system upon doping. The process of efficiently calculating the conductance in a recursive system will now be described with reference to the schematic Fig. 2.4.

Firstly the pristine left-hand and right-hand leads are constructed using the Rubio-Sancho method, which yields the surface Green functions $\hat{S}_L^0$ and $\hat{S}_R$. Disorder is then incorporated by adding on cells containing impurities (steps a) and b) in Fig. 2.4) to the left-hand lead using the standard recursive approach which updates the surface Green function to $\hat{S}_L^i$ after i scattering region cells. When a desired number of cells have been added (N) to the device region (step c)) the two leads can then be connected through the Dyson equation. The DC

conductance is then calculated through the resulting interface of the two leads using the Kubo formula, setting $i = N$ and $j = R$ in Eq. 2.27. The desired Green functions $\hat{G}_{NN}$, $\hat{G}_{RR}$ and $\hat{G}_{RN}$ in the Kubo expression above are related to the surface Green functions by

$$\hat{G}_{NN} = (\hat{I} - \hat{S}_L^N \hat{V}_{LR} \hat{S}_R \hat{V}_{RL})^{-1} \hat{S}_L^N$$

$$\hat{G}_{RR} = (\hat{I} - \hat{S}_R \hat{V}_{RL} \hat{S}_L^N \hat{V}_{LR})^{-1} \hat{S}_R$$

$$\hat{G}_{RN} = \hat{S}_R \hat{V}_{RL} \hat{G}_{NN}.$$

where the retarded/advanced designation has been omitted. This technique will be used to study the scattering properties of impurity bonding types in Chap. 6.

2.6 Chapter summary

In this chapter the general mathematical foundations needed to support the work throughout this thesis have been lain, without reference to any specific physical system. The concept of Green functions in the context of condensed matter physics were introduced (Sec. 2.1) and their links to the carrier propagation and electronic phenomena such as the local density of states were discussed. The power of Green functions is that they can describe changes in the electronic properties of a system in the presence of perturbations or localised disorder, situations which arise frequently in real nanoscale systems. The effect of these changes to the original system are incorporated into the Green functions formalism by the Dyson equation (Sec. 2.2). To demonstrate the usefulness of this technique, the effect on the Green functions for a general con-

densed matter system was calculated for substitutional impurities (Sec. 2.2.1) and adsorbates (Sec. 2.2.2). The direct link between Green functions and several key electronic quantities, a product of the former's relation to the propagation of the charge carriers, was also shown. In Sec. 2.3 equations were derived that express the spatially-resolved quantities of LDOS (ρ) and electron occupation (n) in terms of Green functions. When used in conjunction with the Dyson equation, this allows one to study the real-space modulations in these electronic quantities, a phenomenon which was introduced in the preceding chapter as Friedel oscillations. In Sec. 2.4 it was shown how the Lloyd Formula method can be used to derive the changes in global density of states, global charge and global electronic energy of a system through knowledge only of the system Green functions and the local perturbation. Deriving these quantities and expressing them in this way allows for the maximum amount of mathematical transparency to be achieved for the work in this thesis, something which is not achievable using purely computational methods such as DFT. In the final section of this chapter recursive techniques were introduced along with the Kubo formula for DC conductance. These are advantageous when a fast numerical result is sought, such as in the case of investigating large amounts of disorder via configurational averaging. It should be emphasised that the discussion in this chapter have been extremely general and are applicable to any condensed matter system where a suitable Hamiltonian can be found. In the next chapter it will be shown how these Hamiltonians and the associated Green functions can be obtained for graphene and carbon nanotubes by exploiting the periodicity of the system, circumventing the need for recursive techniques.

Chapter 3

Green functions of graphene and carbon nanotubes

It was shown in the preceding chapter how Green functions directly relate to the electronic properties of the materials they describe. The aim of this thesis is to investigate, with a maximal amount of mathematical transparency, the behaviour of these quantities in graphene and carbon nanotubes and how they are affected by doping. It is therefore key that the Green functions of graphene and nanotubes are derived and in this chapter this will be done using a second nearest neighbour non-orthogonal tight-binding model.

A common first step for calculating the Green functions of a system is to find a suitable Hamiltonian which describes the atomic orbitals and their bonding in the material. It would then be straightforward to obtain the corresponding Green functions computationally through the recursive methods derived in

the previous chapter. Although this approach is reasonably accurate it can be computationally expensive and is effectively a 'black box' calculation, missing the details of any underlying physical processes. Because of this limitation, Green functions become much more powerful when they can instead be expressed in a simple mathematical form. This in turn allows for expressions to be derived for related quantities e.g. the local density of states. There has been extensive work done on carbon-based materials and the Green functions of these systems since their discovery. In particular, analytic expressions for the Green functions of graphene have been derived and used to describe phenomena as magnetic coupling between impurities [83, 88–90] and Friedel oscillations [39, 91]. It is common for these analytic Green functions to use a nearest-neighbour approximation for the tight-binding Hamiltonian, as well as the assumption of an orthogonal basis for the electron wavefunctions. It has been shown that this rudimentary approximation limits the scope of the resulting Green functions [92–96]. Reich et al. [97], for instance, have shown that such an approximation is valid only in the linear regime around the Dirac point. It is clear that an improvement of this approximation can be made by extending the range of the interactions contained in the Hamiltonian, and this is the main focus of this chapter. Specifically, the nearest neighbour model found in the aforementioned cited works will be extended to include electron propagation between second nearest neighbours and the effect of wavefunction overlap between the p_Z orbitals of neighbouring lattice sites. Besides extending the scope of the Green functions beyond the linear energetic regime, a second nearest neighbour with overlap model is necessary to describe the electronic structure of nanoribbons [98], tight-binding modelling of impurities using certain self-consistent methods [99] and modelling the changes in the density of states in the local region around a vacancy in the lattice [100].

Furthermore it will be shown that previous methods for approximating the off-diagonal Green functions in high symmetry directions using a stationary phase approximation (SPA) [47] can be modified to work for the extended case. The usefulness of the SPA is that it allows the off-diagonal Green functions to be written in a closed form without any integration required, as opposed to the exact computational method where, as it will be shown, at least one integral is always necessary. These approximations of the off-diagonal Green functions improve in accuracy with increasing separations, as such being perfectly suited for in-depth analysis of long-range impurity-related phenomena in graphene investigated in later chapters.

The chapter is organised as follows. Firstly the mathematical description for graphene using the extended Hamiltonian is introduced (Sec. 3.1.1) along with the associated eigenvalues and eigenvectors (Sec. 3.1.2) and the dispersion relation (Sec. 3.1.3). Using these results the graphene Green functions are then derived in double and single integral form in Sec. 3.1.4 and Sec. 3.1.5 respectively. The Green functions for the nearest neighbour sans overlap model are also stated 3.1.6. It is then shown how the integral Green functions for both models can be approximated reasonably accurately in the high symmetry directions of the lattice using the SPA, allowing for a closed-form analytic expression of the Green functions (Sec. 3.2). Sec. 3.3 demonstrates two approaches to obtaining the Green functions of carbon nanotubes - via quantisation and via recursive methods. The band gaps of various carbon nanotubes are then calculated using the different tight-binding models and recursive methods, and the results compared to those found in the literature for DFT calculations of the same systems. The recursive approach is then used to model the effect of stoichiometry on the electronic structure of boron carbonitride nanotubes (BCNTs) in Sec. 3.3.4.

For clarity it will be useful to refer to the different kinds of tight-binding assumptions as: first nearest-neighbour with no overlap (FN); second nearest-neighbour with no overlap (SN); and second nearest-neighbour with overlap (SNO). The derivation of the Green functions for graphene and nanotubes using the SNO tight-binding model constitutes a novel piece of work and was published in a peer-reviewed journal [101]. The work on BCNTs was also part of a peer-reviewed publication [102].

3.1 Graphene

3.1.1 Mathematical description of the graphene lattice

In this section the mathematical description of the graphene lattice using the SNO approximation will be outlined, in order to form a foundation for the derivation of the lattice Green functions. The method expands a derivation by Saito et al. [103] of the dispersion relation with nearest-nearest neighbour hopping and wavefunction overlap (SNO model).

Graphene is a hexagonal lattice of carbon atoms but can be thought of as being composed of two triangular and inter-penetrating sublattices, which will be referred to as the black ($\bullet$) and white ($\circ$) sublattices. A two atom unit cell is chosen containing one atom from each sublattice as demonstrated in Fig. 3.1 with the C-C inter-atomic distance being 1.42 angstrom [104]. The stability of graphene arises from its bonding structure, where carbon atoms in the lattice are bound strongly via sp^2 hybridised orbitals formed through a combination of the s, p_x and p_y orbitals. The remaining p_z orbitals exist perpendicular to

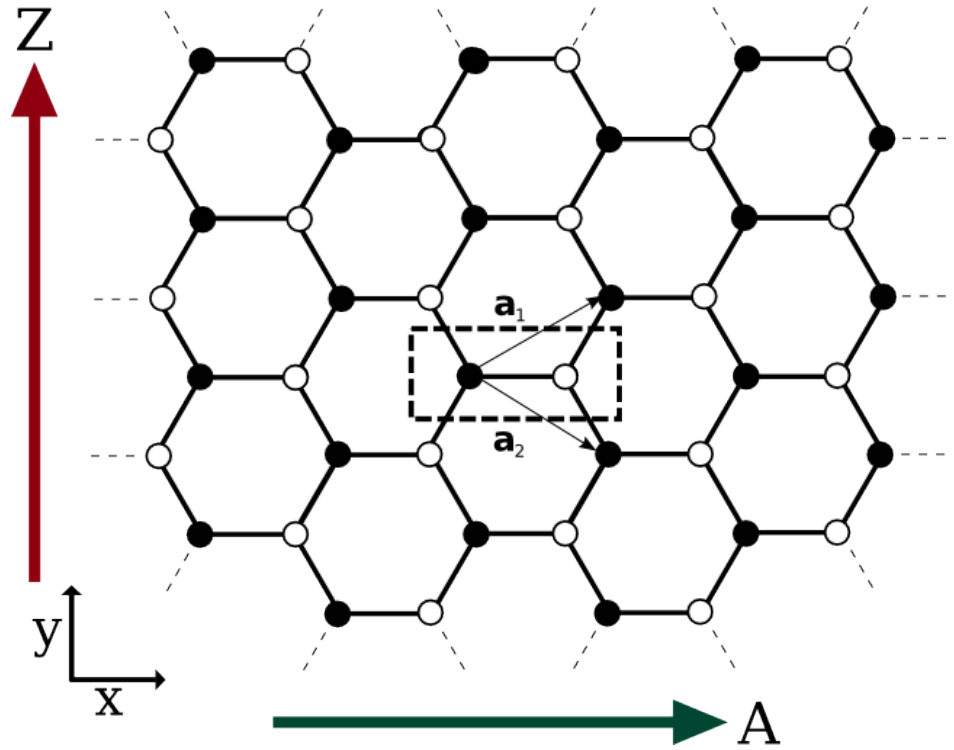

Figure 3.1: Schematic of a small part of the graphene lattice showing the primitive lattice vectors $\mathbf{a}_1 = \left\{\frac{3a}{2}\hat{\mathbf{x}}, \frac{\sqrt{3}a}{2}\hat{\mathbf{y}}\right\}$ and $\mathbf{a}_2 = \left\{\frac{3a}{2}\hat{\mathbf{x}}, -\frac{\sqrt{3}a}{2}\hat{\mathbf{y}}\right\}$. The honeycomb structure can be viewed as a bipartite lattice of two interpenetrating triangular sublattices, shown here by the black and the white atoms. A two atom unit cell, containing one atom from each sublattice, is enclosed by the dashed lines. Using these vectors the location of any unit cell in the lattice is defined as $\mathbf{r} = m\mathbf{a}_1 + n\mathbf{a}_2$ where $m, n \in \mathbb{Z}$. There are two high-symmetry directions in the lattice, the armchair and zigzag directions, and these are indicated by A and Z respectively.

the crystal plane and form π bonds between each other, each orbital containing a single conduction electron. It is assumed that each atom in the lattice has one electron orbital that participates in the electronics. This is reasonable as the covalently bonded orbitals are much lower in energy, and the $3s$ orbitals much higher in energy, than the $2p_Z$ orbitals. The SNO approach further assumes each atom can interact with three first-nearest neighbours belonging to

the opposite sublattice, and six second-nearest neighbours belonging to the same sublattice. The wavefunction overlap, quantified by the dimensionless parameter s, is assumed to be non-zero between first-nearest neighbours only.

This system is described by the real-space Hamiltonian

$$\begin{aligned}\hat{H} = \epsilon_0 &\left(\sum_{\mathbf{r}} |\mathbf{r}, \bullet\rangle \langle \mathbf{r}, \bullet| + |\mathbf{r}, \circ\rangle \langle \mathbf{r}, \circ| \right) \\ &+ t \Bigg(\sum_{\mathbf{r}} |\mathbf{r}, \bullet\rangle \Big(\langle \mathbf{r}, \circ| + \langle \mathbf{r} - \mathbf{a_2}, \circ| + \langle \mathbf{r} - \mathbf{a_1}, \circ| \Big) \\ &+ |\mathbf{r}, \circ\rangle \Big(\langle \mathbf{r}, \bullet| + \langle \mathbf{r} + \mathbf{a_2}, \bullet| + \langle \mathbf{r} + \mathbf{a_1}, \bullet| \Big) \Bigg) \\ &+ t' \Bigg(\sum_{\mathbf{r}} |\mathbf{r}, \bullet\rangle \Big(\langle \mathbf{r} - \mathbf{a_1}, \bullet| + \langle \mathbf{r} - \mathbf{a_2}, \bullet| + \langle \mathbf{r} + \mathbf{a_1} - \mathbf{a_2}, \bullet| \\ &+ \langle \mathbf{r} + \mathbf{a_1}, \bullet| + \langle \mathbf{r} + \mathbf{a_2}, \bullet| + \langle \mathbf{r} + \mathbf{a_2} - \mathbf{a_1}, \bullet| \Big) \\ &+ |\mathbf{r}, \circ\rangle \Big(\langle \mathbf{r} + \mathbf{a_1}, \circ| + \langle \mathbf{r} + \mathbf{a_2}, \circ| + \langle \mathbf{r} + \mathbf{a_2} - \mathbf{a_1}, \circ| \\ &+ \langle \mathbf{r} - \mathbf{a_1}, \circ| + \langle \mathbf{r} - \mathbf{a_2}, \circ| + \langle \mathbf{r} + \mathbf{a_1} - \mathbf{a_2}, \circ| \Big) \Bigg)\end{aligned} \tag{3.1}$$

where the vector $\mathbf{r}$ is defined as per Fig. 3.1 and is summed over the entire system. The parameters t and t' are negative energies denoting the first nearest neighbour and second nearest neighbour hopping integrals respectively, and ϵ_0 corresponds to the onsite energy of each carbon atom. Accurate values of these parameters can be found by matching the band structure obtained using this method with that found through DFT [97, 105]. It will be often useful to express all energies in units of the first nearest neighbour hopping $t = -2.7eV$. Using the parametrisation of Reich et al. [97] gives $t' = -0.037\,|t|$, $s = 0.1$ and $\epsilon_0 = 0.111\,|t|$.

The impossibility of inverting a matrix like $\hat{H}$ in Eq. 3.1 which describes an infinite system was explained in the previous chapter. To get around this issue, one can exploit the translational symmetry of the lattice - it is periodic under the translations $\mathbf{a_1}$ and $\mathbf{a_2}$ and so the electronic wavefunction must also respect this symmetry. This justifies the use of Bloch waves as solutions for these wavefunctions in the crystal. This is done by projecting the real-space Hamiltonian onto a basis set in reciprocal space defined using Bloch waves. The transformation between real space and reciprocal space can be performed via a Fourier Transform. This makes it possible to express the real space Hamiltonian in reciprocal space as a diagonalised 2x2 matrix $\hat{H}(k)$, from which point it is straightforward to get the Green functions required.

The Fourier Transform from real space to reciprocal (**k**-) space is defined as

$$|\mathbf{k}, A\rangle = \frac{1}{\sqrt{N}} \sum_r e^{i\mathbf{k}.\mathbf{r}} |\mathbf{r}, A\rangle ,$$

with the inverse transform given by

$$|\mathbf{r}, A\rangle = \frac{1}{\sqrt{N}} \sum_k e^{-i\mathbf{k}.\mathbf{r}} |\mathbf{k}, A\rangle$$

where N is the number of atomic sites and $\mathbf{k} = k_x\mathbf{k_x} + k_y\mathbf{k_y}$ defines the momentum vector of the electrons. Applying these transforms to $\hat{H}$ in Eq. 3.1 produces the desired diagonalised 2×2 Hamiltonian $\hat{H}(\mathbf{k})$.

$$\hat{H}(\mathbf{k}) = \begin{pmatrix} \epsilon_0 + t'g(\mathbf{k}) & tf(\mathbf{k}) \\ tf^*(\mathbf{k}) & \epsilon_0 + t'g(\mathbf{k}) \end{pmatrix} \tag{3.2}$$

where for convenience the functions

$$f(\mathbf{k}) = 1 + e^{i\mathbf{k}.\mathbf{a_1}} + e^{i\mathbf{k}.\mathbf{a_2}}$$

$$g(\mathbf{k}) = 2\left(\cos(\mathbf{k}.\mathbf{a_1}) + \cos(\mathbf{k}.\mathbf{a_2}) + \cos(\mathbf{k}.\mathbf{a_1} + \mathbf{k}.\mathbf{a_2})\right)$$

have been introduced.

3.1.2 Eigenvalues and eigenvectors of the diagonalised Hamiltonian

The eigenvalues of the Hamiltonian correspond to its energy spectrum. These are calculated by finding the solutions to the secular equation

$$\det\left(\hat{H} - \epsilon\hat{S}\right) = 0.$$

The matrix $\hat{S}$ is the wavefunction overlap matrix, defining how the orbitals on neighbouring lattice sites interact with each other. It can be written explicitly in diagonalised form as

$$\hat{S}(\mathbf{k}) = \begin{pmatrix} 1 & sf(\mathbf{k}) \\ sf^*(\mathbf{k}) & 1 \end{pmatrix}.$$

The non-orthogonality of orbitals is commonly expressed mathematically as

$$\langle\phi_a|\phi_b\rangle = s$$

where ϕ_a and ϕ_b describe states on neighbouring lattice sites. $\hat{S}$ becomes equiv-

alent to the identity matrix in the FN and SN models.

The solution to the secular equation for the Hamiltonian obtained in Eq. 3.2 gives spectral solutions

$$\epsilon_{\pm}(\mathbf{k}) = \frac{\epsilon_0 + t'g(\mathbf{k}) \pm t\,|f(\mathbf{k})|}{1 \pm s\,|f(\mathbf{k})|}.$$

Here the $+$ sign corresponds to the valence energy band and the $-$ sign to the conduction energy band. This energy-momentum relation, also called the dispersion relation, is extremely important for understanding the physics of carriers in the crystal. Its consequences will be discussed in more detail shortly in Sec. 3.1.3. Following from this calculation it is straightforward to identify the eigenvectors of the system, which can be done using the time-independent Schrödinger equation

$$\hat{H}\,|\Psi\rangle = \epsilon \hat{S}\,|\Psi\rangle\,.$$

Assuming the eigenvectors have the form

$$|\Psi\rangle = \begin{pmatrix} A_1 \\ A_2 \end{pmatrix}$$

yields

$$\begin{pmatrix} \epsilon_0 + t'g & tf \\ tf^* & \epsilon_0 + t'g \end{pmatrix} \begin{pmatrix} A_1 \\ A_2 \end{pmatrix} = \epsilon_{\pm} \begin{pmatrix} 1 & sf \\ sf^* & 1 \end{pmatrix} \begin{pmatrix} A_1 \\ A_2 \end{pmatrix}. \tag{3.3}$$

It is useful at this point to remind the reader that the complex quantity $f(\mathbf{k})$ (and indeed any complex quantity) can be written in terms of its magnitude and a phase factor, i.e. $f = |f|\, e^{i\phi}$ so $f^* = |f|\, e^{-i\phi}$. Using some basic algebraic manipulation Eq. 3.3 can be solved for A_1 and A_2, and along with normalising by requiring $\langle \Psi_\pm | \Psi_\pm \rangle = 1$ gives

$$|\Psi_\pm\rangle = \frac{1}{\sqrt{2}} \begin{pmatrix} 1 \\ \pm e^{i\phi} \end{pmatrix}$$

for the system's eigenvectors. The two-component eigenstate (or spinor) $|\Psi_\pm\rangle$ arises from the bipartite nature of the graphene lattice, as each sublattice is acting as a degree of freedom analogous to massless spin-$\frac{1}{2}$ fermions in the Dirac equation. This similarity between the sublattice index and spin degrees of freedom is called the *pseudospin*. Using the spinor with the Fourier transform yields the momentum state for electrons in both conduction and valence bands in the dual sublattice basis

$$|\mathbf{k}, \pm\rangle = \frac{1}{\sqrt{2N}} \sum_r e^{-i\mathbf{k}.\mathbf{r}} (|\mathbf{r}, \bullet\rangle \pm e^{-i\phi} |\mathbf{r}, \circ\rangle). \tag{3.4}$$

3.1.3 Electronic dispersion

Examining the dispersion relation $\epsilon(k_x, k_y)$ can shed light on a lot of important underlying physics that will be used shortly. For convenience the general reciprocal space wavevectors are changed to dimensionless forms

$$k_A = \frac{a k_x}{2}$$

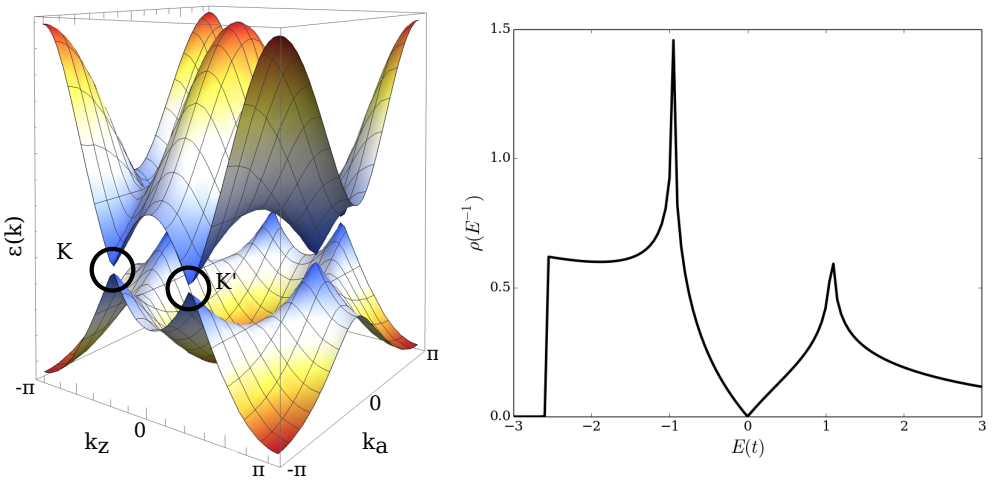

Figure 3.2: Electronic dispersion relation of graphene using the SNO approximation and Eq. 3.5 (left), along with the related density of states is (right). The six points in the first Brillouin zone shown on the left, where the conduction and valence bands touch but do not overlap, are the Dirac points. For intrinsic graphene the Fermi surface consists solely of these six points. These can be divided into two inequivalent sets called the K and K' points, two of which are indicated on the diagram positioned at $K = (-\frac{\pi}{a}, -\frac{\pi}{3a})$ and $K' = (-\frac{\pi}{a}, \frac{\pi}{3a})$. This is explained further in the text. A two-dimensional contour plot of the left-hand plot of the electronic dispersion is shown in Fig. 3.3.

$$k_Z = \frac{\sqrt{3}ak_y}{2}$$

where the subscripts refer to the high-symmetry armchair and zigzag directions of the system (c.f. Fig. 3.1). With this substitution the dispersion relation found in the last section can be rewritten as

$$\epsilon_{\pm}(k_A, k_Z) = \frac{\epsilon_0 + t'g(k_A, k_Z) \pm t\,|f(k_A, k_Z)|}{1 \pm s\,|f(k_A, k_Z)|}. \tag{3.5}$$

and this is plotted for both bands in Fig. 3.2 with the associated density of states.

The six points in reciprocal space at the edge of the Brillouin zone where the conduction and valence points touch are called Dirac points. These correspond to $\epsilon(k_A, k_Z) = 0$ and the dispersion relation around these points is linear. This can be most easily seen in close to $E = 0$ in the density of states spectrum on the right-hand side of Fig. 3.2. This linearity around the Fermi level gives rise to much of the interesting electronic properties of graphene [106]. The six Dirac points are in fact not all unique and can be divided into groups of two in-equivalent Dirac points K and K' which arise from the two inequivalent sublattices. This understanding of the dispersion relation and the Brillouin zone will be useful in the next section. A low-energy approximation of the dispersion relation is derived in the Appendix B.1 and will be useful in Chap. 5 for approximating certain Green functions.

3.1.4 Derivation of lattice Green functions

By diagonalising the graphene Hamiltonian and finding the associated eigenvalues and eigenvectors it is possible to find the Green functions for the system using Eq. 2.2, which is repeated here for ease of reference

$$\hat{G} = \lim_{\eta \to 0} \sum_{\mathbf{k}} \sum_{\pm} \frac{|\mathbf{k}_{\pm}\rangle \langle \mathbf{k}_{\pm}|}{E - \epsilon_{\pm}(\mathbf{k})}.$$

The infinitesimal imaginary part $i\eta$ has been absorbed into the energy E from this point onwards. To find the Green function between two sites in the lattice j and l on the α and β sublattices, the operator form of $\hat{G}$ can be projected onto the real-space basis

$$
\begin{aligned}
g_{ij}^{\alpha,\beta} &= \langle j,\alpha|\,\hat{G}\,|l,\beta\rangle \\
&= \sum_{\mathbf{k}}\sum_{\pm}\frac{\langle j,\alpha|\mathbf{k}_{\pm}\rangle\,\langle\mathbf{k}_{\pm}|l,\beta\rangle}{E-\epsilon_{\pm}(\mathbf{k})}.
\end{aligned}
$$

The sum over momentum space can be transformed into an integral over the Brillouin zone. The following steps are fairly tedious so for brevity only the case where $\alpha = \beta = \bullet$ will be explained in detail. The results for the other combinations will be stated.

Using the definition of $|\mathbf{k}_{\pm}\rangle$ from Eq. 3.4 and the non-orthogonality condition it can be written that the numerator term

$$
\begin{aligned}
\langle j,\bullet|\mathbf{k}_{\pm}\rangle &= \frac{1}{\sqrt{2N}}\sum_{\mathbf{r}} e^{-i\mathbf{k}.\mathbf{r}}\,\langle j,\bullet|\left(|\mathbf{r},\bullet\rangle \pm e^{-i\phi}\,|\mathbf{r},\circ\rangle\right) \\
&= \frac{1}{\sqrt{2N}} e^{-i\mathbf{k}.\mathbf{r}_j}(1 \pm s\,|f|).
\end{aligned}
\tag{3.6}
$$

A similar process shows that $\langle\mathbf{k}_{\pm}|j,\bullet\rangle = \langle j,\bullet|\mathbf{k}_{\pm}\rangle$. As $N \to \infty$ is clearly divergent for an infinite system, the following trick can be employed to switch the summation to an integral over the first Brillouin zone (FBZ)

$$
\frac{1}{N}\sum_{\mathbf{k}} \to \frac{1}{\Omega}\int\int_{\mathrm{FBZ}} d^2\mathbf{k}
$$

where $\Omega = 2\pi^2$ is the area of the FBZ which can be seen from Fig. 3.3. The FBZ naturally has a hexagonal shape which makes the integral required for calculating $g_{ij}^{\alpha,\beta}$ inelegant. By exploiting the periodicity and symmetry of reciprocal space it is possible to choose instead a rectangular area that is wholly

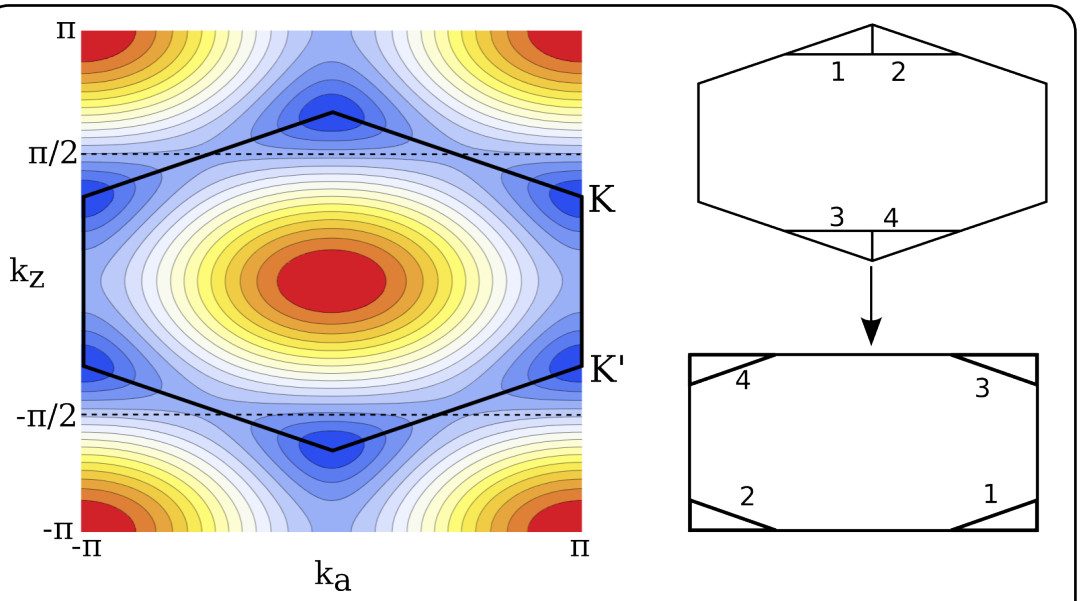

Figure 3.3: First Brillouin zone of graphene with the irreducible K and K' points as shown in Fig. 3.2. To facilitate the integral over this area, required for calculation of the Green function, the symmetry of the reciprocal space can be used. If the hexagon is divided by the $k_Z = \pm\pi/2$ lines as shown in the upper right diagram it is easy to rearrange these sections into the rectangle in the bottom right, and these areas are completely equivalent to each other vastly simplifying the calculation of the integral. The area of this resulting rectangle and thus the first Brillouin zone is $2\pi^2$.

equivalent to the FBZ. This is demonstrated in Fig. 3.3 and makes the process of integration much simpler.

Piecing together these elements the system Green functions can be written in double integral form

$$g_{jl}^{\alpha,\beta} = \frac{1}{2\pi^2}\int_{-\pi/2}^{\pi/2} dk_z \int_{-\pi}^{\pi} dk_A \sum_{\pm} \frac{\gamma_{\pm}(1 \pm s\,|f(ka,kz)|)^2 e^{ik_A(m+n)+ik_Z(m-n)}}{E(1 \pm s\,|f|) - \epsilon_0 - t'g(ka,kz) \mp t\,|f(ka,kz)|} \tag{3.7}$$

using $\mathbf{r_l} - \mathbf{r_j} = m\mathbf{a_1} + n\mathbf{a_2}$ as per Fig. 3.1 and the $\gamma_{\pm}^{\alpha,\beta}$ functions are defined as

$$\gamma_{\pm}^{\alpha,\beta}(E) = \begin{cases} 1 \pm s\,|f(ka,kz)| & \text{for } g_{j,l}^{\bullet,\bullet} \text{ and } g_{j,l}^{\circ,\circ} \\ sf^*(ka,kz) \pm e^{i\phi} & \text{for } g_{j,l}^{\bullet,\circ} \\ sf(ka,kz) \pm e^{-i\phi} & \text{for } g_{j,l}^{\circ,\bullet} \end{cases} .$$

Although g_{jl} in its current form completely describes the second nearest neighbour system with overlap, its calculation is computationally expensive due to the necessity of double integration. In the next section it will be shown how one of the integrals in Eq. 3.7 can be solved analytically through contour integration, providing an equivalent solution with an improvement of one to two orders of magnitude in computation time.

3.1.5 Single integral expression for the lattice Green functions

The methods of complex analysis, in particular contour integration [107], can be used to solve either one of the two integrals in Eq. 3.7. In this section it will be used to evaluate the integral over k_A analytically, such that the resulting single-integral expression is quicker to calculate computationally than the double-integral version derived in the previous section.

Beginning by identifying the integral to be evaluated as

$$I_1 = \frac{1}{2\pi^2} \int_{-\pi/2}^{\pi/2} dk_A \sum_{\pm} \frac{\gamma_{\pm}(1 \pm s\,|f|)^2 e^{ik_A(m+n)+ik_Z(m-n)}}{E(1 \pm s\,|f|) - \epsilon_0 - t'g \mp t\,|f|} \tag{3.8}$$

a contour can be formed in the complex k_A plane as shown in Fig. 3.4.

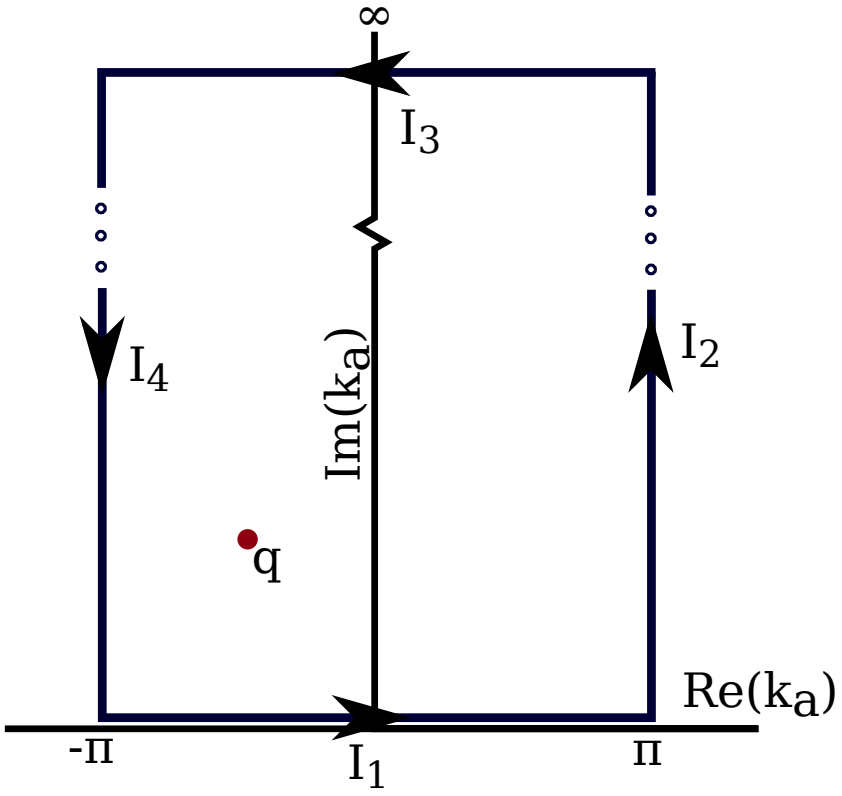

Figure 3.4: Integration contour (black) chosen in the complex k_A plane with an example of a pole in the integrand (q) indicated by the red circle. The direction of the contour is indicated by the arrows. The integral I_3 is taken as $\mathrm{Im}\, k_A \to \infty$. It follows from residue theorem that the sum of the integrals $I_1 + I_2 + I_3 + I_4$ is equal to $2\pi i$ multiplied by the sum of residues within the contour.

In general a function of the form $\frac{u(z)}{v(z)}$ has poles (points where the function diverges) for values z_0 where the denominator $v(z_0) \to 0$, so-called simple poles. Using Cauchy's residue theorem [107] the sum of the integrals, $I_1 + I_2 + I_3 + I_4$ along the contour in Fig. 3.4 can be related to the value of the integral over k_A by

$$\oint_C dz f(z) = 2\pi i \sum_{z_0} \mathrm{Res}\, f(z_0)$$

The residues of the function $\frac{u(x)}{v(x)}$ with simple poles at the points x_0 are defined

as $\mathrm{Res}\,\frac{u(x_0)}{v'(x_0)}$ where v' is the first differential of v with respect to z. Thus for I_1 a simple pole q occurs whenever the condition

$$E(1 \pm s\,|f|) - \epsilon_0 - t'g \mp t\,|f| = 0$$

is satisfied for values of k_A. Whether the plus or minus sign is taken, they yield the same solutions for $q_\pm$,

$$\begin{aligned}\cos q_\pm = \frac{1}{8t'^2 \cos k_z} \\ \times \Bigg((E^2s^2 - 2Est + t^2 + 2Et' - 2\epsilon_0 t' + 4t'^2) - 8t'^2 \cos^2 k_z \\ \pm (t - Es)\sqrt{E^2s^2 - 2Est + t^2 + 4Et' - 4\epsilon_0 t' + 12t'^2} \Bigg). \end{aligned} \quad (3.9)$$

When the inverse cosine for $q_\pm$ is taken the choice of sign implicit in this inverse operation is made such that $\mathrm{Im}(q_\pm) > 0$, ensuring the pole exists in the contour. It should be emphasised that the sign in the brackets of Eq. 3.9 results from the square root and is independent of the $\pm$ choice in the sum of Eq. 3.8.

Concerning the sum of the integrals $I_1 + I_2 + I_3 + I_4$ it can be shown from the periodicity of the integrand that $I_2 = -I_4$. Additional simplification can be made when $m = n \neq 0$ the exponential $e^{ik_A(m+n)}$ vanishes along the top of the contour indicated by I_3. However, care must be taken in the case $m = n = 0$ as the integrand I_3 no longer vanishes. It can be shown through functional analysis that the contribution is finite, going as $\sim -Es$ and arising purely as a result of the wavefunction overlap. Although an exact closed-form solution of I_3 is not obtainable, it can either be calculated through computational methods or using a functional form for the linear solution. Due to the symmetry of the lattice, such special care is only needed for the diagonal Green function $g^{\bullet\bullet}_{00}$

when $s \neq 0$, as $g_{00}^{\bullet\circ}$ or $g_{00}^{\circ\bullet}$ can be found using non-zero values of m and n for which I_3 vanishes. Hence the integral I_1 can otherwise be shown to be equal to

$$I_1 = 2\pi i \sum_{\pm} \sum_{q} \frac{\gamma_{\pm} |f| (1 \pm s|f|)^2 e^{iq(m+n)+ik_Z(m-n)}}{2\cos k_z \sin q(2t|f| \pm (t - Es))}$$

and so

$$g_{jl}^{\alpha,\beta} = A + \frac{i}{2\pi} \int_{-\pi/2}^{\pi/2} dk_Z \sum_{q} \sum_{\pm} \frac{\gamma_{\pm} |f| (1 \pm s|f|)^2 e^{iq(m+n)+ik_Z(m-n)}}{\cos k_z \sin q(2t|f| \pm (t - Es))} \tag{3.10}$$

where

$$A = -\frac{1}{2\pi^2} \int_{-\pi}^{\pi} dx \int_{\pi/2}^{-\pi/2} \sum_{\pm} \frac{(1 \pm sf_A)^3 dk_Z}{E(1 \pm sf_A) - \epsilon_0 - t'(f_A^2 - 3) \mp tf_A} \tag{3.11}$$

for the diagonal $g_{00}^{\bullet\bullet}$ case only, and $A = 0$ otherwise. The $\pm$ of $q_{\pm}$ has been removed as the sum over all q values caters to either choice. Additionally,

$$f_A = \lim_{y \to \infty} \sqrt{1 + 4\cos(x + iy)\cos k_Z + 4\cos^2 k_Z}.$$

The necessity of including the extra integral A for the diagonal Green function is demonstrated clearly when the uncorrected and corrected Green functions are compared. These are shown in Fig. 3.5 and Fig. 3.6 respectively.

It is useful to compare the calculated LDOS between the FN (the Green function of which will be derived in the next section), SN and SNO tight binding models. A plot of the LDOS spectrum of the three models is shown in Fig. 3.7. Although the behaviour around the Dirac Point is similar between all three, it can be seen that inclusion of second nearest neighbour interactions in the Hamiltonian changes the electron-hole symmetry in the electronic structure.

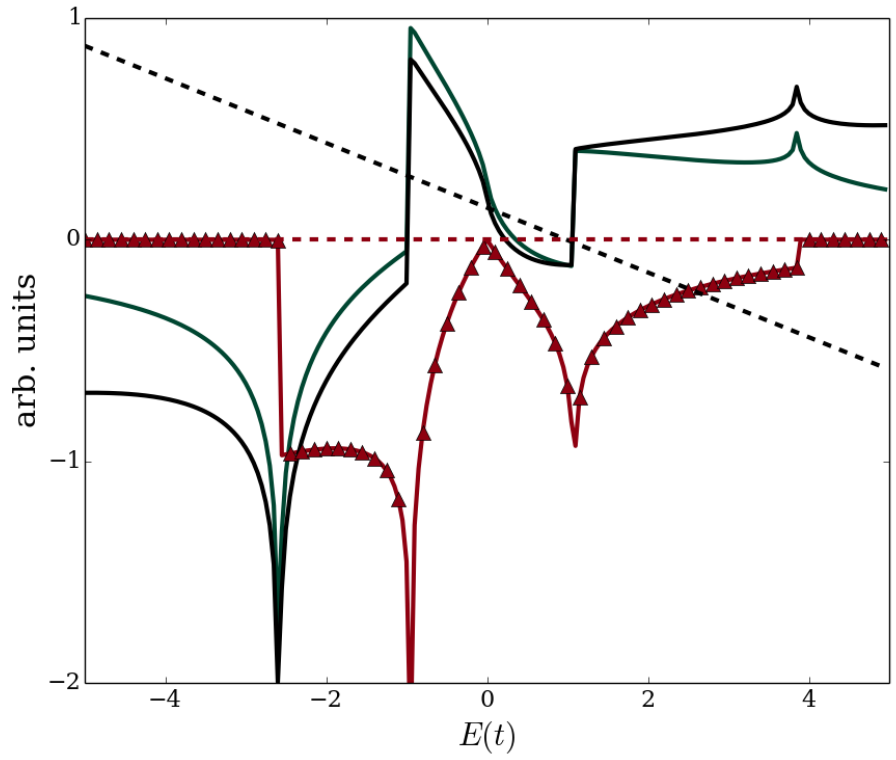

Figure 3.5: Comparisons of the Green function $g^{\bullet\bullet}_{00}$ calculated through the double integral (green solid line and red solid line for real and imaginary parts) and single integral without the corrective term applied (black solid line and red triangles for real and imaginary parts). Also shown is the value of A from Eq. 3.11 with real and imaginary parts indicated by the black and red dashed lines respectively.

Furthermore there is a drastic change in the spectrum when wavefunction overlap is accounted for, as shown by the black solid line.

This summarises the discussion of the Green functions of graphene using the SNO and SN models. Beginning from a Hamiltonian with next-nearest neighbour interactions with a non-orthogonal basis the lattice Green function has been derived, a double-integral function over the FBZ in reciprocal space. An

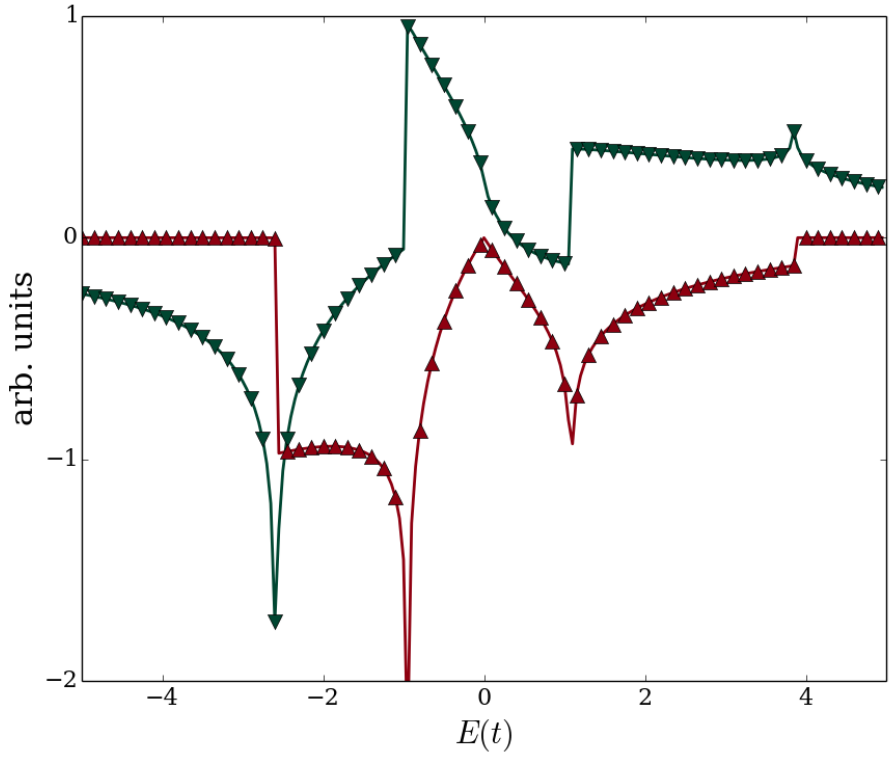

Figure 3.6: Comparisons of the Green function $g^{\bullet\bullet}_{00}$ calculated through the Double Integral (black solid line and red solid line for real and imaginary parts) and Single Integral with the correction term applied (green triangles and black diamonds for real and imaginary parts).

additional step was also shown which reduces the Green function to a single integral, making its computation less time-consuming.

3.1.6 First nearest neighbour Green functions

The discussions in this work can be made much simpler by virtue of the fact that much of the physics in graphene relies on the behaviour in the linear dis-

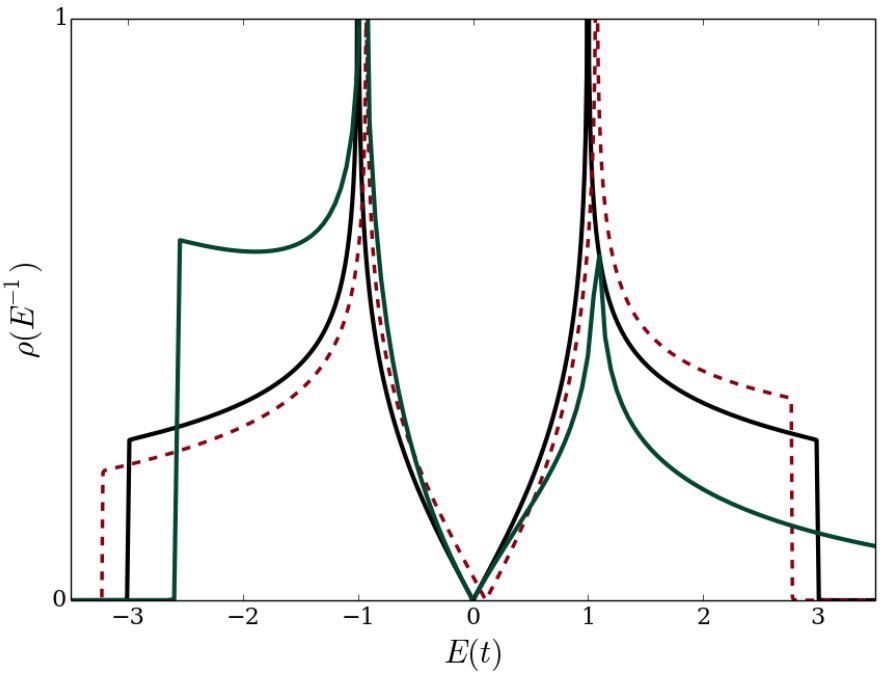

Figure 3.7: Local Density of States (LDOS) spectrum comparison of the FN (black), SN (red dashed) and SNO (green) models. Introduction of t' or s destroys the electron-hole symmetry.

persion regime around the Dirac point where the Fermi energy $E_F = 0$. By inspection of Fig. 3.7 and the general Green function behaviour one can see the FN model (where $\epsilon_0 = 0$, $t' = 0$ and $s = 0$) can be used without any loss of generality, and it will now be derived. The derivation follows the same prescription as was used for the SNO model, albeit with vastly simpler algebra. The equivalent expression for the general Green function $g_{jl}^{\alpha,\beta}$ in this regime (c.f. Eq. 3.10) is

$$g_{jl}^{\alpha,\beta} = \frac{i}{4\pi t^2} \int_{-\pi/2}^{\pi/2} dk_Z \frac{N^{\alpha,\beta}(E) e^{iq_A(m+n)+ik_Z(m-n)}}{\cos k_z \sin q} \tag{3.12}$$

where

$$q_A = \pm \cos^{-1}\left(\frac{\frac{E^2}{t^2} - 1 - 4\cos^2 k_Z}{4\cos k_Z}\right)$$

when the first integral over the k_A direction is solved, and

$$g_{jl}^{\alpha,\beta} = \frac{i}{4\pi t^2}\sum_{\pm}\int_{-\pi}^{\pi} dk_A \frac{N^{\alpha,\beta}(E)e^{ik_A(m+n)+iq_Z^{\pm}(m-n)}}{\sin 2q_Z^{\pm} + \sin q_Z^{\pm}\cos k_A} \tag{3.13}$$

where

$$q_Z^{\pm} = \pm \cos^{-1}\Big(-\frac{1}{2}(\cos k_A \pm \sqrt{\frac{E^2}{t^2} - \sin^2 k_A})\Big)$$

when the first integral over the k_Z direction is solved. In both cases

$$N^{\alpha,\beta}(E) = \begin{cases} E & \text{for } g_{j,l}^{\bullet,\bullet} \text{ and } g_{j,l}^{\circ,\circ} \\ f(q,k_Z) & \text{for } g_{j,l}^{\bullet,\circ} \\ f^*(q,k_Z) & \text{for } g_{j,l}^{\circ,\bullet}. \end{cases}.$$

These forms of the general Green function vastly simplify much of the mathematics used in later chapters, without much loss of generality in the systems that will be considered. As mathematical transparency is required it is often sufficient to use only the FN approximation. In the next section it will be shown how off-diagonal Green functions g_{jl} for both the FN and SNO approaches can be approximated along the crystallographic high-symmetry directions using a stationary phase approximation.

3.2 Stationary phase approximation

The stationary phase approximation (SPA) is a method to approximate quickly oscillating integrals of the form

$$\int dy F(y) e^{i\phi(y)x}. \tag{3.14}$$

The basic principle is assuming that sizeable x values lead to large variations in the phase term which in turn leads to large and rapid oscillations of the integrand. When integrated, these different oscillatory sections will be added together leading to a situation analogous to constructive and destructive interference. While the majority of these sections cancel out, regions around points of stationary phase (y_0) will not. It is apparent then that Eq. 3.14 can be approximated by simply considering the integrand behaviour around these stationary points. Mathematically speaking, a stationary point exists whenever the condition

$$\left.\frac{d\phi}{dy}\right|_{y_0} = 0$$

is satisfied. The behaviour of $\phi(y)$ around these points can be found by expanding it via Taylor series

$$\phi(y) \approx \sum_{y_0} \left[\phi(y_0) + \frac{1}{2}\left.\frac{d^2\phi}{dy^2}\right|_{y_0} (y - y_0)^2 + \dots\right]$$

and substituting into Eq. 3.14. Assume for the moment only one stationary point exists. Approximating $\phi(y)$ to second-order and assuming that $F(y)$ is slowly varying around stationary point y_0 allows for $F(y)$ to be brought out-

side the integral, along with $e^{i\phi(y_0)x}$ which is constant in y, to give

$$\int dy F(y) e^{i\phi(y)x} = F(y_0) e^{i\phi(y_0)x} \int dy e^{i\frac{1}{2}\frac{d^2\phi}{dy^2}(y-y_0)^2 x}.$$

The integral part of the above is similar to the Gaussian integral centred around y_0 which has the well-known solution

$$\int_{-\infty}^{\infty} dx e^{-ax^2} = \sqrt{\frac{\pi}{a}}.$$

Combining this result with the previous steps gives the stationary phase approximation

$$\int dy F(y) e^{i\phi(y)x} \approx \sum_{y_0} F(y_0) e^{i\phi(y_0)x} \sqrt{\frac{2i\pi}{\phi''(y_0)x}} \tag{3.15}$$

where a sum has been taken over y_0 to account for the existence of several stationary points. Comparison of this equation to the Green functions of the SNO and FN models, given in Eq. 3.10 and Eq. 3.12 respectively, shows that the SPA can be used to approximate them well, given the condition that the sites j and l are separated by a large distance which would cause the integrands to oscillate rapidly as $m + n \gg 1$. The main reason to do this is that it allows for the derivation of a completely analytic expression for the off-diagonal Green functions in the system, which will become extremely important in later chapters. For example, inter-impurity interactions, Friedel oscillations and electron scattering by dopants are often expressed using long-range off-diagonal Green functions. This is a great help in trying to model these phenomena in a mathematically transparent manner. To demonstrate the applicability of the SPA, in this section the off-diagonal Green functions for SNO and FN models will be found where j and l are assumed to be separated sufficiently in the armchair direction (where $m = n$, see Fig. 3.1). A similar methodology can be applied

to find SPA expressions for Green functions in other directions also. For both FN and SNO models the single integral form of the Green function is used where the solved integral was the one over the k_A direction. The reasoning behind this is that the resulting equations only have stationary points in these directions when the Green function required is also in the armchair direction. When calculating the SPA along the zigzag direction it is required to the other k_Z solved integral for the same reasons.

3.2.1 Second nearest-neighbour approximations

The analogy between the single integral version of g_{jl} in Eq. 3.10 and the SPA expression in Eq. 3.15 becomes more apparent when a distance term $D = m+n$ is introduced. This also counts the unit cells along the armchair direction between j and l ($\frac{D}{2}$, which can be inferred by Fig. 3.1) which when substituted into Eq. 3.10 yields

$$g_{jl} = \frac{i}{2\pi}\int_{-\pi/2}^{\pi/2} dk_Z \sum_q \sum_{\pm} \frac{\gamma_{\pm}\left|f\right|\left(1+s\left|f\right|\right)^2 e^{iqD}}{\cos k_z \sin q(2t\left|f\right| \pm (t-Es))}.$$

Identifying q as equivalent to the phase term ϕ in Eq. 3.15 allows the stationary points to be determined algebraically using the condition

$$\frac{dq_{\pm}}{dk_z}|_{q_0} = 0.$$

The second order differential of $q_{\pm}$ is more tricky to determine and its algebraic expression is extremely lengthy so it is not included here. Alternatively it can be found numerically using $\frac{d^2 q_{\pm}}{dk_z^2} = \lim_{h\to 0} \frac{q'(k_z+h)-q'(k_z)}{h}$ to a very high degree of accuracy. The exact expression of the closed-form Green function is not

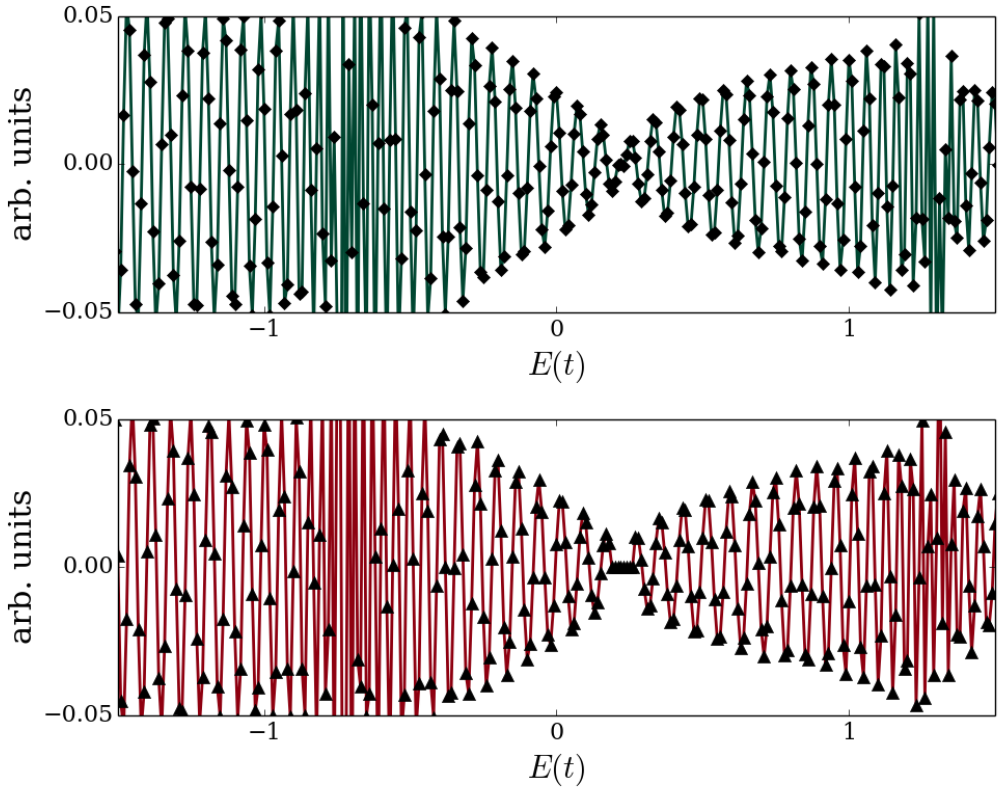

Figure 3.8: Comparison of single integral (points) and SPA calculations (continuous) of the Real (top) and Imaginary (bottom) parts of the Green function g_{jl} for a separation of $m + n = 80$ in the armchair direction, same sublattice.

included here as it is extremely long and not particularly insightful, however the numerical results will be shown.

A comparison between the single integral and SPA solution for g_{jl} is demonstrated in Fig. 3.8 where sites j and l share the same sublattice and are separated by a distance of $D = 80$. This approximation works for all sublattice arrangements and improves in accuracy with increasing separations. A much more concise expression for the Green function can be derived when using the

FN approximation, and this will be shown now.

3.2.2 First nearest neighbour; no overlap

It was explained in Sec. 3.1.6 that most of the interesting physics of graphene occurs around the Dirac point, where the Fermi level lies if they system is pristine. It was shown that the LDOS obtained using the FN approximation closely matches that of the SNO model in this region. However, the former gives a vastly simplified form of g_{jl} compared to the more nuanced SNO approximation. This is quite useful as it allows for simpler mathematical descriptions of Friedel oscillations and related phenomena. This will greatly benefit later discussions, and in this section an expression for g_{jl} will be derived using the SPA in the FN approximation.

Beginning in a similar way to the method used for the SNO SPA Green function in the previous section, the expression for g_{jl} given by Eq. 3.12 for the FN model bears many similarities to the SPA integral of Eq. 3.15. The Green function considered here will be in the armchair direction between sites on the same sublattice ($m = n$ and $\alpha = \beta$) which is given by

$$g_{jl}^{\alpha,\beta} = \frac{iE}{4\pi t^2} \int_{-\pi/2}^{\pi/2} dk_Z \frac{e^{iq_A(k_Z)(m+n)}}{\cos k_Z \sin q_A(k_Z)}$$

and the phase term

$$q_A(k_Z) = \pm \cos^{-1}\left(\frac{\frac{E^2}{t^2} - 1 - 4\cos^2 k_Z}{4\cos k_Z}\right).$$

With this expression the points of stationary phase, denoted k_Z^0, and the required first and second order derivatives of $q(k_Z)$ can be found. The phase

term is replaced by the Taylor expansion

$$q_A(k_Z) \approx q_A(k_Z^0) + q_A'(k_Z^0)(k_Z - k_Z^0) + \frac{1}{2}q_A''(k_Z^0)(k_Z - k_Z^0)^2 + \dots$$

To make the distinction between the full version of q_A and the terms in its Taylor expansion the substitution $q_A(k_Z^0) = Q$ for the zeroth order derivative and $q_A''(k_Z^0) = W$ for the second order derivative will be made. Imposing $q'(k_Z) = 0$ gives two sets of stationary points

$$k_Z^0 = \begin{cases} 0 & |E| < |t| \\ \pm\cos^{-1}\left(\frac{\sqrt{t^2-E^2}}{2t} \quad |E| > |t|\right) \end{cases} \tag{3.16}$$

When considering the SPA around energies of $|t|$ it is sometimes necessary to include contributions from both cases. Through substitution

$$Q(E) = \begin{cases} \pm\cos^{-1}\left(-\sqrt{1-\frac{E^2}{t^2}}\right) & |E| < |t| \\ \pm\cos^{-1}\left(\frac{E^2-5t^2}{4t^2}\right) & |E| > |t| \end{cases}$$

and

$$W(E) = \begin{cases} \pm\frac{E^2+3t^2}{E\sqrt{t^2-E^2}} & |E| < |t| \\ \pm\frac{E^2+3t^2}{\sqrt{(t^2-E^2)(E^2-9t^2)}} & |E| > |t|\,. \end{cases}$$

The stationary phase approximation for g_{jl} is then

$$g_{jl}^{\alpha=\beta} = \frac{iE}{4\pi t^2}\sum_{k_Z^0}\sqrt{\frac{2i\pi}{W(E)(m+n)}}\frac{e^{iQ(E)(m+n)}}{\cos k_Z^0 \sin Q(E)}$$

where the exact values of k_Z^0 summed over are determined by Eq. 3.16. Using the expressions for Q and W it follows that g_{jl} is described by the approxima-

tion

$$g_{jl}^{\alpha=\beta} \approx -\sqrt{\frac{2}{i\pi}} \frac{\sqrt{E}}{\sqrt{(E^2+3t^2)\sqrt{t^2-E^2}}} \frac{e^{iQ(E)(m+n)}}{m+n} \tag{3.17}$$

when $E \leq |t|$ and

$$g_{jl}^{\alpha=\beta} \approx \frac{iE}{4\pi t^2} \sqrt{\frac{2i\pi}{D}} e^{iQ(E)D} \frac{\sqrt{\sqrt{(t^2-E^2)(E^2-9t^2)}}}{\sqrt{\pm 1}\sqrt{1-(\frac{E^2-5t^2}{4t^2})^2}\sqrt{E^2+3t^2}}$$

when $E > |t|$. Similarly, expressions for $g_{jl}^{\alpha\beta}$ for armchair separation when $\alpha \neq \beta$ can be obtained using this prescription. Generally, any off-diagonal Green function g_{jl} can be expressed concisely in the form

$$g_{jl}(E) = A(E) e^{iQ(E)D} \frac{1}{\sqrt{D}} \tag{3.18}$$

where the coefficients $A(E) = \bar{A}(E) N^{\alpha,\beta}(E)$ splits A into sublattice independent and dependent terms, the former given by

$$\bar{A}(E) = \sqrt{\frac{2i}{\pi}} \frac{1}{\sqrt{E(E^2+3t^2)\sqrt{t^2-E^2}}}$$

and the latter defined in Sec. 3.1.6.

As in the case of the SNO model, these Green functions expressions are extremely accurate giving a result similar to that shown in Fig. 3.8, working best for separations beyond a few lattice spacings along the high symmetry directions. An example of this accuracy is for an armchair separation of D = 5 the agreement between analytic and numerical calculations of g_{jl} has an error of less than 1% over 95% of the energy spectrum. The derivation of the stationary phase approximation for g_{jl} wraps up the discussion of this chapter on the

Green functions of the periodic graphene lattice.

3.3 Carbon nanotubes

It is a straightforward exercise to use the Green function of the SNO and FN models to obtain the Green function for a carbon nanotube (CNT). This can be done through the quantisation of the momentum in the circumferential direction of the desired tube geometry. An integer number of electron wavelengths is required along this direction to preserve continuity of the wavefunction. In this section the Green function of a zigzag CNT (or ZZNT), so-called because the circumferential direction lies in the zigzag direction as indicated in Fig. 3.1, will be derived within both the SNO and FN approximations. In the final subsection the band gaps obtained using this method will be compared to a recursive FN model and recent DFT results from the literature [108]. This methodology can also be extended to armchair CNTs (ACNTs) by imposing a similar suitable quantisation condition.

CNTs in general are particularly interesting because their electronic characteristics are uniquely determined by their geometry and width N_C, where N_C is an integer indicating how many unit cells are in the circumferential direction. The quantisation of the electron momentum gives rise to one-dimensional lines of allowed momenta in reciprocal space. The locations where these lines intersect with the graphene Fermi surface determine the CNT's electronic structure - if lines cross the Dirac points then the tube is metallic. It is well known that such nanotubes are metallic for widths $N_C = 0 \pmod 3$, and semi-conducting otherwise [109].

3.3.1 Via bulk graphene Green functions

Beginning with the double integral expression for the graphene lattice SNO Green function in Eq. 3.7, the momentum in the k_Z direction for a ZZNT must be quantised such that $k_Z = \frac{\pi j}{N_C}$, where j is an integer running from 0 to $N_C - 1$, in order to satisfy the quantisation condition. As a consequence of this, what was originally an integral over the Brillouin zone in the Green function must be adapted to a discrete summation as only quantised values of k_Z are allowed. This change is expressed mathematically as

$$\frac{1}{\pi}\int dk_Z \to \frac{1}{N_C}\sum_j$$

and upon substitution into Eq. 3.7 results in a single-integral expression. This can then further be solved using the contour integration methods of Sec. 3.1.5, yielding a fully analytic and exact expression for the CNT Green function g_{jl} with no integration required:

$$g_{jl} = \frac{i}{2N_C}\sum_j\sum_q\sum_{\pm}\frac{\gamma_{\pm}\left|f\right|\left(1 \pm s\left|f\right|\right)^2 e^{iq_Z^{\pm}(m+n)+i\frac{\pi j}{N_C}(m-n)}}{\cos\left(\frac{\pi j}{N_C}\right)\sin q_Z^{\pm}(2t\left|f\right| \pm (t - Es))}. \tag{3.19}$$

The poles here are similar to those of Eq. 3.10 but with the quantized k_Z momentum. Following the same steps with the FN model leads to a similar equation

$$g_{jl} = \frac{i}{4t^2 N_C}\sum_j\frac{N^{\alpha,\beta}e^{iq_A(m+n)+i\frac{\pi j}{N_C}(m-n)}}{\cos\left(\frac{\pi j}{N_C}\right)\sin q_A} \tag{3.20}$$

the coefficients are the same as those used in the bulk FN Green function in Eq. 3.12. Recursive methods introduced for a general system in Sec. 2.5 will now be applied to the case of a carbon nanotube, an alternate way of obtaining the system Green functions numerically. Following this the electronic spectra from the FN, SNO and recursive methods will be compared to those found in the literature using other methods.

3.3.2 Via recursive methods

From previous discussion of the recursive method (Sec. 2.5) it has been shown that the matrices required for building a system using either the standard or Rubio-Sancho approaches are the unit-cell Hamiltonian $\hat{H}_U$ and the connecting matrices $\hat{V}_{LR}$ and $\hat{V}_{RL}$ which connect the unit cells together. In this section it will be shown how these matrices are constructed for a ZZNT with a width of 7 atoms, hereafter referred to as a 7-ZZNT, a schematic of which is depicted in Fig. 3.9. It is common in the literature to see the geometry of a nanotube defined by a chiral vector

$$\mathbf{C}_h = n\mathbf{a}_1 + m\mathbf{a}_2$$

that determines the crystallographic wrapping. As a result any nanotube geometry can be written concisely as (n, m), with armchair nanotubes defined by $m = n$ and zigzag by $m = 0$. Nanotubes with neither armchair or zigzag geometries are called chiral nanotubes. In this notation the 7-ZZNT in Fig. 3.9 is a $(3, 0)$ nanotube.

The Hamiltonian describing this 7-ZZNT using the numbering scheme in Fig. 3.9 is the 14×14 matrix

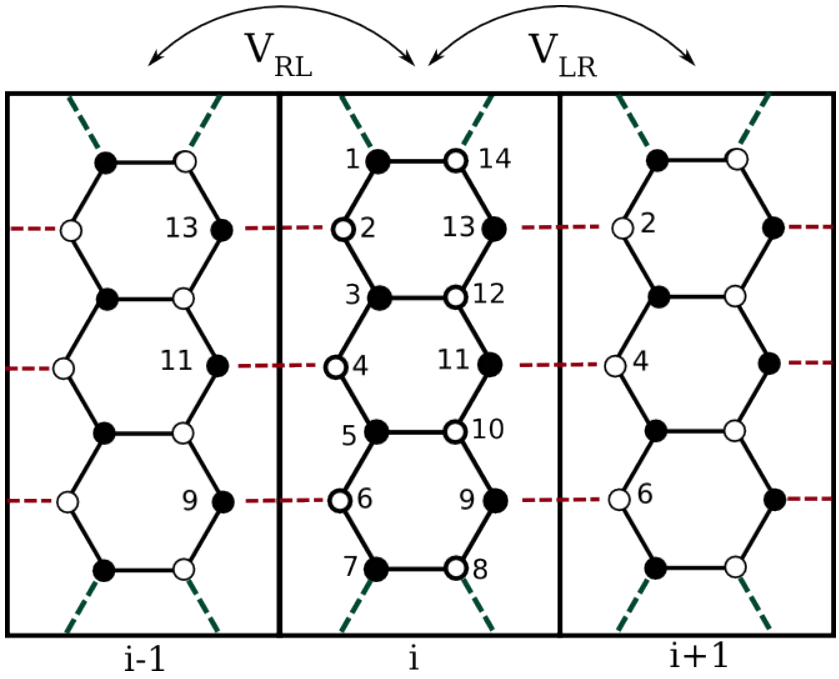

Figure 3.9: Two-dimensional projection of a 'flattened' 7-ZZNT unit cell used for the recursive methods outlined in this section. The central unit cell i contains 14 atoms numbered sequentially, a key feature is the circumferential wrapping demonstrated by the green bonds connecting the top and bottom atoms in the unit cell. The red bonds correspond to connections between neighbouring unit cells described by hopping matrices $\hat{V}_{LR}$ (i+1) and $\hat{V}_{RL}$ (i-1).

$$\hat{H}_U = \begin{pmatrix} \epsilon_1 & t_{1,2} & 0 & \dots & t_{1,7} & \dots & t_{1,14} \\ t_{2,1} & \epsilon_2 & t_{2,3} & \dots & 0 & \dots & 0 \\ 0 & t_{3,2} & \epsilon_3 & \dots & 0 & \dots & 0 \\ \vdots & \vdots & \vdots & \ddots & \vdots & \vdots & \\ t_{7,1} & 0 & 0 & \dots & \epsilon_7 & \dots & 0 \\ \vdots & \vdots & \vdots & \vdots & \vdots & \ddots & \vdots \\ t_{14,1} & 0 & 0 & \dots & 0 & \dots & \epsilon_{14} \end{pmatrix}$$

N_C	1st N.N.	2nd N.N. w/Overlap	DFT	1st N.N. (Recursive)
7	1.358 eV (146.5%)	1.377 eV (148.6%)	0.927 eV (100%)	1.2609 eV (136.0%)
11	0.929 eV (81.6%)	0.942 eV (82.7%)	1.139 eV (100%)	0.8613 eV (75.6%)
13	0.748 eV (86.5%)	0.759 eV (87.7%)	0.865 eV (100%)	0.6939 eV (80.2%)
17	0.596 eV (81.2%)	0.604 eV (82.4%)	0.734 eV (100%)	0.5535 eV (75.4%)
19	0.516 eV (83.7%)	0.523 eV (84.9%)	0.617 eV (100%)	0.4779 eV (77.5%)

Table 3.1: Comparison of the calculated band gap for various semi-conducting ZZNTs using different methods. Each value has in parentheses its percentage difference from the DFT calculated values [108] for that particular CNT. An important caveat of the band gaps obtained from the tight-binding method is their strong dependence on the parametrisation of the system. The values in this table were calculated using $t = 2.7$eV, $t' = 0.1$eV and $s = 0.1$.

where ϵ_i labels the onsite energy of site i and t_{ij} refers to the hopping energy between sites i and j. The hopping matrices $\hat{V}_{RL} = \hat{V}_{LR}^T$ can also be written down with the only non-zero elements for the former being given by

$$(\hat{V}_{RL})_{2,13} = t_{2,13}$$

$$(\hat{V}_{RL})_{4,11} = t_{4,11}$$

$$(\hat{V}_{RL})_{6,9} = t_{6,9}.$$

The system can now readily be constructed by either recursive technique and the density of states, and therefore the band gap, calculated. In the next section the band gaps for various ZZNTs will be calculated using the appropriate FN and SNO Green function equations and the recursive tight-binding approach of this section. These will then be compared to the band gaps obtained from the literature.

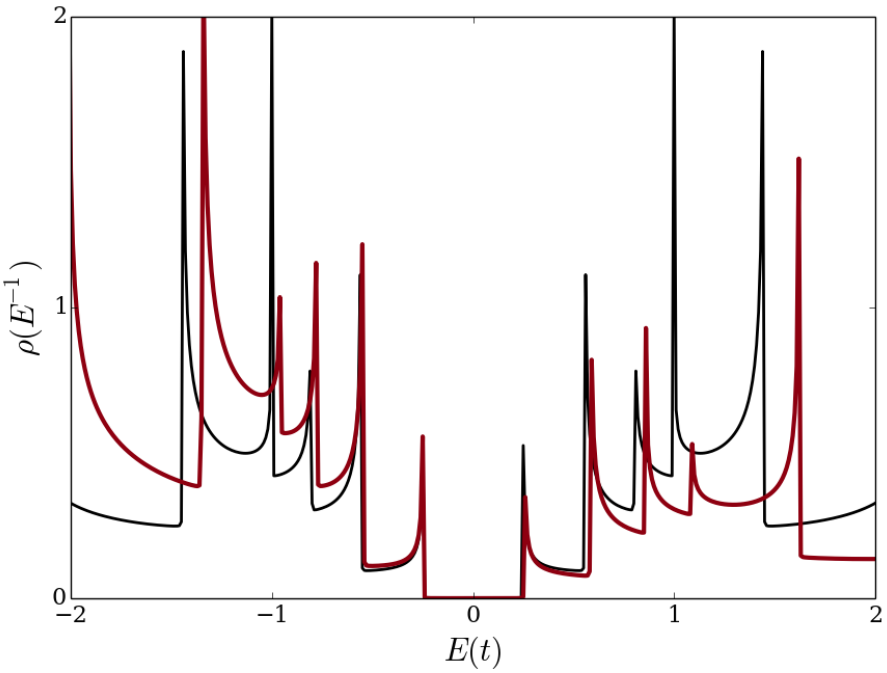

Figure 3.10: Local density of states spectrum of a 7-ZZNT calculated using the FN (black) and SNO (red) models. The features of the spectrum are markedly different between models, yet the behaviour around the band gap remains similar.

3.3.3 Band gap comparisons between different methods

Three different methods have been developed for calculating the system Green functions of any width ZZNT and thus the density of states and band gap for each case: SNO and FN through momentum quantisation and FN-based recursive. Each method relies on different assumptions and naturally one expects their reliability to be ranked in the order above. To quantify these differences the band gap of non-metallic ZZNTs can be calculated directly from the density of states and the results of this are shown in Table 3.1. These values are

also compared to the most recent accepted band gap values found through the B3LYP DFT method, believed to be the most reliable quantum chemistry tool for such a task [108]. Ultimately it can be seen that the band gaps calculated using the second nearest neighbour model are only slightly better than those calculated using the first nearest neighbour method. Although the behaviour of the LDOS spectrum is drastically different between the two models (see Fig. 3.10), the behaviour around the band gap is largely identical. This bears similarities to the case of graphene. In both cases the inclusion of extra terms in the Hamiltonian has a striking impact on the overall DOS spectrum and the system Green functions, however the behaviour around the band gap or Dirac point is largely unaffected. As the other chapters in this thesis will deal with Green functions and associated quantities around these low-energy points it is deemed sufficient to use an FN model in these cases. Doing so vastly simplifies the mathematics and allows the derivation of closed-form analytic approximations for many of the electronic quantities whose investigation is the main goal of the thesis. The advantage of being able to express them in a mathematically transparent way uncovers the underlying physical mechanisms at play, something that is not possible using other methods.

In the next section variations of the band gap in nanotubes constructed of boron carbon and nitrogen will be studied. These variations occur when the particular symmetries or chemistry of the tube are changed.

3.3.4 Stoichiometry of boron carbon nitride nanotubes

Since their discovery in the early 1990's, boron carbonitride nanotubes (BCNTs) with their intriguing electronic properties intermediate between metallic

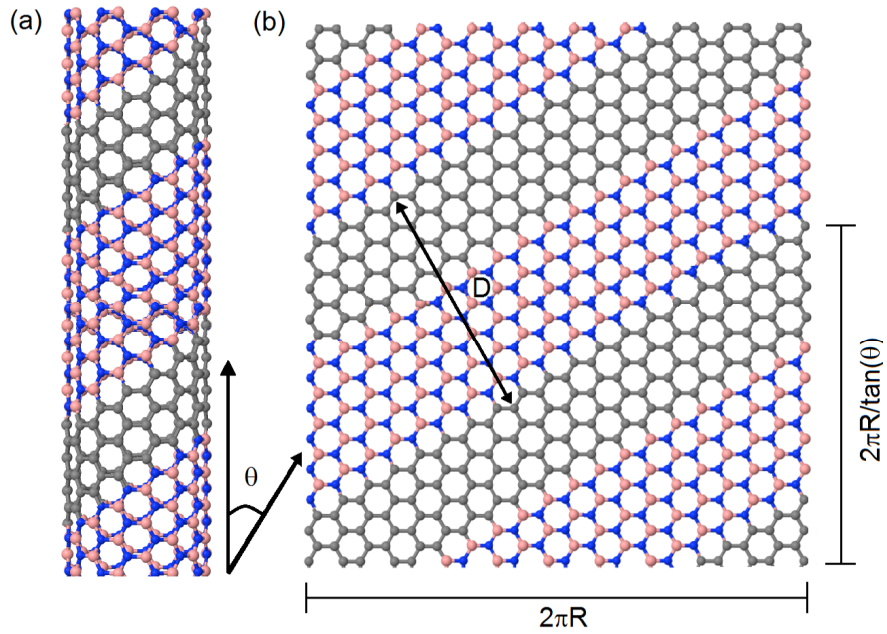

Figure 3.11: Schematic representation of a BCNT with radius R and a helical angle θ. Pink balls correspond to B atoms, grey balls correspond to C atoms and blue balls correspond to N atoms, shown as the actual tube (a) and the unwrapped tube (b). The strips of carbon atoms follow a helical path along the nanotube axis, characterized by θ and that the strips have width $2\pi R$, defining a unit cell with length $2\pi R/\tan(\theta)$. D is defined in the picture as the distance between equivalent atoms of neighbouring strips.

carbon nanotubes and dielectric boron nitride nanotubes (BNNTs), have attracted a lot of research interest both experimentally and theoretically [110–115]. It has been suggested from theoretical insights that by tailoring the distinct stoichiometries of these nanotubes, that is the relative amounts of boron carbon and nitrogen and how they are distributed in the tube, it would be possible to change their electronic properties. The natural conclusion is that by controlling this process it might be possible to engineer the physical properties of such nanotubes by an adequate control of the atomic distribution. It should be emphasised, however, that while CNTs, BNNTs and BCNTs can be

synthesised quite easily in a laboratory, precise control over their crystal geometry, size and stoichiometry is beyond the reach of experimental techniques at present.

Using methods from Sec. 2.5 and Sec. 3.3.2 the stoichiometry of BCNTs is now investigated along with its role in affecting the electronic band gap. BCNTs are bonded similar to CNTs with the exception that the onsite and hopping energies do not take the same value, and in fact differ depending on the atomic species and the specific bond. The work in this section was done in contribution to the publication [102], specifically looking at how the introduction of a helical angle θ defining the geometry of the carbon and boron-nitride strips that make up the nanotube affects the electronics. A schematic of a nanotube with a helical angle is shown in Fig. 3.11 and Fig. 3.12. The quantised Green function approach employed to find the band gap in the last section is not suitable for the case of BCNTs due to the large unit cells required, making such a solution unwieldy.

While the Hamiltonian and hopping matrices are similar in form to the CNT, the following changes must be made. The onsite energies for B atoms and N atoms take the values $\epsilon_B = +2.33$eV and $\epsilon_N = -2.50$eV respectively, in relation to the C onsite energy ($\epsilon_C = 0$eV). The values for the hopping integrals are $t_{C-C} = -3.0$eV, $t_{B-C} = -2.7$eV, $t_{C-N} = -3.14$eV and $t_{B-N} = -2.81$eV where the subscript denotes the bond connecting atomic species [116].

Inversion of the Hamiltonian gives the Green function $\hat{g}$ through Eq. 2.19 which can then be used to produce the complete BCNTs Green functions using recursive methods. The density of states of the structures is then calculated by taking a trace of the resulting matrix elements combined with Eq. 2.8 for the local density of states at each site. Two examples are shown in Fig. 3.13 for a

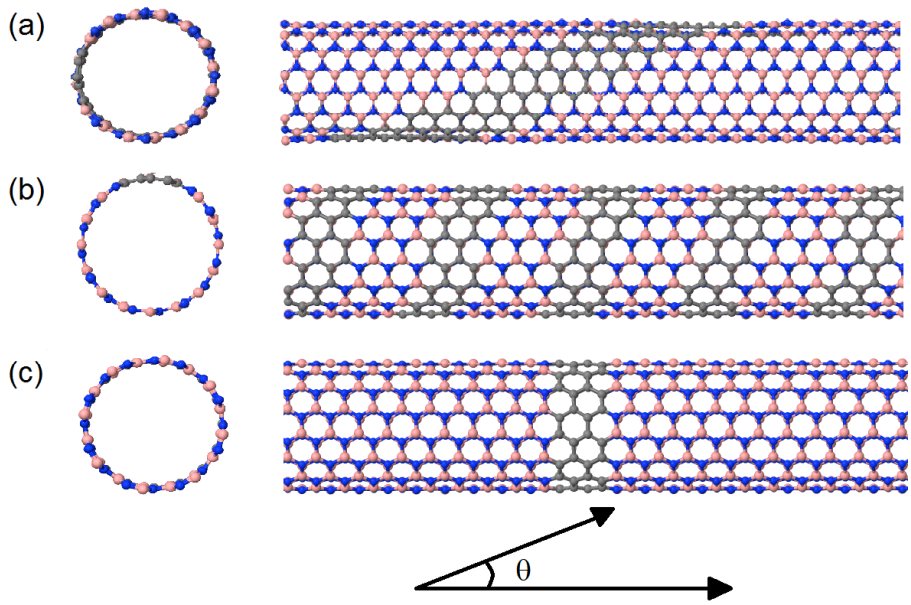

Figure 3.12: Axial and lateral illustrations of the BCNTs with helical angles (a) $\theta = \pi/6$, (b) $\theta = 7\pi/18$ and (c) $\theta = \pi/2$. Here, subtle distortion of the walls due to the C atom strips can be observed.

BNNT and a helical BCNT with a helical angle of $\theta = 0$, comparing the two shows clearly shows the impact of the carbon strips on the electronic structure.

Furthermore it is straightforward to investigate how the electronic band gap changes with θ, which is done by altering the initial Hamiltonian and hopping matrices. The result of this is shown in Fig. 3.14 showing non-monotonic dependence of the band gap with θ.

This trend can be explained by an interference in the electron wavefunctions in the nanotube, caused by scattering by the carbon strips, giving rise to modulations in the electronic properties. By Fig. 3.11(b) it can be seen that the carbon strips can be considered as linear scatters periodically separated by the distance $D = 2\pi R\cos(\theta)$. The scattering situation is analogous to the Krönig-

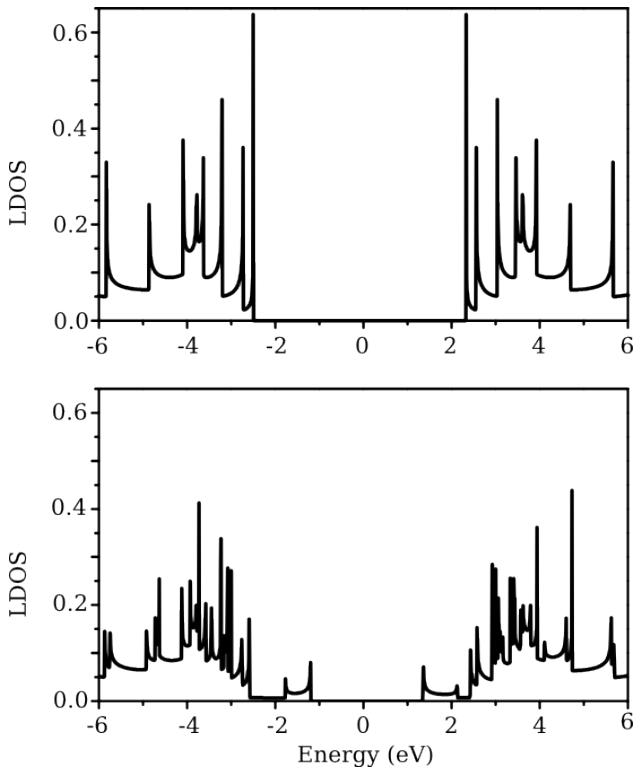

Figure 3.13: Density of states spectrum calculated using the Rubio-Sancho method of a pristine BN nanotube (top) and a helical BCNTs (bottom) with $\theta = 0$.

Penney model [117], where equidistant linear scatterers generate an interference pattern in the electronic wavefunction which can be constructive or destructive depending on D, which in the case of BCNTs is dependent on θ also. The natural conclusion is that this interference pattern is responsible for the occurrence of the size-dependent oscillations of the energy band gap as a function of the helical angle of the carbon strips. Thus if the helical angle of the carbon strips in the BCNTs can be controlled, it would be possible to produce nanotubes with made-to-order band gaps.

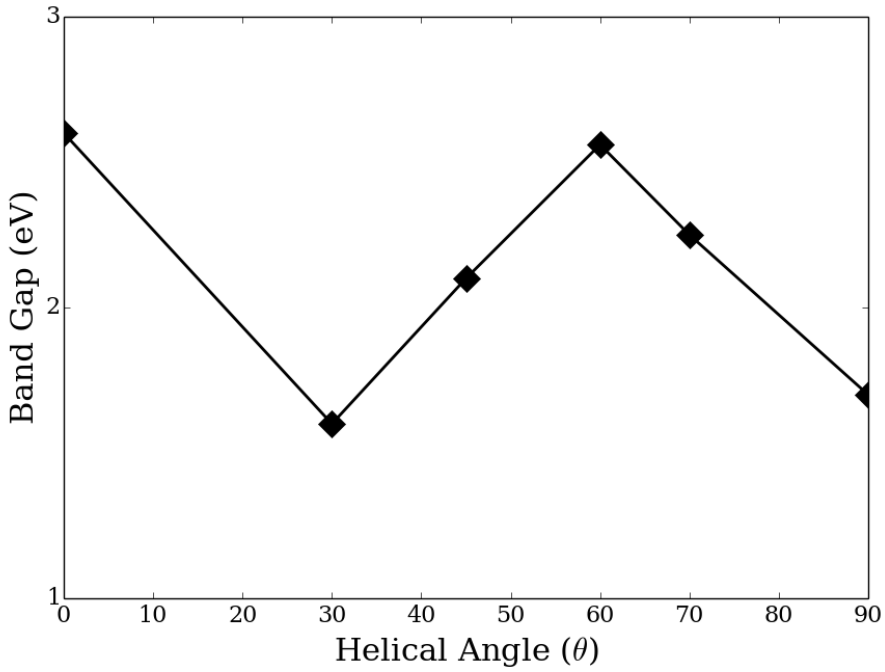

Figure 3.14: Variations of the electronic band gap as a function of θ show a non-monotonic relation. The gap is obtained directly from the DOS spectrum (e.g. Fig. 3.13).

3.4 Chapter summary

In this chapter suitable Hamiltonians and the associated Green functions have been derived for graphene and carbon nanotubes in Sec. 3.1 and Sec. 3.3 respectively. In the latter case it was shown how they can be calculated using either the graphene Green functions with enforced boundary conditions or via recursive techniques. The Green functions for the graphene lattice using a Hamiltonian accounting for first and second nearest neighbour interactions and the inclusion of a non-orthogonal basis for the electron wavefunctions have been derived. Previous derivations found in the literature for these Green functions

have only been done using a first nearest neighbour model with no wavefunction overlap. The advantage of this extended model is clear when considering extended defects and grain boundaries, which are often dealt with using recursive Green functions methods in nanoribbons, as such this new formalism allows a more general study of their qualitative behaviour. Related to the behaviour of electrons in the system, the concepts of the dispersion relation, Brillouin zone and the local density of states for both graphene and carbon nanotubes were introduced to serve later discussions.

Using contour integration it was shown that the resulting double integral expression for the graphene Green functions can be simplified to yield a single integral expression, a great benefit to their computational calculation. It was also demonstrated that in certain cases when the Green function is between two lattice sites at a large distance, this single integral can be approximated using the stationary phase approximation, further reducing the lattice Green functions into a simple analytic form (Sec. 3.2). The advantage of having the system Green functions in this form is that they can be combined with the quantities and methods derived in Chap. 2 to investigate the effects of impurities in the lattice in a mathematically transparent manner. This will be undertaken in Chap. 5 in the study of Friedel Oscillations.

Carbon nanotubes are closely linked in structure to the graphene lattice and their Green functions can be derived reasonably straightforwardly if the graphene Green functions are known by imposing periodic boundary conditions. This was done and the density of states was calculated directly using the first nearest neighbour and second nearest neighbour with overlap models. The calculation of the Green functions using recursive methods was also demonstrated. These different methods of obtaining the band gap were compared to *ab-initio*

results in the literature for a range of different nanotubes. Ultimately it was found that while the band gap remains largely unaffected by expanding the approximation of the model, the energy spectrum profile of the LDOS outside this region is quite different. This is similar to the spectrum of the graphene lattice, where the low-energy behaviour is largely unaffected by the extra hopping terms in the Hamiltonian to the next nearest neighbours and the inclusion of overlap. It is clear that the extended model of second nearest neighbour interactions with wavefunction overlap is only necessitated for investigating specific scenarios. As the bulk of this thesis investigates mainly low-energy behaviour of electronic quantities the first nearest neighbour model will be adopted for all work done in the remaining chapters. The advantage of this is that the Green functions are much simpler in form, hence it is possible to write concise expressions for the variations in these electronic quantities due to perturbations of the system by impurities. The chapter finished by applying recursive methods to a study of the helical angle of boron caronitride nanotubes and boron nitride nanotubes and how it affects the band gap. The work presented in this chapter on the calculation of the graphene Green functions using second nearest neighbour with overlap approximation, and the work on BCNTs, were published in peer-reviewed journals ([101] and [102] respectively).

Chapter 4

An inverse modelling scheme for dopants in graphene

The parameters used for the tight-binding description of nanoscale materials, for example ϵ_0 and t for graphene, are commonly found through matching the band structure obtained through DFT calculations to that using the tight-binding methods [118–124]. Specifically, these parameters are finely tuned to get a satisfactory reproduction of the band structure around the most interesting points in the electronic dispersion - for graphene this is the linear behaviour around the Dirac points. This can also be employed for finding tight-binding parameters for impurities, e.g. for example onsite energies and hopping integrals, however the process itself can be tedious and in the worst case scenario even unreliable (DFT systematically underestimates band gaps when compared to experiment, using the GW approximation can correct this however [125]). Because of this caveat it is prudent to look for alternative methods

that can get around these issues.

In this chapter a method for obtaining these parameters using an inverse modelling procedure. Similar methods have been applied to carbon nanotubes in the past where the finite density of states at zero Fermi energy makes those studies simpler [71–73]. This is a self-consistent method which uses the numerical values such as changes in occupation on lattice sites Δn and binding energies ΔE calculated through *ab-initio* in conjunction with their tight-binding Lloyd equations derived in Chap. 2. Ordinarily the impurity parameters would be known and the goal is to calculate unique values of unknown quantities like Δn and ΔE, the equations to do this were covered in Chap. 2. However if the impurity is described by N *unknown* parameters but some information about the response of the system is known (for example DFT can give information about the charge redistribution Δn) the problem can be inverted by choosing a system of N equations expressed in terms of the parameters but where the solutions are known. While these equations are highly non-linear they can be solved simultaneously and a unique set of impurity parameters can be determined. This process is called the inverse modelling method. The benefit of this method is that one can arrive at a suitable parametrisation without reference to the band structure, relying instead completely on quantitative results available from DFT. In this chapter parametrisations will be found for three common dopants found in real graphene systems - substitutional nitrogen and boron in Sec. 4.1 and a top adsorbed hydrogen atom in Sec. 4.2. It should be emphasised that the inverse modelling method is general and can be extended to other impurity species and systems if required. Indeed, the work in this chapter builds on previous research which applied the same formalism to doped CNTs [71–73].

4.1 Substitutional impurities

In the case of graphene the simplest substitutional impurities to consider are atomic boron or nitrogen as they are a similar size and form similar chemical bonds compared to the carbon atoms in the lattice. For this reason they can be introduced easily in a variety of experimental graphene growth processes with little effect on the crystal structure. In this section the inverse modelling method will be applied to find unique values of the onsite energy λ that characterise substitutional nitrogen and boron in graphene. It was shown in Chap. 2 that a system that has a substitutional impurity of onsite energy λ placed at site A described by the perturbation potential

$$\hat{V} = |A\rangle\, \lambda\, \langle A| \tag{4.1}$$

will respond by experiencing a shift in quantities such as local and global charge, Δn and ΔN, as well as the global electronic energy ΔE. Generally speaking these quantities are all expressed in terms of the matrices $\hat{g}$ and $\hat{V}$ by the set of equations

$$\Delta n_j = -\frac{2}{\pi}\,\mathrm{Im}\int_{-\infty}^{E_F} dE\, \langle j|\, \hat{g}\hat{V}[\hat{I} - \hat{g}\hat{V}]^{-1}\hat{g}\, |j\rangle$$

$$\Delta N = (\Theta(E_F - \epsilon_a) - C_0) - \frac{2}{\pi}\,\mathrm{Im}\ln\det\left(\hat{I} - \hat{g}\hat{V}\right)\Big|_{E_F}$$

$$\Delta E = E_F \Delta N + \frac{2}{\pi}\,\mathrm{Im}\int_{-\infty}^{E_F} dE \ln\det\left(\hat{I} - \hat{g}\hat{V}\right)$$

and since $\hat{V}$ is known by Eq. 4.1 these can be rewritten as

$$\Delta n_j = -\frac{2}{\pi}\,\mathrm{Im}\int_{-\infty}^{E_F} dE \frac{g_{jA}\lambda g_{Aj}}{1 - g_{jj}\lambda} \tag{4.2}$$

$$\Delta N = -\frac{2}{\pi} \operatorname{Im} \ln(1 - g_{AA}(E_F)\lambda) \tag{4.3}$$

$$\Delta E = E_F \Delta N + \frac{2}{\pi} \operatorname{Im} \int_{-\infty}^{E_F} dE \ln(1 - g_{AA}\lambda). \tag{4.4}$$

Here the subscript j refers to an arbitrary lattice site. As only a single parameter is sought it seems initially that any equation can be used for the inverse modelling procedure. It will be now demonstrated, however, that care must be taken even in this simple case and the local change in charge Δn_j is in fact the only viable choice.

Boron has one electron less than carbon and nitrogen has one electron extra which means that their introduction to graphene causes the system to be positively (p-) or negatively (n-) doped and $\Delta N = -1$ and $\Delta N = 1$ respectively. Because no integration is required in the calculation of ΔN one would initially be inclined to believe that this would be the easiest way to calculate λ. However due to the vanishing onsite Green function g_{AA} at $E_F = 0$ a solution cannot be found. Not only does this directly cause problems in determining ΔE, but ΔE would itself be tricky to evaluate using DFT anyway. The reason for this is that in tight-binding ΔE corresponds to *only* the band contribution to the total energy, whereas the change in total energy between perturbed and unperturbed systems in DFT involves the physical breaking of bonds and other effects. Values for local charge variations, however, can usually be found without much issue. Therefore to demonstrate the technique the equation for Δn_j will be used alone and ΔE discarded.

In Fig. 4.1 the quantity Δn_A, the change in charge on the impurity site, has been calculated by inserting a large range of λ values into Eq. 4.2 and plotting the result. By interpolation of the resulting points it was possible to find a cor-

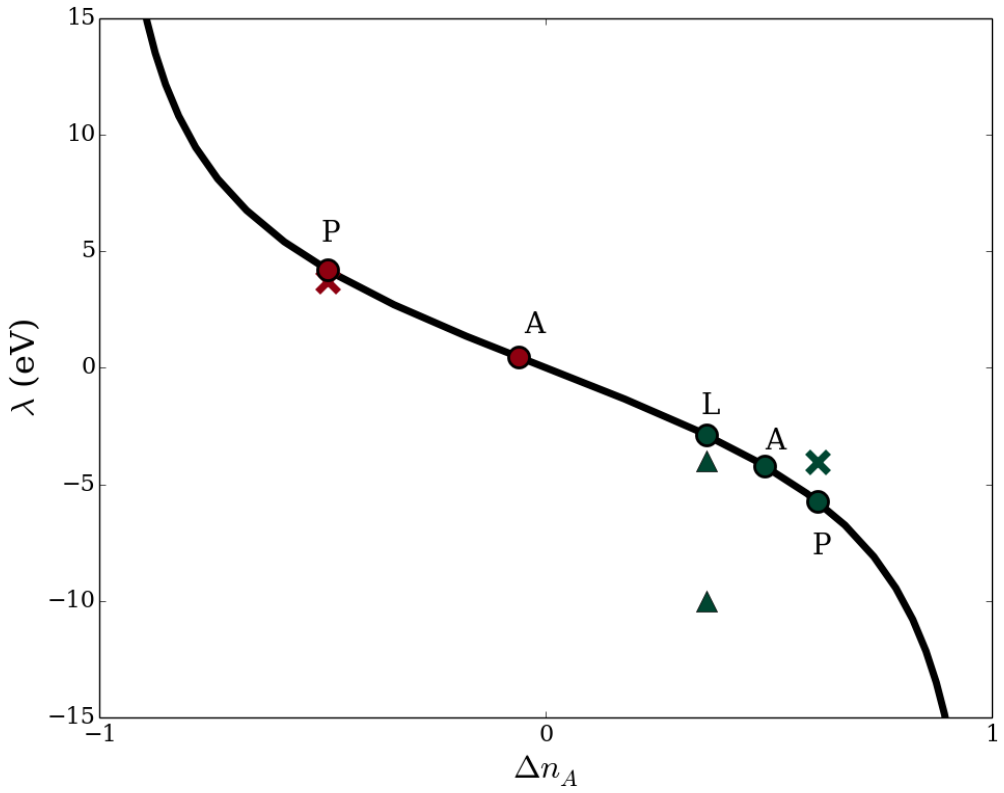

Figure 4.1: Curve relating the possible solutions for λ with the corresponding input Δn_A values (black). Particular values for Δn_N (Δn_B) were taken from the literature and corresponding λ values calculated as the green (red) circles lying along the curve. These circles are indexed by the initial of the referenced manuscript's primary author - Al-Aqtash [126], Pedersen [99] or Lambin [127]. The latter two authors also calculated λ values in their manuscripts using different methods. These are shown as crosses (Pedersen with self-consistent tight-binding) and triangles (Lambin with band structure matching).

respondence between Δn_A and λ directly whereby the input of Δn_A returns a unique λ value. The computed values are as follows and the subscript of Δn_A and λ_A will be changed to denote the impurity type for the remainder of this section - either N (nitrogen) or B (boron). As only the impurity site occupation

changes will be considered the explicit designation of choosing site A becomes redundant. DFT results by Al-Aqtash et al. [126] found onsite occupation changes of $\Delta n_N = +0.49$ for nitrogen and $\Delta n_B = -0.06$ for boron, which give $\lambda_N = -4.2eV$ and $\lambda_B = +0.45eV$ from the interpolated Δn_A, λ relation. These values have been plotted on the Δn_A, λ curve in Fig. 4.1 as green and red circles respectively and labelled A. Pedersen et al. [99] calculated onsite occupation changes using a self-consistent tight-binding method and found occupation values of $\Delta n_N = +0.61$ and $\Delta n_B = -0.49$. The inverse modelling procedure yields $\lambda_N = -5.75eV$ and $\lambda_B = +4.2eV$ for this input pair and these are marked by the green and red circles labelled P in Fig. 4.1. In the paper by Pedersen et al. λ_N and λ_A were also calculated using their self-consistent model. Their calculations found the parameters $\lambda_N = -4.06eV$ and $\lambda_B = +3.70eV$ and these are shown in Fig. 4.1 by the green and red crosses respectively. Comparing the self-consistent approach of Pedersen et al. to the inverse modelling procedure it can be seen that they produce very similar parametrisations. DFT calculations by Lambin et al. [127] for nitrogen found an occupation of $\Delta n_N = 0.36$ which corresponds to $\lambda_N = -2.9eV$ and is indicated by the green circle labelled L in Fig. 4.1. Lambin et al. also used their method to calculate tight-binding values for nitrogen using band structure matching with their DFT calculation. They obtained two possible values - either $\lambda_N = -4eV$ or $\lambda_N = -10eV$ - and these are marked on Fig. 4.1 by the green triangles. Upon direct comparison it can be seen that Lambin's first value is similar to the one obtained using the inverse modelling approach, however the second would correspond to a much more dramatic increase in occupation. In overview of Fig. 4.1 it is clear that the inverse modelling procedure compares favourably to other methods, especially Pedersen's self-consistent method.

The central result of a curve describing the λ and Δn_A relation can also be used

to consider limiting cases of λ. Recall from Chap. 2 that a vacancy is characterised by an onsite potential $\lambda \to \infty$, where $\Delta n_A \to -1$ corresponding to a complete absence of charge on this site. The LDOS spectrum for this case consists of a single bound state removed to infinity which is therefore inaccessible to electrons. The result of $\Delta n_A = -1$ for $\lambda \to \infty$ can be shown without any numerical calculation as

$$\begin{aligned}\lim_{\lambda\to\infty} n_A &= -\frac{2}{\pi}\,\mathrm{Im}\int_{-\infty}^{E_F} dE\Big(g_{AA} + \frac{g_{AA}\lambda g_{AA}}{1 - g_{AA}\lambda}\Big) \\ &\approx -\frac{2}{\pi}\,\mathrm{Im}\int_{-\infty}^{E_F} dE\Big(g_{AA} + (-g_{AA})\Big) \\ &= 0\end{aligned}$$

which is valid away from the resonance energy. Vacancies will be discussed in much more detail in Chap. 5. The opposite case where $\lambda \to -\infty$ corresponding to a hypothetical quantum dot-like structure with zero-dimensional confinement has a similar mathematical approach, except here the bound state is removed to negative infinity which yields $n_A = 2$ upon integration to $E_F = 0$.

4.2 Adsorbed impurities

In this section the inverse modelling method will be used to find a set of parameters describing a top adsorbed hydrogen atom in graphene. Atomic hydrogen (index a) is the simplest adsorbed impurity to consider and is represented by a single orbital with energy level ϵ_a containing a single electron ($C_0 = 1$) that is connected to a single host carbon atom A by the perturbation

$$\hat{V} = \tau\,|a\rangle\,\langle A| + c.c.$$

as was shown in Sec. 2.2.2. Having designated the two unknown parameters as ϵ_a and τ a corresponding pair of equations in Δn_a, Δn_A or ΔE are sought where the solutions are known via *ab-initio* methods. These will then be solved simultaneously to give an associated set of unique values for ϵ_a and τ. $\Delta N = 0$ is excluded from the set of possible equations as

$$\ln\det\left(\hat{I} - \hat{g}(E)\hat{V}\right)|_{E_F=0} = 0 \,\forall\, \{\tau, \epsilon_a\} \;\because g_{AA}(E_F = 0) = 0.$$

However it would be possible to use it if the parametrisation were extended, for example to include onsite energy changes of the host atom. The quantities ΔE and Δn_a (but usually not Δn_A) are routinely calculated in *ab-initio* studies of hydrogen adsorption on graphene and as such are readily available from the literature [128–131]. It should be noted here that the values for ΔE from the ab-initio results have been assumed to be physically equivalent to those in tight binding. This may not always be the case as tight-binding considers only the electronic contribution to ΔE while DFT can include other effects such as exchange correlations. While in principle the electronic contribution alone can be extracted from the calculation, these values are rarely available in the literature and hence the assumption stated above.

The solutions to the system of equations

$$\Delta n_a = -\frac{2}{\pi}\,\mathrm{Im}\,\frac{g_{aa}^3\tau^2}{1 - g_{AA}g_{aa}(\epsilon_a)\tau^2}$$

and

$$\Delta E = (2\Theta(E_F - \epsilon_a) - C_0)\epsilon_a + \frac{2}{\pi}\,\mathrm{Im}\int_{-\infty}^{E_F} dE \ln\left(1 - g_{AA}g_{aa}(\epsilon_a)\tau^2\right)$$

can now be plotted over a suitable region in the ϵ_a, τ parameter space. The

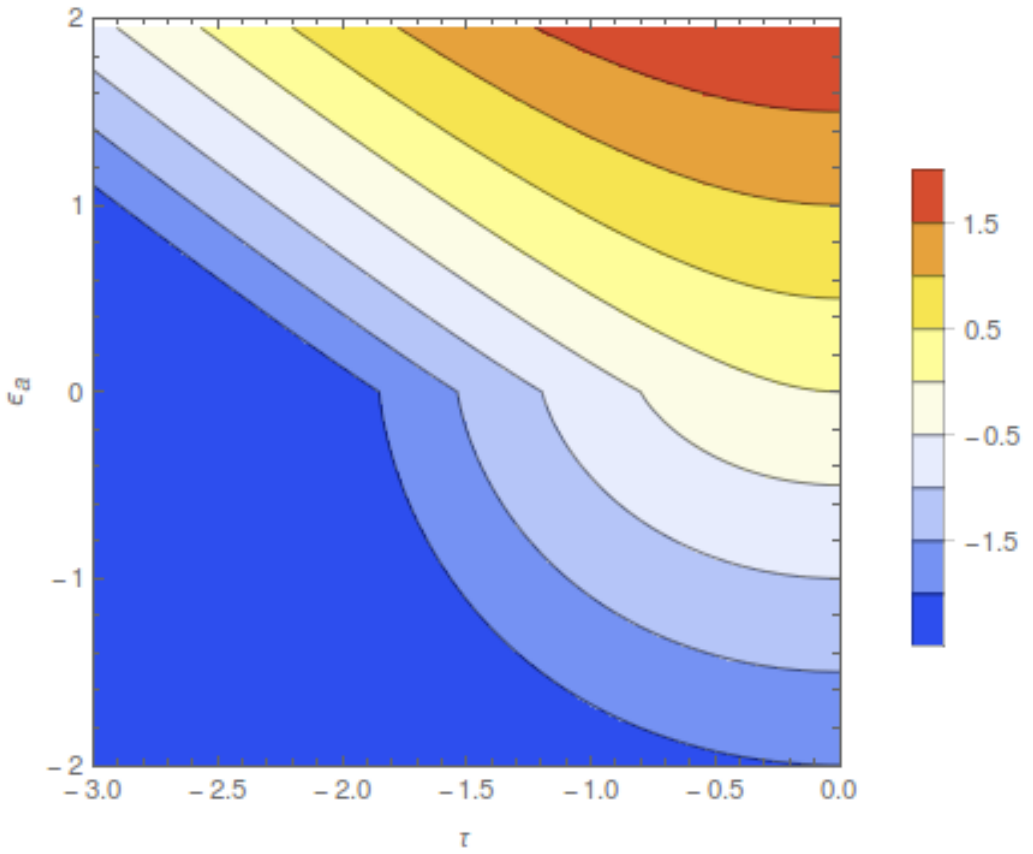

Figure 4.2: Contour plot of the variations in ΔE in units of t across a region of the ϵ_a, τ parameter space.

results are shown separately in Fig. 4.3 and Fig. 4.2 respectively. The results for Δn_a show that if the onsite energy is positive then the adsorbate loses charge and vice versa which should be expected as $E_F = 0$ in the system, hence the charge should redistribute in this manner. The results for ΔE show a decrease in total energy with increasing τ, whereas increasing ϵ_a results in higher ΔE.

Despite the non-linearity of these equations the resulting surfaces are smooth with no discontinuities across the parameter space. These surfaces can then be combined, interpolated and minimised via multi-objective optimisation rou-

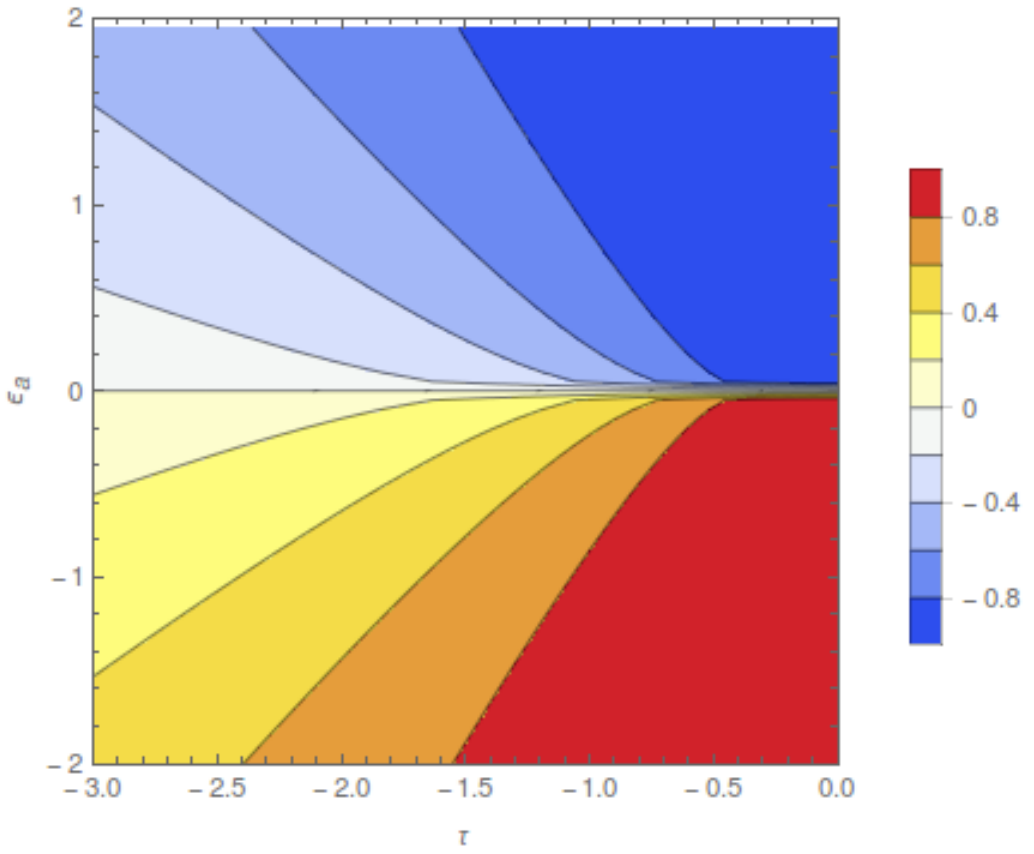

Figure 4.3: Contour plot of the variations in Δn_a over the ϵ_a, τ parameter space

tines to find unique values of ϵ_a and τ for corresponding input values of Δn_a and ΔE obtained from the literature. One particular benefit of this method of interpolation is that once the parameter space surface is known for an impurity, the trial of new Δn_a and ΔE values is extremely quick.

Results are shown in Table 4.1 for four sets of Δn_a and ΔE input values found in the literature. The outputs ϵ_a and τ can be compared directly to other tight-binding parametrisations for hydrogen. Band structure matching by Wehling et al.[132], Schmidt et al. [133] and Bang et al. [134] have obtained the tight-

$\Delta E(eV)$	Δn_a	$\epsilon_a(t)$	$\tau(t)$	Reference
-0.59	-0.37	$+0.02$	-0.58	[128]
-0.97	-0.37^*	$+0.03$	-0.74	[129]
-1.4	-0.37^*	$+0.03$	-0.88	[130]
-0.81	$+0.164$	-0.025	-0.6	[131]

Table 4.1: Δ_E and Δn_a input values with corresponding ϵ_a and τ values produced from the inverse modelling method. The asterisks indicate the re-use of Δn_a where a value was not provided in the reference.

binding parameters: $\epsilon_a = 0.66\,|t|$, $\tau = -2.2\,|t|$; $\epsilon_a = 0.14\,|t|$, $\tau = -2.15\,|t|$; and $\epsilon_a = 0$, $\tau = -2.1\,|t|$ respectively. $H+$ adatoms have also been investigated by Robinson et al. [135] who found $\epsilon_a = 0.06\,|t|$, $\tau = -1.93\,|t|$. The onsite energy values calculated using the inverse modelling method in Table 4.1 are typically small, and compare favourably to those found with those found by Schmidt et al. and Bang et al. However, this approach systemically underestimates the overlap integral which is found to be substantially weaker than the lattice hopping, compared to approximately $2t$ found with the band structure matching method. It was suggested that ΔE could be overestimated as tight-binding considers the electronic energy only versus ab-initio which includes additional effects. This does not explain the difference and this reasoning can be understood by inspection of Fig. 4.2. A smaller input value for the total energy generally results in a reduction in τ, not an increase. Throughout this chapter it has been assumed that the atomic sites closest to the point of contact with the adsorbate, or sites near to the impurity site itself in the case of substitutional atoms, do not undergo any kind of perturbation. This is called the *efficient screening hypothesis* [71]. It is well known that in a metallic system the charge density can act in such a way to screen out extraneous electric fields, however this effect is mitigated in low-dimensional systems. Therefore it could be more satisfactory to relax this hypothesis and extend the parametrisation to

include changes in the onsite energies of other lattice sites when modelling these interactions.

4.3 Chapter summary

In this chapter the tight-binding parameters for substitutional nitrogen and boron and adsorbed hydrogen impurities were calculated using an inverse modelling procedure. It was demonstrated that an impurity described by N unknown tight-binding parameters (e.g. onsite energy) can be parametrised by simultaneously solving a system of N associated tight-binding equations where the solutions are known. The equations used were global change in charge ΔN, local change in charge Δn and global change in electronic energy ΔE which were derived in Chap. 2. These quantities are routinely calculated using ab-initio techniques and exact values were taken from the available literature, allowing for determination of corresponding impurity parameters. In the case of boron and nitrogen the inverse modelling procedure produces results that compare favourably to other tight-binding parametrisation methods such as band-structure matching and self-consistent tight-binding. Similar values for λ in three out of four cases where direct comparison could be made. Concerning adsorbed atomic hydrogen, a good match of parameters to those in the literature is not found and the procedure is more challenging. While the onsite energy appears consistent, the inverse modelling method systematically underestimates the value of the hopping integral τ, yielding values approximately a third of those found using band structure matching approaches. This could possibly be resolved by relaxing the efficient screening hypothesis and this should be the immediate focus of future work on the topic.

Chapter 5

Friedel oscillations

In this chapter a framework is presented within which the Friedel oscillations (FOs) resulting from various kinds of impurities are investigated from both a numerical and an analytic 'pen and paper' point of view using the methods from Chap. 2 and Chap. 3. Both graphene, and carbon nanotubes with armchair and zigzag geometries, are investigated and a variety of impurity types considered. Previous studies examining the behaviour of FOs in the LDOS $\Delta\rho$ and carrier density Δn in graphene have relied on two assumptions - a linearisation of the electronic band structure near the Dirac points and the introduction of a momentum cut-off [39–41, 45]. The work in the first section of this chapter will be the development of a model that does not rely on these assumptions and approximations (Sec. 5.1). In the second part of this chapter (Sec. 5.2) a similar method will be applied to carbon nanotubes. Owing to their reduced dimensionality the Friedel oscillations display significantly different behaviour. One particularly interesting aspect of their behaviour is that the

features of the FOs in both systems are dictated by the bipartite nature of the underlying lattice, where the FOs are not only a function of distance but also of sublattice. This is important as it will be a key ingredient in the modelling of the sublattice segregation effect which will be done in Chap. 7. The work on Friedel oscillations in graphene was published as Ref. [91].

5.1 Graphene

The FOs in the $\Delta\rho$ and Δn that arise in graphene resulting from a single substitutional impurity, a pair of spatially separated substitutional impurities, vacancies, and realistic instances of the more commonly found top and bridge adsorbed atoms, will be investigated. For each case an analytic expression for the FOs will be derived using the stationary phase approximation (SPA) technique from Sec. 3.2 and corroborated with numerical calculations to confirm the predicted behaviour. For each impurity type studied in this chapter the corresponding perturbed system Green function was derived using the Dyson equation methods in Sec. 2.2.

5.1.1 Weak substitutional impurities

To begin, the FOs in $\Delta\rho_i$ and Δn_i on sites i close to a substitutional impurity will be investigated. The impurity is characterised by onsite energy $\lambda = 2.7\text{eV} = |t|$ and is situated on site A on the black sublattice a distance D away from i as demonstrated in Fig. 5.1. The armchair direction is specified here as the SPA will be used to calculate the FOs along this direction. This is described

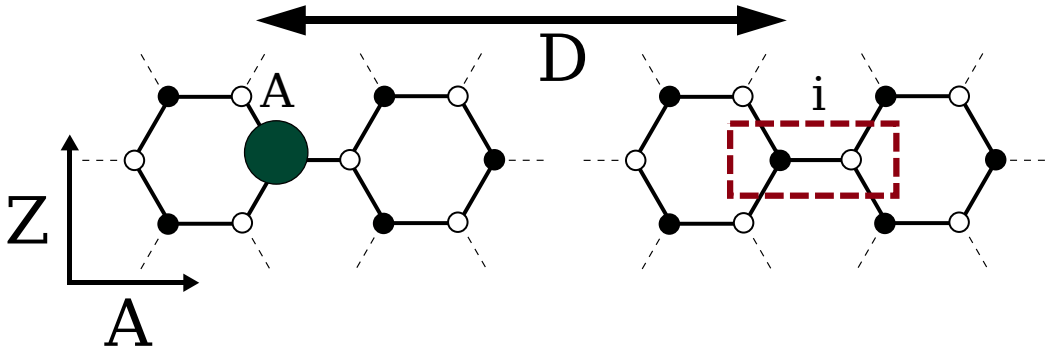

Figure 5.1: Substitutional impurity placed at A with a second lattice site labelled i which is a distance of $\frac{m+n}{2} = \frac{D}{2}$ unit cells away in the armchair direction. In the text the modulations in charge density at site i caused by the impurity at A are investigated and characterised. The axes indicate the armchair and zigzag high symmetry directions of the graphene lattice.

by the perturbation

$$\hat{V} = \lambda \left|A\right\rangle \left\langle A\right|$$

and the diagonal Green function of site i in the perturbed system is

$$\Delta G_{ii}^{Subs.} = \frac{g_{iA}^2 \lambda}{1 - g_{AA}\lambda}$$

as shown in Chap. 2. Knowledge of the onsite Green function immediately allows for the determination of the changing LDOS spectrum at any lattice site in the system. This is plotted in Fig. 5.2 at the location of the impurity site itself ($i = A$) for varying λ values. Increasing λ changes the position and magnitude of the resonant state and for large values leads to a bound state outside the regular bulk states.

A numerical evaluation of the spatial modulations in Δn_i at other sites in the system can be made using Eq. 2.9 which yields the contour plots in Fig. 5.3. Here the site i has been scanned across all the nearby lattice sites on the black

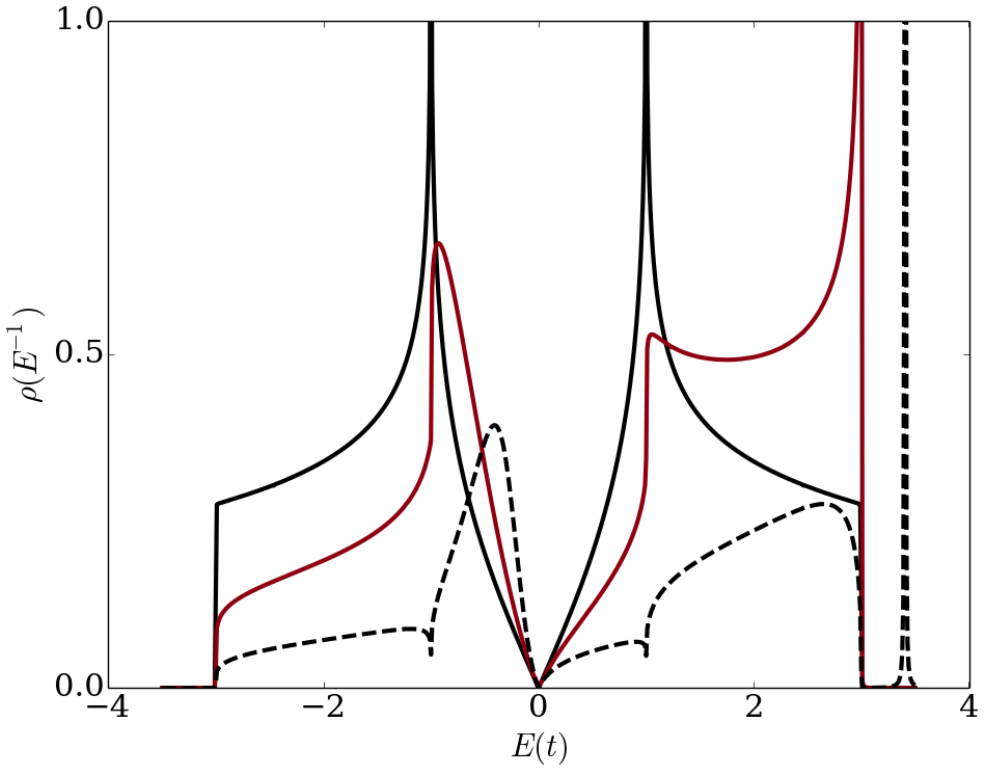

Figure 5.2: LDOS spectra of impurity site A for $\lambda = 0$ (pristine, black), $\lambda = 2$eV (red) and $\lambda = 6$eV (black dashed). Note the appearance of a bound state for the final value.

and white sublattices separately and the system is at a Fermi energy of $E_F = 0.2|t|$. The wavelength of this oscillation pattern depends directly on E_F - by increasing E_F reduces the oscillation wavelength and vice versa. Comparing the results for each sublattice it is clear that each one has a different response, with Δn_i swapping signs between the sites in the same unit cell. This signature is important when considering multiple impurities which will be discussed in Sec. 5.1.2 and for the sublattice asymmetry phenomenon in Chap. 7.

To shed light on the underlying physics it is useful to consider a cross-section

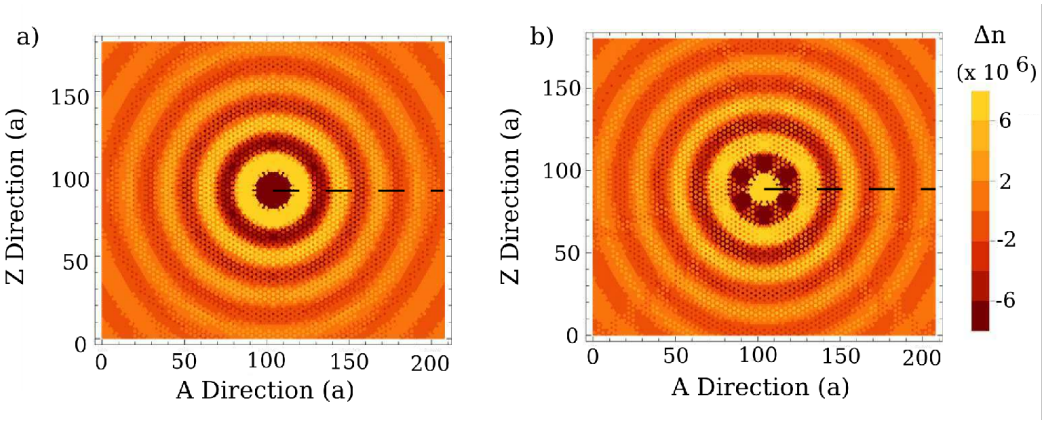

Figure 5.3: The FOs in Δn_i produced by a substitutional impurity of strength $\lambda = 0.1|t|$ on the (a) black and (b) white sublattices at $E_F = 0.2|t|$ with the impurity located at the centre, calculated using Eq. 2.9. The units of the A and Z directions are in a, the C-C bond separation.

of the Δn_i and $\Delta \rho_i$ profiles generated using this method. Consider the cross-section taken along the armchair direction as specified previously, originating at the impurity position at the origin and moving away as indicated by the dashed lines in Fig. 5.3. It should be noted at this point that the behaviour in the zigzag direction could equally be looked at, however the oscillations in Δn_i and $\Delta \rho_i$ along this direction exhibit a well understood period-3 oscillatory behaviour which would needlessly obfuscate the results [48]. However for the sake of completeness the Friedel oscillations in Δn along the zigzag direction will be shown later in this chapter in Fig. 5.6. As the Friedel oscillation behaviour is otherwise the same in either direction, and the mathematics is simpler along the armchair direction, this investigation will progress with the armchair behaviour only. Using a combination of the SPA approach, introduced in Sec. 3.2, and the Born Approximation for weak scatterers of strength $\lambda \lesssim |t|$ such that the denominator of $\Delta G_{ii}^{Subs.}$ is approximately equal to 1, it is

possible to approximate

$$\Delta G_{ii}^{Subs.} \approx g_{iA}^2 \lambda.$$

This then yields

$$\Delta\rho_i \approx -\frac{2}{\pi}\mathrm{Im} g_{iA}^2 \tag{5.1}$$

and

$$\Delta n_i^{Subs.} \approx -\lambda\frac{2}{\pi}\mathrm{Im}\int_{-\infty}^{\infty} dE f(E) g_{iA}^2 \tag{5.2}$$

for the LDOS and carrier density oscillations caused by the weak impurity. The Fermi function

$$f(E) = \frac{1}{1+e^{(E-E_F)/k_BT}},$$

where k_B is the Boltzmann constant, has been introduced in the Δn integral. This has been implicit up to this point as the zero-temperature limit $T \to 0$ has been assumed. In both $\Delta\rho_i$ and Δn_i the Green function g_{iA}^2 can be expressed using the general SPA equation for an armchair separated Green function which was derived previously in Eq. 3.18 as

$$g_{iA}^2 \approx \frac{\bar{A}(E)^2 (N^{\alpha\beta}(E))^2 e^{2iQ(E)D}}{D}.$$

Immediately it is possible to approximate the LDOS oscillations using the analytic Eq. 5.1 and the definition of A and Q from Sec. 3.2.2. This is compared to the numerical results of the LDOS cross section in Fig. 5.4 where an excellent match is seen. It is clear both from the figure and the form of Eq. 5.1 that $\Delta\rho$ decays as D^{-1} away from the Dirac point as

$$\Delta\rho \sim -\frac{2}{\pi}\,\mathrm{Im}\,\frac{\bar{A}(E)^2 (N^{\alpha\beta}(E))^2 e^{2iQ(E)D}}{D}.$$

Additionally it can be seen that the oscillation period is determined by the

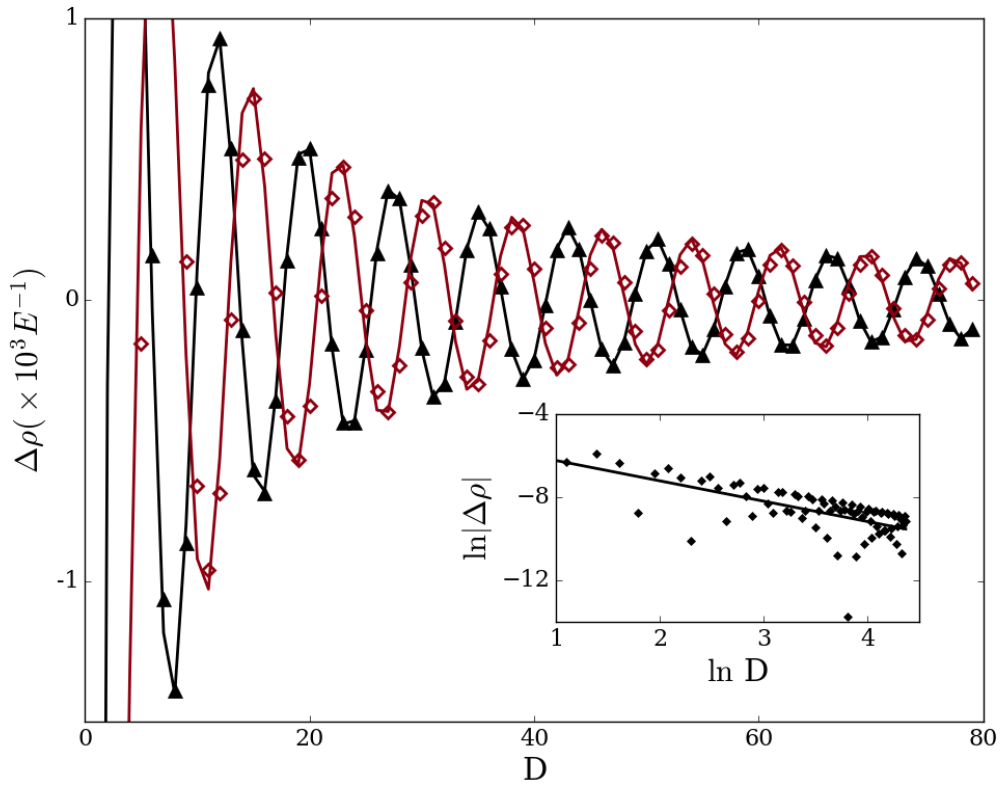

Figure 5.4: Cross-section of $\Delta\rho_i$ for the same impurity and locations, with numerical results for the black (white) sublattice given by the black, solid (red, hollow) symbols. Analytic SPA results are given by the corresponding lines, and the inset shows a log-log plot of the data, the line corresponding to a decay of D^{-1}.

phase factor Q linked directly to the Fermi wavevector k_F of the system. In the Born approximation limit the SPA can be used to show that when $E = 0$ the density of states oscillations disappear. However there exist limiting cases where the oscillations do *not* disappear at $E = 0$, such as vacancies, and these will be discussed shortly.

The derivation of an analytic closed-form expression for Δn_i requires special

care due to being in integral form. Making the necessary substitutions the carrier density equation can be written

$$\Delta n_i^{Subs.} \approx -\frac{\lambda}{D}\frac{2}{\pi}\mathrm{Im}\int_{-\infty}^{\infty} dE \frac{\mathcal{B}(E)e^{2iQ(E)D}}{1+e^{(E-E_F)/k_BT}}$$

where

$$\mathcal{B}(E) = \bar{A}(E)^2(N(E))^2.$$

The analytic approximation can be found by solving via contour integration in the upper-half of the complex energy plane, the poles in the integrand being given by the Matsubara frequencies $E_p = E_F + i(2p+1)\pi k_B T$ and p is an integer labelling the poles.

From Cauchy's residue theorem the integral required can be expressed as a sum over the poles in the integrand:

$$\Delta n_i^{Subs.} \approx \frac{-2\lambda k_B T}{\pi D} 2\pi i \,\mathrm{Im}\sum_p \mathcal{B}(E_p)e^{2iQ(E_p)D}.$$

The functions $\mathcal{B}(E)$ and $Q(E)$ can then in turn be expanded around E_F as

$$\mathcal{B}(E) = \sum_l \frac{1}{l!}\mathcal{B}^{(l)}(E-E_F)^l$$

and to a first-order approximation

$$Q(E) \approx Q^{(0)}(E) + Q^{(1)}(E)(E-E_F)$$

where the notation $X^{(\ell)}$ denotes the ℓ^{th} derivative of the function X with re-

spect to energy. The expression for $\Delta n_i^{Subs.}$ then becomes

$$\Delta n_i^{Subs.} \approx \frac{-4\lambda k_B T}{D} \operatorname{Im} \sum_l \frac{i}{l!} \mathcal{B}^{(l)} e^{2iQ^{(0)}D} \sum_p e^{2iQ^{(1)}(E_p - E_F)D} (E_p - E_F)^l.$$

The inner sum over the poles p can be simplified by noticing that $\frac{d^l}{dD^l} e^{\alpha\beta D} = \alpha^l \beta^l e^{\alpha\beta D}$ so that

$$\sum_p e^{2iQ^{(1)}(E_p - E_F)D} (E_p - E_F)^l = \frac{1}{(2iQ^{(1)})^l} \frac{d^l}{dD^l} \sum_p e^{2iQ^{(1)}(E_p - E_F)D}.$$

Using the definition of the Matsubara frequencies this new summation over p can be shown to be

$$\sum_p e^{2iQ^{(1)}(E_p - E_F)D} = \frac{1}{2 \sinh 2Q^{(1)} \pi k_B T D}$$

which in the limit of zero temperature goes as $\frac{1}{4Q^{(1)}\pi k_B T D}$, this $k_B T$ term now cancelling with the one in the numerator of $\Delta n_i^{Subs.}$. Working with $\Delta n_i^{Subs.}$ again

$$\begin{aligned}
\Delta n_i^{Subs.} &\approx \frac{-4\lambda}{D} \operatorname{Im} \sum_l \frac{i}{l!} \mathcal{B}^{(l)} e^{2iQ^{(0)}D} \frac{1}{(2iQ^{(1)})^l} \frac{d^l}{dD^l} \frac{1}{4Q^{(1)}\pi D} \\
&\approx -4\lambda \operatorname{Im} e^{2iQ^{(0)}D} \sum_l \frac{i}{l!} \mathcal{B}^{(l)} \frac{1}{D} \frac{1}{i^l (2Q^{(1)})^l} \frac{1}{2\pi (2Q^{(1)})} \frac{d^l}{dD^l} \frac{1}{D} \\
&\approx -\frac{2\lambda}{\pi} \operatorname{Im} e^{2iQ^{(0)}D} \sum_l \frac{i}{l!} \mathcal{B}^{(l)} \frac{1}{D} \frac{1}{i^l (2Q^{(1)})^{l+1}} \left(\frac{(-1)^l l!}{D^{l+2}}\right) \\
&\approx -\frac{2\lambda}{\pi} \operatorname{Im} e^{2iQ^{(0)}D} \sum_l \frac{\mathcal{B}^{(l)}}{(2iQ^{(1)})^{l+1}} \frac{1}{D^{l+2}}.
\end{aligned} \tag{5.3}$$

This is better expressed in the form

$$\Delta n_i^{Subs.} \sim \lambda \frac{2}{\pi} \operatorname{Im} \sum_{\ell=0}^{\infty} \frac{\Gamma_\ell(E)}{D^{\ell+2}} e^{2iQ^{(0)}D}\,. \tag{5.4}$$

where the sum coefficients $\Gamma_\ell(E)$ are related to the SPA coefficients and defined as

$$\Gamma_\ell(E) = \frac{(-1)^\ell \mathcal{B}^{(\ell)}}{(2q^{(1)})^{\ell+1}}. \tag{5.5}$$

From these equations the behaviour of Δn with E_F and D can be determined fairly straightforwardly. Clearly in the case of $D \gg 1$, and given that the first-order term $l = 0$ is finite, an oscillatory decaying function should be recovered with a wavelength determined by the phase factor Q^0 and a decay rate of approximately $\sim D^{-2}$. The numerical values can be calculated using the expressions for $\mathcal{B} = \bar{A}^2(N(E))^2$ and Q from Sec. 3.2.2 which for low energies $E < |t|$ are

$$\mathcal{B}^0(E) = \frac{2}{i\pi} \frac{(N^{\alpha,\beta}(E))^2}{E(E^2+3t^2)\sqrt{t^2-E^2}}$$

$$Q^{(0)}(E) = \pm \cos \frac{-\sqrt{t^2-E^2}}{t}.$$

The analytic approximation of Δn given by Eq. 5.4 is plotted against a numerical calculation in Fig. 5.5. Excellent agreement between the two is found for distances beyond a few unit cells. It should be noted that the numerical results are calculated by converting the original integral form $\Delta n = -\frac{2}{\pi}\int_{-\infty}^{E_F} dE \Delta G_{ii}$ to be over the imaginary energy axis. Doing so avoids discontinuities in the integrand caused by resonances and van-Hove singularities which would make its evaluation challenging. The process of converting these integrals is is explained in detail in Appendix A.

More interestingly when E_F coincides with the Dirac point, as is the case for undoped graphene, it is found that the oscillations disappear and a faster decay rate of D^{-3} is observed. In the case of the zigzag direction the period-3 behaviour is still apparent but otherwise there is no apparent oscillation behaviour. This absence of oscillation can be explained through the commensu-

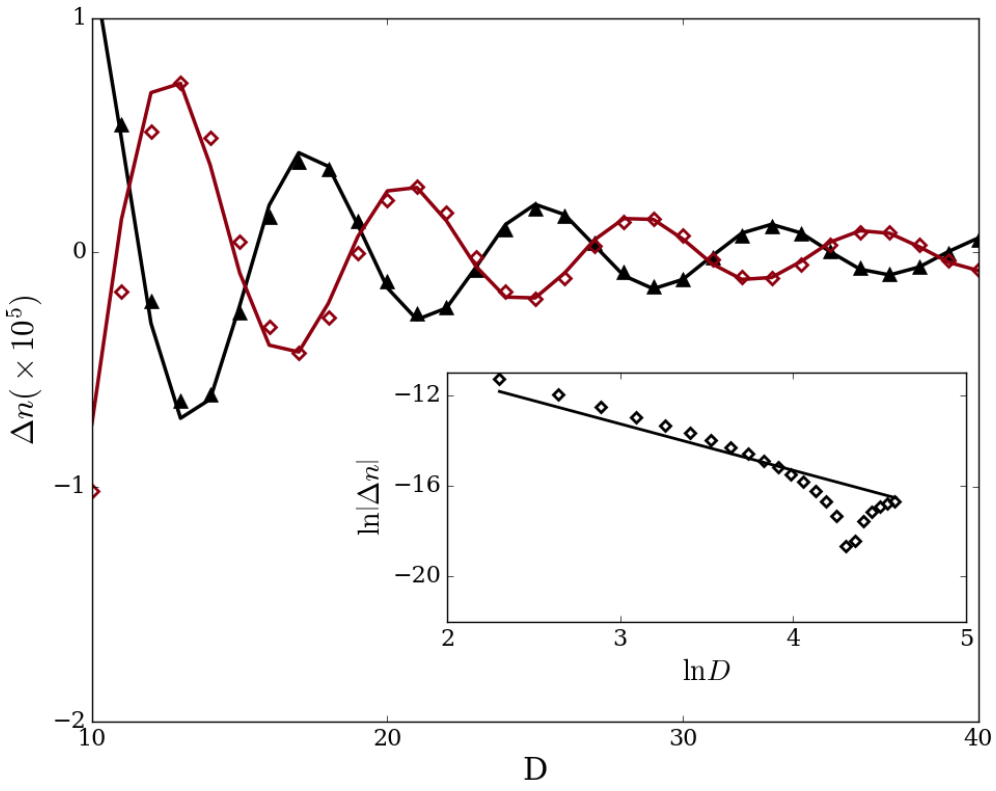

Figure 5.5: Cross-section of Δn along the dashed line shown in Fig. 5.3 with parameters $E_F = 0.2|t|$ and $\lambda = -1$eV : numerical (black line) vs SPA (black triangles) on the black sublattice and numerical (red line) vs SPA (red diamonds) on the white sublattice. Inset: log-log of data from the numerical calculation on the black sublattice (black diamonds) and a regression line corresponding to a decay of D^{-2}.

rability of the oscillations with the lattice spacing, and furthermore this can be seen by inspecting the analytic form of Δn_i derived in Eq. 5.4. With the sum over l the function $B^0 \to 0$ for $l = 0$, so that the next leading sum term, $l = 1$, becomes dominant and this explains the D^{-3} behaviour due to the $\frac{1}{D^{l+2}}$ dependence. For $l = 0$ the phase term $Q^0 \to \pi$ which causes the sign-changing oscillations to become commensurate with the lattice spacing because $D \in \mathbb{Z}^+$,

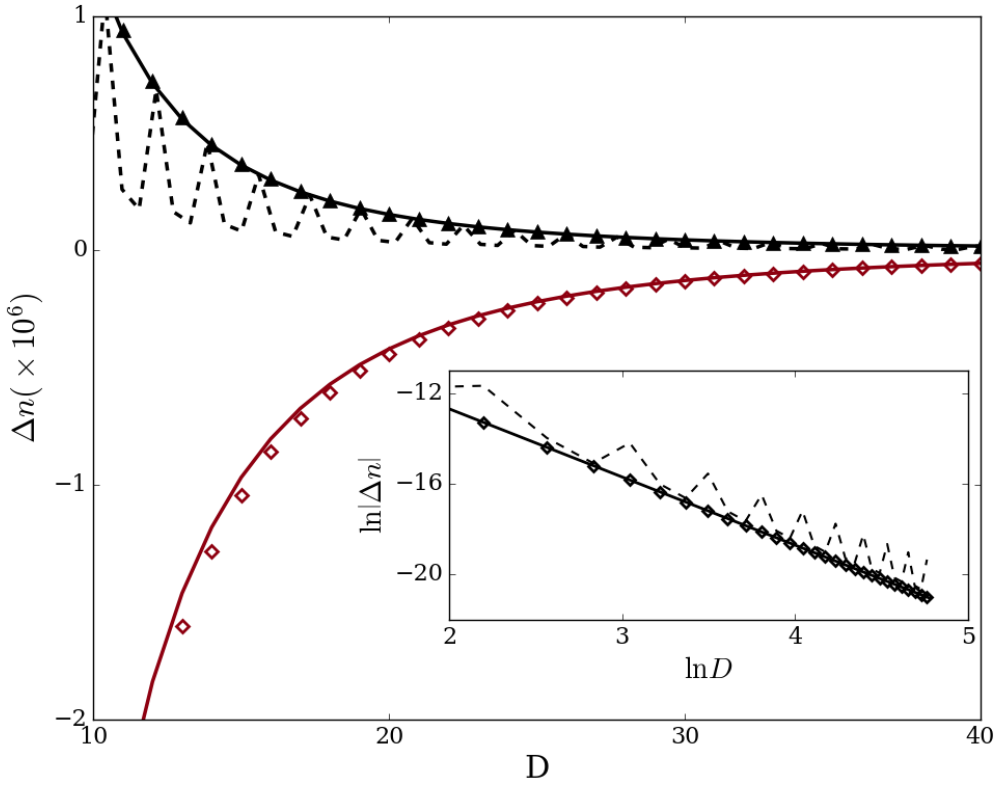

Figure 5.6: Δn as Fig. 5.5 with $E_F = 0$. Also shown are the oscillations along the zigzag direction on the black sublattice (dashed black line) which have been rescaled by a factor of $\sqrt{3}$ due to the mismatch between unit cell distance of the armchair and zigzag directions. The period-3 variation of the zigzag oscillations is explained in the text. The absence of oscillations in both directions, other than the period-3 behaviour, is caused by commensurability with the lattice spacing and a quicker decay. The decay rate of D^{-3} is demonstrated by the regression line in the inset.

hence the oscillatory behaviour seemingly disappears for all terms in the series. It should be noted that $2q$ oscillations still occur when moving between sublattices and that this behaviour only occurs when the spatial modulations

are separated by sublattice. Using Eq. 3.18 it can be shown that

$$B^{(1)}(E_F = 0) = \begin{cases} \frac{2i}{3\pi t^3} & \text{for } \alpha = \beta \\ -\frac{2i}{3\pi t^3} & \text{for } \alpha \neq \beta \end{cases}$$

hence the same sublattice and opposite sublattice solutions for Δn have the same magnitude but different sign. This approximation does not match the numerical calculation precisely. The general functional form is captured, however, and the two methods are different by a numerical factor. Multiplication of the analytic SPA form by 0.8 and 2.2 for same and opposite sublattice cases respectively produces an excellent match and this is demonstrated in Fig. 5.6. This requirement is perhaps not surprising given the extensive approximations done during the preceding derivation, e.g. the Born approximation. Also shown is numerical data for the Δn oscillations in the zigzag direction, where a period-3 behaviour can be seen. This behaviour arises from the periodicity and symmetry of the lattice and can be found in other quantities, such as indirect magnetic coupling [48].

The difference in sublattice response is quite clear in the cross-sections of FOs in $\Delta\rho$ in Fig. 5.4 and Δn in Fig. 5.6 and Fig. 5.5. In each case the sign of the fluctuation is opposite for neighbouring sites on opposite sublattices, but with similar magnitude and the same oscillation period. The opposing sign of the oscillations is a signature of FOs in other electronic quantities such as the RKKY interaction[39, 48, 89, 136–141] between magnetic impurities. The results from this section agree with previous work [39, 41], but due to the SPA method requiring large D these approximations are only valid for the long-range FO behaviour in the range of 5 or more unit cells. Short wavelength features which are present in the region immediately surrounding an impurity

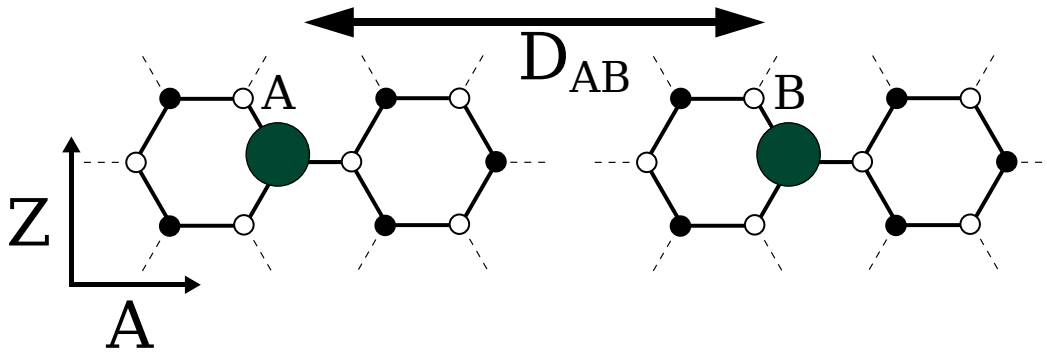

Figure 5.7: Schematic of two substitutional impurities at lattice sites A and B separated by a distance of D_{AB} unit cells. The axes indicate the armchair and zigzag high symmetry directions of the graphene lattice.

will not be captured as a consequence. This behaviour has been more thoroughly investigated using Bessel functions by Bacsi and Virosztek [39, 40]. In addition to what is shown in Fig. 5.4, Fig. 5.5 and Fig. 5.6 an excellent agreement was found between numerical and analytic calculations across the entire energy spectrum and all sublattice configurations.

5.1.2 Multiple weak substitutional impurities

In this section the above process will be repeated for a system with two scatterers. In this scenario the mutual presence of the impurities gives rise to an interference term in the Green functions and hence the FOs. When considering two or more substitutional impurities the matrix $\hat{V}^{Subs.}$ from the last section can be extended to include additional sites simply by adding the necessary extra perturbations at the corresponding locations. For example if two identical substitutional impurities with onsite energy λ are placed in the lattice on sites

A and B, as shown in Fig. 5.7, the matrix $\hat{V}$ can be described by

$$\hat{V} = \lambda |A\rangle \langle A| + \lambda |B\rangle \langle B| .$$

The resulting Δn profile calculated using Eq. 2.9 is plotted in Fig. 5.8 (a) for two such impurities spaced by 40 unit cells in the armchair direction with a Fermi energy of $E_F = 0.2|t|$. As this lies in the region of linear dispersion the interference pattern that arises is similar to that seen in classical waves theory. Considering weak scatterers only, i.e. $\lambda \lesssim |t|$, then applying the Born approximation in the same way as the case for a single scatterer, to first order

$$\Delta n_i^{Mult.} \approx -\frac{2}{\pi}\mathrm{Im}\int dE f(E)(\Delta n_A + \Delta n_B + \Delta n_{AB}). \tag{5.6}$$

The quantities

$$\Delta n_A = g_{iA}\lambda g_{Ai},$$

$$\Delta n_B = g_{iB}\lambda g_{Bi},$$

and

$$\Delta n_{AB} = 2g_{iA}g_{AB}g_{Bi} - g_{iA}g_{AA}g_{Ai} - g_{iB}g_{BB}g_{Bi}$$

have been used for convenience.

Clearly the terms Δn_A and Δn_B arise from the effects of the individual isolated impurities (c.f. Eq. 5.2), however Δn_{AB} contains cross terms between the impurities at A and B, suggesting that the impurities experience an interference effect where they can 'feel' the presence of each other through the conducting electrons in the medium. The SPA approach that was used in the last section for the single impurity can be adapted and applied to all three terms, where the integration of Δn_A and Δn_B will be identical to the single impurity case.

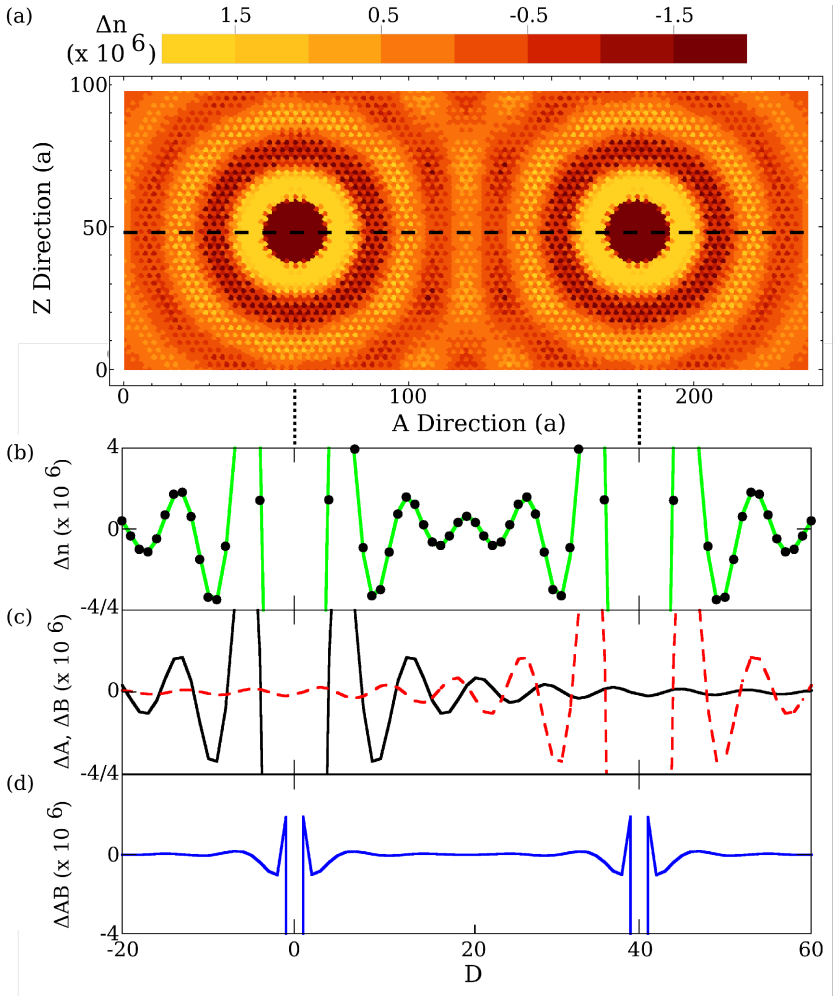

Figure 5.8: (a): Numerical simulation of Δn FOs on the black sublattice for two weak scatterers $\lambda = 0.1|t|$ separated by 40 unit cells in the armchair direction at $E_F = 0.2|t|$. (b) Cross section of Δn along the dashed line in the top contour plot of analytic (green) and numerical (black symbols) calculations. (c) and (d): Contributions to Δn from the terms Δn_A (black), Δn_B (red, dashed) and Δn_{AB} (blue) per Eq. 5.6.

The interference term Δn_{AB} can also be approximated well if A and B are at least a few unit cells apart. Clearly Δn_{AB} is dependent on both λ^2 and the separation of A and B so one should expect this term to decay quickly in a system with weak scatterers.

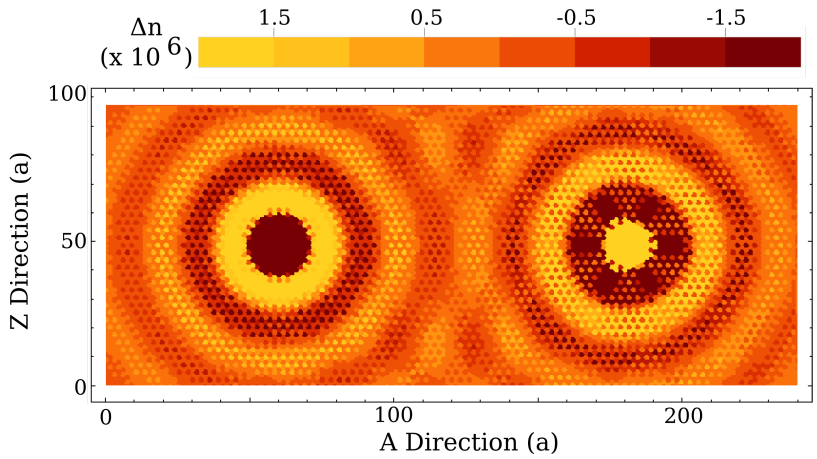

Figure 5.9: Numerical simulation of Δn FOs on the black sublattice for two weak scatterers $\lambda = 0.1|t|$ separated by 40 unit cells in the armchair direction at $E_F = 0.2|t|$.

The derivation of the analytic form of Δn begins by considering a cross-section along the armchair direction between the two impurities. The numerically calculated values for this cross-section are indicated by the black dashed line in Fig. 5.8 (a) and plotted as the black data points in Fig. 5.8 (b). Following the SPA process used before one can derive separate expressions for each term in Eq. 5.6, however they are particularly cumbersome and lengthy so they are not shown here. The resulting approximation of Δn is shown in Fig. 5.8 (b) as the green line showing a very good agreement with the numerical solution. The strength of this mathematically transparent approach is that it is possible to decompose the different contributions to Δn and understand the interference mechanism. Indeed if the contributions from Δn_A, Δn_B and Δn_{AB} are considered individually one can see that the dominant contribution to Δn comes from the isolated impurities given by Δn_A (black curve) and Δn_B (red curve) in Fig. 5.8 (c) with only a small contribution from Δn_{AB} which is plotted in Fig. 5.8 (d).

In the case that the impurities A and B are instead placed on opposite sublattices the resulting Δn profile is drastically different. A contour plot of this is shown in Fig. 5.9 and should be compared to the same sublattice case in Fig. 5.8 (a). It can be seen that the act of switching B to the white sublattice induces an inversion in the Δn_B contribution to Δn, resulting in a more complex interference pattern as it has the opposite sign.

When the impurities are placed very close together or if they are no longer weak scatterers the SPA breaks down. In addition to the interference term Δn_{AB} becoming much larger and less accurate through the SPA, the region of significant overlap between the Δn_A and Δn_B increases and the FO patterns observed become more complex. For very close impurities one would expect a change in parametrisation also, due to other interactions e.g. Coulomb repulsion. A contour plot of Δn of two such situations is shown in Fig. 5.10 where the impurities are placed together as nearest neighbours (opposite sublattices, right panel) or next-nearest neighbours (same sublattices, left panel) as shown schematically in the plot insets. In the case of same sublattice configurations the sublattice dependent behaviour noted in the single impurity scenario is still present. In contrast, the nearest-neighbour case where it has been mostly washed out due to a superposition of the features observed in panels a) and b) of Fig. 5.8. This would have the effect of making such oscillations difficult to detect experimentally, for example if the resolution of the atomic tip in an STM probe is poor [39]. These strikingly different interference patterns present clear signatures for the two cases, and this general qualitative difference in FOs may make impurity configurations easier to distinguish experimentally. Moreover the interference effect is an important quantity to consider when investigating FOs in other quantities, and will be discussed later in the context of preferential doping configurations.

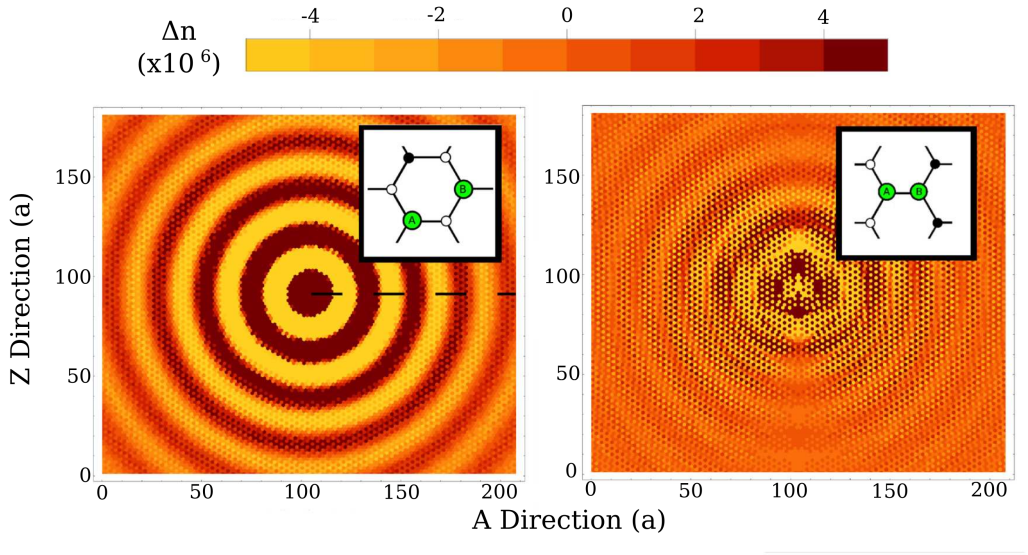

Figure 5.10: Black sublattice plots for quasi-nearest neighbour impurities (left) and impurities sharing the same unit cell (right) as demonstrated in the insets for $\lambda = |t|$ and $E_F = 0.2|t|$.

5.1.3 Vacancies

Vacancies in the lattice are caused by the removal of an atom from the crystal structure. Recall from their introduction in Sec. 2.2.1 that they can be effectively modelled within tight-binding by a substitutional impurity with onsite potential $\lambda \to \infty$. Taking the limit in such a way means that the regular substitutional impurity Green function

$$\Delta G_{ii} = \frac{g_{iA}^2 \lambda}{1 - g_{ii}\lambda}$$

can be approximated as

$$\lim_{\lambda \to \infty} \Delta G_{ii} = -\frac{g_{iA}^2}{g_{ii}}$$

thus the carrier density variations are

$$\Delta n_i^{Vac.} \approx -\frac{2}{\pi}\mathrm{Im}\int_{-\infty}^{\infty} dE \frac{f(E)g_{i0}^2}{-g_{ii}}. \tag{5.7}$$

It should be noted that at the location of the vacancy $g_{iA} = g_{00}$ in Eq. 5.7, which leads to $\Delta n_A = -1$ corresponding to a complete depletion of electrons on this site. In this model the onsite LDOS at the vacancy consists of a delta function-like bound state that is removed to infinity and is therefore inaccessible to electrons. The spectrum is fully suppressed except at the resonance energy λ as can be seen through

$$G_{AA} = g_{AA} + \frac{g_{AA}^2\lambda}{1 - g_{AA}\lambda}$$

and taking the limit for a vacancy

$$\lim_{\lambda\to\infty} G_{AA} = g_{AA} + (-g_{AA}) = 0.$$

For the other sites in the system ΔG_{ii} is finite and can be calculated. The pristine diagonal Green function g_{ii} required to do this can be approximated very well for energies in the linear regime (up to around $E_F \sim |t|/2$) and this is shown in Appendix B.2 to be

$$g_{ii} \approx \frac{2}{\sqrt{3}\pi t^2} E \ln\frac{|E|}{3t} - i\frac{|E|}{\sqrt{3}t^2}. \tag{5.8}$$

This approximation then allows Eq. 5.7 to be solved in a similar fashion to that of the single substitutional impurity. The Green function g_{ii} is dependent only on energy and so it can be absorbed into the Γ_ℓ term in Eq. 5.4 and Eq. 5.5. As there is no pole in the upper half plane for the resulting integrand the evaluation method remains unchanged from the weak impurity case.

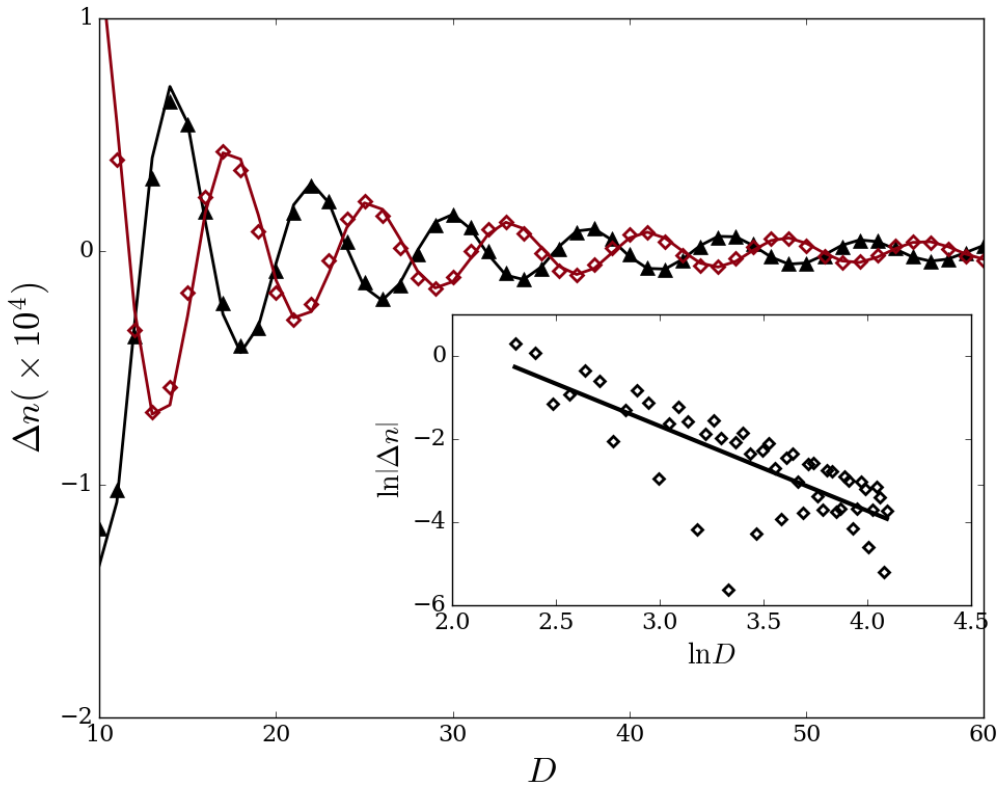

Figure 5.11: Friedel oscillations due to a vacancy. Cross-section of numerical (points) and analytic (continuous) solutions for the FOs in Δn on the black (black data) and white (red data) sublattices along the armchair direction. The FOs have been produced by a vacancy at site $D = 0$ and the Fermi energy fixed at $E_F = 0.2\,|t|$. Inset is a log-log plot of the main data (black diamonds) showing a decay of D^{-2} indicated by the red dashed line.

Comparing the numerical and analytic solutions for a finite E_F in Fig. 5.11 an excellent agreement can be seen between the two. It should be noted that the general features are similar to those noted for weaker impurities, namely sign-changing oscillations and a D^{-2} decay. Interestingly when $E_F = 0$ there is a complete absence of FOs - that is $\Delta n = 0$ at all sites except the vacancy (which still has $\Delta n = -1$) and the system is otherwise identical to the pristine state.

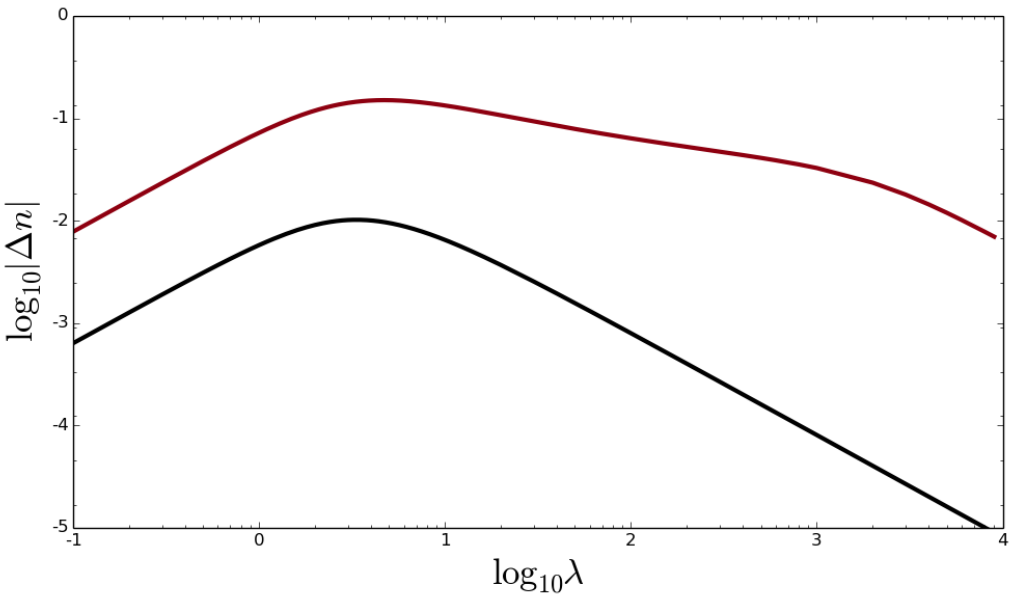

Figure 5.12: Log-log plot of $|\Delta n|$ vs. λ at a Fermi energy of $E_F = 0$ on the nearest black (black line) and white (red line) sublattice sites to a vacancy. For $\lambda \gg 1$ and $\lambda \ll 1$, the amplitude of Δn_1 becomes very small with a maximum amplitude at $\lambda \approx 5t$, with a positive sign on B and a negative sign on A.

This curious behaviour is found on both sublattices and is in stark contrast to the case of weaker scatterers where the non-oscillatory D^{-3} behaviour was noted. Understanding this requires examination of the imaginary-axis integral that required solving in order to calculate Δn (note this is *not* Eq. 2.14). This has been used in all the numerical calculations of Δn as it avoids the problem of evaluating discontinuities in the integrand, and is explained fully in Appendix A. It will now be shown that the behaviour of the individual Green functions along the imaginary axis determines the presence or absence of the carrier density oscillations. Converting the integral yields the expression

$$\Delta n_i^{Vac.} \sim Re \int_\eta^\infty dx \frac{g_{iA}^2(E_F + ix)}{g_{ii}(E_F + ix)} . \tag{5.9}$$

At $E_F = 0$ both g_{ii} and g_{iA}, if i is on the black sublattice, become entirely imaginary along the integration range. Similarly in the case that i is on the white sublattice g_{i0} becomes entirely real. This ensures that on both sublattices the integrand becomes entirely imaginary over the integration range, hence Δn vanishes since it depends on the real part of the integrand only. Thus in the limit of large values of λ the perturbations described by Eq. 5.9 will vanish. This is verified numerically in Fig. 5.12 where Δn is calculated on the nearest (black curve) and next-nearest (red dashed curve) sites to the vacancy as λ is increased at $E_F = 0$. Another interesting result of this calculation is that there is a resonance potential of $\lambda \approx 4t$ for the black sublattice site and $\lambda \approx 10t$ for the white sublattice site which causes the largest amplitude in Δn. It should be emphasised that this disappearance of Δn in the $\lambda \to \infty$ limit occurs only at $E_F = 0$, whereas other energies will show the familiar D^{-2} oscillatory pattern.

Concerning the effect of a vacancy on the Friedel oscillations in the LDOS it is straightforward to evaluate $\Delta\rho_i$ from the $\Delta G_{ii}^{Vacancy}$ approximation. Again there exists a clear asymmetry between the black (minority - less atoms) and white (majority) sublattices at the Dirac point, which arises from the limiting behaviour of the Green functions in this regime. Contrasted with this is the behaviour at sites on the minority sublattices which in the limit $g_{iA}^{\bullet\bullet} \to 0$ sending $\Delta\rho$ on such sites to zero, and $g_{iA}^{\bullet\circ} \to +i\infty$ on the majority sublattice causing a divergence. This behaviour is the widely predicted mid gap resonance states seen in many previous works and comes from the electron wavefunction itself [94, 142–144]. The state's amplitude decays as $1/D$ from the vacancy. The existence of this zero-energy state can also be proved from linear algebra for a bipartite lattice with an uneven number of sites between sublattices called Lieb's theorem [145]. LDOS spectra demonstrating the appearance of this behaviour at sites close to the vacancy are shown in Fig. 5.13.

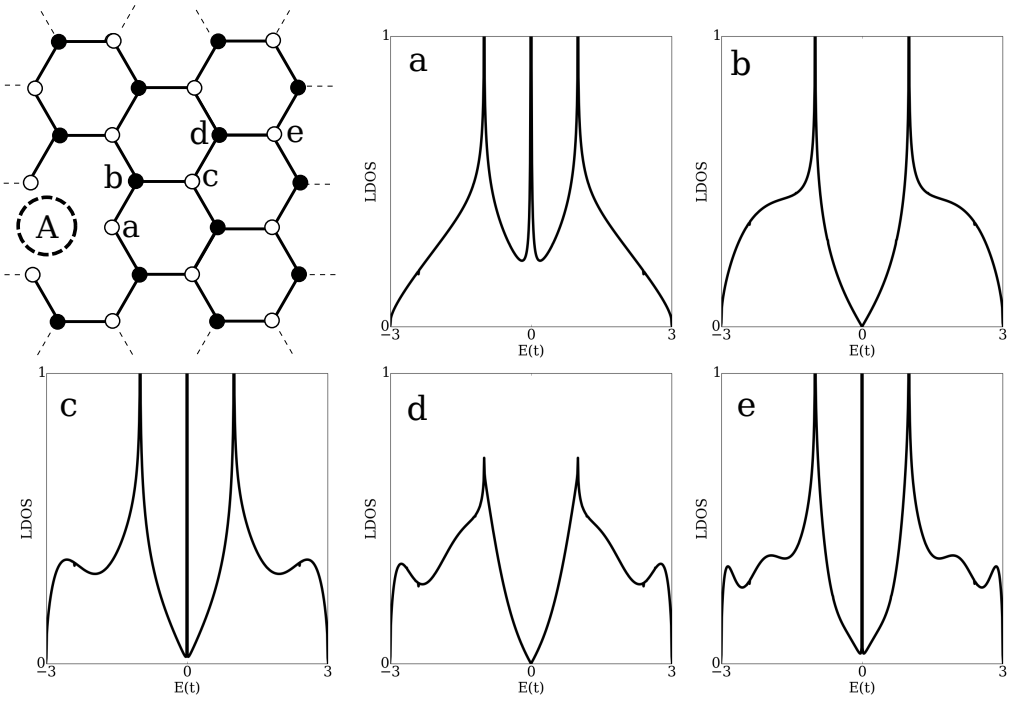

Figure 5.13: LDOS spectra corresponding to the labelled sites close to vacancy site A. The mid gap state appears only on the majority (white) sublattice as shown in sub-plots a, c and e.

The LDOS peak at the Dirac point on the majority sublattice sites, and the absence of one on the minority sublattice sites, is connected to the phenomenon of vanishing Δn in the vacancy case studied earlier. The introduction of a vacancy deforms the LDOS at each site, but the number of states on all other lattice sites is conserved such that $-\frac{2}{\pi}\,\mathrm{Im}\int_{-\infty}^{\infty} dE\rho = 2$. Electron-hole symmetry is preserved for a resonance at exactly $E = 0$ and thus the LDOS remains symmetric around about the Dirac point for sites on either sublattice. The carrier density, being simply the integral of the LDOS up to $E_F = 0$, is thus unaffected by the vacancy and hence $\Delta n = 0$ for all other lattice sites. Possible extensions to this work, involving more intricate defect configurations such as divacancies and pentagon-heptagon configurations, are discussed in the final chapter

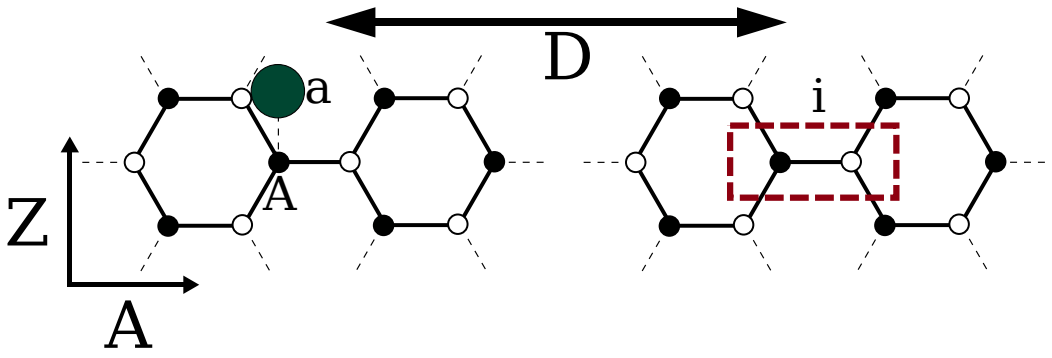

Figure 5.14: Schematic of a top adsorbed impurity (onsite index a) bonded to host site A in the graphene lattice. A second lattice site labelled i is a distance of D away with axes indicating the high-symmetry armchair and zigzag directions.

of the thesis.

5.1.4 Adsorbates

In this section the FOs in Δn will be investigated for top adsorbed and bridge adsorbed impurities. An analytic expression will first be sought for Δn_i^{Top}, the FOs in charge density induced by a top adsorbed impurity. Then the case of Δn_i^{Bridge} will be discussed. Both of these quantities can be found using similar methods to that of a single substitutional atom. The perturbation that describes the former case, shown schematically in Fig. 5.14, is represented by

$$\hat{V} = |a\rangle \, \tau \, \langle A| + |A\rangle \, \tau^* \, \langle a|$$

so

$$\Delta G_{ii} = \frac{g_{iA}^2 |\tau|^2 g_{aa}}{1 - g_{aa} g_{ii} |\tau|^2}.$$

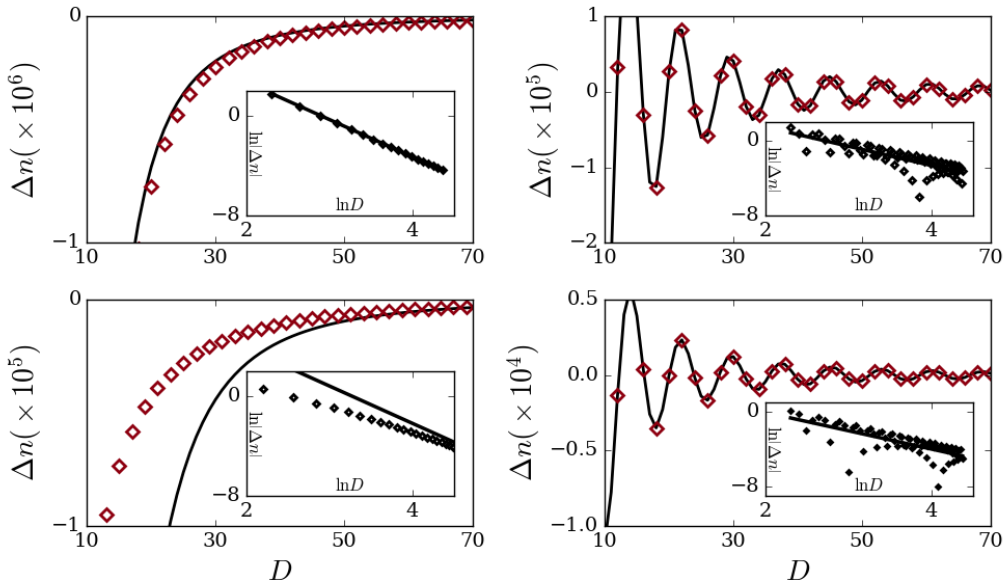

Figure 5.15: FOs in Δn_i^{Top} due to top adsorbed OH^- (top row) and H^+ (bottom row) with the top two cases show both $E_F = 0$ (left panels) and $E_F = 0.2|t|$ (right panels) and the numerical data (black) is compared with the analytic expression (green) for each impurity. The inset of each plot shows a log-log version of the main plot, here the red lines corresponding to the D^{-2} fits for both $E_F = 0.2|t|$ plots and D^{-3} for the other cases. Due to the parametrisation of the H^+ adatom, the SPA is a poor match to the numerics at $E_F = 0$ away from the asymptotic limit.

Here, ΔG_{ii} is analytic in the upper half plane with no poles other than those at the Matsubara frequencies. Again the approximation of g_{ii} restricts the results to the linear regime. Two realistic dopants are considered - hydroxyl (OH^-) and hydrogen (H^+) - which take the tight-binding parameters $\epsilon_{OH-} = -2.9|t|$, $\tau_{OH-} = 2.3|t|$ for hydroxyl [135] and $\epsilon_{H+} = -t/16$, $\tau_{H+} = 2t$ for hydrogen [132]. Δn cross-sections for these impurities are shown in Fig. 5.15 at $E_F = 0$ and $E_F = 0.2\,|t|$ where an excellent match between numerical (black circles) and analytic (green lines) solutions can be seen for all cases with the ex-

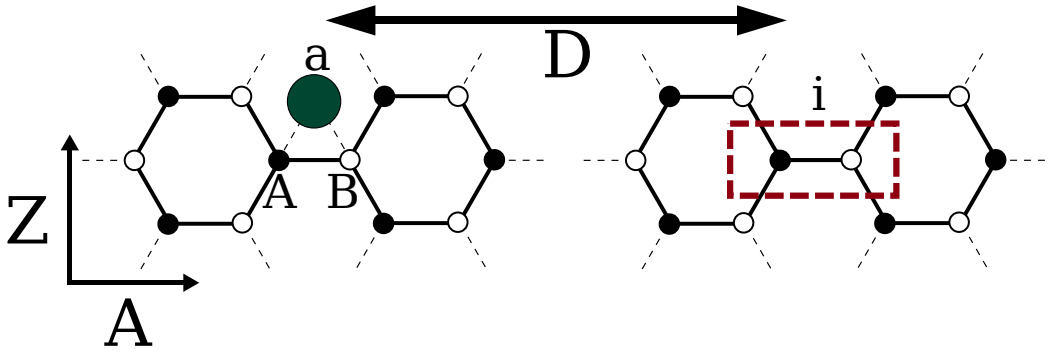

Figure 5.16: Schematic of a bridge adsorbed impurity (onsite index a) bonded to host sites A and B in a single unit cell in the graphene lattice. Another lattice site labelled i is a distance of D away with axes indicating the high-symmetry armchair and zigzag directions. The Friedel oscillations experienced at site i as a result of the bridge adsorbed impurity will be discussed in the text.

ception of hydrogen at $E_F = 0$. The onsite energy ϵ_{H+} is close to the Dirac point and this leads to a resonance condition here, hence it is required to look much further away (approx. 100 unit cells) to see agreement between numerical and analytic solutions. A clear change in the decay rate in the region close to the adsorbate in Fig. 5.15 (c) can be seen with an eventual D^{-3} rate far from the adsorption site, this has been studied recently by Mkhitaryan and Mishchenko [146]. In the case $E_F \neq 0$ a decay rate of D^{-2} is found for both hydroxyl and hydrogen, with D^{-3} at the Dirac point, with proviso, matching the behaviour of a substitutional impurity. This should be expected due to the possibility of modelling the effect of the adatom through a self-energy term replicating a substitutional atom [74].

Altering the onsite energy to $\epsilon_a = E_F = 0$ forces a resonance condition and confirms previous findings where the adatom behaviour can be similar to that of a vacancy [132] and the Δn_i^{Top} FOs disappear completely, which one may

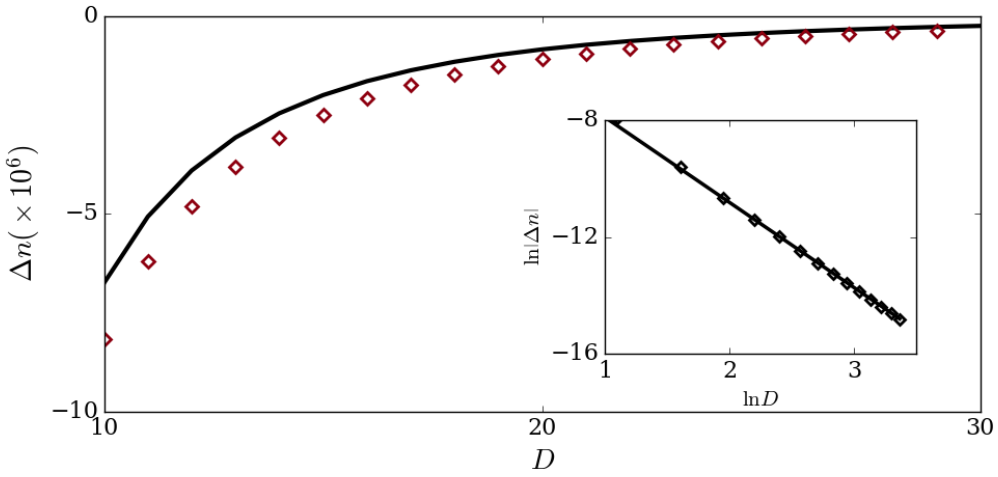

Figure 5.17: The charge density perturbations for a bridge adsorbed carbon adatom shown here as a numerical calculation (red data points) do not vanish at the Dirac point, unlike the top adsorbed bonding type impurity, due to cross-sublattice interferences. The black line indicates an approximation of $\Delta n_i^{\text{Bridge}}$ using the stationary phase approximation, it deviates from the numerical result by a constant factor of 1.2.

expect, for example, in the case of a top adsorbed carbon. However, carbon prefers a bridge adsorbed configuration [147] and due to this bonding type the interference effects from the two host sites, which are on opposite sublattices, lead to finite charge density perturbations at the Dirac point. As consequence of the symmetry breaking the same way relative to each sublattice, the FOs on both sublattices will be the same hence it does not matter on which sublattice the site i is chosen. Realistic carbon atoms can also be considered in this framework by approximating the onsite energy $\epsilon \approx 0$ and $\tau = t$, the same as atoms in the graphene lattice. The presence of FOs in $\Delta n_i^{\text{Bridge}}$ for the bridge adsorbed carbon at $E_F = 0$ can be seen by considering a situation like that shown in

Fig. 5.16. The perturbation matrix

$$\hat{V} = |A\rangle \tau \langle a| + |B\rangle \tau \langle a| + \text{c.c.}$$

that describes this bridge adsorbed atom yields

$$\Delta G_{ii}^{\text{Bridge}} = \frac{(g_{iA} + g_{iB})^2 g_{aa} \tau^2}{1 - (g_{AA} + g_{AB} + g_{BA} + g_{BB}) g_{aa} \tau^2}. \tag{5.10}$$

In Sec. 5.1.3 it was noted that, when considering imaginary axis integration of off-diagonal GFs at $E_F = 0$, that g_{ab} is either entirely real (for opposite sublattice propagators) or entirely imaginary (for same sublattice propagators). However from the form of ΔG_{ii}^{Bridge} it is clear that there will exist both real and imaginary terms in the integrand for $\Delta n_i^{\text{Bridge}}$, which was not the case for top adsorbed or vacancy impurities. This cross-sublattice interference is key to the non-vanishing $\Delta n_i^{\text{Bridge}}$ FOs for all bridge adsorbed atoms, regardless of parametrisation. In Fig. 5.17 a numerical plot of the familiar D^{-3} decay in $\Delta n_i^{\text{Bridge}}$ at the Dirac point is shown. The usual D^{-2} oscillations are recovered with doping. Using the SPA an approximation of the Dirac point behaviour can be obtained. From Eq. 5.10 in this limit the diagonal Green function

$$\lim_{E \to 0} \Delta G_{ii} = \frac{(g_{i1} + g_{i2})^2}{-(g_{12} + g_{21})}.$$

Using the SPA Green functions the numerator is approximated by

$$(g_{i1} + g_{i2})^2 \approx \frac{\bar{A}^2 e^{2iQD}}{D} (E + f(k))^2$$

and then through the Matsubara frequency method it can be shown that if

$$B(E) = \bar{A}^2 (E + f(k))^2$$

then the zeroth order term

$$B^{(0)}(E) = \frac{4i(E+t)(E^2 + i\sqrt{\frac{E^2}{t^2}}t\sqrt{t^2-E^2})}{\pi t^2\sqrt{t^2-E^2}(E^2+3t^2)}$$

is zero in the limit $E = 0$. The first order term

$$\lim_{E\to 0} B^{(1)}(E) = -\frac{4}{3\pi t^3}$$

which is finite, and thus the decay of $\Delta n_i^{\text{Bridge}}$ goes as D^{-3}. A comparison to the numerical result is shown in Fig. 5.17 showing the same characteristic decay rate but smaller by a constant of 1.2.

5.2 Carbon nanotubes

The methods for studying the Friedel oscillations in graphene will now be extended to the case of substitutional impurities in carbon nanotubes. The behaviour of the resulting spatial modulations in $\Delta\rho$ and Δn will be investigated using numerical calculations followed by the derivation of closed-form SPA-based expressions of these quantities (Sec. 5.2.1). The effect of increasing the nanotube diameter will then be studied in Sec. 5.2.2, showing that in the limit of infinite diameter the behaviour of the Friedel oscillations transitions to that seen in graphene.

5.2.1 Substitutional impurities

As with the case of graphene, the change in the diagonal Green function at site i due to an impurity of strength λ placed at site A is

$$\Delta G_{ii} = \frac{g_{iA}^2 \lambda}{1 - g_{ii}\lambda}$$

however the system Green functions are different. It is known from Chap. 3 that the Green functions for an ACNT are

$$g_{jl} = \frac{i}{4t^2 N_C} \sum_j \sum_{\pm} \frac{N(E) e^{i\frac{2\pi j}{N_C}(m+n) + iq_Z^{\pm}|m-n|}}{\cos\left(\frac{\pi j}{N_C}\right) \sin q_Z^{\pm} + 2\sin 2q_Z^{\pm}}$$

where

$$q_Z^{\pm} = \pm \cos^{-1}\left(-\frac{1}{2}\cos\left(\frac{\pi j}{N_C}\right) \pm \frac{1}{2t}\sqrt{E^2 - t^2 \sin^2(\frac{\pi j}{N_C})}\right)$$

and

$$g_{jl} = \frac{i}{4t^2 N_C} \sum_j \frac{N(E) e^{iq_A(m+n) + i\frac{\pi j}{N_C}(m-n)}}{\cos\left(\frac{\pi j}{N_C}\right) \sin q_A}$$

for a ZZNT where

$$q_A = \pm \cos^{-1}\left(\frac{\frac{E^2}{t^2} - 1 - 4\cos^2(\frac{\pi j}{N_C})}{4\cos\left(\frac{\pi j}{N_C}\right)}\right).$$

The Friedel oscillations that arise in $\Delta\rho$ and Δn can then immediately be determined. Numerically calculated cross-sections using these equations are shown in Fig. 5.18 where a nitrogen impurity of $\lambda = -4$eV has been placed at the origin.

It is clear from the plot that Friedel oscillations in nanotubes display drastically different behaviour compared to graphene. First consider the modulations in

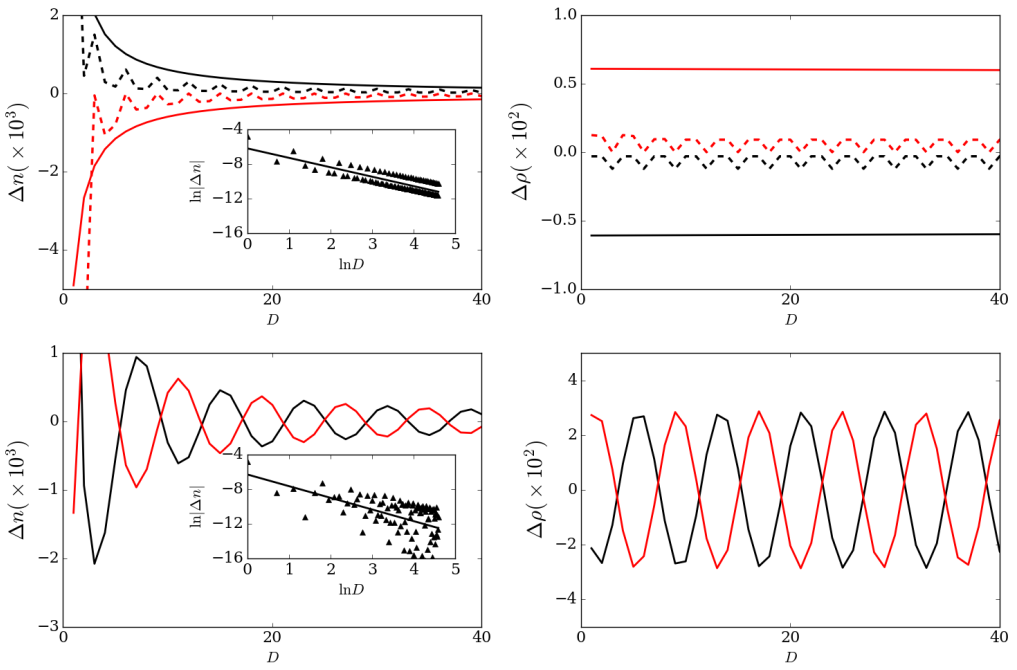

Figure 5.18: Cross-sections of the Friedel oscillations in Δn (left panels) and $\Delta\rho$ (right panels) in a carbon nanotube of width $N_C = 6$ atoms as a result of a substitutional impurity of strength λ at site $D = 0$. Geometry is indicated by the solid (armchair) and dashed (zigzag) lines, with sublattice indicated by colour (same as impurity - black, opposite - red). The Fermi energy is $E_F = 0$ in the top panels and $E_F = 0.2\,|t|$ in the bottom panels. The inset plots of Δn are log-log plots of the same sublattice data taken from the main plot (black triangles) and a linear regression demonstrating D^{-1} decay as the black line.

$\Delta\rho$ in the right-hand panels. The most interesting property is that there is no decay with distance, regardless of E_F or whether the nanotube has armchair or zigzag geometry. Because of the reduced dimensionality of the system the modulations in $\Delta\rho$ do not dissipate and propagate along the system without dying away. This is in stark contrast to graphene where D^{-1} decay is observed (c.f. Fig. 5.4). Again each sublattice responds differently to the impurity, forming almost a mirror image of each other about $\Delta\rho = 0$. Additionally

the period-3 behaviour is evident in the zigzag nanotube, and this effect is already well understood as coming from the component of the Fermi wavevector along the axial direction. Because of this more complicated behaviour it has been omitted from the $E_F \neq 0$ plot for clarity, but it should be noted that it shows the same oscillation period as the armchair case. When $E_F = 0$ the commensurability effect occurs due to the lattice periodicity matching that of the Friedel oscillations, and the oscillations seemingly disappear. The most immediate aspect of the Friedel oscillations in Δn (Fig. 5.18 left-hand panels) is that they exhibit a decay of D^{-1} regardless of E_F. This is illustrated by the linear regression line shown in the inset of the plots. Again it is seen that a commensurability effect exists at $E_F = 0$, as well the period-3 behaviour intrinsic to the zigzag nanotubes is apparent.

The behaviour of the Friedel oscillations in this case can be explained using the stationary phase approximation and the Matsubara frequency method that was applied to graphene in the previous section. From the form of g_{jl} given above the form of this given via the stationary phase approximation for either nanotube geometry is

$$g_{jl} = \sum_j A(E, j) e^{iQ(E,j)D}$$

which does not have a distance decay so clearly the oscillations in LDOS will not decay either. An explanation of the behaviour of Δn is more involved. Consider a weak impurity $\lambda \ll 1$ and apply the Born approximation as in Sec. 5.1.1, then the modulation in Δn can be written

$$\Delta n \sim -\frac{2\lambda}{\pi} \int_{-\infty}^{\infty} f(E) g_{iA}^2.$$

Using the SPA approximation and the Matsubara frequency method this can

be approximated by

$$\Delta n \sim \frac{2}{\lambda}\pi \,\mathrm{Im} \sum_{j,k} e^{2iQ^{(0)}D} \sum_{l} \frac{(A^2)^{(l)}}{(2iQ^{(1)})^{l+1}} \frac{1}{D^{l+1}}. \tag{5.11}$$

Unlike the case of graphene the term $(A^2)^{(l)}$ does *not* disappear at $E = 0$, for example the lowest order term

$$\lim_{E\to 0}(A^2)^{(0)} = \frac{1-t^4}{48N_C^2 t^4}$$

for $j = 0$ in the armchair nanotube. If the $l = 0$ term in the expansion of Eq. 5.11 is non-zero then the decay rate of Δn is D^{-1} regardless of E. When $E \to 0$, $Q^{(0)} \to \pi$, and so the oscillation period $e^{2iQ^{(0)}D}$ is commensurate with the lattice spacing as was seen in the case of graphene.

5.2.2 Effect of increasing diameter

The different decay rates in the Friedel oscillations between nanotubes and graphene must be reconciled if this theory is to be self-consistent. By increasing the diameter of the nanotube in the limiting case of infinite diameter the behaviour should transition to that of graphene. The decay rate parameter α is defined as giving the decay rate D^{α} for the Friedel oscillations. A plot of α for the Friedel oscillations in Δn versus the nanotube diameter N_C is presented in Fig. 5.19 for both armchair and zigzag nanotubes at both $E_F = 0$ and $E_F \neq 0$. Only the same sublattice case is considered. It is clear that the Friedel oscillation behaviour does indeed return to that of graphene when the nanotube diameter is increased. It should be noted that nanotubes with such large diameters as depicted in Fig. 5.19 are inherently unstable and that such sizes are

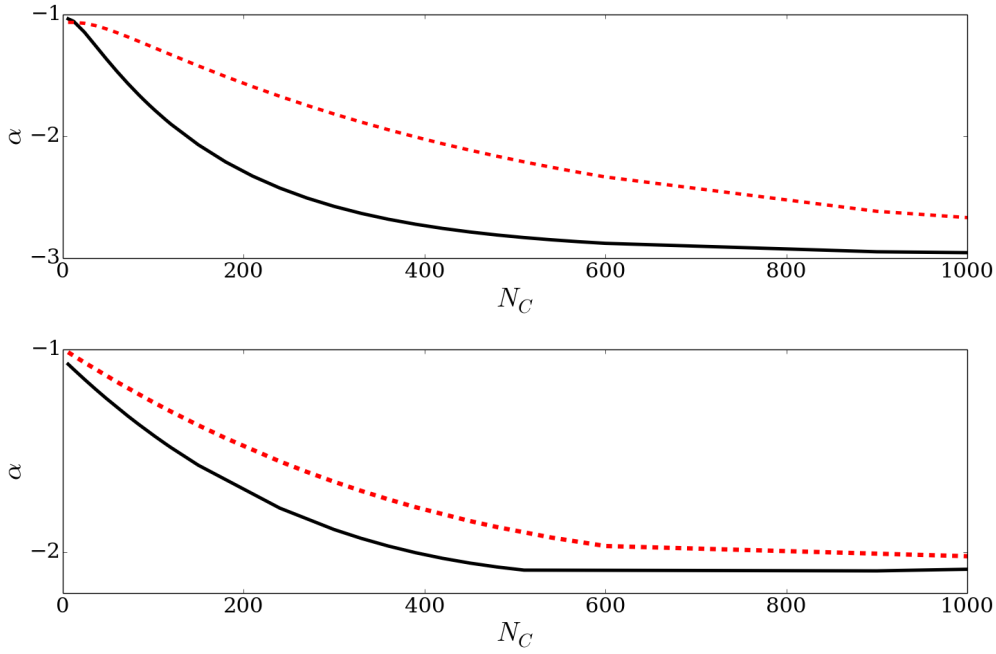

Figure 5.19: Decay rate α of the Friedel oscillations in Δn on the impurity sublattice as a function of nanotube diameter, with $E_F = 0$ (top) and $E_F \neq 0$ (bottom) for armchair (black solid) and zigzag (red dashed) geometries. Because of the difficulty in determining an accurate decay rate in the $E_F \neq 0$ case, an average of values was taken over $E_F = 0.05\,|t|$, $E_F = 0.1\,|t|$ and $E_F = 0.2\,|t|$ and the resulting data points fitted with a regression curve.

only investigated to show the self-consistency of the model.

5.3 Chapter summary

In this chapter closed-form analytic expressions for Friedel oscillations in carrier density (Δn) and local density of states ($\Delta \rho$), caused by symmetry breaking in the lattice, have been derived along the high symmetry directions in graphene and carbon nanotubes by employing a stationary phase approxima-

tion of the lattice Green Functions. Good agreement was found in comparison to numerical calculations for a variety of impurity types in the long-range limit.

In Sec. 5.1 the FOs in graphene were studied. It was found that the FOs in $\Delta\rho$ exhibit an oscillatory decay profile, with a period determined by the Fermi energy E_F and decaying with distance (D) as D^{-1} for all impurities for $E_F \neq 0$. The FOs in Δn show a similar behaviour but with a faster decay rate of D^{-2} when $E_F \neq 0$. At the Dirac point $E_F = 0$, FOs in Δn away from substitutional, top and bridge adsorbed impurities were found to decay with as D^{-3}. This change in behaviour is due to the oscillation period becoming commensurate with the lattice spacing. In the case of vacancies and a resonant top adsorbed carbon Δn is unchanged from the pristine case on all lattice sites due to the symmetry of electron and hole states in the LDOS profile around the Dirac point. The top adsorbed carbon is, however, less energetically favoured than the more naturally occurring bridge adsorbed carbon. When changed to the bridge adsorbed configuration, it can be shown that cross-sublattice interference between propagators arising from the bonding arrangement ensures Δn does not vanish at $E_F = 0$ in this case.

A similar study was conducted with carbon nanotubes in Sec. 5.2.1. In this case the reduced dimensionality of the system, as well as the non-vanishing density of states at $E_F = 0$, results in distinctly different behaviour in the Friedel oscillations present in $\Delta\rho$ and Δn. A single substitutional impurity was used as the symmetry breaking agent and both armchair and zigzag geometries were considered. The oscillations in $\Delta\rho$ were found to *not* decay with distance D, and the oscillations in Δn shown to decay as D^{-1}. A commensurability effect at $E_F = 0$ is found but unlike the case of graphene the decay rate does not

change. This behaviour was then explained using the SPA Green functions derived in Chap. 3. In the limit of increasing diameter it was shown that the decay in both $\Delta\rho$ and Δn returns to the values seen in graphene. In the following chapter the role of scattering by impurities will be investigated using similar techniques to those used in this chapter. The work on Friedel oscillations in graphene was published in [91].

Chapter 6

Scattering suppression and symmetry breaking

Owing to its two-dimensional structure and excellent conductivity with low noise, graphene-based materials have generated a large amount of interest in their application to chemical sensing. When a concentration of dopants is introduced to the system the conductivity is modified due to scattering. By measuring this change in conductivity the concentration can be determined, in some cases with sensitivity in the sub parts-per-million range [148]. The question of which substances graphene can detect well, i.e. those with a large impact on transport properties, seems quite open-ended due to the overwhelming number of possibilities. While *ab-initio* techniques work well on a case-by-case basis it would be more beneficial to have a general approach to guide the search more directly. In this chapter a method will be proposed to do this based on the techniques applied to Green functions and Friedel oscillations

from the previous chapters. The method will be used to determine which impurity species are suitable for gas sensing applications, from a general standpoint. It will be shown that the scattering, and therefore the changes in conductance, rely more on the type of bonding of the adsorbate than on the exact dopant species. More specifically it is demonstrated that central adsorbed dopants have a very minor effect on the transport properties around the Dirac point compared to top and bridge adsorbed. This suggests the top and bridge adsorbed are more suited for sensor applications as the effect is more dramatic.

Evidence supporting this is shown using two methods - through the real-space Green functions of bulk graphene in Sec. 6.1 and a numerical simulation of conductance in a graphene nanoribbon in Sec. 6.3. The proposed mechanism is the phase difference between Green functions leads to an interference effect, which in turn suppresses the scattering for central adsorbed impurities such that the perturbed system Green function $G = g + \Delta G$ is similar to the pristine one. Physically this means that electrons travelling through the system are not scattered, despite the presence of the impurity. A similar interference effect can be observed experimentally with an STM when the atomic tip is centered in the middle of a graphene hexagon, the location of the central adsorbed impurity considered here. This causes the hexagon centers in the graphene to appear as corrugation holes on the resulting STM image. Calculations have shown that this arises from destructive interference of the coupling terms between the atomic tip and the six carbon atoms around the perimeter of the hexagon [149, 150]. To back up the explanation that an interference effect is responsible for scattering suppression, it is shown in Sec. 6.2 that straining the system uniaxially alters the phase difference between the propagators that were causing the interference, mitigating this effect and thus enhancing the scattering. This suggests that central adsorbed impurities could instead function as part

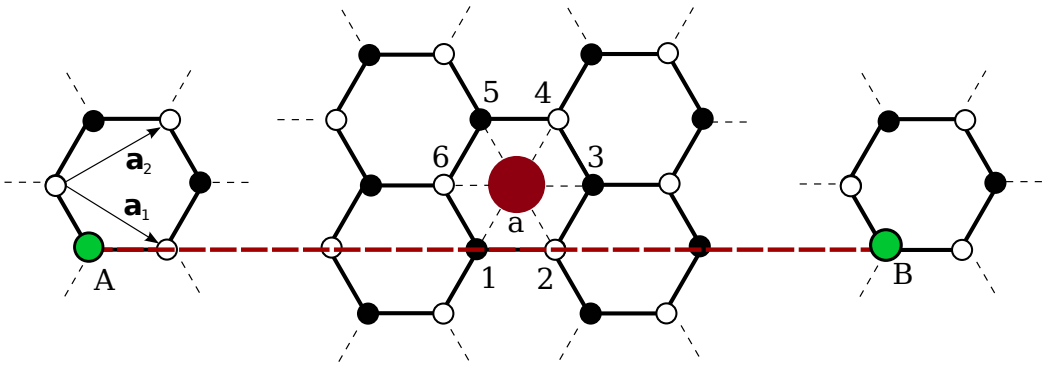

Figure 6.1: Schematic of a central adsorbed impurity (index a) connected to the sites indexed $R = \{1, 2, 3, 4, 5, 6\}$ by overlap integral τ. Electron propagation between lattice sites A and B is examined, aligned along the armchair axis indicated by the dashed line, which is scattered by the impurity at a.

of a highly sensitive graphene strain sensor. The work in this chapter is part of Ref. [151]. In the paper complimentary methods developed by the other authors are described which support the same conclusion as the work shown here. These alternative methods use momentum-space Green functions and the scattering cross-section.

6.1 Quantifying scattering

In this section the quantity ΔG_{AB} corresponding to the propagation between some lattice sites A and B will be compared for top, bridge and central adsorbed impurities. A schematic of the central adsorbed case is shown in Fig. 6.1. The configuration of A and B will be fixed at 20 unit cells separation in the armchair direction, and both will be located on the black sublattice. For this reason the subscript AB is redundant and will be dropped, instead the type of

impurity placed between A and B will be denoted in the subscript index. The perturbation matrices for the three adsorbate types are given by

$$\hat{V}_t = |1\rangle \tau \langle a| + H.c.$$

$$\hat{V}_b = |1\rangle \tau \langle a| + |2\rangle \tau \langle a| + H.c.$$

$$\hat{V}_c = \sum_{i \in R} |i\rangle \tau \langle a| + H.c.$$

where $R = \{1, 2, 3, 4, 5, 6\}$ and for ease of notation the matrices have subscript indices for top (t), bridge (b) and central adsorbates (c). In the case of centre bonded impurities the bonding to each host site may not always be identical and depends on how the impurity hybridises. The possibilities are [152]: (i) It may hybridize equally with all six neighbouring carbon atoms $\tau_i = \tau$, which is the case for s and d_{z^2} orbitals; (ii) It may have a π-phase difference in the hybridisation of the adsorbed impurity with the two different sublattices, $\tau_1 = \tau_3 = \tau_5 = -\tau_2 = -\tau_4 = -\tau_6 \equiv \tau$, which is typical of f-orbitals; (iii) For a d_{xy} orbital, $\tau_1 = \tau_4 = 0$ and $\tau_2 = \tau_5 = -\tau_3 = -\tau_6 = 3\tau/2$; (iv) for a $d_{x^2-y^2}$ orbital, $\tau_1 = \tau_4 = \tau$ and $\tau_2 = \tau_3 = \tau_5 = \tau_6 = -\tau/2$. In this chapter the focus is on the first possibility for the sake of simplicity, where the values of $|\tau_i|$ are the same for all $i \in R$.

The scattering is quantified by the Green function $\Delta G_{AB} = \langle A| \hat{g}\hat{V}\hat{G} |B\rangle$ which can be calculated using the Dyson equation as

$$\Delta G_t = \frac{g_{A1} g_{1B} \Sigma}{1 - g_{11}\Sigma}$$

$$\Delta G_b = \frac{(g_{A1} + g_{A2})(g_{1B} + g_{2B})\Sigma}{1 - 2(g_{11} + g_{12})\Sigma}$$

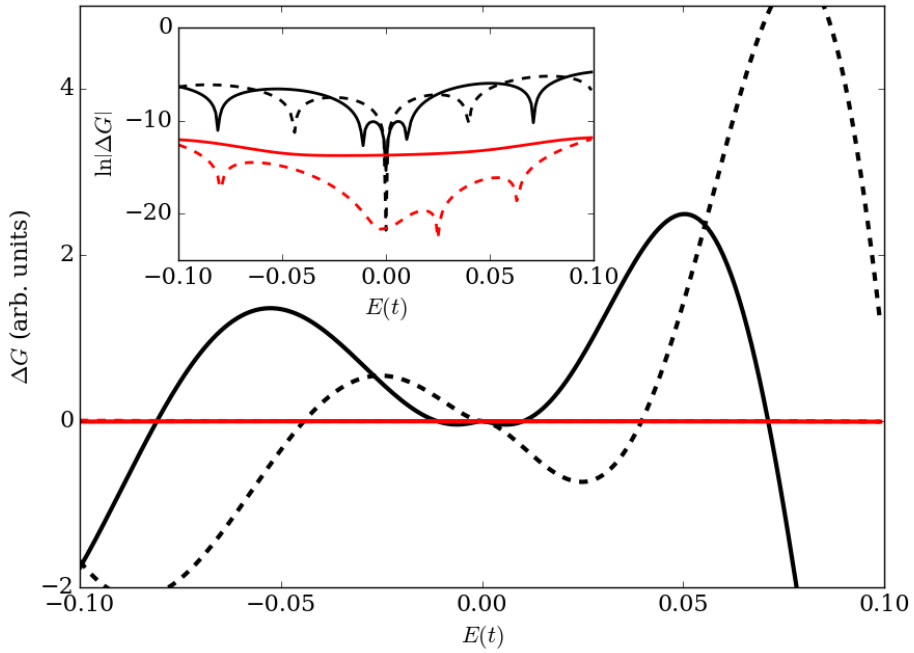

Figure 6.2: Real (solid) and imaginary (dashed) parts of ΔG_t (black) and ΔG_c (red) around the Dirac point. The impurities are parametrised by $\epsilon_a = |t|$ and $\tau = -2\,|t|$. Due to the large difference in magnitude a log-linear plot of the same data is shown as inset.

$$\Delta G_c = \frac{\left(\sum_{i=1}^{6} g_{Ai}\right)\left(\sum_{j=1}^{6} g_{jB}\right)\Sigma}{1 - 6(g_{11} + 2g_{12} + 2g_{13} + g_{14})\Sigma}.$$

The lattice symmetries of graphene have been used to reduce the Green functions g into a small set of equivalent propagators and $\Sigma = g_{aa}\tau^2$ is the self-energy of the impurity which is the same in all three cases.

A plot of ΔG_t and ΔG_c around the Dirac point is shown in Fig. 6.2, ΔG_b has been omitted as the behaviour is fairly similar to ΔG_t. The impurities have been parametrised by $\epsilon_a = |t|$ and $\tau = -2\,|t|$, chosen so as to place the resonance energy away from the Dirac point which would have obfuscated the

functional behaviour. In Sec. 6.3 the effect of this resonance in realistic scenarios will be discussed. Additionally, the qualitative behaviour of the various ΔG are not dependent on the parametrisation. Clearly ΔG_c is many orders of magnitude smaller than ΔG_t (and ΔG_b) meaning the scattering is greatly suppressed in the central adsorbed case. Endeavours will now be made to find why this behaviour occurs. The similarities in the equations for ΔG permit the writing of a general form

$$\Delta G_X = \alpha_X \beta_X T_X \qquad \text{where} \qquad T_X = \frac{\Sigma}{1 - \gamma_X \Sigma}$$

for the impurity type X. The coefficients can be inferred from the previous set of equations and T is the scattering matrix introduced in Chap. 2. By examining these components individually their effect on the overall scattering behaviour can be determined.

6.1.1 Green function component behaviour

In this section the individual behaviour of the component Green functions of ΔG_X will be investigated. A plot of T_t and T_c is shown in Fig. 6.3, again the behaviour of T_b is similar to T_t so it is omitted. As was found with ΔG, the central adsorbed case is several orders of magnitude smaller than the top adsorbed, the imaginary part exhibiting the most drastic difference. The changing behaviour of T_X between cases arises from the parameters

$$\gamma_t = g_{11}$$

$$\gamma_b = 2(g_{11} + g_{12})$$

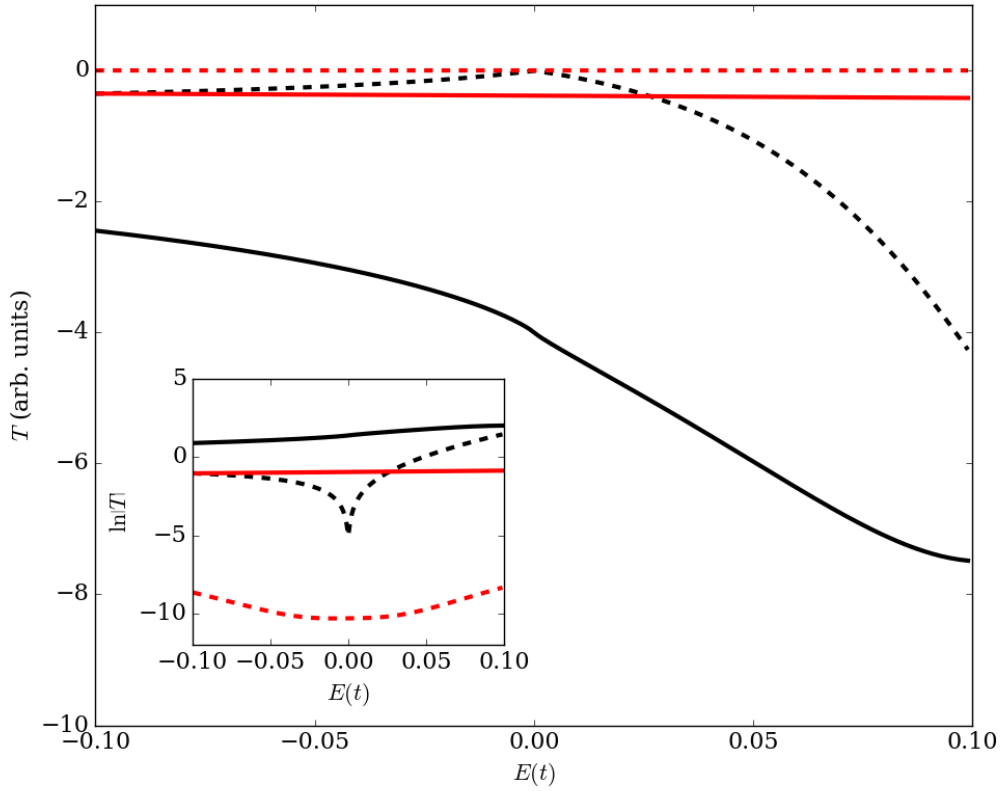

Figure 6.3: Real (solid) and imaginary (dashed) parts of T_t (black) and T_c (red) around the Dirac point. The impurities are parametrised by $\epsilon_a = |t|$ and $\tau = -2\,|t|$. Due to the large difference in magnitude a log-linear plot of the same data is shown as inset.

$$\gamma_c = 6(g_{11} + 2g_{12} + 2g_{13} + g_{14}).$$

From inspecting the component Green functions it can be shown that in the low energy region

$$\mathrm{Im}(g_{11}) \approx -2\,\mathrm{Im}(g_{13})$$

$$\mathrm{Im}(g_{14}) \approx -2\,\mathrm{Im}(g_{12})$$

which leads to cancellations in γ_c which in turn explains the vanishing imaginary part of T_c. For the real part there is no cancellation of terms, rather γ_c takes a large value due to the large number of single Green functions added together has the effect of reducing $\mathrm{Re}(T_c)$. However this does not seem to account for the diminished scattering of the central adsorbed case alone. It follows that the remaining terms α_c and β_c in the numerator of ΔG_c must be giving rise to the suppressed scattering. A plot of $\alpha_X \beta_X$ for top and central adsorbed impurities is shown in Fig. 6.4. The similarity with the plot of ΔG_X in Fig. 6.2 should be noted. Clearly the qualitative features and the small magnitude of ΔG_c are coming from these terms almost exclusively. Recall

$$\alpha_t = g_{A1}, \qquad \alpha_b = g_{A1} + g_{A2}$$

and

$$\alpha_c = g_{A1} + g_{A2} + g_{A3} + g_{A4} + g_{A5} + g_{A6}.$$

Assuming A and the impurity location are sufficiently separated these Green functions can be approximated by the SPA expression for the long-range Green functions (Sec. 3.2.2)

$$g_{ij}(E) \approx \frac{\bar{A}(E) N(E) e^{iq(E)D}}{\sqrt{D}}.$$

If A is at a distance D in the armchair direction clearly

$$\alpha_t \approx \frac{\bar{A}(E) e^{iq(E)D}}{\sqrt{D}} \Big(E \Big)$$

and

$$\alpha_b \approx \frac{\bar{A}(E) e^{iq(E)D}}{\sqrt{D}} \Big(E + f(\mathbf{k}) \Big)$$

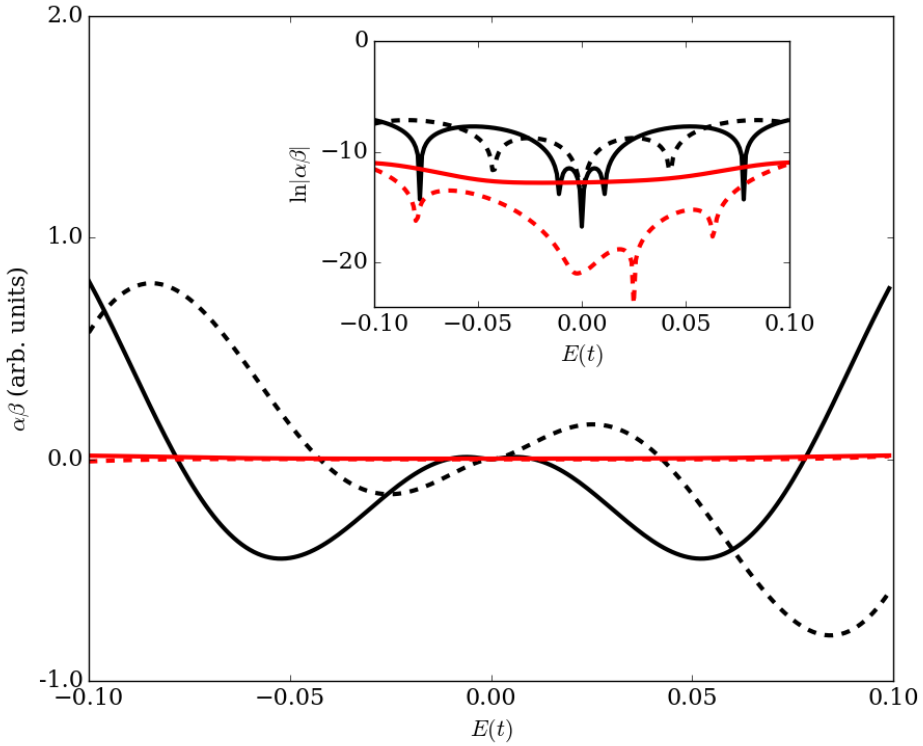

Figure 6.4: Real (solid) and imaginary (dashed) parts of $\alpha_t\beta_t$ (black) and $\alpha_c\beta_c$ (red) around the Dirac point. The impurities are parametrised by $\epsilon_a = |t|$ and $\tau = -2\,|t|$. Due to the large difference in magnitude a log-linear plot of the same data is shown as inset.

however for the central adsorbed case the majority of Green functions lie slightly off the armchair axis. This can be resolved by inclusion of a phase factor, as demonstrated in Fig. 6.5. The term α_c can then be written

$$\begin{aligned}\alpha_c &\approx \frac{\bar{A}(E)e^{iq(E)D}}{\sqrt{D}}\Big(E(1+e^{i\mathbf{k}\cdot\mathbf{a}_1}+e^{i\mathbf{k}\cdot(\mathbf{a}_1-\mathbf{a}_2)})+f(\mathbf{k})(1+e^{-i\mathbf{k}\cdot\mathbf{a}_2}+e^{i\mathbf{k}\cdot(\mathbf{a}_1-\mathbf{a}_2)})\Big)\\ &\approx \frac{\bar{A}(E)e^{iq(E)D}}{\sqrt{D}}\Big(Ef(\mathbf{k})+f^2(\mathbf{k})e^{-i\mathbf{k}\cdot\mathbf{a}_2}\Big).\end{aligned}$$

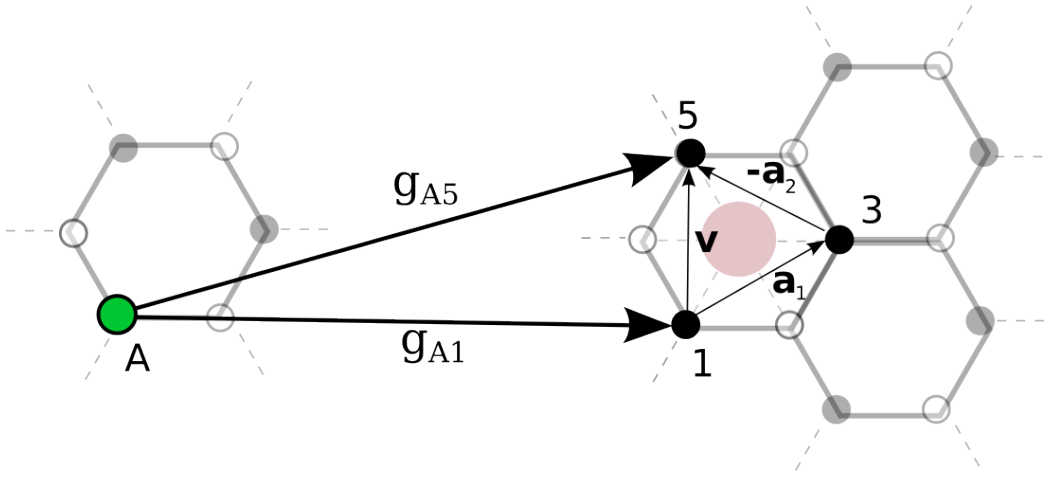

Figure 6.5: While g_{A1} can be expressed through the SPA directly g_{A5} requires an extra phase term as it lies slightly off the armchair axis. The corrective term is $e^{i\mathbf{k}\cdot\mathbf{v}}$ where $\mathbf{v} = \mathbf{a}_1 - \mathbf{a}_2$ where $\mathbf{a}_1$ and $\mathbf{a}_2$ are the conventional real-space lattice vectors of graphene.

where the simplification has been done using

$$f(\mathbf{k}) = 1 + e^{i\mathbf{k}.\mathbf{a_1}} + e^{i\mathbf{k}.\mathbf{a_2}}.$$

In the low-energy limit, momentum values are confined to the linear region around the Dirac points so the approximation

$$f(\mathbf{k}) \approx \sqrt{3}a\,|\delta\mathbf{k}|$$

can be used (see Appendix B.1). Therefore to first order $\Delta G_t \sim E^2$ and $\Delta G_b \sim E^2$ but $\Delta G_c \sim E^2\,|\delta\mathbf{k}|^2$, hence the scattering of central adsorbed impurities vanishes in the low-energy limit.

6.2 Uniaxial strain

The results of the last section show that the source of the scattering suppression of the central adsorbed impurity comes from the interference of Green functions arising from the symmetry breaking in the lattice. Therefore by breaking the lattice symmetry by uniaxial strain the interference should be reduced and the scattering increased. In this section uniaxial strain will be introduced to graphene and the behaviour of $\alpha_c\beta_c$ in the small strain limit will be examined. It will be shown that a linear strain term appears which is independent of q, so the scattering should no longer be suppressed and is instead enhanced by increasing the strain. This is corroborated with numerical calculations of ΔG_c, T_c and $\alpha_c\beta_c$.

Uniaxial strain can be introduced via the strain tensor [153]

$$\mathbf{\Omega} = \Omega \begin{pmatrix} \cos^2\theta - \sigma\sin^2\theta & (1+\sigma)\sin\theta\cos\theta \\ (1+\sigma)\sin\theta\cos\theta & \sin^2\theta - \sigma\cos^2\theta \end{pmatrix}$$

where Ω is the strain parameter (up to around a physically achievable maximum of 0.2 for graphene), $\sigma = 0.165$ is the Poisson ratio for graphite and θ is the angle of applied strain taking values $\theta = 0$ and $\theta = \frac{\pi}{2}$ for zigzag and armchair strain respectively. Graphene has extraordinary elastic properties and can withstand reversible deformations of approximately 20% depending on direction of strain [154]. The act of straining it modifies the physical and electronic structure by changing the bond lengths in the system and destroying the six-fold symmetry. While this would also affect the different overlaps τ_i between the impurity and the host this will not be altered in the following calculations. This is done so as to isolate the effect of the changing lattice sym-

metry, its inclusion would serve only to enhance the effect by further changing the symmetry.

Any vector $\mathbf{v}^0$ in the unstrained system undergoes the transformation

$$\mathbf{v} = (\mathbf{I} + \mathbf{\Omega}) \cdot \mathbf{v}^0,$$

for example the new primitive lattice vectors are

$$\mathbf{a}_1 = \frac{3}{2}a(1+\Omega)\hat{x} + \frac{\sqrt{3}}{2}a(1-\sigma\Omega)\hat{y}$$
$$\mathbf{a}_2 = \frac{3}{2}a(1+\Omega)\hat{x} - \frac{\sqrt{3}}{2}a(1-\sigma\Omega)\hat{y}.$$

Concerning electronic structure the change in bond lengths has been accommodated using an equation shown by Pereira et al. [153] which gives expressions for the three different hopping values between nearest neighbour atoms. Using this prescription the strain-dependent Green functions can be derived in a similar way to the regular lattice Green functions shown in Chap. 3. Their derivation along with the long-range SPA form have been derived previously by Power et al. [155] and in the interest of conciseness will not be shown here. To briefly demonstrate the effect of strain on the electronic structure the LDOS is shown in Fig. 6.6 for cases of unstrained and armchair strain of $\Omega = 0.2$. The spectral range has been reduced by around 80%, having undergone compression along the energy axis (spectral compression), and two new singularities have been formed. In unstrained graphene the van-Hove singularities in the spectrum coincide with the hopping integral energy t, however by breaking the symmetry of the system the differing bond lengths results in two separate t values. This is the source of the extra peaks and the altered density of

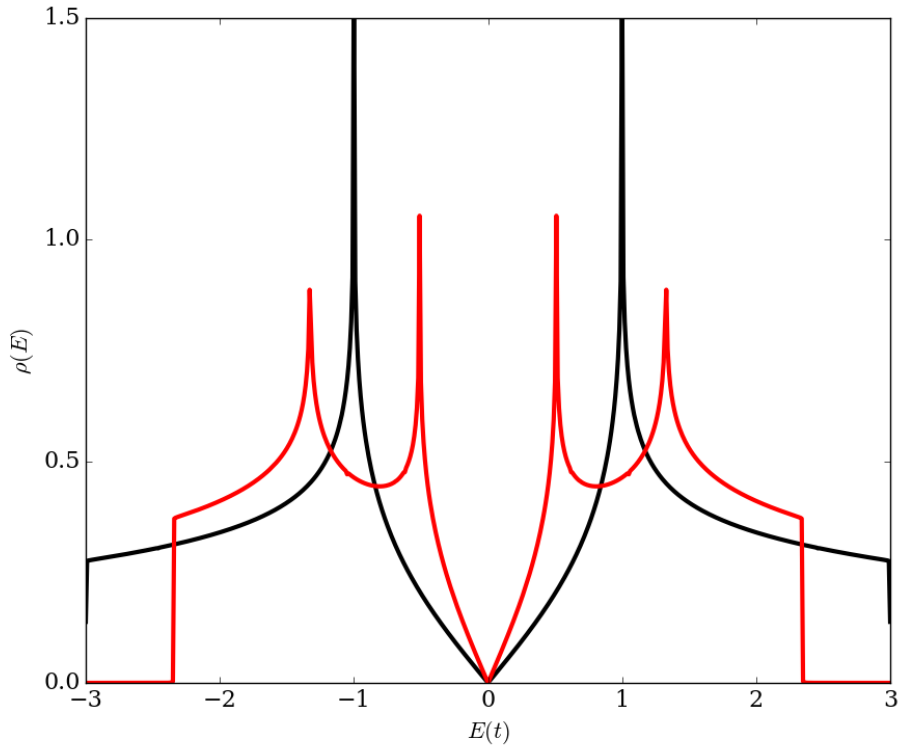

Figure 6.6: Graphene's LDOS spectrum for $\Omega = 0$ (black) and $\Omega = 0.2$ (red) uniaxial armchair strain.

states. A plot of ΔG_t and ΔG_c for armchair strain of $\Omega = 0.2$ is shown in Fig. 6.7 and should be directly compared to the unstrained case in Fig. 6.2. It is immediately clear that the scattering is enhanced for the central adsorbed impurity and that it is now comparable in magnitude to the top adsorbed case. Compared to the unstrained case the scattering of the top adsorbed has also increased by an order of magnitude, which can be seen by comparing the scales of Fig. 6.7 and Fig. 6.2. The oscillatory behaviour of both functions has increased due to the spectral compression of the system Green functions, as was demonstrated with the LDOS spectrum in Fig. 6.6.

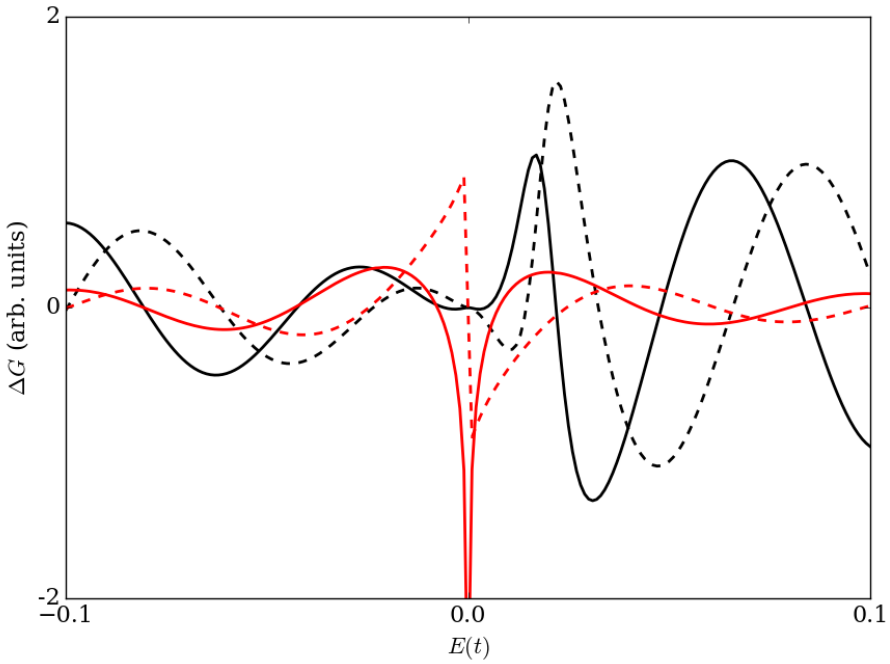

Figure 6.7: Real (solid) and imaginary (dashed) parts of ΔG_t (black) and ΔG_c (red) around the Dirac point with uniaxial armchair strain of $\Omega = 0.2$. The equivalent unstrained plot is shown in Fig. 6.2. The impurities are parametrised by $\epsilon_a = |t|$ and $\tau = -2\,|t|$.

The source of the scattering enhancement of the central adsorbed impurity, whether arising from T_c or $\alpha_c\beta_c$, will now be investigated. A strain dependent form of α_c will be derived and the behaviour of the function around the Dirac points examined. This causes the appearance of a q independent term which is linear in Ω, and this explains the increase in scattering in ΔG_c as it does not disappear in the low-energy limit. It should be noted that with increasing strain the position in momentum space of the Dirac points changes and does not follow the border of the FBZ in reciprocal space, unlike the unstrained case. It is possible to write a closed-form expression for this movement as a function

of strain, or to calculate it numerically, however this would make a similar expansion to that below extremely lengthy and the same general result would be found. As the limit $\Omega \to 0$ is taken the assumption that the Dirac point position has not moved can be rationalised, and that the forthcoming solution represents the first order response to the applied strain.

Using the strain-dependent SPA Green functions it is straightforward to rewrite a strain dependent α_c

$$\alpha_c(E,\Omega) \approx \frac{\bar{A}(E,\Omega)e^{iq(E,\Omega)D}}{\sqrt{D}} \times \Big(E(1+e^{i\mathbf{k}\cdot\mathbf{a}_1}+e^{i\mathbf{k}\cdot(\mathbf{a}_1-\mathbf{a}_2)})+f(\mathbf{k},\Omega)(1+e^{-i\mathbf{k}\cdot\mathbf{a}_2}+e^{i\mathbf{k}\cdot(\mathbf{a}_1-\mathbf{a}_2)})\Big)$$

where $\bar{A}(E,\Omega)$, $q(E,\Omega)$ and $f(\mathbf{k},\Omega)$ are now strain dependent and

$$\mathbf{k}\cdot\mathbf{a}_1 = k_x\frac{3}{2}a(1+\Omega)+k_y\frac{\sqrt{3}}{2}a(1-\sigma\Omega)$$
$$\mathbf{k}\cdot\mathbf{a}_2 = k_x\frac{3}{2}a(1+\Omega)-k_y\frac{\sqrt{3}}{2}a(1-\sigma\Omega).$$

The substitution $k_A = \frac{3}{2}ak_x$ and $k_Z = \frac{\sqrt{3}}{2}ak_y$ can be made as was done with the unstrained case to yield

$$f(\mathbf{k},\Omega) = 1+e^{ik_A(1+\Omega)+ik_Z(1-\sigma\Omega)}+e^{ik_A(1+\Omega)-ik_Z(1-\sigma\Omega)}.$$

Substituting this into $\alpha_c(E,\Omega)$ and dropping the $\frac{\bar{A}(E,\Omega)e^{iq(E,\Omega)D}}{\sqrt{D}}$ prefactor gives

$$\alpha_c \sim e^{ik_Z(1-\sigma\Omega)}\Big(3+E+2\cos\left(-2k_Z(1-\sigma\Omega)\right) + 2(2+E)\cos\left(k_Z(1-\sigma\Omega)\right)+ i\sin\left(k_A(1+\Omega)\right)(1+E+2\cos\left(-2k_Z(1-\sigma\Omega)\right))\Big).$$

If an expansion around the Dirac point $k_A = \pi$ and $k_Z = \frac{\pi}{3}$ is taken along with a first-order expansion in Ω

$$\alpha_c \sim h(E, \Omega) + \mathcal{O}(\delta\mathbf{k})$$

where

$$\begin{aligned} h(E,\Omega) = e^{\frac{i}{3}\pi(1-\sigma\Omega)}\Big(&- 3\cos(\pi\Omega) - E\cos(\pi\Omega) + 4\cos\Big(\frac{\pi(1-\sigma\Omega)}{3}\Big) \\ &+ 2E\cos\Big(\frac{\pi(1-\sigma\Omega)}{3}\Big) - 2\cos(\pi\Omega)\cos\Big(\frac{2\pi}{3}(1-\sigma\Omega)\Big) - i\sin(\pi\Omega) \\ &- iE\sin(\pi\Omega) - 2i\cos\Big(\frac{2\pi}{3}(1-\sigma\Omega)\Big)\sin(\pi\Omega)\Big) \end{aligned}$$

which is finite. In the limit of small energy and strain this becomes

$$\begin{aligned} h(E \ll 1, \Omega \ll 1) \sim \Omega^2 \frac{\pi^2 e^{i\frac{\pi}{3}}}{3}(3 - 2i\sqrt{3}\sigma - \sigma^2) \\ + E\frac{\pi e^{i\frac{\pi}{3}}}{\sqrt{3}}\Big(\Omega(\sigma - \sqrt{3}i) + \Omega^2\frac{\pi}{6\sqrt{3}}(9 - 6\sigma - \sigma^2(1 + 2i\sqrt{3}))\Big) \end{aligned}$$

which is non-zero at $E = 0$.

At all energies, if $\Omega = 0$, it is evident that $h = 0$ so $\alpha_c \sim \mathcal{O}(\delta\mathbf{k})$ which agrees with the unstrained case of α_c presented in the previous section. If $\alpha_c \approx \beta_c$ is assumed, which is reasonable if sites A and B are a similar distance from the impurity, then

$$\Delta G_c \sim h^2(E, \Omega) + \mathcal{O}(\delta\mathbf{k})^2$$

at low energies and the scattering is no longer suppressed, rather it is enhanced by the degree of strain applied. This is corroborated with numerical results for $\alpha_c\beta_c$ in Fig. 6.8 and Fig. 6.9, and ΔG_c in Fig. 6.7. In all figures it can be seen that the increased strain has enhanced these quantities, leading to a large amount

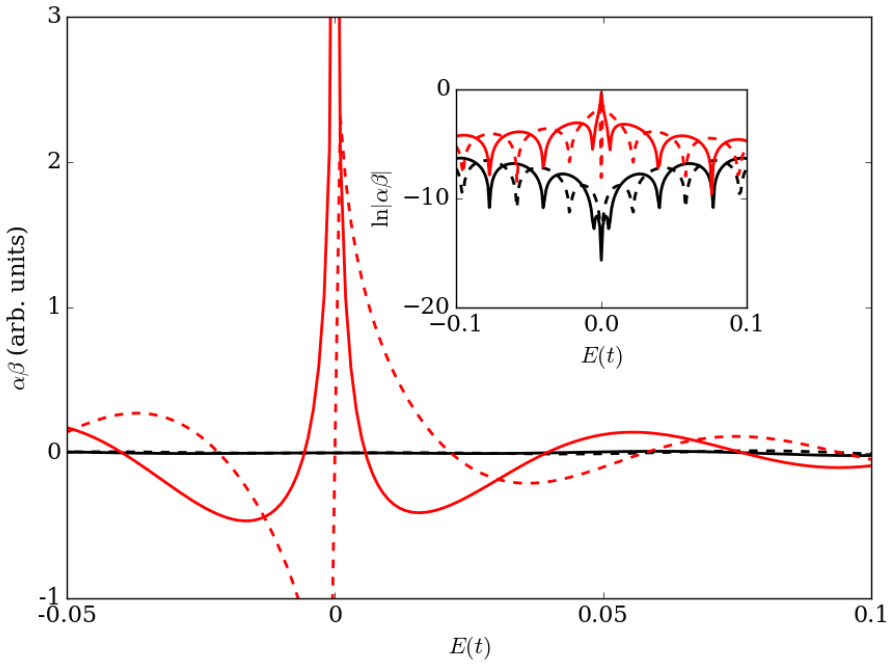

Figure 6.8: Real (solid) and imaginary (dashed) parts of $\alpha_t\beta_t$ (black) and $\alpha_c\beta_c$ (red) around the Dirac point with uniaxial armchair strain $\Omega = 0.2$. The equivalent unstrained plot is shown in Fig. 6.4. The impurities are parametrised by $\epsilon_a = |t|$ and $\tau = -2\,|t|$. Due to the large difference in magnitude a log-linear plot of the same data is shown as inset.

of scattering for the central adsorbed impurity. Concerning the top adsorbed impurity, the only change in $\alpha_t\beta_t$ is spectral compression, which was shown to arise from the Green functions of the system. Clearly

$$\alpha_t\beta_t \approx \left(\frac{\bar{A}(E,\Omega)e^{iq(E,\Omega)D}}{\sqrt{D}}E\right)^2$$

depends only on a single long-range Green function and as such there is no strain-dependent phase term, hence the unchanging magnitude upon straining.

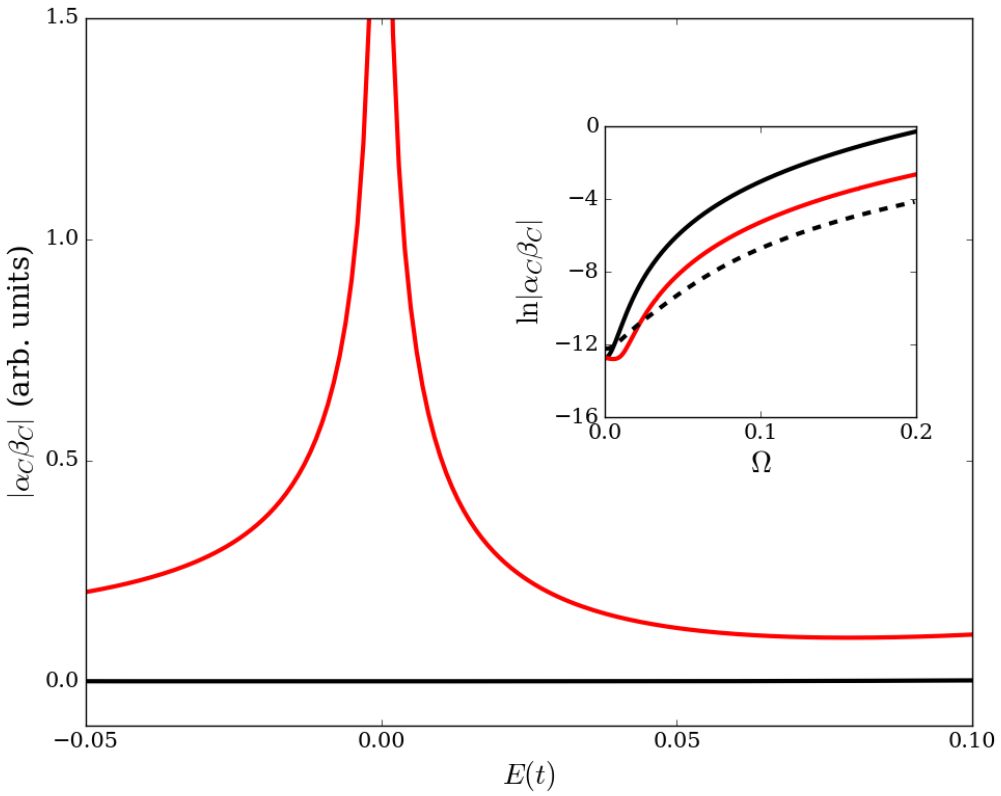

Figure 6.9: $|\alpha_c\beta_c|$ as a function of E for central bonded impurities. The black (red) line corresponds to the case of unstrained (strained $\Omega = 0.2$) impurities. Inset shows the logarithm of the difference between the two curves of the main panel plotted as a function of uniaxial strain for fixed values of energy. The black line corresponds $E = 0$, red for $E = 0.01\,|t|$ and dashed for $E = 0.05\,|t|$.

The behaviour of the T-matrix with strain can also be studied. This is plotted numerically in Fig. 6.10 and should be compared to the unstrained case in Fig. 6.3. Remarkably the only change in T_t comes from the spectral compression of the Green functions which has shifted the features towards the charge neutrality point, however the overall magnitude is unchanged from the unstrained case. This shows that the apparent increase in ΔG_t is coming from the

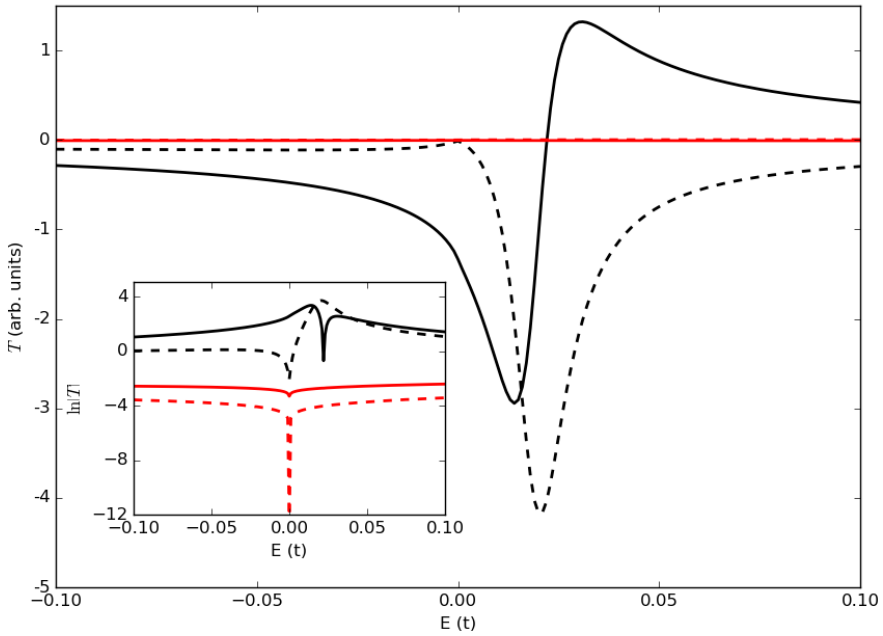

Figure 6.10: Real (solid) and imaginary (dashed) parts of T_t (black) and T_c (red) around the Dirac point with uniaxial armchair strain $\Omega = 0.2$. The impurities are parametrised by $\epsilon_a = |t|$ and $\tau = -2\,|t|$. Due to the large difference in magnitude a log-linear plot of the same data is shown as inset.

spectral compression only and not from other effects. Concerning T_c, a small dip can be observed in the real part, however it has a similar magnitude to the unstrained value. $\mathrm{Im}(T_c)$ however is no longer suppressed as the Green function interference within the intra-impurity host sites has diminished - a consequence of breaking the underlying system symmetry through strain. The minimal change in T_X further supports the hypothesis that the long-range Green function interference is what determines the scattering behaviour.

In this section it has been shown that the suppression of the scattering for a

central adsorbed impurity observed in unstrained graphene can be mitigated by the introduction of uniaxial strain. In the unstrained case considered in the previous section it was found that destructive interference between long-range propagators reduces the scattering amplitude. By applying strain this alters the symmetry of the underlying system and the interference becomes increasingly less destructive, enhancing the scattering to the same order of magnitude as is exhibited for top and bridge adsorbed impurities. It was also shown that the scattering behaviour of top and bridge adsorbates in a strained system is modified only through spectral compression of the Green functions and not through interference effects. In the next section these arguments will be supported further by investigating the effect of different dopant species on the conductance through a graphene nanoribbon. It will be shown that the scattering suppression leads to no diminished conductance in the central adsorbed case, even with high impurity concentrations.

6.3 Electrical conductance

In this section the electrical conductance of graphene nanoribbons doped by a concentration of top or central adsorbed impurities is investigated. The doped systems are built recursively using the methods introduced in Sec. 2.5.3. A schematic of an 8-atom wide graphene nanoribbon with an armchair edge (abbreviated 8-AGNR) constructed in this manner is shown in Fig. 6.11 and the DC conductance calculated using the Kubo formula of Eq. 2.27. The pristine conductance spectrum for this system is shown in Fig. 6.12. The focus of this investigation will be on the area immediately surrounding zero energy, which like bulk graphene is the most accessible region of the spectrum for experimen-

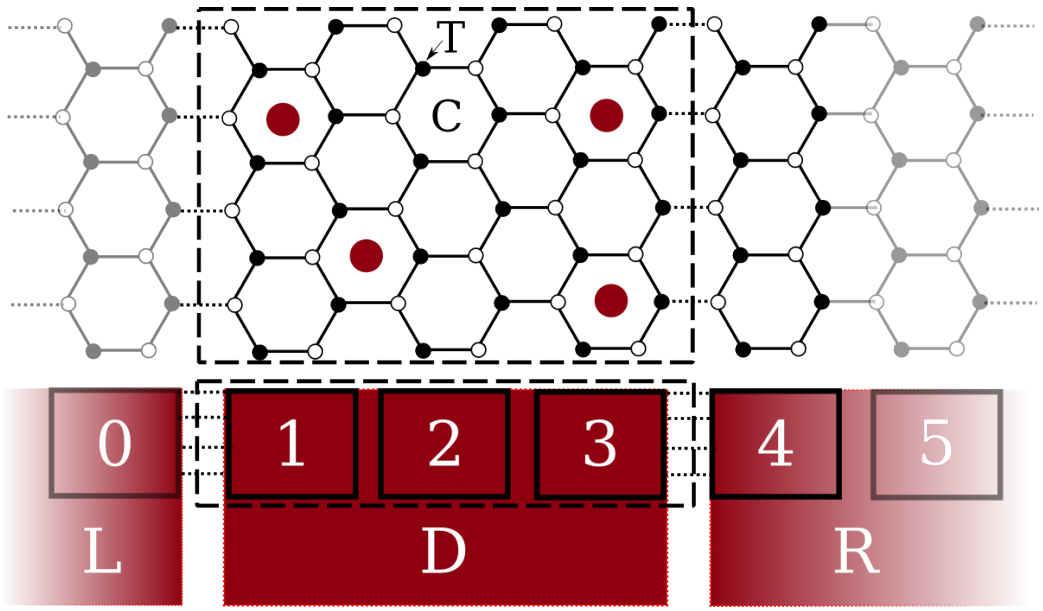

Figure 6.11: Schematic of a doped 8-AGNR (top) with unit-cell representation (bottom). The system is constructed using a 16-atom unit-cell similar to that shown for nanotubes in Sec. 3.3.4 - two semi-infinite leads (L and R) are connected to a region (D), enclosed by the dotted box, which contains impurities. Here the central region has length three unit cells and contains four central adsorbed impurities. The conductance is calculated through the interface between cells labelled 3 and 4 using the Kubo formula.

tal applications. The advantage of using recursive methods is the possibility to handle the large number of possible configurations needed to simulate a realistic doping scenario and produce a statistical average. Leading on from the argument that central adsorbed impurities in intrinsic graphene have very little scattering close to the Dirac point, here it will be shown that the conductance of a nanoribbon device with sizeable concentrations of central adsorbed impurities is virtually unmodified in comparison to the pristine case. The suppression of conductance changes is a consequence of the scattering suppression, which prevents the back-scattering of electrons down the nanoribbon. The unchanging conductance of the central adsorbed impurity case stands in stark contrast

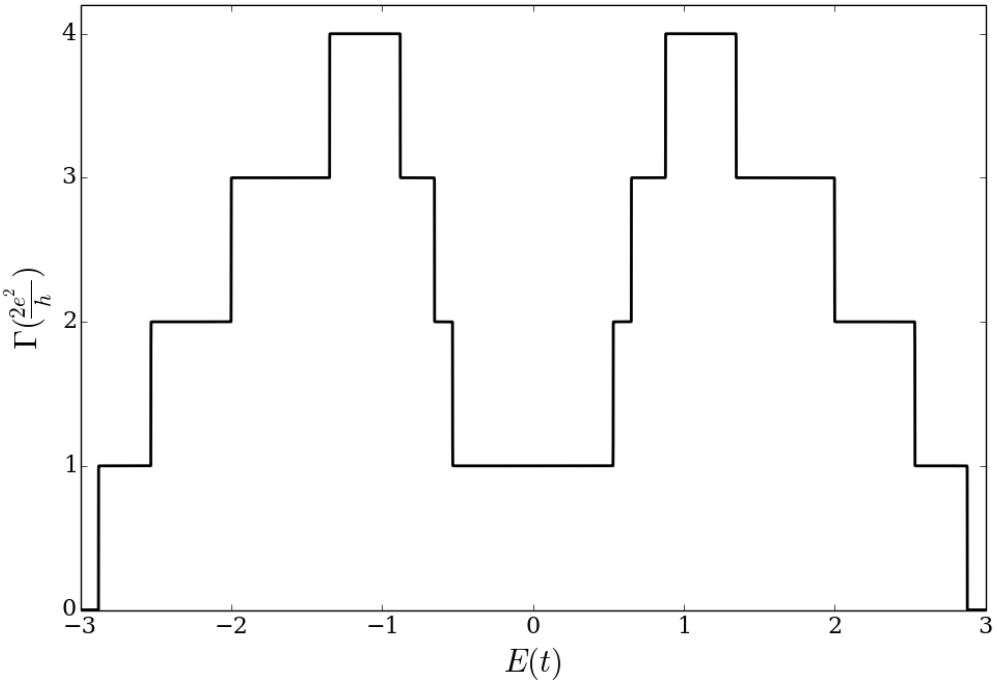

Figure 6.12: Conductance through a pristine 8-AGNR which is always an integer multiple of the quantum of conductance $\frac{e^2}{h}$.

to top adsorbed impurities which exhibit an appreciable reduction in conductance, even for modest dopant concentrations. The consequence of this is that gas sensors which rely on electrical measurements can be expected to be far less sensitive to dopant species that tend to adsorb at the central hexagon site.

The first step is considering the modification of the conductance produced by a single dopant in the scattering region. It should be clarified that systems contain either top or central adsorbed impurities, not both. The top adsorbed impurity is connected to site T and the central to site C labelled in Fig. 6.1. Both impurity species were parametrised by $\epsilon_a = 0.3\,|t|$ and $\tau = -2\,|t|$. These parameters were chosen in order to shift the usual self-energy resonance (de-

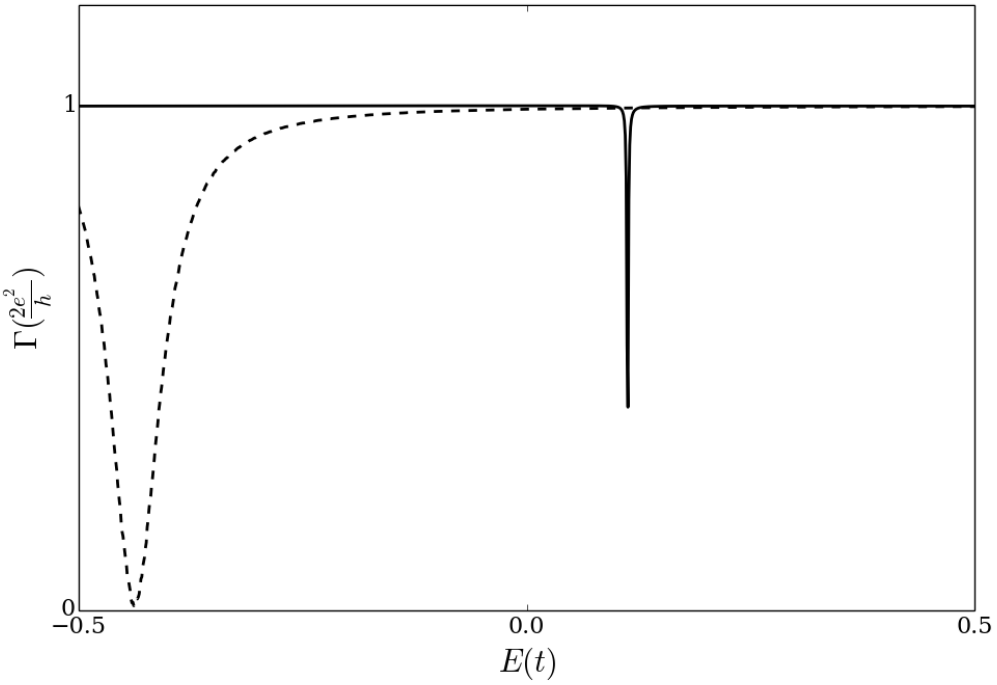

Figure 6.13: Conductance spectrum for an 8-AGNR with a single top adsorbed (dashed) or central adsorbed (solid) impurity. Both impurities have the parameters $\epsilon_a = 0.3\,|t|$ and $\tau = -2\,|t|$. The pristine conductance in this region is exactly 1. The position in the spectrum of both of these resonances changes slightly depending on where the impurity is placed with respect to the width of the nanoribbon, however the other features remain unchanged.

termined by divergence in $g_{aa} = \frac{1}{E-\epsilon_a}$) away from the Dirac point to prevent obfuscation of the results. A plot of the conductance around zero energy is shown in Fig. 6.13.

Clearly top adsorbed impurities reduce the conductance much more drastically than their central adsorbed counterparts, the conductance in the former case being significantly reduced across a wide range of the spectrum. In contrast, the conductance of central adsorbed impurities is almost identical

to the pristine case with the exception of a narrow resonance energy around $E = 0.11\,|t|$. This corroborates the argument made throughout this chapter, that central adsorbed impurities do not scatter conduction electrons at low energies. To check this is not a quirk of the chosen parameters, supporting evidence is shown in Fig. 6.14 of $\Gamma(E = 0.11\,|t|)$ against a varying onsite energy ϵ_a which confirms the observed resonance exists for an extremely specific impurity parametrisation only. The resonance energy is analogous to the divergence in the T-matrix $T_c = \frac{\Sigma}{1-\gamma_C \Sigma}$ discussed in the previous sections, where an energy can be found such that $\gamma_c(E)\Sigma(E) = 1$ and scattering is enhanced. This is clearly coincidental and requires fine tuning of either E or the impurity parameters to produce this. Recent research by Garcia et al. [156] has studied Anderson localisation driven by adatom disorder in graphene. They found that despite the suppression of the scattering cross section due to destructive interference in central adsorbed impurities, the system undergoes an Anderson metal-insulator transition but only for particular values of the doping and the impurity resonance energy. The results shown in Fig. 6.13 and Fig. 6.14 suggest that such a transition would require a very precise parameter tuning.

The change in conductance as a result of a finite impurity concentration can also be considered. The system is built as shown in Fig. 6.11 with a scattering region of 100 cells, following the prescription described in Sec. 2.5.3. A given number of impurities corresponding to a concentration are then added throughout this region via a random process. Configurational averaging is then carried out by taking the average conductance of 1000 systems for each concentration value. Results are shown in Fig. 6.15. A very small percentage (0.01%) of top adsorbed impurities is sufficient to reduce the conductance of a graphene ribbon to 50% of its pristine value whereas no reduction can be seen for central adsorbed scatterers, requiring extreme magnification of the initial

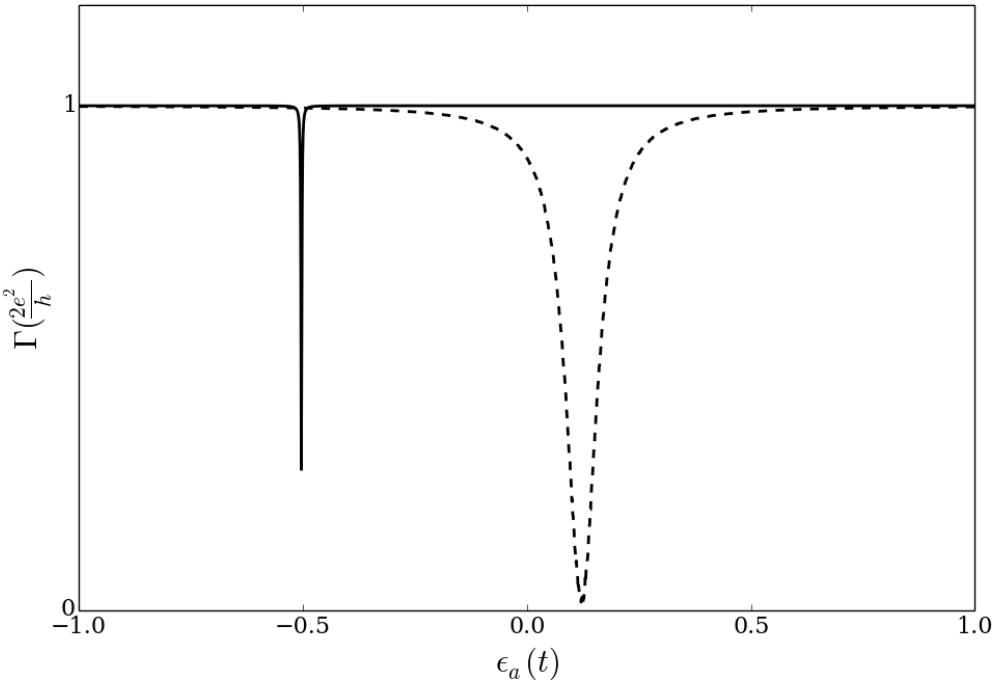

Figure 6.14: Conductance at $E = 0.11\,|t|$ versus impurity parameter ϵ_a in an 8-AGNR with a single top adsorbed (dashed) or central adsorbed (solid) impurity.

plot to distinguish the change from the pristine value (see inset). This negligible change in conductance, even for relatively large values of concentration, confirms the hypothesis that even at appreciable concentration levels the central adsorbed impurities exhibit virtually no scattering at low-energies.

6.4 Chapter summary

In this chapter it was argued that central adsorbed impurities in graphene have their scattering suppressed due to symmetry effects and destructive interfer-

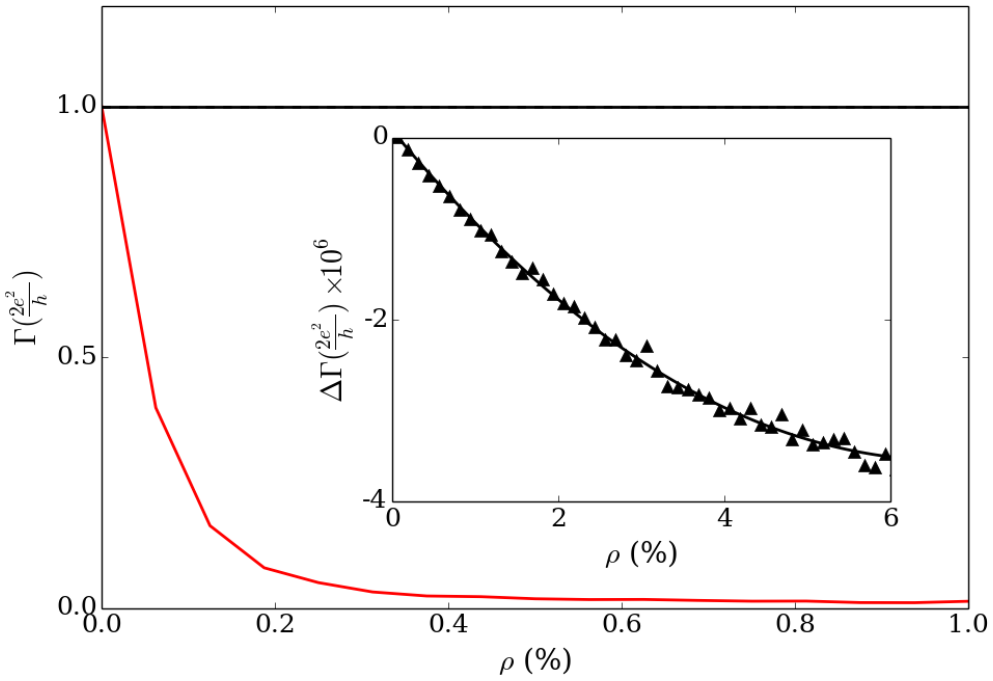

Figure 6.15: Conductance as a function of the impurity concentration ρ. The red (black) line corresponds to the case of top adsorbed (central adsorbed) impurities. The parameters $E_F = 0$, $\tau = -2t$ and $\epsilon_a = 0.3t$ were used. As the change in conductance for the central adsorbed case is hard to distinguish at this scale the inset shows a magnified version of change in conductance from pristine ($\Delta\Gamma$) for this case. The configurational average calculation data is plotted as black triangles with a polynomial regression as the black line provided as a visual aid. This indicates that the conductance does decrease with increasing ρ, but extremely slowly. All data points were averaged over 1000 configurations.

ence of the long-range propagators. Furthermore it was shown that top and bridge adsorbed impurities do not suffer from this issue. The natural conclusion of this is that graphene would function as a good sensor for chemicals preferring the latter two adsorption profiles, but that central adsorbed are far from ideal from this purpose. Nevertheless, they could be used for sensitive

strain sensors where the underlying hexagonal symmetry of the lattice, the source of the scattering transparency, is broken and the scattering greatly enhanced. It was shown that this can be done by applying uniaxial strain, as altering the system in such a manner reduces the destructive interference and lifts the suppression of the scattering cross-section of central adsorbed impurity. This directly demonstrates that graphene hosting central adsorbed impurities can function as efficient strain sensors. Despite the simplicity of the model these findings are extremely general - that these effects do not depend on the parametrisation of the impurities but on their symmetry breaking instead. By classifying dopants according to their bonding symmetry this leads to a more efficient way of identifying strong and weak scatterers. Rather than using a trial and error approach the work in this chapter offers an alternative method to establish good candidate substances for graphene sensors.

Chapter 7

Sublattice segregation of impurities in carbon nanomaterials

A frequently discussed issue in this thesis is that one of the main problems with using regular graphene for electronics applications - e.g. ultra high-speed transistors, integrated circuits and other novel devices [8, 32] - is the absence of a band gap in the electronic band structure. This lack of band gap means that any field effect transistors made using the material would be unable to be switched off, rendering it useless as a logic device. In the introduction chapter, experimental research involving nitrogen doped graphene was discussed as a method to produce this band gap, and moreoever that the gap is tunable by varying the impurity concentration. The conventional doping process distributes the impurities randomly in the lattice which has a detrimental effect on the electronic transport due to scattering, as was illustrated in the previous chapter. In Sec. 1.3 a refinement of the method which circumvents the

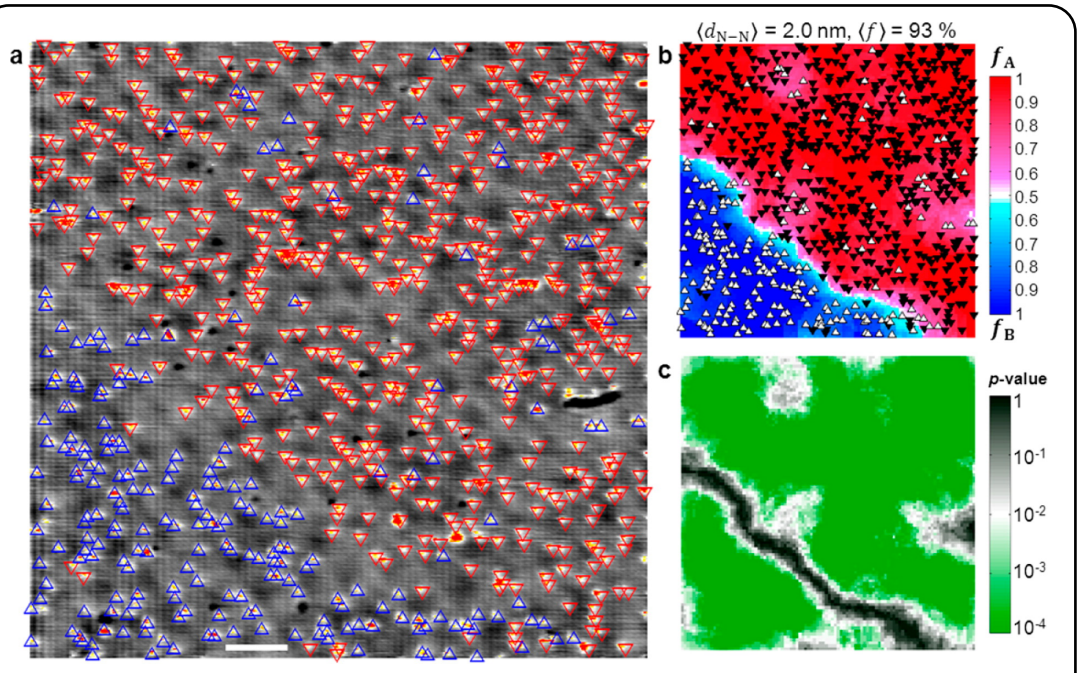

Figure 7.1: Distribution of nitrogen dopants in CVD (pyridine)-grown doped graphene. (a) STM image (100 x 100 nm^2 , 1 V, 1 nA) of CVD-grown doped graphene on Cu(111). Dopant sublattices are highlighted by red (A) and blue (B) triangles. Scale bar = 10 nm. (b) Spatial analysis of sublattice distribution. Down black triangle = sublattice A. Up white triangle = sublattice B. f_A (or f_B) represents the fraction of dopants in sublattice A (or B) within a local radius. The colour scale represents f_A and f_B and ranges from 0.5 (white) to 1 (red and blue for A and B, respectively). $\langle d_{N-N} \rangle$ = average inter-dopant separation. $\langle f \rangle$ = average degree of sublattice segregation. (c) Map of p-values corresponding to the ratios shown in map b, obtained under a null hypothesis. Adapted with permission from [62].

scattering problem was introduced - sublattice segregation of the dopants. An overview of the current theoretical and experimental research was given with the main result being that there is quasi-ballistic electron transport on the undoped sublattice [60–64]. This bypasses the problem of increased scattering with larger band gaps and takes the segregation effect from a mere theoretical curiosity to a potentially very powerful tool. The physical mechanism

behind the phenomenon of the sublattice ordering is still debated, however there is mounting evidence that demonstrates the segregation effect occurring in a variety of other scenarios. These were also outlined in Sec. 1.3. If the segregation is observed in other situations it suggests that it is not solely a CVD growth-based phenomenon, as was originally proposed, and so a fuller understanding is required. It is clear that if the mechanism behind this effect can be understood and harnessed it would offer new possibilities at the very least for graphene-based electronic devices. Even more tantalising is the prospect that it could arise with other dopants or even other materials. With this as motivation, this final investigatory chapter is devoted to formulating a physical explanation of the sublattice segregation effect, based on the mathematical framework developed over the course of this thesis.

Using the techniques derived throughout this work it will be demonstrated that this phenomenon arises through inter-impurity interactions in the sample, mediated by the conduction electrons. The structure of the chapter is as follows. In Sec. 7.1 the foundations of the model are lain with a thorough investigation of the energetic behaviour of two nitrogen impurities embedded in bulk graphene. This is done by studying Friedel oscillations in the total energy ΔE as a function of the spatial configuration of the impurities. Experiment has found that nitrogen pairs in close proximity will exhibit next-nearest neighbour ordering. Using the model for a single pair of impurities at a distance apart, the case of *pairs of pairs* of impurities will also be studied. In both cases it is found that the impurities will prefer a same sublattice ordering if the system Fermi energy is $E_F = 0$, that is to say their energy is lowered in this configuration. The oscillations in ΔE are masked by commensurability with the lattice spacing, as was seen in the Friedel oscillations in Δn and $\Delta\rho$ in Chap. 5. When $E_F \neq 0$ the oscillations appear in ΔE and these vary with the exact value of

E_F. A supporting argument for these findings can be made through the SPA Green functions and this is shown in Sec. 7.1.2. In Sec. 7.2 the two impurity case is extended to a finite concentration of them. The increase in dopant concentration causes a corresponding increase in E_F away from the Dirac point, necessitating a more nuanced approach. Starting with a two-dimensional Poisson distribution of impurities and assuming that pairwise interactions will be dominant, the lowest energy configuration for the ensemble is calculated as a function of concentration. It follows that these interactions and the underlying Friedel oscillations are driving the sublattice segregation effect. While these oscillations would normally be averaged out in the case of randomly distributed impurities, in graphene they have almost the same periodicity as the lattice. As a result the total interaction energy of the impurities in the system does not vanish and instead is lowered for the sublattice segregated situation. A surprising outcome of this method is the existence of a critical concentration of impurities, just under 1%, beyond which the effect is predicted to no longer exist. This could explain why early experiments using higher concentrations did not observe the effect. To demonstrate the flexibility and robustness of the interaction-based model, other scenarios will be proposed in which the segregation effect should occur. The first scenario considered is metallic CNTs of varying sizes with armchair and zigzag geometries, where a concentration of top adsorbed hydrogen impurities are distributed on the surface. This is covered in Sec. 7.3. As demonstrated in Sec. 5.2 their reduced dimensionality decreases the decay rate of the underlying Friedel oscillations, enhancing the inter-impurity interactions. A Monte Carlo method is used to model a disordered distribution of the adsorbates which are then relaxed into their lowest energy state using the pairwise interaction model. Sublattice segregation is found, being most pronounced at dilute concentrations and narrow diameter

CNTs. A second scenario is presented in Sec. 7.4 where Gaussian strain functions as the initial sublattice symmetry breaking operation, instead of it being caused by an impurity. This destroys the sublattice symmetry of the system and causes an imbalance in the energetic favourability of each sublattices, as a consequence an adsorbate will prefer to adsorb on one sublattice over the other. Furthermore it is shown that the energetic imbalance between sublattices is tunable with the strain applied.

7.1 Inter-impurity interaction energy

In Chap. 5 it was reported that Green functions methods can be used to calculate the spatial oscillations in Δn and $\Delta\rho$ caused by the introduction of impurities in graphene. Furthermore it was shown that when two or more impurities are introduced into a system they can experience a coupling, which is mediated by the conduction electrons. An example of this was the interference effect seen in Δn for two substitutional impurities in Sec. 5.1.2. Consider now the change in a system's total electronic energy ΔE due to the presence of two substitutional impurities. If they are placed at lattice positions A and B and have onsite energy λ the perturbation is described by

$$\hat{V} = |A\rangle\,\lambda\,\langle A| + |B\rangle\,\lambda\,\langle B|\,.$$

The expression for ΔE was derived in Eq. 2.17 and is given here again for convenience

$$\Delta E = E_F \Delta N + \frac{2}{\pi}\,\mathrm{Im}\int_{-\infty}^{E_F} dE\,\ln\det\left(\hat{I} - \hat{g}\hat{V}\right).$$

where the factor of 2 accounts for spin degeneracy. The term $E_F\Delta N$ will be omitted from here on as it is configuration independent and a constant, depending only on the impurity type (for two nitrogens, $\Delta N = 2$). Due to the functional similarity with Δn one already naturally expects that the arrangement of the two impurities will be important. Therefore by calculating ΔE as a function of the relative positions of the two impurities there will be certain configurations that are more energetically favourable than others. It is possible to identify two separate contributions to ΔE by expanding the integrand

$$\begin{aligned}
\ln\det\left(\hat{I}-\hat{g}\hat{V}\right) &= \ln\det\begin{pmatrix} 1-g_{AA}\lambda & -g_{AB}\lambda \\ -g_{BA}\lambda & 1-g_{BB}\lambda \end{pmatrix} \\
&= \ln\Big((1-g_{AA}\lambda)(1-g_{BB}\lambda)-g_{AB}^2\lambda^2\Big) \\
&= \ln\left(((1-g_{AA}\lambda)(1-g_{BB}\lambda))(1-\frac{g_{AB}^2}{(1-g_{AA}\lambda)(1-g_{BB}\lambda)})\right) \\
&= \ln((1-g_{AA}\lambda)(1-g_{BB}\lambda))+\ln\left(1-\frac{g_{AB}^2}{(1-g_{AA}\lambda)(1-g_{BB}\lambda)}\right) \\
&= 2\ln(1-g_{AA}\lambda)+\ln\left(1-\frac{g_{AB}^2}{(1-g_{AA}\lambda)^2}\right)
\end{aligned} \tag{7.1}$$

where for the last line the equivalence $g_{AA} = g_{BB}$ was used. The first term is associated with the individual impurities and is clearly independent of the separation of A and B. Upon integration, this term is equal to the energy

$$\Delta E_1 = \frac{2}{\pi}\mathrm{Im}\int dE f(E)\ln(1-g_{AA}\lambda). \tag{7.2}$$

This quantity is equal to the system energy change when a single nitrogen impurity is added, hence it is both separation and configuration independent and so takes a constant value in this scenario.

The second term in the full ΔE integrand is an interaction term dependent on the impurity configuration, which can be inferred through the presence of the off-diagonal GF g_{AB}. This term is defined as the interaction energy ΔE_{AB}, which in full form is

$$\Delta E_{AB} = \frac{2}{\pi}\mathrm{Im}\int dE f(E)\ln\left(1 - \frac{g_{AB}^2\lambda^2}{(1-g_{AA}\lambda)^2}\right). \tag{7.3}$$

It is now clear that the total energy change can be written in terms of the separate configuration independent and configuration dependent contributions

$$\Delta E = 2\Delta E_1 + \Delta E_{AB}.$$

To investigate the energetic favourability of different configurations a dimensionless configuration energy function (CEF) for substitutional impurities

$$\beta^S(E_F) = \frac{\Delta E_{AB}}{|2\Delta E_1|}\,. \tag{7.4}$$

should be defined. This quantity describes the change in energy of the system due to the interference between the two impurities, relative to the total energy change in the system for two non-interacting (infinitely separated) impurities. Positive values of the CEF correspond to less favourable configurations whereas negative values correspond to favourable configurations which decrease the total energy of the system. By calculating the CEF for different impurity configurations it can be established which ones are energetically favourable, and thus more likely to be realised in experiment. A map of $\beta^S(E_F = 0)$ values for a large number of different configurations is shown in Fig. 7.2. The nitrogen impurities are characterised by the parametrisation $\lambda_N = -10$eV given by Lambin et al. [127].

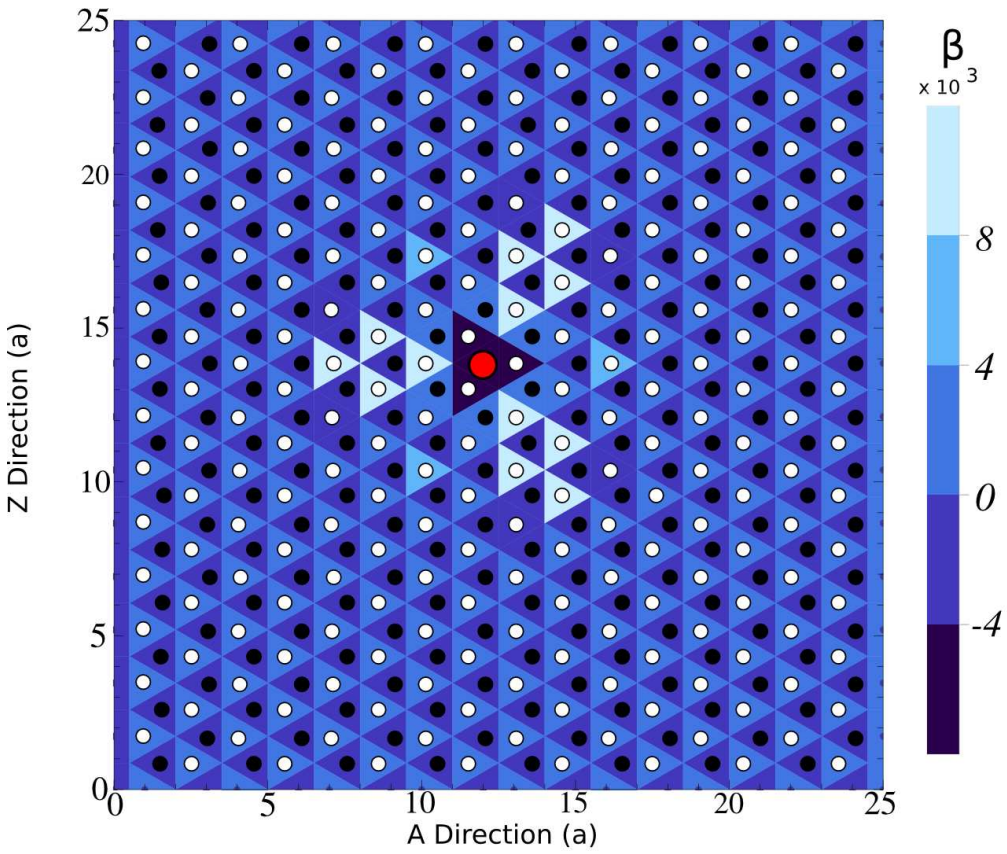

Figure 7.2: Contour plot of the calculated CEF β^S for a substitutional nitrogen impurity fixed at the center (red) and a second nitrogen impurity being moved around nearby lattice sites at $E_F = 0$. Each impurity is characterised by the same onsite energy $\lambda_N = -10$eV. Each site is then colour coded according to the value of β^S for that configuration.

To understand the figure, one impurity is fixed at the red circle corresponding to a site on the black sublattice. β^S is then calculated with the second impurity located at each of the sites on the map, with the shading of the triangle surrounding each site corresponding to the β^S value for that configuration. It is apparent that, with the exception of nearest-neighbour site impurities, a general trend exists where the second impurity prefers to locate on the same sublattice as the initial impurity. This trend gives rise to the chequerboard-like

pattern seen in Fig. 7.2 where same sublattice (black) sites are surrounded by darker triangles, corresponding to lower energy configurations, than the opposite sublattice (white) sites. The discrepancy in the nearest-neighbour results is most likely due to the parametrisation being too limited - if impurities are placed in close proximity to one another they will interact and hence a more delicate parametrisation should be used as was argued in Chap. 5. By utilising an alternative parametrisation (e.g. $\lambda = -4$eV as was found in Chap. 4) the inconsistent local behaviour is indeed removed and same sublattice configurations are favourable universally, confirming the sensitivity of results for local sites to the impurity parametrisation.

As with the case of FOs in Δn and $\Delta\rho$ it is useful to consider a cross section of β^S. Doing so can clarify the underlying mathematical behaviour and this is shown in Fig. 7.3 for different impurity configurations with an armchair separation. The case identical to the contour plot depicted in Fig. 7.2 is shown in the upper-left panel and it is clear that the same sublattice configuration has an opposite sign to the opposite sublattice case at all separations D, indicating that it is always lower in energy. The magnitude of β decays as D^{-3} in both cases which is the same decay rate that was found for the Δn FOs in Chap. 5. This is not by coincidence and can be explained by examining the form of g_{AB} which determines the distance dependence of ΔE_{AB} in Eq. 7.3. Furthermore, expanding ΔE_{AB} to first order in λ results in a similar equation to Eq. 5.2 for the FOs in Δn. It follows that a similar decay profile should be expected. The two impurity case is plotted again for $E_F \neq 0$ in the upper-right panel of Fig. 7.3, revealing an oscillatory behaviour and D^{-2} decay rate which again matches the qualitative Δn behaviour. It can be seen then that the FOs both in Δn and β^S display the same distance dependent behaviour due to the similar dependence on off-diagonal Green functions that appears in both quantities. A

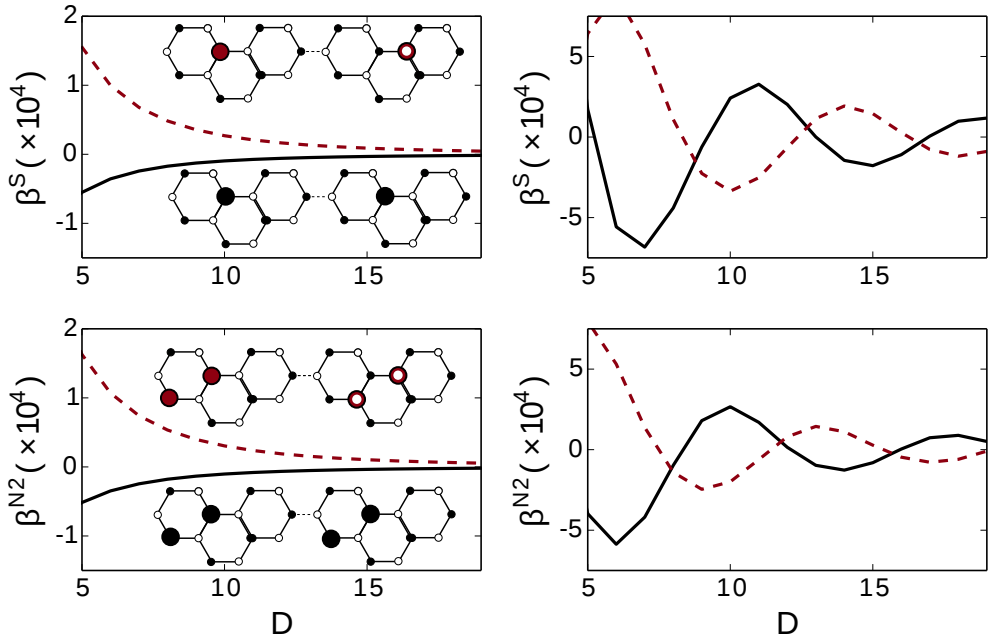

Figure 7.3: Upper-left: Cross-section of Fig. 7.2 along the armchair direction with the fixed impurity at $D = 0$ on the black sublattice. The data for the CEF on black (white) sublattice sites away along the cross-section are indicated by the black (red dashed) line showing the D^{-3} decay profile and the inset schematics show the corresponding configuration in both cases. Upper-right: similar to above but with a Fermi Energy $E_F = 0.2|t|$. The presence of Friedel oscillations can be seen with a decay of D^{-2}. Bottom-left: two pairs of impurities. β^{N2} is plotted as a function of D for $E_F = 0$. Bottom-right: same as the bottom-left panel but with $E_F = 0.2|t|$. This exhibits the same features as the case of two isolated impurities with a slight phase shift.

supporting argument to the numerical calculation suggesting the ubiquitous preference for same sublattice configurations at $E_F = 0$ is presented shortly in Sec. 7.1.2 using the SPA Green functions.

7.1.1 Pairs of impurities

Recent experimental observations, corroborated by DFT calculations, suggest that two nitrogen impurities in close proximity to each other prefer to occupy sites on the same sublattice in a quasi-neighbouring configuration [60, 61] hereon referred to as $N_2^{\bullet\bullet}$ configuration. This configuration is preferred over the nearest-neighbour configuration $N_2^{\bullet\circ}$ which was calculated as being the most favourable configuration in the last section using the parametrisation $\lambda = -10$eV. Schematics of these two configurations were shown in the chapter on Friedel oscillations in Fig. 5.10 where the resulting Δn profiles were studied. Despite the limitations of the tight-binding model for small separations, it was shown that the parametrisation $\lambda = -4$eV removes this short-range inconsistency and a fit to the experimentally observed configuration obtained. While this is rather simplistic and neglects effects such as orbital hybridisation between the impurities, it produces the correct configuration. The crux of these arguments for the proposed mechanism behind the sublattice segregation does not rely on the physics of this short-range behaviour of $N_2^{\bullet\bullet}$ or $N_2^{\bullet\circ}$ pairs, but rather the general long-range behaviour for either single impurities or pairs.

One huge advantage of using a Friedel oscillation based approach is that they can be used to study systems with multiple $N_2^{\bullet\bullet}$ type impurities. Experimental evidence suggests that not only do pairs of nitrogen impurities prefer the $N_2^{\bullet\bullet}$ to the $N_2^{\bullet\circ}$ configuration, but that a *pair of pairs* of the $N_2^{\bullet\bullet}$ impurities prefer to locate on the same sublattice. In other words, that two $N_2^{\bullet\bullet}$ or two $N_2^{\circ\circ}$ impurities are formed in preference to one of each. Numerical investigation of such systems using DFT calculations is limited to small separations which makes it

difficult to explore the behaviour which emerges in more highly-doped larger scale systems. Moreover when considering large distributions of impurities, the total interaction energy in the system should be expected to scale with the number of possible pairs in the system, going as $\sim N^2$ for N impurities. By extending the model discussed for single substitutional nitrogen dopants in the previous section, it is possible to investigate these types of systems. In this scenario the individual impurities are now $N_2^{\bullet\bullet}$ or $N_2^{\circ\circ}$ defects, shown as insets in the bottom-left panel of Fig. 7.3. Consider a $N_2^{\bullet\bullet}$-type impurity at location A and introduce a second $N_2^{\bullet\bullet}$ or $N_2^{\circ\circ}$ impurity a distance D away at site B. The CEF can be calculated for such a configuration analogously to Eq. 7.4,

$$\beta^{N2}(E_F, D) = \frac{\Delta E_{AB}^{N2}}{|2\Delta E_1^{N2}|}\,, \tag{7.5}$$

where now ΔE_1^{N2} is the total change in energy of introducing a single $N_2^{\bullet\bullet}$ or $N_2^{\circ\circ}$ impurity. This quantity is plotted for the case when the second impurity is also a $N_2^{\bullet\bullet}$ (black curve) and when it is a $N_2^{\circ\circ}$ (red dashed curve) in the upper-right panel of Fig. 7.3. Similar to the pairs of single impurities case, same sublattice impurity configurations are also preferential in the pairs of pairs scenario.

To benchmark these calculations, it is worth comparing the results for ΔE_{AB}^{N2} to the DFT calculation performed by Lv et al. [61] for a single value of separation. Calculations were performed for both two $N_2^{\bullet\bullet}$-type impurities and for a configuration with one $N_2^{\bullet\bullet}$ and one $N_2^{\circ\circ}$. In both cases the impurity pairs had a separation of approximately $D = 7$. An energy difference of 14meV is reported using the DFT calculation[61] compared to 2.3 meV for the tight-binding model and in both cases the double $N_2^{\bullet\bullet}$ configuration was more energetically favourable. The numerical discrepancy between the results is to

be expected due to the overly simple parametrisation of $N_2^{\bullet\bullet}$ employed in the tight-binding model that was used. The qualitative results however are not strongly affected by the local impurity parametrisation, indicating that the long-range sublattice ordered doping behaviour may not be unique to nitrogen. This is discussed more in a later section where the behaviour of an infinite ensemble of nitrogen impurities is studied (Sec. 7.2). It should be emphasised that the same sublattice configuration preference is found for all separations in the model, explaining the long-ranged ordering seen in experiment [60, 61].

In a similar manner to that discussed for substitutional impurities, a finite concentration of $N_2^{\bullet\bullet}$ impurities shifts the Fermi energy away from the Dirac point and introduces oscillations in $\beta^{N2}(D)$. These oscillations, seen in the bottom-right panel of Fig. 7.3 produce regions away from the initial $N_2^{\bullet\bullet}$ impurity where a $N_2^{\circ\circ}$ is more favourable than a second $N_2^{\bullet\bullet}$ impurity. However, small increases in E_F would preserve the same sublattice preference in local regions. This suggests that larger scaled nitrogen doped systems may have alternating domains where each of the sublattices is dominant, and this prediction is consistent with experimental observations [61]. An extension of the model discussed here to include a more accurate parametrisation of the individual $N_2^{\bullet\bullet}$ impurities would provide a transparent and computationally efficient method to explore the formation and size of such domains, and to determine their dependence on the concentration of N dopants and the resultant Fermi energy shift.

7.1.2 Alternate method using the SPA

A supporting pen-and-paper argument for the ubiquitous preference for same sublattice configurations of impurities at $E_F = 0$ can be made using the stationary phase approximation. Consider the cases where two substitional impurities at a large distance of D apart in either a same or opposite sublattice configuration. The former will be energetically preferred whenever the inequality

$$\Delta E_{\bullet\bullet} - \Delta E_{\bullet\circ} < 0$$

is satisfied. Assuming the Born approximation is valid this can be rewritten using the previously derived expressions for ΔE_{AB} as

$$\mathrm{Im}\int_{-\infty}^{E_F} dE((g_{AB}^{\bullet\circ})^2 - (g_{AB}^{\bullet\bullet})^2) < E_F\,\mathrm{Im}((g_{AB}^{\bullet\circ})^2 - (g_{AB}^{\bullet\bullet})^2) \tag{7.6}$$

where the log function has been expanded to first order. Using the SPA the Green functions can be approximated by $g_{AB}^{\alpha\beta} \sim \frac{\bar{A}N^{\alpha\beta}e^{iQD}}{\sqrt{D}}$ and thus

$$(g_{AB}^{\bullet\circ})^2 - (g_{AB}^{\bullet\bullet})^2 = \bar{A}\frac{e^{iQD}}{\sqrt{D}}(f(k)^2 - E^2)$$

can be substituted in to both sides of Eq. 7.6. The integral in Eq. 7.6 has the same form as that used for Δn (Eq. 5.4) and as a consequence can be solved via the Matsubara frequency method. When this is done, the resulting version of Eq. 7.6 can be rearranged to give the much simpler inequality

$$\frac{1}{3\pi t D^3} > 0$$

at $E_F = 0$. As $D > 0$ this condition is always true, given that D is suitably large enough for this approximation to apply. Thus same sublattice configurations are always preferable for two substitutional impurities at large distances and this is valid independent of the parameter λ, meaning other impurities should exhibit the same effect.

7.2 Nitrogen doped graphene

The behaviour of a finite concentration of nitrogen impurities embedded in an infinite graphene lattice will now be modelled. The goal here is to show, in a mathematically transparent manner, that Friedel oscillations in the local density of states driven by the presence of substitutional impurities are responsible for breaking the sublattice symmetry, thereby causing the experimentally observed segregation effect.

Consider bulk graphene with nitrogen impurities randomly distributed over both sublattices with concentrations $\rho_\bullet$ and $\rho_\circ$ denoting the impurity concentration on the black and white sublattices respectively. This distribution of impurities is very similar to a Poisson point process, particularly at low concentrations where the discreteness of the lattice becomes less apparent. There exists two limiting situations of the impurity distributions. The first is where $\rho_\bullet = \rho_\circ$, corresponding to an even distribution between sublattices. The second is where either $\rho_\bullet = 0$ or $\rho_\circ = 0$, physically equivalent cases, meaning all the impurities in the system are on only one of the two sublattices. Naturally there is the added requirement that $\rho_{Total} = \rho_\bullet + \rho_\circ$ and for simplicity only pairwise interactions are assumed. This is a fair assumption to make as it was shown in the previous sections that the energetic coupling decays as D^{-2} for pairwise

interactions, but decays much faster for higher order interactions involving more impurities. Another added requirement is that E_F must be readjusted to above the Dirac point as the system is n-doped by the introduction of the nitrogen impurities. This could be ignored in the previous cases where only a handful of impurities were embedded in the infinite system, as the shift in these situations would be infinitesimal. The relationship between ρ and E_F can be found as follows. Every impurity added will shift the Fermi level such that the filled states in the global DOS spectrum shifts by ρZ where $Z = 1$ is the number of valence electrons donated in the case of the nitrogen. Assuming a dilute enough distribution of impurities that does not affect the linearised band structure around the Dirac point too greatly, the linear spectrum of the global DOS is characterised by

$$\rho(E) = -\frac{2}{\pi} \operatorname{Im} g_{00}$$

which using the low energy approximation for $\operatorname{Im} g_{00}$ given in Appendix B.2 is

$$\rho(E) \approx \frac{2E}{\sqrt{3}\pi t^2}.$$

Assuming the filled states forms a right angle triangle the Fermi level shift can be approximated as

$$\rho_{Total} = \frac{1}{2} E \frac{2E}{\sqrt{3}\pi t^2}$$

which through rearranging gives

$$E_F = t\sqrt{\sqrt{3}\pi\rho_{Total}}.$$

If an impurity A on sublattice γ_1 is chosen at random then in its frame of ref-

erence it is located at the centre of the system, experiencing an effective total energetic coupling from all the other impurities in the system. This can be expressed as a sum of pairwise ΔE_{AB} terms where B is summed over all the other impurity sites, i.e. $\sum_j \Delta E_{Aj}$. Expanding ΔE_{AB} in Eq. 7.3 using $\lambda \ll 1$ and following the Matsubara frequency method demonstrated for Δn in Chap. 5 this interaction can be shown to go as (c.f. Eq. 5.3)

$$\Delta E_{AB} \sim -\frac{2\lambda^2}{\pi} \operatorname{Im} \sum_{l=0} \frac{B^{(l)} e^{2iq^{(0)}D}}{(2q^{(1)})^{l+1} D^{l+2} i^{1-l}}.$$

with B and q as defined for Δn. This gives a good approximation for $\lambda \ll 1$ however for realistic impurities with larger λ values it is better to use the functional form

$$\Delta E_{Aj} \sim \frac{\alpha \cos\left(2QD_{Aj} + \phi\right)}{D_{Aj}^2}, \tag{7.7}$$

where α and ϕ are fitted, a plot of this is shown in Fig. 7.4 showing very good agreement. Assuming a low E_F the Green functions of the system and thus the approximate functional form of ΔE_{Aj} is isotropic, so the distance dependence can be assumed to be valid for all spatial directions, not just armchair separations, and so Eq. 7.7 can be recast as a function of radial separation r in place of D which was used primarily for armchair separations only.

From the findings of the last section it is known that this total energetic coupling must be a function of the relative position of the other impurities and their sublattice arrangements. As the total energetic coupling for a single impurity is known a sum can be taken over all impurities to approximate the total energetic coupling in the system as

$$\mathcal{E} \approx \frac{1}{2} \sum_i \sum_{j \neq i} \Delta E_{ij} \tag{7.8}$$

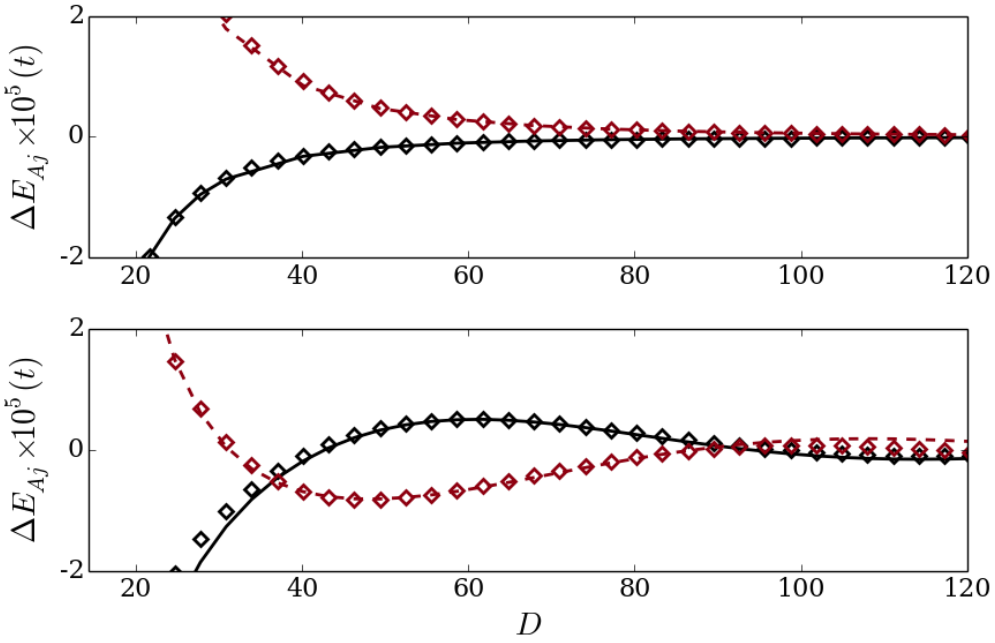

Figure 7.4: ΔE_{Aj} plotted as a function of the separation between impurities, (top) $E_F = 0$; (bottom) $E_F = 0.05\,|t|$, both using the impurity parametrisation $\lambda = -4eV$. Solid (dashed) lines and circular (triangular) symbols represent ΔE_{Aj} when A and j are on same (opposite) sublattices. Symbols are the numerically evaluated values, whereas the lines follow the fitted function $\frac{\alpha \cos 2QD+\phi}{D^2}$ as explained in the text.

where the sum has been halved to account for the double counting of interaction energies. It will now be shown how to approximate this using a simple argument. Consider an annulus with inner radius r and infinitesimal width dr formed around the central impurity A and that the oscillation of ΔE_{Aj} is slow enough that the discreteness of the lattice can be ignored. The area of this ring is $2\pi r dr$ and contains $2\pi r dr \rho_\bullet$ and $2\pi r dr \rho_\circ$ impurities on the black and white sublattices respectively. It follows that the impurities in the region are at distance r away from site A on sublattice γ_1 and will contribute an energy $\Delta E_{Aj}^{\gamma_1\gamma_2}$ to the sum $\sum_j \Delta E_{Aj}$ where γ_2 denotes the sublattice of j. This leads to

two distinct cases which from the results shown in Fig. 7.4 are known to have opposite signs:

$$\Delta E_{Aj}^{\gamma_1\bullet}(r) \approx \frac{\alpha\cos\left(2Qr+\phi\right)}{r^2}$$

and

$$\Delta E_{Aj}^{\gamma_1\circ}(r) \approx \frac{\beta\cos\left(2Qr+\psi\right)}{r^2}$$

where $\alpha \approx -\beta$. Hence the energetic contribution of all impurities in the ring is $2\pi r dr(\rho_\bullet \Delta E_{Aj}^{\gamma_1\bullet}(r) + \rho_\circ E_{Aj}^{\gamma_1\circ}(r))$. Integrating over r yields an approximation for the total interaction energy experienced by impurity A on sublattice γ_1 as

$$\sum_j \Delta E_{Aj} \approx 2\pi\Big(\rho_\bullet \int_{\sigma_{\gamma_1\bullet}}^{\infty} drr\Delta E_{Aj}^{\gamma_1\bullet} + \rho_\circ \int_{\sigma_{\gamma_1\circ}}^{\infty} drr\Delta E_{Aj}^{\gamma_1\circ}\Big)$$

where $\sigma_{\gamma_1\gamma_2}$ is the distance from a site on the γ_1 sublattice to the nearest site on the γ_2 sublattice. By symmetry considerations

$$\int_{\sigma_{\bullet\bullet}} drr\Delta E_{Aj}^{\bullet\bullet} = \int_{\sigma_{\circ\circ}} drr\Delta E_{Aj}^{\circ\circ} = S_1$$

and

$$\int_{\sigma_{\bullet\circ}} drr\Delta E_{Aj}^{\bullet\circ} = \int_{\sigma_{\circ\bullet}} drr\Delta E_{Aj}^{\circ\bullet} = S_2$$

which vastly simplifies the above result. These integrals cannot be solved analytically but their numerical solution converges quickly with increasing r.

The total energetic coupling in the system $\mathcal{E}$ (Eq. 7.8) can now be determined following a sum over all the impurities in the system using the previous equations without loss of generality - the previous arguments hold assuming the impurities are spread homogeneously throughout the system and their distribution is similar to the Poisson point process. Taking the sum over the entire

system gives

$$\mathcal{E} \sim N_\bullet \sum_j \Delta E_{Aj}^{\bullet\gamma_j} + N_\circ \sum_k \Delta E_{Ak}^{\circ\gamma_k}$$

with $N_\gamma = \lim_{R\to\infty} \pi R^2 \rho_\gamma$ denoting the number of impurities on the γ sublattice and the sum terms

$$\sum_j \Delta E_{Aj}^{\bullet\gamma_j} = 2\pi\Big(\rho_\bullet S_1 + \rho_\circ S_2\Big)$$

and similarly

$$\sum_k \Delta E_{Ak}^{\circ\gamma_k} = 2\pi\Big(\rho_\bullet S_2 + \rho_\circ S_1\Big).$$

These equations can be further simplified by defining f to be the fraction of impurities on the black sublattice, or $\rho_\bullet = \rho_{Total} f$ and so $\rho_\circ = \rho_{Total}(1-f)$. This results in a description of the global system energy as a function of the number of impurities on each sublattice. When the energy is minimised as a function of f it reveals the most energetically favourable configuration of the system. Expanding $\mathcal{E}$ and dividing by πR^2 to get the total interaction energy of the system per unit area gives the concise form

$$\frac{\mathcal{E}}{\pi R^2} \sim \pi \rho_{Total}^2 (2f^2(S_1 - S_2) - 2f(S_1 - S_2) + S_1. \tag{7.9}$$

7.2.1 Critical concentration of impurities

Provided $S_2(\lambda) > S_1(\lambda)$, the function $\frac{\mathcal{E}}{\pi R^2}$ has minima at $f = 0$ and $f = 1$ and this case is plotted in Fig. 7.5 by the solid black line. This corresponds to the most energetically favourable configuration being the fully asymmetric one, where all the impurities occupy only one of the two sublattices. This suggests the impurity sublattice segregation in graphene is indeed a feature of the multiple scattering effects between pairs of impurities, captured in the

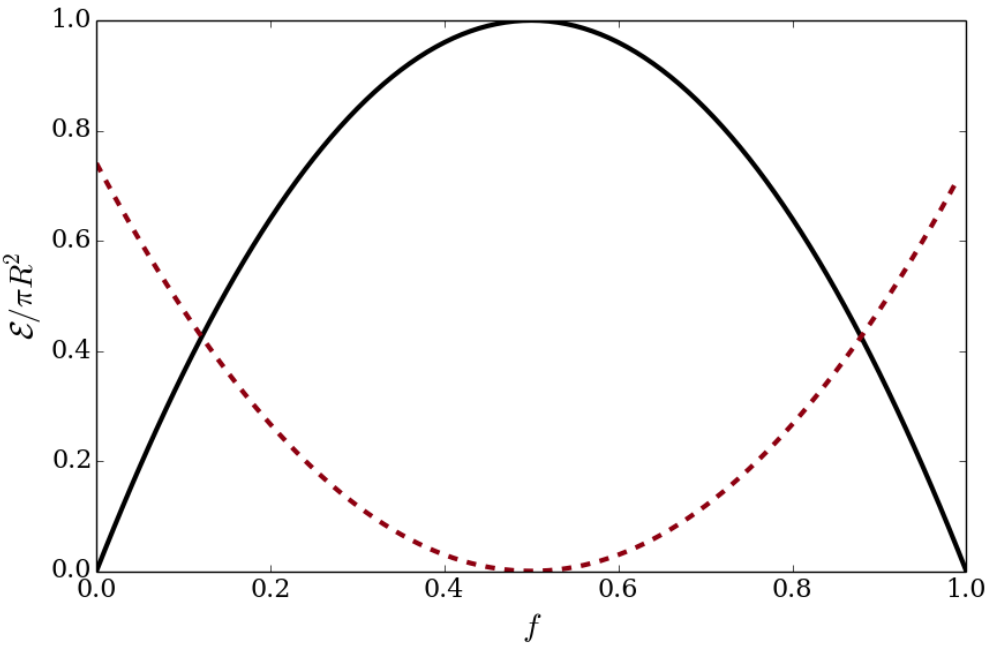

Figure 7.5: A normalized plot of the total pairwise interaction energy per unit area against the fraction of impurities occupying sublattice A with $\lambda = -4eV$. The solid black (dashed red) line is calculated with a total concentration $\rho = 0.7\%$ ($\rho = 0.9\%$), below (above) the critical concentration ρ_c. For concentrations above ρ_c one would not expect to see sublattice segregation as the system energy is minimised at $f = \frac{1}{2}$.

quantities $S_1(\lambda)$ and $S_2(\lambda)$. Increasing ρ reveals that this is not always the case. In cases where $S_2(\lambda) < S_1(\lambda)$ the favourability switches to the fully symmetric case. This is shown in Fig. 7.5 by the red dashed line which shows that total pairwise interaction energy has a minimum at $f = \frac{1}{2}$. When $S_1(\lambda) = S_2(\lambda)$ this is defined as the limiting case of *critical concentration*. At concentrations higher than this one would not expect to see the sublattice segregation.

To illustrate the magnitude of $\frac{\mathcal{E}}{\pi R^2}$ its value at some typical concentration, the difference between its maxima and minima and the size of this difference can

also be computed. As this quantity has dimensions of energy per unit area, it is useful to consider the difference between the energies of the sublattice segregated ($f = 0$ or $f = 1$) and sublattice unsegregated ($f = \frac{1}{2}$) states over the typical area occupied by a single impurity, which is a function of the concentration. For example, a concentration $\rho = 0.3\%$ and parametrisation $\lambda = -4$eV yields a difference in energy of -880meV. A typical value for the energy difference per unit area for an impurity in the system can be compared between the $f = 0$ and $f = \frac{1}{2}$ cases. The energy difference is sizeable and increases fairly linearly from -1440meV to -50meV as the concentration increases from 0.1% to 0.8%, the estimated maximum critical concentration attainable for nitrogen. Assuming that the system is at room temperature and thermal noise of $k_B T = 25$meV present, one would still expect to see the segregation effect near 0.8% in these calculations.

Throughout this section the importance of the exact parametrisation λ has been emphasised as its choice will affect the quantitative results. To clarify its effect Fig. 7.6 shows the the variation in critical concentration ρ_c as a function of λ. The exact λ value for nitrogen can be calculated in several different ways which results in several different possible values. The two parametrisations introduced in Chap. 4 are $\lambda(N) = -4$eV and $\lambda(N) = -10$eV. It can be seen that for $\lambda(N) = -4$eV the sublattice segregation should occur up until concentrations of $\sim 0.8\%$, as demonstrated in Fig. 7.6, well above the experimentally reported values of $\sim 0.1\% - 0.3\%$ [60–62]. However, in the case of $\lambda(N) = -10$eV the critical concentration falls to 0.1%, only slightly below the experimentally reported values. While the quantitative results are dependent on the parametrisation the main consequence of Fig. 7.6 that warrants emphasis is that a critical concentration exists for all values of λ. In other words this inter-impurity interaction model suggests there will always exist a maximum concentration up

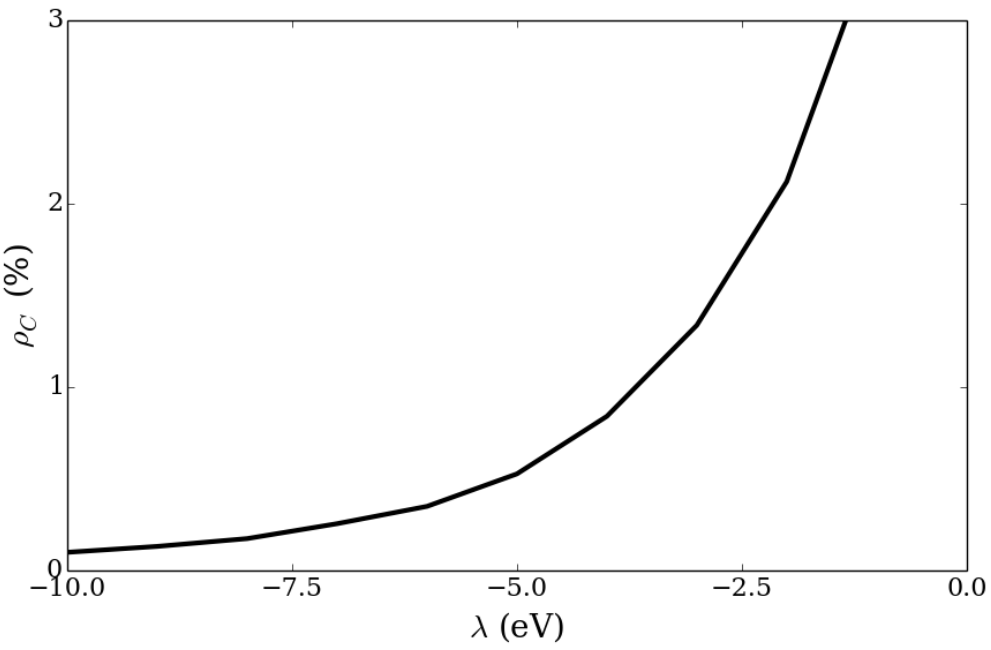

Figure 7.6: Onsite energy λ plotted against the critical concentration ρ_c. Nitrogen impurities are most commonly parametrised by $\lambda(N) = -4eV$ or $\lambda(N) = -10eV$, corresponding to critical concentrations of 0.8% and 0.1% respectively.

to which the segregation effect exists, and that this can be tested experimentally. It is worth noting that the finite size of the experimental domains and their clearly defined edges are not handled in this model but can be explained by non-uniformities in the substrate structure, for example step edges, leading to a disruption in the inter-impurity interactions. An alternative possibility is that the combined oscillations in ΔE from a large ensemble of impurities occupying one sublattice may average out in such a way that an opposite sublattice preference could be more energetically favourable for an impurity, or a collection of them, placed some distance away.

In conclusion, in this section it has been reported that the most energetically

favourable state for a dilute ensemble of substitutional nitrogen impurities in graphene is one where they occupy the same sublattice. This arises from the behaviour of Friedel oscillations in the inter-interaction energy ΔE_{AB}. This interaction is mediated by the electrons in the graphene which are normally averaged out in the case of randomly dispersed impurities. The interplay of distribution and interaction energy leads to a proposed critical concentration, beyond which the segregation effect should disappear. Due to the structural similarity with nitrogen, as was outlined in Chap. 5, it seems straightforward to extend this model to boron. This is difficult as it is known to interact strongly with Cu substrates, which in this model would destroy the effect [99]. Nevertheless the work here is very general and opens up the possibility of applying similar methods to other kinds of systems to find novel ways to induce the asymmetry effect. This will be shown in Sec. 7.3 for CNTs with hydrogen impurities and Sec. 7.4 for Gaussian strain. In both cases it is predicted that the segregation effect should still be observable, demonstrating the robustness of the hypothesis that inter-impurity interactions and Friedel oscillations are responsible.

7.3 Carbon nanotubes with hydrogen

It is clear from the work presented in Sec. 3.3 and Sec. 5.2.1 that the introduction of dopants to CNTs can change their electronic properties. Current research aims to tailor their electronic structure through controlling the dopant positioning. Monoatomic hydrogen is perhaps the simplest dopant to consider from both an experimental and a theoretical point of view, and the doping of CNTs and other nanostructures with hydrogen is well understood due to its

current use in research for future energy storage [14–16, 157–167]. Although nitrogen doped CNTs are well documented in the literature, hydrogen is an adsorbed impurity, instead of being an sp^2 bonded substitutional impurity like nitrogen. The advantages of using hydrogen instead of nitrogen is that the doping can be applied post-synthesis of the graphene sheet and that the adsorbates can migrate atop the graphene with little energy [168–170]. This is not the case for nitrogen [62, 171–173], although there is a small amount of recent evidence of sublattice asymmetry being produced using high temperature annealing after post synthesis doping [70]. Research on nitrogen doping in CNTs specifically has predicted a large difference in transport response between segregated and unsegregated doping patterns [174, 175].

The findings of the last section concerning nitrogen segregation in graphene suggest that the effect should occur in other metallic nanostructures. The inter-impurity energetic coupling, which has been proposed as the mechanism behind the phenomenon, decays according to the dimensionality d of the system, generally going as D^{-d}. Therefore in the case of CNTs it will decay as D^{-1} compared to the quicker D^{-2} shown for graphene. This is supported by the work done concerning Friedel oscillations in Δn and $\Delta\rho$ that was undertaken in Sec. 5.2.1. It is natural, therefore, to suspect that CNTs could be a good candidate to test the presence of the segregation effect in other materials.

In this section the existence of sublattice asymmetry of adsorbed atomic hydrogen atoms in CNTs will be studied. The reduced degrees of freedom means that the previous approach using a probability distribution will not work in this case. Instead a Monte Carlo method will be used to simulate the doping of a large number of CNTs, and the configuration is allowed to relax to approximate the lowest energy state. The details of the method are outlined

in Sec. 7.3.1. A brief numerical study of two hydrogen impurities is then undertaken in Sec. 7.3.2 to aid understanding of the pairwise interactions in the system. The calculation for the finite concentration is then done in Sec. 7.3.3 and the results discussed. It is found that the hydrogen adsorbates will exhibit sublattice segregation in a similar way to substitutional nitrogen dopants in graphene. As a result of using a statistical method an exact value of the critical concentration cannot be determined, however a general trend of diminishing sublattice segregation with increasing concentration or CNT diameter can be seen. Typically, a narrow nanotube (width ≤ 12 atoms) will have a sublattice imbalance ratio of 2:1 with same sublattice clusters forming.

7.3.1 Tight-binding and Monte Carlo model

The mathematical framework of the inter-impurity interaction energy in graphene and Friedel oscillations in nanotubes will be used as a basis for the Monte Carlo simulations. The additional effects of the geometry and size of the CNTs can be investigated, along with the propensity for the adsorbed hydrogen to cluster. The analytic approach used for nitrogen doped graphene cannot be used in this case as the system is no longer isotropic, hence a fully computational model will be used. The FN approximation framework will be used and again only pairwise interactions will be assumed. The atomic hydrogen adsorbates will be characterised by an onsite energy $\epsilon_a = 0.66\,|t|$ relative to the Dirac point energy of graphene and higher than the system Fermi energy, and hopping integral $\tau = 2.2t$ with a single carbon host site labelled A. As a satisfactory parametrisation could not be found for hydrogen using the inverse modelling procedure in Chap. 4, the parametrisation used here was taken from several sources in the literature which used band structure matching [135, 176,

177]. The addition of two of these hydrogen impurities to the system (with their onsite indices labelled a and b and connecting to carbon sites A and B respectively) is described by the perturbation

$$\hat{V} = |A\rangle \tau \langle a| + |B\rangle \tau \langle b| + c.c.$$

As a result of having the same onsite energy ϵ_a, both impurities have the same onsite Green function

$$g_{aa} = g_{bb} = \frac{1}{E - \epsilon_a}.$$

The energetic coupling between the two can then be found through the familiar Lloyd equation (see Eq. 2.18) as

$$\begin{aligned} \Delta E_{AB} &= \frac{2}{\pi} \mathrm{Im} \int dE f(E) \ln\left(1 - \frac{g_{AB} g_{BA} g_{aa} g_{bb} \tau^4}{(1 - g_{AA} g_{aa} \tau^2)(1 - g_{BB} g_{bb} \tau^2)}\right) \\ &= \frac{2}{\pi} \mathrm{Im} \int dE f(E) \ln\left(1 - \frac{g_{AB}^2 (g_{aa} \tau^2)^2}{(1 - g_{AA} g_{aa} \tau^2)^2}\right) \end{aligned} \tag{7.10}$$

When expressed in terms of the self-energy $\Sigma = g_{aa}\tau^2$ the similarity with the ΔE_{AB} expression for nitrogen in graphene (Eq. 7.3) becomes more obvious. In the case of nitrogen it was found that the exact parametrisation of the impurity can affect the quantitative results but that the qualitative behaviour remains the same. The parametrisation of hydrogen used here captures the close range behaviour expected of pairs of hydrogens in graphene and CNTs whereby they prefer to occupy opposite sublattices to each other [168, 169, 178–180]. The aim of this section is to model whether sublattice asymmetry can occur in CNTs with adsorbed hydrogen impurities, so the behaviour produced by this parametrisation should be sufficient for this purpose. Whilst numerous calculations of pairs of hydrogen adatoms based on DFT have shown that op-

posite sublattice configurations are more preferable, these are inadequate for considering the long-range disorder to be modelled here. Firstly, the symmetry breaking caused by the adsorption of the dopant and the subsequent E_F shift will induce Friedel oscillations in the electron density leading to a long-range spatial oscillation in the energetics of the preferred configuration. This is the long-range behaviour that leads to the asymmetry, so DFT is not adequate to model the system as is required. Additionally, the periodic nature of the DFT unit cell used to calculate these preferred configurations, effectively forming a superlattice, is also problematic when considering these interactions especially when a small cell is used.

The calculation of the ground state for a system with only 2 impurities is relatively simple computationally, but the complexity of this calculation increases as the number of impurity pairs increases. It is possible, however, to approximate the ground state using a Monte Carlo method. The strength of Monte Carlo methods are that they can be used to simulate large complex systems where arriving at an exact numerical solution is difficult due to the scale or complexity of the problem. These techniques have previously been used to look at sublattice segregation in general adsorbates on graphene [181].

Consider a section of nanotube of length L with a distribution of N adsorbates randomly attached to host carbon atoms in the system like in Fig. 7.7. Using the equation for the interaction energy ΔE_{AB} provided by Eq. 7.10 and assuming only pairwise interactions, one can approximate the ground state by repeating the following procedure: choosing an impurity; summing all pairwise interaction energies between itself and the other impurities; and then comparing this energy to the same energy when the impurity has been moved to a nearby site (hereafter referred to as $\Delta E_{AB}^{\text{Switch}}$), as demonstrated in Fig. 7.7

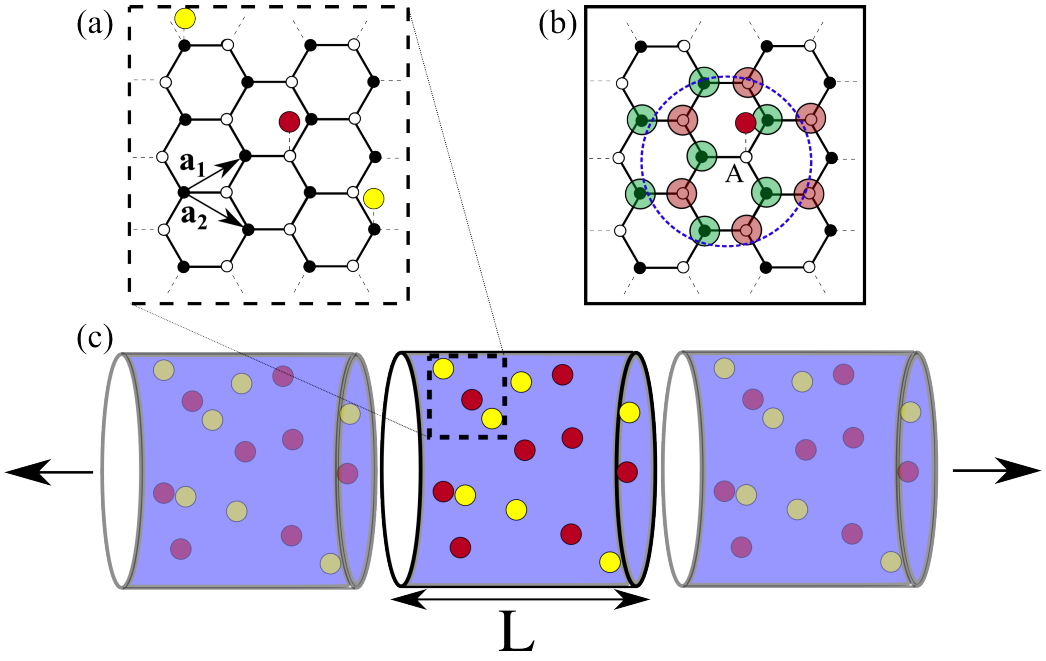

Figure 7.7: Schematic representation of a ZZNT doped with atomic hydrogen. (a) shows three adsorbates bonded to different carbon host sites and colour coded depending on the sublattice of the host. This is a close-up of the dashed box region in the larger ZZNT system shown in (c), where an ensemble of $N = 15$ impurities are shown in a central region of length L, which is replicated along the axial direction, indicated by the ghosted copies to the left and right, in order to minimise finite-size effects in the calculation. (b) shows the possible locations within the dashed blue circle region that an impurity at site A in the central unit cell can move to if randomly selected in the iterative Monte Carlo procedure described in the main text, colour coded for opposite (green) and same (red) sublattice sites.

(b). If the second energy is lower then this configuration can be assumed to lowers the total system energy, and the impurity is moved. If the first energy is lower then no change is made. This technique is similar to that used for the computational approach to the Ising model of ferromagnetism in a two-dimensional lattice. The effect of a Boltzmann Temperature T_B can also be

introduced, whereby there is a finite probability

$$p \sim e^{\frac{\Delta E_{AB}^{\text{Switch}}}{k_B T_B}}$$

to move the impurity even though the first energy may be lower. It should be clarified that this iterative method of moving adsorbates is not the same as a dynamics calculation. While energy barriers for diffusion have been calculated to be on the order of, or less than, 1eV [168–170], this will be ignored as the aim is to find the ground state of the system and not model the physical diffusion of adatoms. Moreover, recent research has shown it is possible to lower the energy required for surface diffusion by doping CNTs with substitutional nitrogen [168].

If a concentration of impurities (ρ) is added to the system it is natural, as with the nitrogen case in the last section, to assume the number of electrons and therefore the Fermi Energy E_F will change. To calculate this shift DFT calculations were done with different length and diameter CNT unit cells doped with a single hydrogen and the Fermi level shift was calculated. An average charge transfer of $\frac{1}{12}e$ to the host system per hydrogen was found. By examining the relationship between concentration (function of CNT size) and E_F shift it was found that the relationship is linear and approximated well up to $\rho \sim 10\%$, and that the density of states profile is relatively unchanged at low energies. Other methods of finding this E_F shift using tight-binding have found a higher charge transfer from adatom to the graphene [182] which would result in shorter oscillation periods and a reduction of the predicted segregation effect.

To minimise finite-size effects which are an unfortunate consequence of this

methodology, it is necessary to impose extra conditions. Firstly the central region L and the impurities are replicated along the axis of the nanotube once in each direction in order to approximate the effect of an infinite system. A schematic of this is shown in Fig. 7.7 (c). During the iterative procedure if an impurity in the central region is moved then so are their 'twins' in the replicated sections. Because of the oscillatory nature of the interaction a cut-off of one oscillation period of ΔE_{AB} should be imposed, beyond which the interaction is assumed to be zero. This is to ensure an even contribution to the interaction energy for all the impurities regardless of their position in the central region. Due to the scaling between length L, ρ and E_F this cut-off length is approximately the same as L and for the example system presented in Fig. 7.8 is approximately $D = 180a$. Only metallic CNTs are considered, so the LDOS is finite but flat around $E_F = 0$ the shift in E_F due to the introduction of the impurities must therefore obey $E_F \sim \frac{\rho}{12}$ and hence the oscillation period of the interaction energy changes as $\frac{1}{\rho}$.

7.3.2 Two hydrogen impurities

The behaviour of ΔE_{AB} for two hydrogens in a 6-ACNT is shown in Fig. 7.8 and 7.9, the most important characteristics to note are the difference in short- and long-range behaviours. Although only two impurities are embedded in the system the E_F value has been shifted to simulate a doped system and the specific value corresponds to an impurity concentration of approximately 1.5%. When the impurities are close it is seen that they will prefer to occupy opposite sublattice arrangements as in graphene.

This short-range behaviour gives way to long-range decaying oscillations, com-

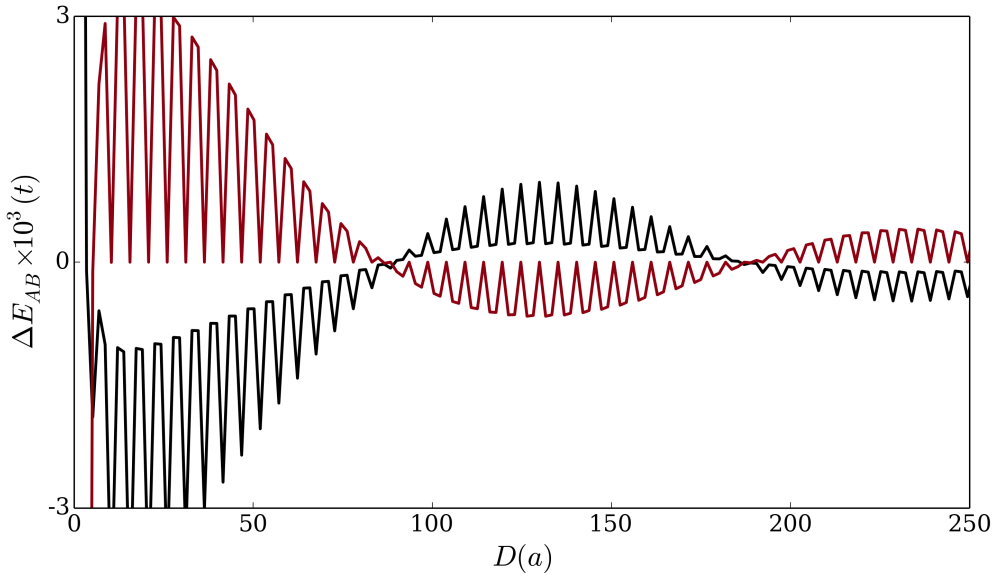

Figure 7.8: Cross-section of ΔE_{AB} between two hydrogen adatoms separated in the axial direction in a 6-ACNT host system with $E_F = 0.033t$ for same sublattice (black) and opposite sublattice (red) configurations.

plete with circumferential symmetry and a distinct period-3 behaviour, characteristic of interactions between impurities with zigzag separation in graphene-like systems, can be observed [183]. The region of short-range behaviour reduces with both increasing concentration, as shown by comparing plots (c) and (d), and increasing the CNT circumference. The overall short-range and long-range behaviours and the oscillation period are very similar in ZZNTs with the exception that the period-3 behaviour is in the circumferential direction, with long smooth decays along the axial direction.

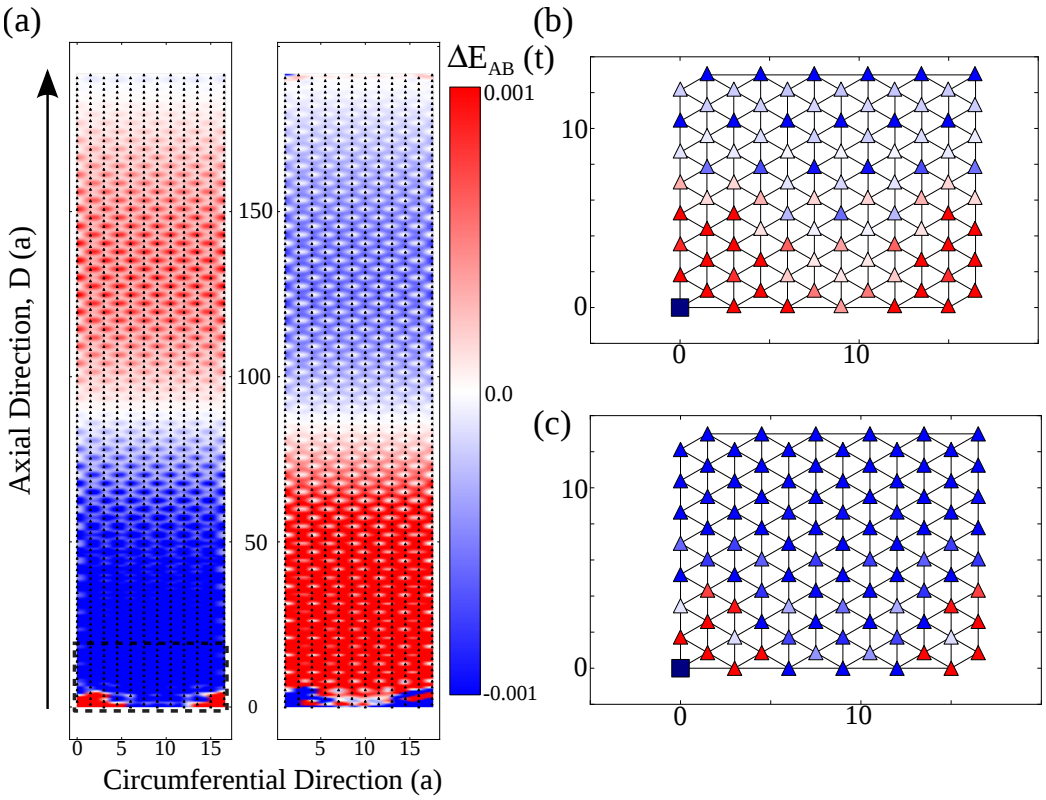

Figure 7.9: The contour plot in panel b extends the cross-section of Fig. 7.8 to sites in the circumferential direction and the results are shown for same sublattice (left) and opposite sublattice (right) configurations where the short- and long-range behaviour is apparent. For clarity, the nanotube has been projected flat and the lattice sites are referred to by their circumferential and axial positions relative to the carbon site hosting the hydrogen impurity at the origin. (b) is a close-up of the dotted region in (a) of the short-range behaviour and (c) the same but at a lower impurity concentration of 0.1%.

7.3.3 Finite concentration of hydrogen

The calculations in this section were done using approximately $N = 40$ impurities for ACNTs and approximately $N = 30$ for ZZNTs, $10N^2$ iterations and 250 randomly generated systems for each concentration and temperature com-

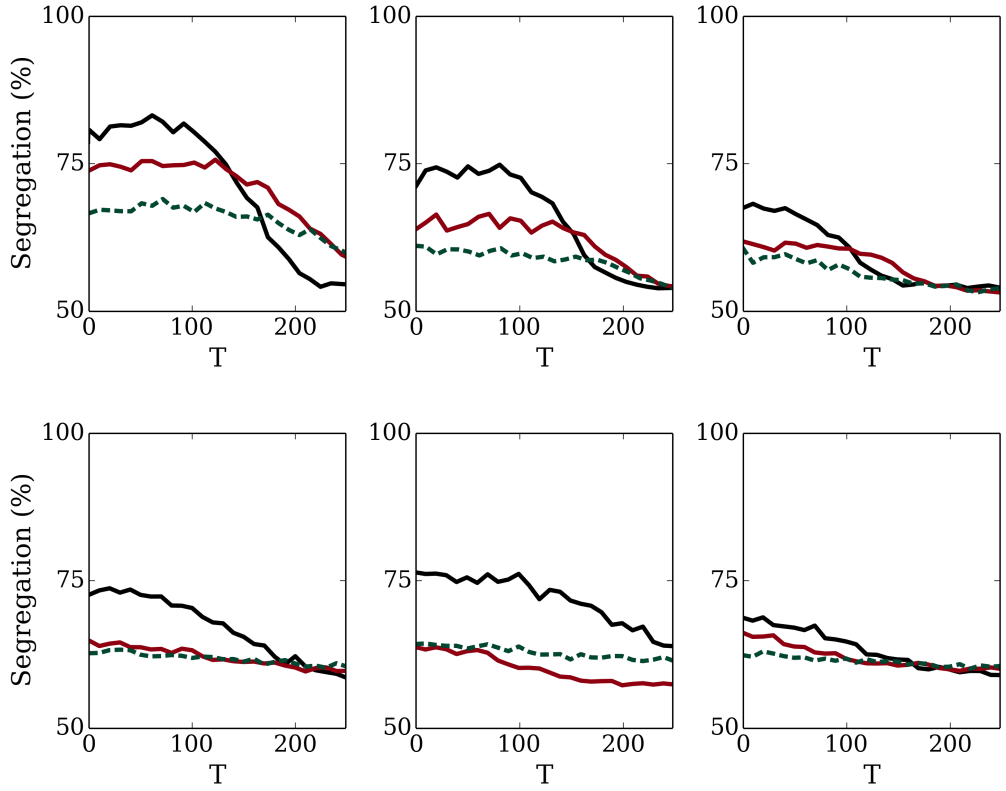

Figure 7.10: Degree of sublattice segregation, i.e. percent of impurities on one sublattice, vs. the Boltzmann temperature for small diameter ACNTs (top row, L-R: $N_C = 6, 9, 12$) and ZZNTs (bottom row, L-R: $N_C = 6, 9, 12$) with atomic hydrogen concentrations of 0.5% (black), 1.0% (red) and 1.5% (dashed green). The relationship is analogous to that of magnetism and temperature in the Ising Model.

bination. The cut-off, directly linked to E_F and thus ρ, determines the exact value of L which in turn affects the value of N, hence why there is a difference in N between ACNT and ZZNT systems.

7.3.3.1 Finite temperature calculation ($T_B > 0$)

Monte Carlo calculations were performed as described previously to investigate the appearance of sublattice asymmetry in ACNTs and ZZNTs with widths defined by $N_C = 6, 9, 12$. The dependence of the sublattice asymmetry on the Boltzmann Temperature for a range of small diameter CNTs with ACNT and ZZNT geometries with different concentrations of hydrogen are shown in Fig. 7.10. A segregation of 100% corresponds to all impurities being on one sublattice whilst 50% corresponds to an equal distribution between the two sublattices. As one would expect, increasing T_B causes the impurities to be randomly ordered and the system will approach a 50% segregation (i.e. unsegregated or symmetric) state. The slower decay of the ZZNTs compared to ACNTs to the equilibrium state of 50% segregation originates from the difference in decay profiles and period-3 behaviour of ΔE_{AB}. In ZZNTs it is harder to push an impurity out of an energetically stable configuration than in an ACNT, hence the broader temperature dependence for the former shown in Fig. 7.10. The relationship between segregation and Boltzmann Temperature indicates there is no meta-stable state at low temperatures, hence the dependence of segregation on the concentration can be investigated at $T_B = 0$. The result in the limit of zero temperature should therefore be a good approximation of the ground state of these systems.

7.3.3.2 Zero temperature ($T_B = 0$)

The relationship between segregation and concentration is plotted in Fig. 7.11 for various CNTs. The effect of increasing concentration and CNT diameter can be seen clearly, both of which lead to a reduction in the predicted seg-

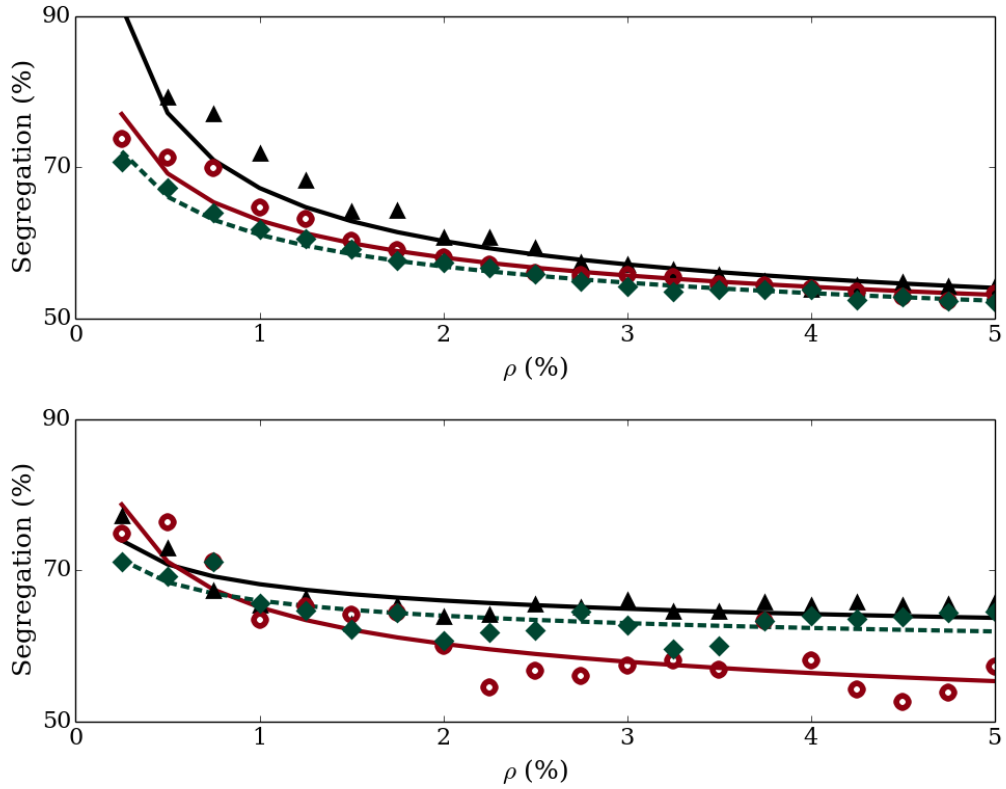

Figure 7.11: Segregation vs. concentration at $T_B = 0$ for $N_C = 6$ (black), $N_C = 9$ (red) and $N_C = 12$ (green) of armchair (top) and zigzag (bottom) geometry, Monte Carlo results are represented by the dots and a corresponding line of best fit satisfying $\sim 50 + \rho^{-\alpha}$ shown as a line. The value of α is $\alpha \approx \frac{1}{4}$ for the armchair geometry and $\alpha \approx \frac{1}{10}$ for the zigzag geometry. Increasing concentration or tube diameter leads to a reduction of the predicted segregation, tending to 50% in the limit of high concentration, a product of the reduction in the axial separation of impurities leading to a dominance in the short-range behaviour of ΔE_{AB}.

regation effect. This can be understood as the long-range ΔE_{AB} oscillations being the driving mechanism of the asymmetry, as was proposed for the effect for nitrogen impurities in graphene. Increasing either concentration or the CNT diameter reduces the average axial separation of the impurities and the

short-range behaviour, which favours opposite sublattice ordering, dominates. This can be corroborated by comparing the k-th nearest neighbour distributions of these systems and this is plotted in Fig. 7.12 comparing low (0.5%) and high (5.0%) impurity concentrations, with segregated and unsegregated configurations respectively, and expected values for a random configuration in a 6-ACNT. The discretised lattice makes identifying the relative sublattice arrangement of the large peaks straightforward. Both low and high concentrations show a large peak corresponding to the nearest neighbour opposite sublattice arrangement. The data for low concentrations also shows a number of peaks at distances beyond a few lattice parameters, which correspond to same sublattice arrangements in much greater amounts than the random data. At high concentrations there are numerous peaks for close separations at much higher frequencies than the random data which points to clustering of the impurities. The second nearest neighbour data shows two close peaks corresponding to opposite (left) and same (right) sublattice arrangements, and these also occur in the first and third nearest neighbour data. Fig. 7.11 further suggests the asymmetry should be higher in ACNTs than ZZNTs, where levels as high as 90% segregation should be observable at concentrations around 0.25% in a 6-ACNT.

Following the trend of increasing diameter and decreasing segregation it seems a natural conclusion to expand the study to graphene by increasing the nanotube width to infinity, and where naively one should expect no segregation to be observed. This conclusion should not be made automatically as there exist subtle but important distinctions to be made between the case of CNTs and graphene. Firstly, pristine graphene is semi-metallic but upon being doped by a finite concentration of hydrogen the band structure is changed considerably, especially around the Dirac point [182], leading to a more complex E_F

shift and effects on the LDOS oscillations which drive the segregation effect. Secondly, these LDOS oscillations behave much differently in graphene decaying as D^{-2} and the directional isotropy of the coupling ΔE_{AB} would allow for more complete analytic calculations as has been shown for substitutional nitrogen impurities in graphene where a segregation effect was shown to exist in Sec. 7.2.

Comparison of the nearest neighbour data in Fig. 7.12 demonstrates that clustering occurs in both high and low segregation systems. This reflects previous findings for hydrogen pairs, both in Sec. 7.3.2 and in the literature, that in close proximity these pairs prefer to occupy host sites on opposite sublattices [169, 178]. It has also been shown by Hornaeker et al. that a similar clustering effect can be observed with hydrogen adsorbates on graphene [184]. At lower concentrations (Fig. 7.12 - left panels) the most frequently found configurations are same sublattice ones, despite the short-range effect, due to the large average axial separation coupled with the long-range oscillatory nature of ΔE_{AB}. This is evident from the location of the peaks in the low concentration data, occurring almost entirely for separations corresponding to same sublattice configurations. Additionally only a small deviation in the expected nearest neighbour profile (with the exception of the short-range peaks) is observed, along with the calculated mean and median values.

These characteristics are in sharp contrast to the high concentration data, shown in Fig. 7.12 (right panels). In this case, there is a much larger degree of clustering, indeed almost all nearest-neighbours will be on the opposite sublattice, and there is a huge difference in the histogram profiles compared to the random distributions. The overwhelming frequency with which one finds opposite sublattice configurations at such short range lends credence to the long-

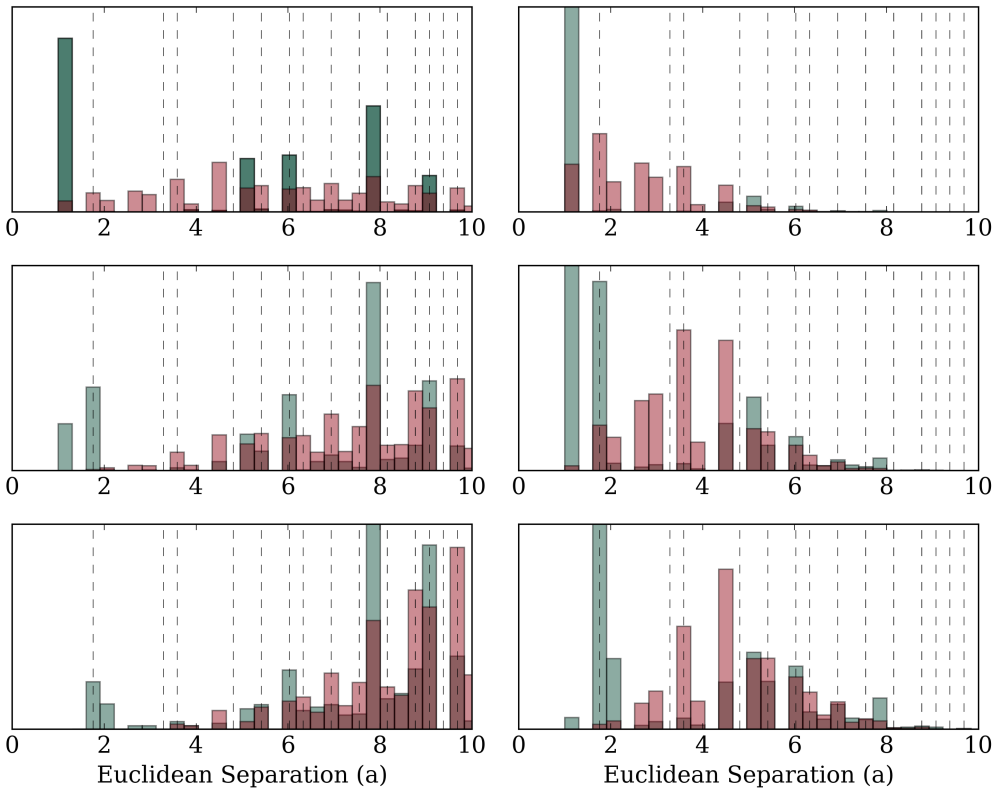

Figure 7.12: Histogram data for first (top), second (middle) and third (bottom) nearest neighbour separations for H pairs in a 6-ACNT with circumference at 0.5% (left) and 5.0% (right) concentrations, comparing measured data (green) to a random distribution (red). The dashed lines indicate distances on the black sublattice.

range versus short-range/axial separation hypothesis, where the behaviour of ΔE_{AB} acts so to cluster the impurities in opposite sublattice configurations at short range.

A clearer illustration of the clustering effect and the short-range behaviour is shown in Fig. 7.13 where the probability of finding impurities in certain short-range configurations is shown and compared for low and high concentrations

and the random data, aggregated from the nearest neighbour data of Fig. 7.12. For both high and low concentrations there is a large increase, 8% and 36% respectively, in the probability of finding a nearest neighbour (opposite sublattice) configuration over what one would expect in a random system. There is also a large increase in next-nearest neighbour (same sublattice) configurations - a consequence of the clustering of impurities. Most interestingly there appear to be preferential configurations, which one would expect from the profile of ΔE_{AB} in Fig. 7.8 and Fig. 7.9. For example, there is a four- to five-fold increase in likelihood for the same sublattice configuration corresponding to the top-right most black site (position $\approx 7.9a$) and, due to lattice symmetry, equivalent sites such as the middle right-most black site at high and low concentrations. Another preferential configuration is found for a separation of $\approx 5.2a$ where the probability is approximately doubled. This is less pronounced than results seen for hydrogenated graphene in the literature [67] where much higher concentrations and both sides of the monolayer were used, but is an interesting effect resulting from the inter-impurity interactions.

In summary, in this section it was reported that the segregation effect is most pronounced for small diameter CNTs with dilute concentrations of impurities, and that the effect decreases when either of these two parameters are increased. The inter-impurity interactions which mediate this interaction have a competing short- and long-range behaviour which tend to prefer opposite and same sublattice configurations respectively, and lead to certain preferential configurations and slight patterning in the lattice. In small diameter tubes with a dilute concentration of impurities the long-range behaviour along the axial direction dominates and the system prefers the segregated state. Increasing the concentration of impurities or the tube diameter reduces this axial separation and the short-range behaviour takes over, forcing the system into a state where

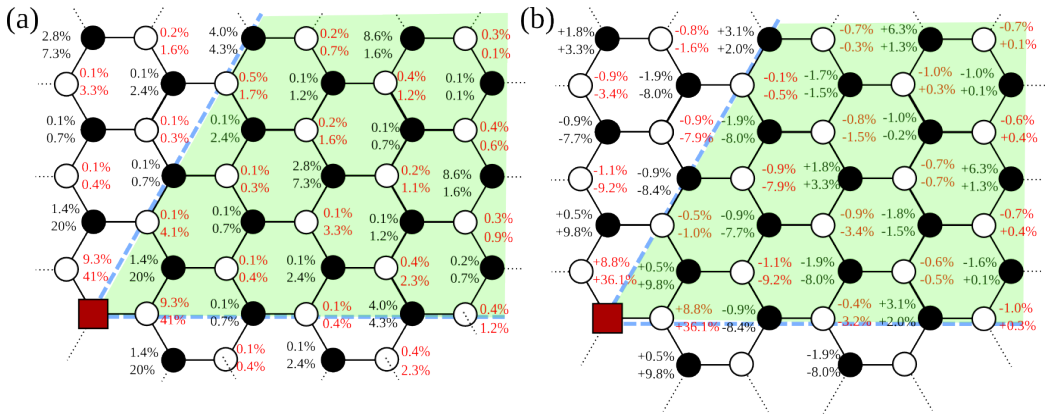

Figure 7.13: (a) Probability for an impurity to occupy a host site, given an initial impurity indicated by the red square, for same sublattice (black) and opposite sublattice (red) arrangements at low (top number) and high (bottom number) concentrations in a 6-ACNT. Due to the symmetry of the system it is possible to allocate irreducible sectors, shown by the green shaded areas, which contain the information on all possible positions in the nanotube in order to simplify the data in this figure. To give some context for these findings, part (b) shows the stark difference between the probabilities shown in (a) and values that would be expected for a random, unrelaxed system.

the sublattices have approximately equal numbers of dopants. The short-range behaviour also leads to clustering and energetically favourable configurations of the impurities, a phenomenon which has been shown before both theoretically and experimentally. The current state of research with respect to general hydrogen doping of CNTs [14, 157–159, 164] and other one-dimensional nanomaterials [160–162], an interest piqued due to their use for hydrogen storage for fuel cells, along with the capability to directly identify dopants and their respective sublattices [171, 173, 185], suggests that testing the findings of this section and previous work in graphene, that inter-impurity interactions lead to a segregation effect, is well within current experimental limits.

7.4 Gaussian strain

Throughout this thesis it has been shown repeatedly that breaking the symmetry of a bipartite lattice system via the introduction of impurities in a sublattice asymmetric manner will produce different signatures in Friedel oscillations on each sublattice. It has been hypothesised that this effect causes some of the atomic sites in the system to be more energetically favourable than others for impurity adsorption. In this chapter a model will be developed to show that breaking the symmetry of graphene using Gaussian strain centred on one of its two sublattices produces a similar effect, and that this is tunable with the strain parameters. This type of strain profile can be produced and maintained by an atomic tip. The results obtained using the tight-binding approach are corroborated with DFT calculations. This presents a novel approach to tailoring the electronics of nanomaterials through controlling impurity placement.

Graphene's low-energy linear dispersion is protected by the symmetry existent between the black and white sublattices [186] and breaking this symmetry is the key ingredient for opening a gap. Up to this point, in this work only chemical doping has been explored as a route to inducing this band gap. However, an alternative method is through mechanically straining the system, for example by the application of uniaxial strain [153, 187]. Yet, the gapless Dirac spectrum of graphene can be quite resilient against the application of planar strain. Theoretical predictions have demonstrated that bulk graphene can support elongations along the armchair direction up to 20% without splitting the degeneracy of the bands at the Fermi level [153]. Sublattice symmetry can be better lifted by inducing out-of-plane deformations in graphene structures such as local centrosymmetric bumps [188–190] and strained nanobub-

bles [191]. According to continuum models in which perturbations are described as effective gauge fields, the local distortion in the graphene structure emulates the presence of a pseudomagnetic field [192] that breaks sublattice symmetry.

In this section, a method is demonstrated to impel foreign objects to favour a particular sublattice by inducing a Gaussian-shaped deformation (bubble) on the graphene sheet. By centring the Gaussian strain on one particular atomic site (i.e. focussed on one sublattice) this will break the sublattice symmetry of the system yielding Friedel oscillations in the LDOS in a similar way to those arising from impurities in Chap. 5. As a result, the system binding energy will be shown to have a spatial dependency underlined by the shape of the deformed region. This effect dictates the placement of impurities at well-defined positions patterned by the Gaussian distortion. It is argued that an additional mechanism to modulate the transport properties of graphene is possible when its sublattice symmetry is broken through the application of this mechanical sublattice asymmetric strain profile.

7.4.1 Patched Green functions method

In this section the process of modelling of a 'bubble' in graphene caused by Gaussian strain will be described in the context of the tight-binding model. Cases like this, where an interesting region with local disorder is embedded in an infinite crystal structure, cannot be efficiently treated with the previous approaches - neither periodic boundary conditions nor the recursive approaches will work as the calculation becomes unwieldy very quickly. Recent work by Settnes et al. [190, 193] has solved this issue using a combination of the two

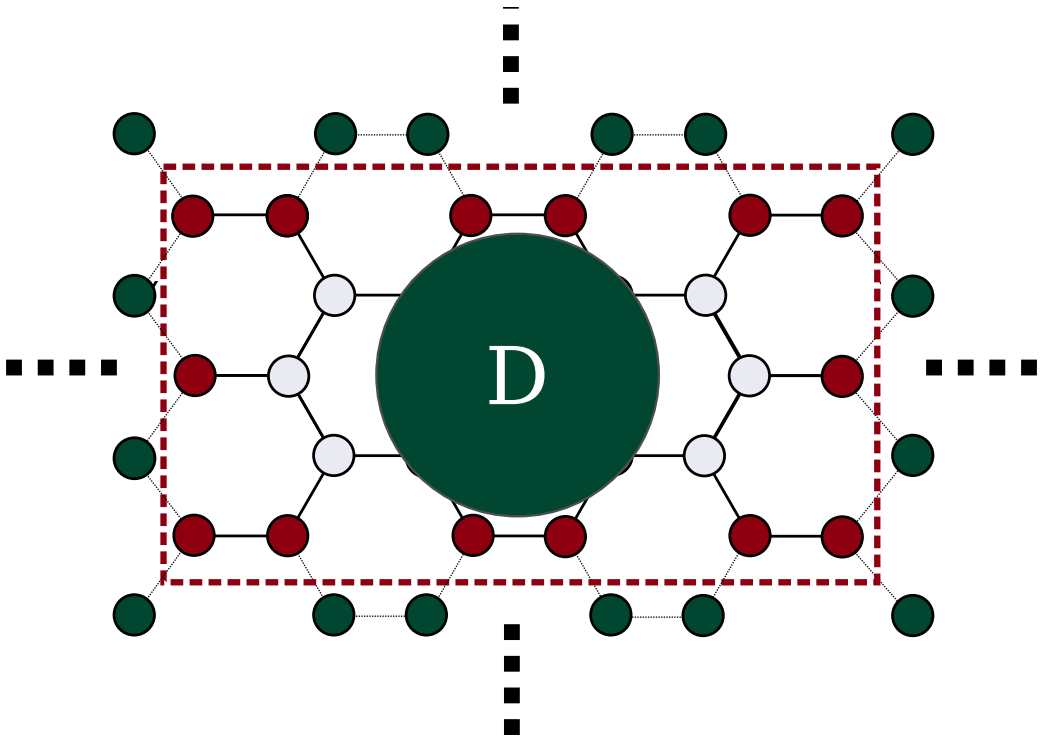

Figure 7.14: Schematic of the patched Green functions method for a disordered region D embedded in the graphene lattice. Red indicates atomic sites at the edge of D which are coupled with the green atomic sites in the bulk, the area occupied by the latter is termed the boundary region.

techniques. In brief the method works with an initial Hamiltonian describing the disordered region only, and models the coupling to the bulk system via self-energy terms. The connection of the two is made through the Dyson equation. The self-energy terms are expressed purely in terms of the periodic lattice Green functions obtained in Chap. 3. The result is that the Green functions of the connected disordered region (denoted $\hat{G}^C_{DD}$ and explained further below) are readily obtained and from there one can derive the energetics using the methods discussed in this chapter.

The first step is considering a disordered region embedded in the graphene

lattice as shown in Fig. 7.14 with Hamiltonian $\hat{H}_{DD}$. This matrix contains all relevant perturbation information, e.g. localised strain effects or lattice defects. The Hamiltonian for the entire system is the block matrix

$$\hat{H} = \begin{pmatrix} \hat{H}_{DD} & \hat{V}_{DB} & 0 \\ \hat{V}_{BD} & \hat{H}_{BB} & \hat{V}_{BS} \\ 0 & \hat{V}_{SB} & \hat{H}_{SS} \end{pmatrix}$$

where $\hat{V}_{\alpha\beta}$ connects systems α and β and the subscripts B, D and S indicate the boundary, disordered and bulk ('sheet') regions respectively. The boundary region is shown in Fig. 7.14 as the dark green coloured atomic sites. It is clear that the matrices $\hat{H}_{BB}$, $\hat{V}_{BS}$, $\hat{V}_{SB}$ and $\hat{H}_{SS}$ can be completely expressed by the bulk lattice Green functions. The aim is to replace these terms by an effective self-energy term Σ_B, much like was done for the recursive methods, containing all the information of the coupling between disordered region and bulk.

Consider the connected and disconnected systems separately, where the latter is formed by setting $\hat{V}_{BD} = \hat{V}_{DB} = 0$ and can be visualised by removal of the disordered region in Fig. 7.14. Using the Dyson equation the Green functions for the connected and disconnected systems can be related to one another. For example, the disordered region in the connected state is described by

$$\hat{G}^C_{DD} = \hat{G}^D_{DD} + \hat{G}^D_{DD}\hat{V}_{DB}\hat{G}^C_{BD}$$

where

$$\hat{G}^C_{BD} = \hat{G}^D_{BB}\hat{V}_{BD}\hat{G}^C_{DD}.$$

The superscripts indicate whether the Green function is in the connected (C) or disconnected (D) system. By substituting $\hat{G}^C_{BD}$ into $\hat{G}^C_{DD}$ and rearranging it

can be shown that

$$\hat{G}^C_{DD} = \frac{\hat{G}^D_{DD}}{\hat{I} - \hat{G}^D_{DD}\hat{\Sigma}_B} = \frac{1}{E\hat{I} - \hat{H}_{DD} - \hat{\Sigma}_B}$$

where $\hat{\Sigma}_B = \hat{V}_{DB}\hat{G}^D_{BB}\hat{V}_{BD}$. Note that this self-energy term is completely independent of the disordered region and relies only on the connection matrices and bulk Green functions.

The term $\hat{G}^D_{BB}$ can also be computed via the Dyson equation. Disconnection of the perturbed region can be done via applying the perturbation $-\hat{V}_{DB}$ which yields

$$\hat{G}^D_{BB} = (\hat{I} + \hat{G}^0_{BD}\hat{V}_{DB})^{-1}\hat{G}^0_{BB}.$$

As long as the interface between the device and boundary regions is continuous, the connected Green functions on the right-hand side of the above equation can be described completely by the bulk lattice Green functions derived in Chap. 3. Substituting this expression into $\hat{\Sigma}_B$ and it is clear that now $\hat{G}^C_{DD}$, the Green function for the connected disordered region, is expressed entirely through only bulk lattice Green functions and the initial Hamiltonian $\hat{H}_{DD}$. This is extremely useful as $\hat{H}_{DD}$ can be tailored rather easily depending on the device region that is modelled. This will be used later in this section to model the effects of the Gaussian strained region embedded in an otherwise pristine graphene system.

To demonstrate how out-of-plane deformations in graphene structures can interfere in the adsorption process of adatoms, two theoretical methodologies were used: (i) a nearest-neighbour tight-binding description in conjunction

with the patched Green function method [190, 193] and (ii) DFT [194, 195]. The latter calculations were performed by Claudia G. Rocha in the School of Physics at Trinity College Dublin. In both methodologies, a top adsorbed hydrogen atom was used as the probing impurity. The same tight-binding parametrisation of hydrogen from the nanotube case considered in the previous section will be used. Although different parametrisations may alter the numerical calculations, the qualitative results obtained in this work remain consistent. The energetics associated with the binding of an impurity to the graphene is again calculated using the Lloyd formula

$$\Delta E_i = \frac{2}{\pi} \int_{\infty}^{E_F} dE \, \mathrm{Im} \ln \det \left(\hat{I} - \hat{g}(E) \hat{V}_i \right) \tag{7.11}$$

where i is the index labelling the host sublattice site, $E_F = 0$ and

$$\hat{V}_i = |a\rangle \, \tau \, \langle i| + c.c.$$

is the local perturbing potential describing the connection between the adatom and the graphene host. As the adatom can attach to either sublattice the perturbing potential must also be indexed with i. The adatom has the usual onsite Green function

$$g_{aa} = \frac{1}{E - \epsilon_a}$$

for an adsorbed impurity.

The strain is incorporated by the patched Green-function approach where a combination of recursive techniques and bulk lattice Green functions is implemented [47]. The Hamiltonian of the central deformed region (c.f. Fig. 7.14) is constructed using a similar method to the unit cell construction for a CNT described in Sec. 3.3.2, but with modifications to the hoppings to account for the

strain. After making the necessary changes, which will be described shortly, the cell is then connected to the bulk system via self-energy elements describing the connections between the scattering region and its boundaries. The deformation is induced by applying circularly symmetric Gaussian strain centred on a particular atomic site given by the formula

$$h_j = Ae^{-d_j^2/b^2}, \tag{7.12}$$

where d_j is the distance between an atom j and the strain centre and A and b are parameters used to shape the Gaussian deformation; A is associated with its out-of-plane amplitude and b is associated with its circular spreading. The ratio between these (squared) values given by $\alpha = \frac{A^2}{b^2}$ determines the strain intensity generated by the bubble. Intensities of $\alpha = 1\%$, 2.5%, 5% and 10% are chosen which reflect values typically found in previous works [154, 196–198]. With the whole scattering region deformed according to Eq. 7.12, the interatomic distances between neighbouring atoms m and n, l_{mn} can be determined. The resulting change in bond lengths leads to a modification of the nearest neighbour hopping of the tight binding Hamiltonian by

$$t_{mn} = te^{\beta(\frac{l_{mn}}{l_0}-1)} \tag{7.13}$$

where $l_0 = 1.42$ Å is the length of an unperturbed C-C bond and $\beta = -3.37$ for graphene [153]. More explicitly, l_{mn} is the Euclidean distance between atoms m and n after the strain is applied, following Eq. 7.12. The electronic hoppings t_{mn} are inserted into the Hamiltonian describing the deformed central region from which its associated Green function $\hat{g}$ can be obtained via the patched Green function method. Finally, the binding energy for the impurity can be

calculated through Eq. 7.11.

Besides the tight-binding calculations, DFT calculations can also be performed using SIESTA code [194, 195] with a generalized gradient approximation (GGA-PBE) [199] for the exchange-correlation potential. While these calculations were undertaken by a collaborator (Claudia G. Rocha), due to their extensiveness the details of them will be discussed here for completeness. Norm-conserving pseudopotentials with core corrections [200] were used along with a split-valence double-ζ basis (DZP) of pseudoatomic orbitals with an orbital confining energy of 0.05 eV, and an energy cut-off of 250 Ry. A graphene supercell with dimensions of approximately 27 $\times$ 26 $\times$ 40 Å were built, within which a Gaussian deformation was formed, altering the atomic positions along the z-axis. The parameters for the deformation are A = 2.16 Å, and b = 4.5 Å , leading to α = 23 % (see Fig. 7.15) and the deformation was centred on a single atomic site in the centre of the cell, yielding a structure similar to the device Hamiltonian H_{DD} in the complimentary tight-binding calculation. No structural relaxation was conducted in the deformed sheet to guarantee that its Gaussian shape is maintained. Upon relaxation the structure would alter slightly into a state where the Gaussian is centred at the middle of a C-C bond, removing the sublattice symmetry. The decision not to relax the structure is justified by an external agent, for instance an atomic tip, maintaining the system in a metastable state. The structural relaxation was only performed after a hydrogen atom was adsorbed, with only atoms in the vicinity of the impurity allowed to relax. This relaxation was conducted using the conjugate gradient algorithm under a 4 $\times$ 4 $\times$ 1 Γ-centred k-mesh and with a maximum force tolerance of 0.03 eV Å^{-1}. The electronic structure of the doped system was subsequently determined in a sampled Γ-centred Brillouin zone with a grid of 16 $\times$ 16 $\times$ 1. From the electronic structure calculation, the spatial LDOS

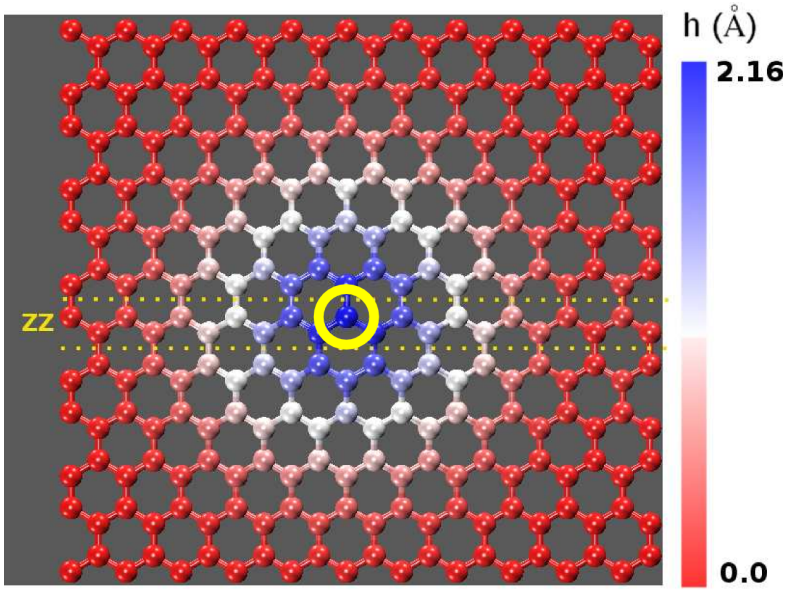

Figure 7.15: Top view of a graphene super cell subjected to a Gaussian deformation of $A = 2.16$ Å and $b = 4.5$ Å ($\alpha = 23\%$). The colour code maps the out-of-plane height (h). The centre of the Gaussian is located on the carbon atom enclosed by the yellow circle. Dashed yellow lines mark a zigzag segment on which projections on site basis are performed within DFT calculations. Calculation and plot by Claudia G. Rocha and used with permission.

distribution was obtained within the energy range of [E_F - 0.5 eV, E_F].

7.4.2 Segregation and Gaussian strain calculations

The distinct signatures in $\Delta\rho$ exhibited by the two sublattices for a bubble characterised by $\alpha = 5\%$ is shown in Fig. 7.16, produced using the tight-binding method. These oscillations were probed for a relatively extreme value of $E_F = 0.5t$ for visual aesthetic reasons, smaller more realistic values will increase the oscillation period. At $E_F = 0$, these oscillations disappear as a

result of lattice commensurability effects and a continuous $1/D$ decay is observed. This is identical to the case of impurities presented in Chap. 5. In the case where strain is applied equally to each sublattice, e.g. at the centre of a hexagon or a C-C bond, the resulting LDOS profiles are identical for both sublattices (not shown). This confirms that the centrosymmetric deformation promotes an imbalance in the LDOS distribution with respect to the two inequivalent sublattices. Similar Friedel oscillations can be found in the DFT results in Fig. 7.17, depicting $\Delta\rho$ projected on each carbon site located along the zigzag direction highlighted in Fig. 7.15.

Similar patterns are observed for the change in electronic energy as a result of adsorbing a H atom on the graphene bubble. Fig. 7.18 shows the short-ranged spatial pattern formed by ΔE calculated for each adsorption site on the patch subjected to strains of $\alpha = 10\%$. It is clear that the energy variation profiles for each carbon sublattices differ largely, although both of them exhibit a particular pattern determined by the sublattice on which the impurity is placed and this sublattice disparity would not be evidenced if the path was flat. The shape of the energy profiles is also not fixed, being heavily dependent on the strain intensity and parametrisation of the impurities. This means that the most energetically favourable positions for impurity adsorption are modulated with respect to the strain intensity α.

While it can be seen from the resulting energy profiles that certain atomic sites are more preferable than others, a more descriptive quantity can be obtained by defining a net energy M which accounts for energetic imbalances between the two sublattices. This quantity is defined as

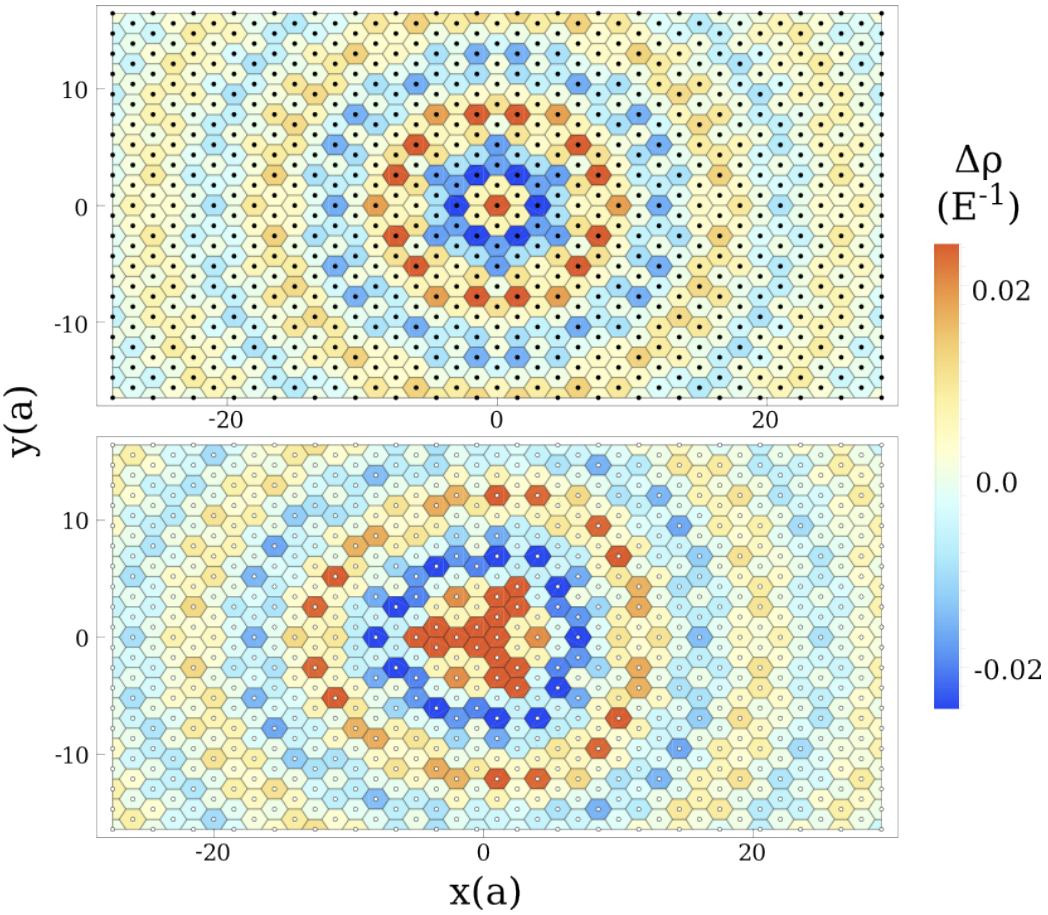

Figure 7.16: Contour plot of LDOS obtained separately for (top panel) black and (bottom panel) white sublattices for a graphene path deformed with a Gaussian strain of $\alpha = 5\%$. The strain is applied at a carbon atom belonging to the black sublattice situated at the origin. The Fermi energy is set at $E_F = 0.5\,t$.

$$M = \sum_{j \in \mathrm{B}} \Delta E_j - \sum_{i \in \mathrm{A}} \Delta E_i \,. \tag{7.14}$$

The value of M describes how much more favourable one sublattice is with respect to the other, therefore serving as a useful metric with which to quantify the sublattice asymmetry. Fig. 7.19 depicts the dependency of M with the am-

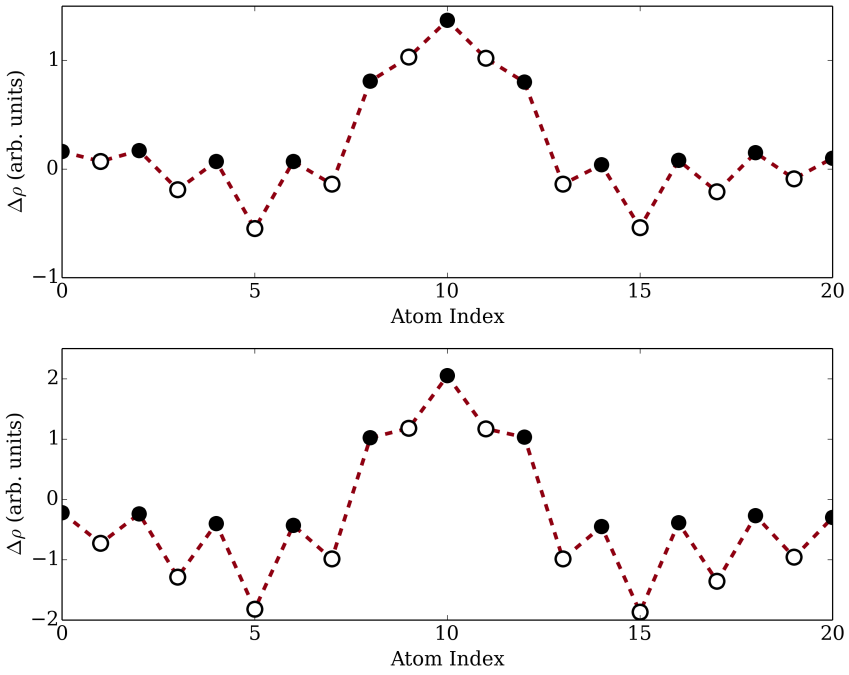

Figure 7.17: $\Delta\rho$ projected on each carbon site along the horizontal zigzag line highlighted in Fig. 7.15. The solid and hollow points correspond to black and white sublattices respectively and these were plotted for two fixed energy values of -0.4 (top) and -0.6 eV (bottom) using the DFT method. Similar to the tight-binding method $\Delta\rho$ is maximum at the site located at the centre of the Gaussian deformation with a decaying oscillation profile as one moves away from this location. Calculation by Claudia G. Rocha and used with permission.

plitude of the Gaussian A for fixed values of α. For small amplitudes, $M \approx 0$ indicating that there is no preferable sublattice for the impurity to adsorb. As the out-of-plane deformation increase, $M > 0$ meaning that it is energetically more favourable for the impurity to adsorb on the same sublattice as the center of the applied strain. This scenario is swapped as the level of deformation of the graphene host increases; eventually the other sublattice turns to be more favourable permanently where an approximate linear decay of M as a func-

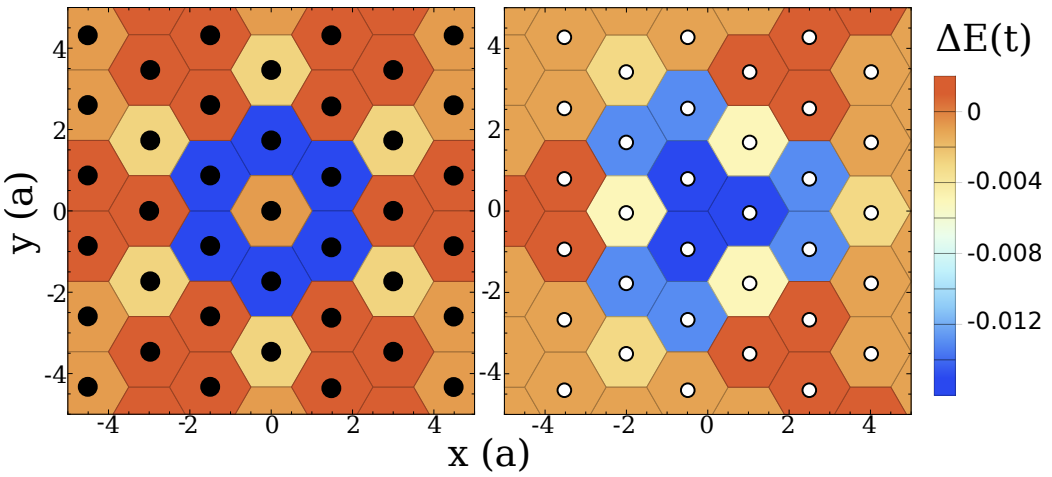

Figure 7.18: Contour plots of the spatial variations in ΔE on the (left panel) black and (right panel) white sublattices for $\alpha = 10\%$ centred at the black sublattice site at the origin. Calculated using the patched tight-binding method. The size of the patched region is 15×15 unit cells.

tion of A can be observed. In fact, the decay ratio of M depends on the strain intensity as depicted in Fig. 7.19. These results confirm that sublattice asymmetry can be achieved via application of Gaussian strain and the most favourable spots for the adsorbants can be tuned with the parameters describing the shape of the bubble.

To demonstrate the amplified asymmetry effect resulting from the deformation, Fig. 7.20 depicts the spatial LDOS obtained within the DFT calculation for the doped graphene supercell with and without the strain deformation. A hydrogen atom is adsorbed over the carbon atom on the black sublattice upon which the Gaussian deformation is centred. Hydrogen top adsorption induces the formation of a sp^3-type hybridization with the carbon atom immediately linked to the hydrogen popping slightly off the graphene base [71], occurring for both deformed and flat graphene platforms. Therefore, the adsorption it-

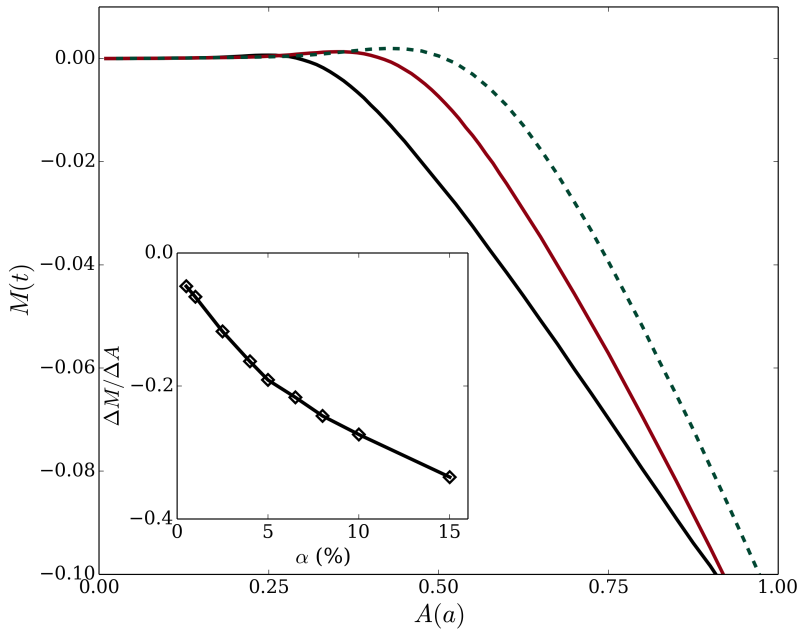

Figure 7.19: M versus A for the same graphene patch (15 $\times$ 15) for distinct values of α. The spreading of the bubble is adjusted in such a way that α is fixed at: (black solid) 2.5%, (red solid) 5%, and (green dash) 10%. Inset diagram: gradient of the linear asymptotic behaviour depicted in the main plot as a function of α. The black line serves as a guide for the eyes.

self already breaks the sublattice symmetry; the LDOS exhibits a characteristic threefold spatial dependency which can be observed in Fig. 7.20. It turns out that the deformation induces a much more well-defined LDOS modulation pattern in the considered energy range of [E_F - 0.5, E_F] eV. The bubble affects the typical threefold symmetry manifested in the spatial LDOS of top adsorbed impurities by intensifying the density of states projected on the atoms of the white sublattice. This shows that the Gaussian deformation can be used to modulate the main fingerprint associated to sublattice asymmetry caused by chemical adsorption. This result also indicates that the out-of-plane distortion establishes a new host environment for subsequent impurities that might ad-

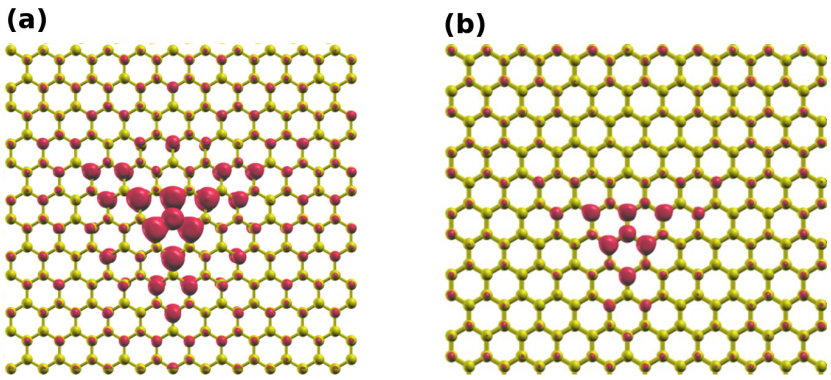

Figure 7.20: Top view of spatial LDOS taken within the energy range [E_F - 0.5 eV, E_F] for a doped graphene sheet (a) with and (b) without the Gaussian deformation. The used isosurface value is 0.0007 e/Å^3. The parameters for the deformation are A = 2.16 Å, and b = 4.5 Å , leading to α = 23 %. The plots were done by using the XCRYSDEN visualization tool [201]. Calculation and plot by Claudia G. Rocha and used with permission.

sorb on the bubble opening up new perspectives for band-gap manipulation in graphene structures.

In this section it has been shown that Gaussian strain can be used to break the sublattice symmetry of pristine graphene. As a result, the sublattices are no longer physically equivalent and one becomes more energetically favourable for adsorption. It was found that the degree of asymmetry and hence the underlying energetic profile of adsorption can be controlled by appropriately changing the strain characteristics. The phenomenon arises from the strain-induced Friedel oscillations in quantities such as the local density of states, in a similar way to that shown with nitrogen in graphene and hydrogen on a CNT shown in the other sections in this chapter. It should be emphasised that the results are again general and only weakly depend on the impurity parametrisation, so should be observable with impurities that also prefer a top adsorbed bonding configuration. Because the transport properties of bipartite

lattices are so sensitive to the spatial distribution of impurities, strain-induced sublattice asymmetry may offer an additional mechanism to engineer the conductivity of graphene.

7.5 Chapter summary

In this chapter the tools developed in the investigation of Friedel oscillations in Chap. 5 were used to describe a possible physical mechanism for the experimentally observed sublattice asymmetry of nitrogen impurities in graphene. Beginning with the case of two single impurities and then two pairs of impurities, it was found that when they are embedded into the system they will find it energetically favourable to occupy the same sublattice forming large-scale domains and this was supported with numerical calculations (Sec. 7.1) and the SPA Green functions method (Sec. 7.1.2). This was then extended to the case of a finite concentration of impurities in Sec. 7.2. A probability distribution was combined with an approximation of the interactions energy in the system, which was expressed as a function of the concentration and the degree of sublattice segregation. For dilute concentrations it was found that the ensemble of impurities will prefer the same sublattice configuration. At higher concentrations this is no longer true, and a critical concentration can be identified where this change from sublattice ordering to random ordering occurs. The exact value of the critical concentration relies on the tight-binding parametrisation of nitrogen that is used but is typically around the same size or larger than experimental concentrations. Estimated values of around 0.8% and 0.1% were obtained using the most common tight-binding parameters for nitrogen. The existence of this critical concentration serves as a convenient

test for the hypothesis that the underlying Friedel oscillations produced by the breaking of the sublattice symmetry are driving the segregation effect, and as a result can be verified experimentally. The benefit of having used this mathematically transparent approach is that it has revealed that this phenomenon should not be unique to nitrogen or graphene. The model was then used to investigate whether sublattice segregation can occur in other systems - metallic CNTs with hydrogen adsorbates in Sec. 7.3 and graphene with Gaussian strain in Sec. 7.4. In both these cases a similar effect was found to exist and that it diminishes with increasing concentration, in the latter case the behaviour can also be controlled externally by the applied strain. As the effect is predicted with Gaussian strain and only a single impurity, this offers the interesting perspective that the sublattice segregation arises from the symmetry breaking of the lattice rather than the act of placing an impurity itself. This is a far more general result and its usefulness should be emphasised, and it underlines the importance of symmetry breaking in determining the electronic properties of nanomaterials, a theme that has been constantly present throughout the thesis. The work done on modelling the three separate scenarios presented in this chapter on nitrogen doped graphene, hydrogen doped CNTs and Gaussian strained graphene was published in the peer-reviewed publications [202], [203] and [204] respectively.

Chapter 8

Summary and future work

This thesis has explored various quantum mechanical phenomena that arise from the introduction of impurities into low dimensional carbon-based nanostructures. A combination of numerical and analytical techniques have been used with the aim to give the maximum amount of mathematical transparency to the work. As a consequence this reveals much about the underlying physical mechanisms at play with these phenomena. Understanding the physics behind doping is important if carbon-based materials are to be used in future technologies, whether the doping is by design or arises naturally during the synthesis of these materials. The work contained in this thesis has shown how this doping can be controlled in some circumstances. This final chapter begins with a section detailing a chapter-by-chapter discussion of the thesis, summarising the main findings. This will be followed by a section discussing possible extensions and future work that could be undertaken using the results of this thesis.

8.1 Summary of thesis

In Chap. 1 carbon-based nanostructures were introduced and an overview given of their usage in current technology. Particular attention was devoted to their use in the field of nanoelectronics. The necessity of being able to induce and control a gap in the electronic spectrum was explained, and one particular method to do this by doping the material with foreign bodies was detailed extensively with an in-depth discussion of current experimental and theoretical work given. Introducing dopants consequentially leads to a change in many of the host systems physical properties, giving rise to several interesting phenomena. The direction of this thesis was motivated by the drive to understand the effect of dopants on carbon-based nanomaterials and an emphasis was put on obtaining mathematically transparent models. This has the benefit of being more revealing of the underlying physical processes at work than purely numerical methods.

Chapter 2 introduced the mathematical methods used throughout the thesis. Beginning with Green functions and their link to electron propagation, several physical quantities of interest were derived e.g. the local density of states, a key concept in condensed matter theory. The Dyson equation was also introduced, which quantifies the change in system Green functions as a result of adding impurities. It was applied specifically to the cases of a substitutional impurity and a variety of adsorbed impurities. The Lloyd formula was then derived which allows changes in global quantities, such as the total system energy, to be expressed purely in terms of the system Green functions and the local perturbation describing the impurity. Finally, recursive methods for obtaining the system Green functions were discussed and their uses in calcu-

lating electronic properties outlined. The work in this chapter was done without reference to any specific physical system and can be used for any material where a suitable tight-binding model can be applied.

Chapter 3 concentrated on deriving the Green functions of graphene and carbon nanotubes, starting with a second nearest-neighbour tight-binding Hamiltonian of the graphene lattice including nearest-neighbour orbital overlap. These Green functions were first expressed as a double integral over the Brillouin zone which makes them computationally expensive to determine. It was shown that this problem can be resolved by using contour integration to solve either one of the integrals. Properties such as the density of states and the electronic dispersion were also derived. Spatial modulations in these quantities result from the introduction of impurities into the system and are directly related to the off-diagonal Green functions. To aid mathematical transparency an approximate analytic closed-form expression was derived for these Green functions using a stationary phase approximation, which also facilitates later discussions. The Green functions of carbon nanotubes are then derived through momentum quantisation of the graphene Green functions. The band gap for various nanotube sizes are then calculated using the first and second nearest-neighbour models and a recursive approach, which are then compared to results from density functional theory found in the literature. The variations of band gap depending on the stoichiometry of boron carbonitride nanotubes is also studied using recursive methods where an oscillation of the band gap is seen as a function of the helical angle of the nanotube.

Chapter 4 focussed on the inverse modelling of impurities using the Lloyd equations derived in Chap. 2. It was argued that the current method to obtain suitable parametrisations of impurities is inefficient and potentially inaccu-

rate. The proposed method is that using numerical results from DFT calculations, such as charge distribution and energy shifts occurring as a result of the presence of the impurity, one can infer the initial parameters that gave rise to these quantities - an inverse problem. This method was applied to the cases of substitutional nitrogen, boron and adsorbed hydrogen. A good match was found in the former cases to values given in the literature which were calculated using a variety of alternative methods. The parametrisation of hydrogen obtained, however, was not similar to those found in the literature. This indicates that the initial assumptions made about screening in the system may need to be reconsidered.

Chapter 5 investigated the phenomenon of Friedel oscillations, spatial modulations in electronic quantities in nanoscale systems as a result of breaking the system symmetry. The work was mainly concerned with oscillations in the density of states and the carrier density in graphene and carbon nanotubes, and how they can be characterised using the system Green functions derived previously in Chap. 3. The stationary phase approximation was used to obtain a closed-form analytic expression for these oscillations for substitutional impurities, vacancies, top and bridge adsorbates in graphene and substitutional impurities in carbon nanotubes. Writing the oscillations in this mathematical manner as opposed to a purely numerical 'black box' calculation uncovers the underlying physics occurring in the system upon doping. For example the phenomenon of commensurability and, in the case of graphene, a quicker decay rate of the oscillations at zero Fermi energy. In the case of vacancies the presence of a midgap resonance and the disappearance of the modulations also at zero Fermi energy. For an adsorbed carbon atom with onsite energy the same as the carbon atoms in the lattice it was shown that when in the top adsorbed configuration it behaves similar to a vacancy. However in the bridge

configuration it behaves like a regular impurity due to cross sublattice interference resulting from the bonding arrangement. It was also demonstrated how inter-impurity interactions arise when two or more impurities are present in these systems and the effect of their relative configuration on the resulting Friedel oscillations investigated.

Chapter 6 focussed on the link between the electronic scattering of impurities and their symmetry breaking properties, with the goal of producing a model by which the suitability of various chemical species for sensing by graphene devices can be determined efficiently. It was shown, both numerically and analytically, that the scattering cross-section of central adsorbed impurities is greatly reduced at energies close to the Dirac point compared to top and bridge adsorbates. The proposed mechanism was the destructive interference of the long-range propagators which arises from the particular symmetry breaking of central adsorbed types. It follows that this scattering invisibility can then be lifted by breaking the underlying bipartite symmetry of the host system. Calculations were done to model the effect of uniaxial strain in such a system and the scattering was enhanced by many orders of magnitude, suggesting graphene with such central adsorbed impurities can function as efficient strain sensors.

Chapter 7 concentrates on the experimentally observed phenomenon of large-scale sublattice segregation of nitrogen impurities in graphene. Using the tools developed in Chap. 5 for Friedel oscillations the case of two substitutional nitrogen impurities is first considered. A closed-form analytic expression that approximates their configuration-dependent interaction energy is derived. It was found that this interaction oscillates spatially in the same way as the carrier density and that at zero Fermi energy the same sublattice configuration

is always energetically preferable. This was then extended to the case of a finite concentration of nitrogen hosted in the graphene lattice. For a dilute concentration it was shown that by considering the pairwise interaction between impurities, as higher order interactions decay faster, the ensemble will lower its energy by being in a sublattice asymmetric distribution. The model has the striking result that there exists a critical concentration between 0.3% - 0.8% where this behaviour changes and a random distribution between the sublattices is predicted to occur. This is testable experimentally and if confirmed would explain similar behaviour seen with other doping scenarios. The hypothesis that the spatial oscillations in the density of states which arise from breaking the system symmetry are responsible for this effect lead to the proposal of two additional scenarios where the effect should be seen and even enhanced. The first was hydrogen adsorbates in carbon nanotubes, where the reduced dimensionality of the system means that the effect should be easier to induce as the inter-impurity interactions decay much slower here. This was done using a Monte Carlo technique and the segregation behaviour was shown to arise in this scenario. The second scenario was a graphene sheet with Gaussian strain applied. It was shown that strain applied which biases one sublattice over the other results in the opposite sublattice becoming more favourable for adsorption, and that the energetic favourability can be further modified by changing the characteristics of the strain. The robustness of the sublattice asymmetry effect through a range of scenarios should be emphasised, and it is hoped that by understanding the mechanisms behind the effect that this could pave the way for novel nanoelectronic devices that exploit it.

8.2 Possible extensions and future work

The work done in this thesis has many possible extensions, both general and more specific, and these will be outlined and discussed in this final section.

From a general standpoint, it was shown that many of the phenomena investigated in this work originate from the breaking of specific symmetries of the host system due to some external perturbative action, for example through doping or strain. While graphene and carbon nanotubes were the main focus of these investigations, the general formalism is readily applicable to other systems where a suitable tight-binding representation can be found. For example, the Green functions methods that formed the bulk of Chapter 2, upon which the models of impurity behaviour in carbon nanostructures were developed, were first introduced without reference to a specific system. Consequentially the Green function-related electronic phenomena such as Friedel oscillations, scattering and sublattice segregation could be studied in these other systems. It should be noted that although the benefit of a mathematically transparent formalism has been emphasised throughout this work, it is not required, and only a suitable Hamiltonian would be needed for these investigations. The Hamiltonian could be parametrised through band structure matching with DFT [118–124]. The generality of these methods is particularly useful with regards to the increasing number of low-dimensional materials being synthesised such as hexagonal boron nitride [24] and transition metal dichalcogenides [205]. While DFT calculations involving impurities in such systems are usually limited to a small handful of configurations, tight-binding would present a viable option to study the alterations to the atomic structure. For example, the recursive method (Sec. 2.5), inverse modelling (Chap. 4) and

the Lloyd equations (Sec. 2.4) would be particularly useful in these situations and could reveal a lot about the electronics in these systems.

Departing from this general viewpoint, much more specific extensions to the work will now be identified. Three main areas will be focussed on and discussed in their own subsections - impurity scattering, inverse modelling and sublattice segregation.

8.2.1 Impurity scattering and Friedel oscillations

Chapter 5 and Chapter 6 sought to find analytic approaches to understanding the related effects of Friedel oscillations and impurity scattering caused by dopants in graphene and carbon nanotubes. The impurity configurations considered were fairly simple and straightforward, so the natural next step to make would be using these methods to look at more intricate doping scenarios. For instance, there are many interesting arrangements involving vacancies described in the literature that have been observed experimentally including: neighbouring vacancy pairs (divacancies); pentagon/heptagon rings caused by rebonding; Stone-Wales defects; and divacancy-caused patterns such as triple pentagon-triple heptagon (555-777) and pentagon-octagon-pentagon (5-8-5) rings [206–211]. The electronic behaviour in these systems could be studied relatively easily using the quick and lightweight approach shown in this thesis, perhaps utilising the second nearest neighbour model with wavefunction overlap which are well suited to handling extended defects and grain boundaries (Chap. 3). Grain boundaries are commonly found in experiments, and so these methods could be used to examine how Friedel oscillations propagate through them. In a similar vein this investigation could be used to in-

vestigate phenomena near the edge of semi-infinite graphene sheets, and the question of how edge geometry affects Friedel-related effects could be investigated as has been done for the RKKY coupling [212].

The main finding of Chapter 6 was the 'invisibility' of central adsorbed impurities to propagating electrons in the host material, a phenomenon which arises from destructive interference of the long-range propagators leading directly to a suppression of the scattering. It would be quite interesting to see if this suppression could be produced with other impurity types or arrangements, whether a particular local configuration of a handful of dopants or a superlattice arrangement of them. The simplest progression would be to examine central adsorbed dopants with a different orbital configuration from the s and d_{z^2} orbital model that was used in Chapter 6, such as f, d_{xy} and $d_{x^2-y^2}$ orbitals. In these cases the τ hoppings between the adsorbate and the carbon host sites are no longer the same for each bond, but still respect particular symmetries. It would be interesting to see if the impurity invisibility still holds in such situations, although a pen and paper approach may be fairly challenging to work with. Regarding more complicated doping arrangements, preliminary calculations have been done but were not included in the thesis where the scattering produced with hexagonal rings of substitutional atoms was examined. The results of the calculations were that, surprisingly, the scattering is not suppressed in this case. This means that the source of the suppression in the central adsorbed case comes from the off-diagonal terms in the perturbation matrix $\hat{V}$ rather than the perturbation of the host sites alone as in the substitutional ring case. With the ring of impurities the cross-sublattice terms act in such a way that the scattering is not suppressed. Additional calculations were also done involving a pair of neighbouring substitutional impurities with opposite λ values where naively one would expect this to lead to a cancellation of the Friedel

oscillations, but this was not found. Instead the perturbations were finite and behaved qualitatively similar to the single impurity case with a similar magnitude and decay rate and exhibiting the commensurability effect at $E_F = 0$. The reason for this can be found in the study of bridge adsorbed impurities in Chapter 5 -recall that it was found that cross-sublattice terms lead to the propagators determining the Friedel oscillations do not destructively interfere. These preliminary findings suggest that the importance of the cross-sublattice effect is more robust than initially presumed, however a more thorough investigation of all the discussions in this paragraph should be conducted and confirmed.

Beyond other impurity configurations, the incorporation of strain effects could also be considered. The strain-dependent Green functions introduced in Chapter 6 could be applied to examining Friedel oscillations in uniaxially strained graphene, as has been done with the SPA approach to the RKKY [155] and the behaviour of Friedel oscillations in such a system has been studied theoretically only very recently [42]. This could lead to interesting results with regards to the commensurability effect, which arises purely from the oscillation period coinciding with the lattice spacing - clearly in a strained system one would expect they would not be equivalent. Furthermore the RKKY studies found a change in decay behaviour and sublattice asymmetry of the RKKY, due to the merging of the two inequivalent Dirac points in the Brillouin Zone caused by inducing strain. Specifically the coupling between two magnetic central adsorbed impurities changed from a decay rate of D^{-3} in the unstrained case to a much quicker D^{-7} when uniaxial strain is applied. Due to the similarity between the RKKY and Friedel oscillations it is reasonable to expect a similar behaviour may be found for the latter [48, 213]. Indeed, current research suggests an innate link between magnetic effects and sublattice symmetry, and

this will be discussed further in Sec. 8.2.3.

8.2.2 Inverse modelling

Inverse modelling was applied in Chapter 4 to finding a suitable set of tight-binding parameters for substitutional nitrogen and boron and top adsorbed hydrogen in a graphene host system. Despite the apparent success of the method in modelling the substitutional impurities the results for hydrogen were far from satisfactory, with the bonding integral being vastly underestimated compared to results found in the literature. The source of the problem is thought to be that screening is quite poor in graphene because of its dimensionality, which necessitates the relaxation of the efficient screening hypothesis discussed in Chapter 4. It is therefore paramount that any future work involving inverse modelling in graphene seeks to resolve this issue, perhaps by extending the perturbation matrix $\hat{V}$ to account for onsite energy changes of the adatom and host site at minimum. If this problem can be overcome the question of other impurity types can then be considered. As shown in Chapter 4 an adequate parametrisation of nitrogen and boron can be obtained using only a single onsite term due to their simple bonding structure and similar atomic size to carbon. It is reasonable to expect that other substitutional impurities would require a more intricate inverse modelling procedure such as inclusion of the modification of bonds and additional energy levels [214]. Magnetic impurities would also be interesting to study, for instance it is known that hydrogen has a magnetic moment and that many transition metals (e.g. Mn, Fe and Co) are magnetic and are centre adsorbed [215]. This would require extending the current model via the Hubbard Hamiltonian and the Hartree-Fock approximation in order to incorporate magnetic effects [48]. The situation of

a pair of hydrogen adsorbates which are adsorbed on different sides of the graphene sheet to each other could also be examined, and would require calculation of two different hopping parameters τ_1 and τ_2. It has been shown that such an arrangement exhibits interesting effects, such as being non-magnetic, and a deeper understanding of this would be useful for discussions of hydrogen storage in graphene and other carbon-based nanomaterials [130]. Besides other impurity types, the inverse modelling procedure could be extended to investigate doping in other materials, given that a sound tight-binding description exists for the host material. Such an extension would be quite useful given the increasing number of nanomaterials being developed - the procedure shown in this chapter could make the study of the impact of dopants on the electronic structure of these systems faster and simpler. On a final note it should be pointed out that the inverse modelling has been used in the past for studying adsorbate distributions on carbon nanotubes with a view to using them as gas sensors [71, 216], something which would also be possible with graphene given the findings of this thesis.

8.2.3 Sublattice segregation

Perhaps the main result of this thesis was the proposed mechanism for the experimentally observed sublattice segregation of nitrogen impurities in graphene. It was found that any change to the graphene lattice (or indeed other bipartite lattice structures) in a sublattice asymmetric manner will induce a different electronic response on each sublattice. Recent theoretical research has predicted that edged graphene will also modulate this effect [217]. It remains to be seen whether the impurity segregation is indeed coming from symmetry breaking interactions alone, which is experimentally testable by the existence

of the critical concentration. The model also predicts that segregation effect can be seen with other dopants and/or other systems and while currently there is only limited experimental research to support this, it is hoped that by disseminating this work that more research can be stimulated in this direction. Beyond the benefit of understanding the sublattice asymmetry mechanism for potential electronics applications, if the effect can be understood and controlled the question of whether it is experimentally feasible to induce a ferromagnetic state in either doped CNTs [179, 218, 219] and graphene [220–223], which arises from sublattice segregation of defects, can also be re-examined. Indeed, there is very promising recent experimental evidence that magnetic hydrogen adsorbates will exhibit long-range ferromagnetic ordering when placed on the same sublattice [224, 225], however the level of atomic manipulation required presents a challenge to realising this on a larger scale than a handful of adsorbates. It should be noted that the authors propose this to be a direct interaction, caused by overlap of the magnetised impurity states, rather than an indirect RKKY-like interaction, however at longer range such an effect should still be visible via the substrate-mediated RKKY interaction.

The robustness of the segregation mechanism could also be examined with respect to uniaxial strain. Using the reasoning from Sec. 8.2.1, strain would remove the commensurability between the lattice spacing and the energetic coupling leading to much more complicated behaviour. This would make a pen and paper approach much more challenging but numerical calculations following the work in Chapter 7 using the strain-dependent Green functions should be sufficient to reveal how robust the effect is to strain. While this may not be very useful from an applications standpoint the source of the segregation lies in this commensurability. Hence a greater understanding of this proposed mechanism and how it responds to strain would be needed for com-

pleteness.

This concludes the discussions of the possible extensions to the work in this thesis. While the simplicity and elegance with which graphene's electronic properties can be expressed, either through 'pen and paper' or relatively lightweight numerical computations, is quite unique, it is clear that the general approach of much of the investigations in the preceding chapters is applicable to other materials. It is therefore hoped that this work will aid future research in low-dimensional nanomaterials and the tailoring of their electronics properties, perhaps serving as a blueprint to direct investigations of the electronic properties of such novel materials.

Appendix A

Change of variable for computation of integrals

A.1 Onsite occupation variations

In Chap. 2 the expression

$$n_i = -\frac{2}{\pi} \operatorname{Im} \int_{-\infty}^{E_F} dE \Delta G_{ii}(E + i\eta) \tag{A.1}$$

for the change in occupation on site i was derived. Performing the numerical integration in order to calculate n_i requires an integration along the real energy axis, however this can present a number of problems. Many integration algorithms use Simpson's rule or similar quadrature routines to evaluate integrals. Problems arise when evaluating the integrals in regions around large diver-

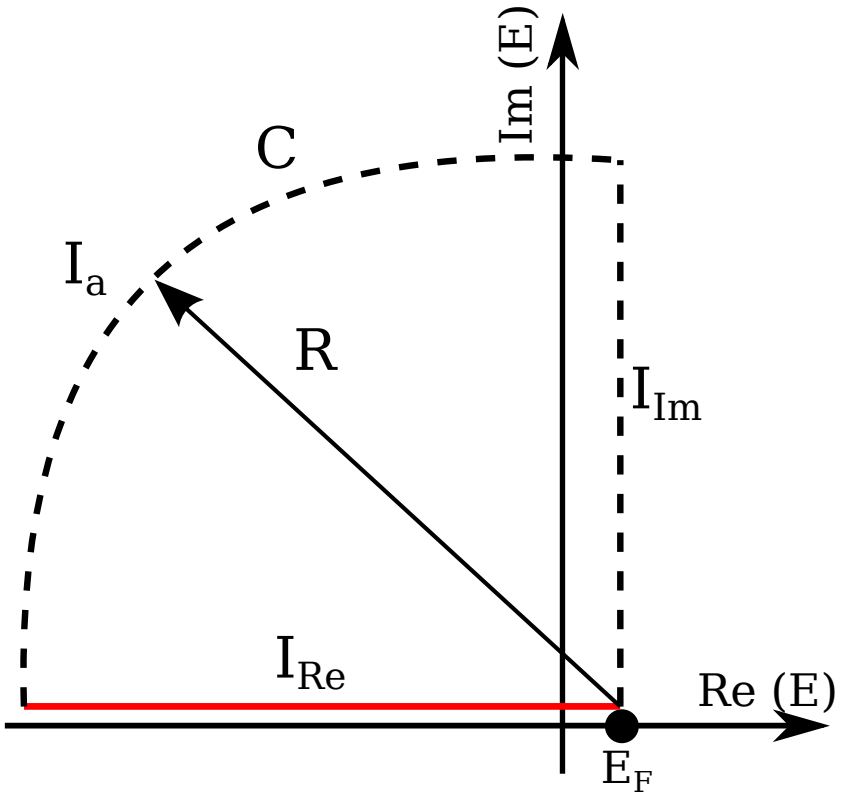

Figure A.1: Numerical calculation of integrals such as n are more easily solved by contour methods in the complex energy plane. The red line indicates the integral I_{Re} in the expression for n_i shown in Eq. A.1. The dashed lines indicate two other integrals I_{Im} and I_a explained in the text which along with I_{Re} form a closed counter-clockwise contour C. The contour encloses no singularities and has an arc of radius $R \to \infty$.

gences. These divergences are common in functions such as G_{ii} which can result from the presence of bound states and resonances in the system spectrum, this makes the calculation of integrals involving these quantities difficult. In the case of n and similar quantities encountered in this thesis, this issue can be resolved by performing the integration over the imaginary energy axis by transforming the integral via Cauchy's theorem. Away from the real axis these integrands generally behave much smoother and without discontinuities.

Consider again the expression for n_i and recall that the retarded Green functions $G_{ii}(z)$ are by their definition analytic in the upper-half of the complex energy plane defined by $y > 0$ if $z = E + iy$. The current integral for n_i in Eq. A.1 lies a small distance $i\eta$ from the real-axis and is indicated by the red line in Fig. A.1 and labelled I_{Re}. A contour C can be formed in the complex energy plane as shown in the same figure and consists of three parts - a line following the initial integral along the real axis (designated I_{Re}), a perpendicular line originating at $E_F + i\eta$ and extending along the imaginary axis up to iR (denoted I_{Im}), and an arc with radius $R \to \infty$ connecting the previous two parts I_a. As G_{ii} defines the quantity n_i and it is analytic within the contour, it follows from Cauchy's theorem that $I_{Re} = -I_a - I_{Im}$. The integral I_a along the arc can be solved by switching the Green function to polar coordinates. Following from the definition $\hat{G} = (E\hat{I} - \hat{H})^{-1}$ clearly $G_{ii}(z) \sim \frac{1}{z}$ so the integrand vanishes along the arc, however the integral itself does not vanish. I_a can be expressed in polar coordinates by the transformation $z = Re^{i\theta}$ as

$$I_a = \int_{\pi/2}^{\pi} (iRe^{i\theta} d\theta) \frac{1}{Re^{i\theta}}$$

which simplifies to

$$I_a = \int_{\pi/2}^{\pi} d\theta i = \frac{i\pi}{2}.$$

If the integrand was a product of two or more Green functions it is clear that I_a would in fact vanish as the integrand would go as $\sim \frac{1}{R^2}$ or faster. The integral I_{Im} is an integral over the imaginary axis

$$I_{Im} = i \int_{\eta}^{\infty} G_{ii}(E_F + iy) dy$$

which behaves much smoother over the integration range than I_{Re}. Through

substituting both the expressions for I_a and I_{Im} into $I_{Re} = -I_a - I_{Im}$ it can be written

$$n_i = -\frac{2}{\pi}\,\mathrm{Im}\Big(-i\int_\eta^\infty G_{ii}(E_F + iy)dy - \frac{i\pi}{2}\Big)$$

or more simply

$$n_i = 1 + \frac{2}{\pi}\,\mathrm{Re}\int_\eta^\infty G_{ii}(E_F + iy)dy.$$

The numerical calculation of this quantity is better than the initial expression for n_i in Eq. A.1 as the integral behaves much smoother and hence is easier to calculate using numerical methods. It is usually necessary to perform an additional change of variables in order to change the integration limits to a finite range to aid computation. The simplest way to do so for integrals of the form of n_i is making the substitution

$$y = \frac{1 + \eta - t}{t}$$

which changes the integration limits $\int_\eta^\infty \rightarrow \int_1^0$ and $dy = -\frac{(1+\eta)}{t^2}$. The initial expression for n_i in Eq. A.1 can then be recast as

$$\begin{aligned} n_i &= 1 - \frac{2}{\pi}\,\mathrm{Re}\int_1^0 \frac{1+\eta}{t^2} dt G_{ii} \\ &= 1 + \frac{2}{\pi}\,\mathrm{Re}\int_0^1 \frac{1+\eta}{t^2} dt G_{ii}, \end{aligned}$$

a form which is much easier to calculate numerically.

A.2 Energy variations

Section 2.4.3 describes the derivation of ΔE, the change in global system energy when a system is perturbed by the introduction of one or more impurities. In both cases of substitutional and adsorbed impurities shown in Eq. 2.17 and Eq. 2.18 respectively there is an integral of the form

$$\Delta E = \frac{2}{\pi} \operatorname{Im} \int_{-\infty}^{E_F} dE \ln \det\left\{\hat{I} - \hat{g}\hat{V}\right\}$$

that must be calculated. Similar to the case of Δn the integral is irregular over the real axis and so to aid numerical calculation it is prudent to transform to the imaginary axis where the integrand is generally much smoother. Again use the fact that retarded GFs are analytic in the upper half plane will be used. The methods of contour integration can be applied, forming a contour similar to that for n shown in Fig. A.1. As this contour encloses no singularities, through Cauchy's theorem it is known that $I_{Re} = -I_{Im} - I_a$.

Consider the integral I_a over the arc. In the limit of $z \to \infty$ the function $\hat{g}(z) \sim \frac{1}{z}$, so $\ln\left(\hat{I} - \hat{g}(z)\hat{V}\right) \sim \ln\left(\hat{I} - \frac{1}{z}\hat{V}\right)$. For large z this logarithmic function is $\frac{1}{z}\hat{V}$ to first order. Using this with the identity $\operatorname{Tr} \ln \hat{X} \equiv \ln \det \hat{X}$ it can be written

$$\begin{aligned} I_a &= \int_{\pi/2}^{\pi} d\theta \operatorname{Tr} iRe^{i\theta}(-\frac{\hat{V}}{R}e^{-i\theta}) \\ &= \int_{\pi/2}^{\pi} d\theta \operatorname{Tr}\left(-i\hat{V}\right) = \frac{-i\pi}{2} \operatorname{Tr} \hat{V}. \end{aligned}$$

The second integral, I_{Im}, running parallel to the imaginary axis is

$$I_{Im} = i\int_{\eta}^{\infty} dx \ln\det\Big(\hat{I} - \hat{g}(E_F + ix)\hat{V}\Big).$$

As with the case of Δn this generally has a very smooth integrand over the integration range and by utilising a change of variable $x = \frac{1+\eta-s}{s}$ and $dx = -\frac{1+\eta}{s^2}ds$ this becomes

$$I_{Im} = i\int_{0}^{1} \frac{1+\eta}{s^2} ds \ln\det\Big(\hat{I} - \hat{g}(E_F + i\frac{1+\eta-s}{s})\hat{V}\Big).$$

Recall that $\Delta E = \frac{2}{\pi}\operatorname{Im} I_r = \frac{2}{\pi}\operatorname{Im}(-I_c - I_i)$ which yields the solution

$$\Delta E = \operatorname{Tr}\hat{V} - \frac{2}{\pi}\operatorname{Re}\int_{0}^{1} \frac{1+\eta}{s^2} ds \ln\det\Big(\hat{I} - \hat{g}(E_F + i\frac{1+\eta-s}{s})\hat{V}\Big).$$

Diagonal elements of $\hat{V}$ contributing to the trace are non-zero only in the case of substitutional impurities, which change the onsite energy of atomic sites in the system. In the case of adsorbates $\hat{V}$ contains only off-diagonal terms and thus $\operatorname{Tr}\hat{V}$ is zero in these cases.

Appendix B

Low energy approximations in the nearest-neighbour regime

B.1 Dispersion relation

It was shown in Chap. 3 that the dispersion relation for graphene using a nearest-neighbour tight-binding Hamiltonian is

$$\epsilon_{\pm}(k_A, k_Z) = t\sqrt{1 + 4\cos k_A \cos k_Z + 4\cos^2 k_Z}$$

which for low energies is linear and is confined around the Dirac points, as can be seen from Fig. 3.2. To show this the above equation can be expanded around one of the Dirac points. The one at $\mathbf{K} = (0, \frac{2\pi}{3})$ can be freely chosen without loss of generality. Re-casting $\epsilon_{\pm}$ to be in the region close to $\mathbf{K}$ defined

as $\mathbf{K}+\delta\mathbf{k}$, and then using the Taylor expansion $\cos\left(\frac{2\pi}{3}+|\delta\mathbf{k}|\,e^{i\theta}\right)$ where θ is the angle from the k_A axis, gives the result

$$\epsilon_{\pm}(|\delta\mathbf{k}|) \approx \sqrt{3}at\,|\delta\mathbf{k}|\,.$$

It is well known that this linear dispersion relation has the consequence that at low energies the electrons behave as massless relativistic particles with a speed of light given by the Fermi velocity $v_F \sim c/300$ [106], according to $\epsilon_{\pm} = \frac{\pm\hbar v_F|\delta\mathbf{k}|}{2\pi}$. Because of this the low energy behaviour of these electrons will behave differently to those in materials with a parabolic dispersion relation, such as common metals.

B.2 Pristine Green functions of graphene

The following is adapted from Katsnelson's method [226]. It will be shown that the onsite Green function for pristine graphene can be approximated at low energies where $E \ll t$ as

$$g_{ii} = \frac{2}{\sqrt{3}\pi t^2} E \ln\frac{|E|}{3t} - i\frac{|E|}{\sqrt{3}t^2}.$$

The density of states can be expressed via the dispersion relation as

$$\rho(E) = \frac{2}{\pi}\frac{q(E)}{|dE/dq|}.$$

Recall the expression for local density of states and its link to the system Green

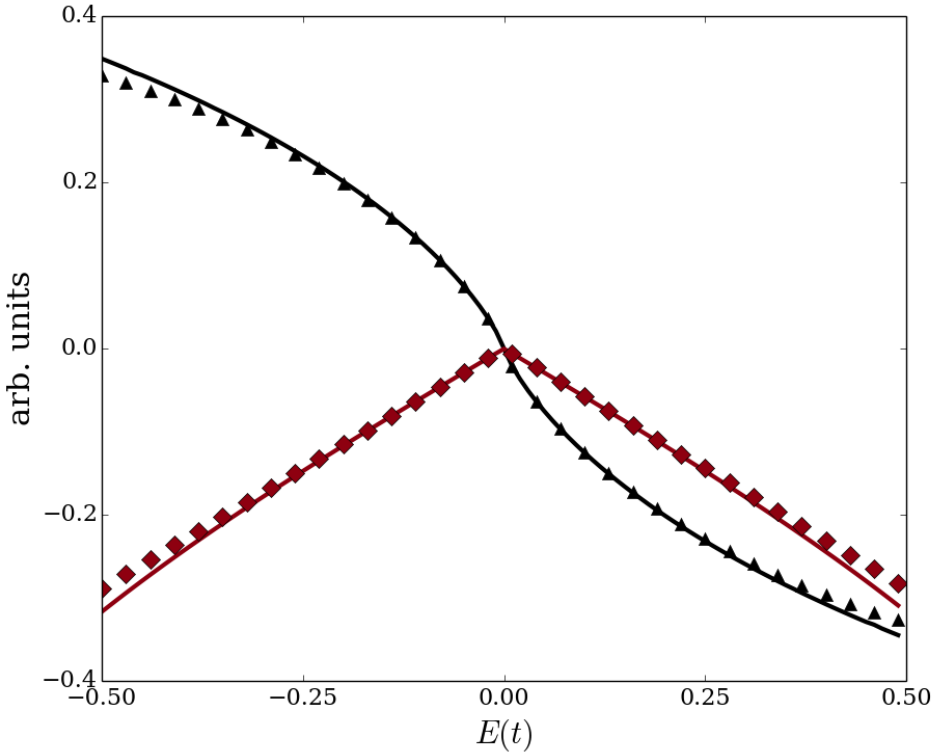

Figure B.1: Comparison of the exact and approximate forms of g_{00} derived in the text, respectively indicated by the black solid and green dashed lines for the real part and the red solid and blue dashed lines for the imaginary part.

function from Eq. 2.8, $\rho(E) = -\frac{1}{\pi}\operatorname{Im} G_{00}$, and the expression for the linear dispersion relation derived in the previous section, $E = \sqrt{3}atq$. Substituting into the above gives the result

$$\operatorname{Im} g_{00}(E \ll t) = -\frac{|E|}{\sqrt{3}t^2}$$

The Kramers-Krönig relations relate the real and complex parts of any function

analytic on the upper-half plane, through which the real part of g_{00} at low energies can be shown to be equal to

$$\mathrm{Re}\, g_{00}(E \ll t) = \frac{2E}{\sqrt{3}\pi t^2} \ln \frac{|E|}{3t}$$

Where $D = 6t$ is a constant determined by the width of the electronic spectrum. The above approximation is good at low energies up to approximately $\pm\frac{|t|}{2}$, which is around the maximum available doping currently possible [227]. A graph comparing the approximate and exact forms of g_{00} is shown in Fig. B.1. It should be noted that several other methods to do this, e.g. using a momentum cut-off and assuming only the region of the momentum space integrals immediately around the K and K' points of the dispersion contribute to the Green function, are available in the literature [228, 229].

Bibliography

[1] C. M. Burns. "Deep Space Homer". *The Simpsons* (1994).

[2] E. Anders and M. Ebihara. "Solar-system abundances of the elements". *Geochimica et Cosmochimica Acta* 46.11 (1982), pp. 2363–2380.

[3] J. Rehder. *Mastery and uses of fire in antiquity*. McGill-Queen's Press-MQUP, 2000.

[4] Pliny the Elder. *Natural History*. McGill-Queen's Press-MQUP, 77.

[5] S. Curtis. "Quarter of the world will be using smartphones in 2016." *The Daily Telegraph* (2014).

[6] D. R. Cumming, S. B. Furber, and D. J. Paul. "Beyond Moore's law". *Philosophical transactions. Series A, Mathematical, physical, and engineering sciences* 372.2012 (2014).

[7] H. J. Caulfield and S. Dolev. "Why future supercomputing requires optics". *Nature Photonics* 4.5 (2010), pp. 261–263.

[8] A. K. Geim and K. S. Novoselov. "The rise of graphene". *Nature materials* 6.3 (2007), pp. 183–191.

[9] G. Binnig, H. Rohrer, C. Gerber, and E. Weibel. "Surface studies by scanning tunneling microscopy". *Physical review letters* 49.1 (1982), p. 57.

[10] H. W. Kroto, J. R. Heath, S. C. O'Brien, R. F. Curl, and R. E. Smalley. "C 60: buckminsterfullerene". *Nature* 318.6042 (1985), pp. 162–163.

[11] S. Iijima. "Helical microtubules of graphitic carbon". *Nature* 354.6348 (1991), pp. 56–58.

[12] M.-F. Yu, O. Lourie, M. J. Dyer, K. Moloni, T. F. Kelly, and R. S. Ruoff. "Strength and breaking mechanism of multiwalled carbon nanotubes under tensile load". *Science* 287.5453 (2000), pp. 637–640.

[13] S. Hong and S. Myung. "Nanotube Electronics: A flexible approach to mobility". *Nature Nanotechnology* 2.4 (2007), pp. 207–208.

[14] C. Liu, Y. Fan, M. Liu, H. Cong, H. Cheng, and M. S. Dresselhaus. "Hydrogen storage in single-walled carbon nanotubes at room temperature". *Science* 286.5442 (1999), pp. 1127–1129.

[15] R. Ströbel, J. Garche, P. Moseley, L. Jörissen, and G. Wolf. "Hydrogen storage by carbon materials". *Journal of Power Sources* 159.2 (2006), pp. 781–801. ISSN: 0378-7753.

[16] Y. Yurum, A. Taralp, and T. N. Veziroglu. "Storage of hydrogen in nanostructured carbon materials". *International journal of hydrogen energy* 34.9 (2009), pp. 3784–3798.

[17] M. F. De Volder, S. H. Tawfick, R. H. Baughman, and A. J. Hart. "Carbon nanotubes: present and future commercial applications". *Science* 339.6119 (2013), pp. 535–539.

[18] Q. Zhang, J.-Q. Huang, W.-Z. Qian, Y.-Y. Zhang, and F. Wei. "The Road for Nanomaterials Industry: A Review of Carbon Nanotube Production, Post-Treatment, and Bulk Applications for Composites and Energy Storage". *Small* 9.8 (2013), pp. 1237–1265. ISSN: 1613-6829.

[19] Q. Cao and S.-j. Han. "Single-walled carbon nanotubes for high-performance electronics". *Nanoscale* 5.19 (2013), pp. 8852–8863.

[20] A. D. Franklin. "Electronics: The road to carbon nanotube transistors". *Nature* 498.7455 (2013), pp. 443–444.

[21] M. M. Shulaker, G. Hills, N. Patil, H. Wei, H.-Y. Chen, H.-S. P. Wong, and S. Mitra. "Carbon nanotube computer". *Nature* 501.7468 (2013), pp. 526–530.

[22] R. Peierls. "Bemerkungen über umwandlungstemperaturen". *Helv. Phys. Acta* 7 (1934), pp. 81–83.

[23] L. Landau and E. Lifshitz. "Statistical physics, vol. 5". *Course of theoretical physics* 30 (1980).

[24] C. Oshima and A. Nagashima. "Ultra-thin epitaxial films of graphite and hexagonal boron nitride on solid surfaces". *Journal of Physics: Condensed Matter* 9.1 (1997), p. 1.

[25] K. Novoselov, D. Jiang, F. Schedin, T. Booth, V. Khotkevich, S. Morozov, and A. Geim. "Two-dimensional atomic crystals". *Proceedings of the National Academy of Sciences of the United States of America* 102.30 (2005), pp. 10451–10453.

[26] B. Lalmi, H. Oughaddou, H. Enriquez, A. Kara, S. Vizzini, B. Ealet, and B. Aufray. "Epitaxial growth of a silicene sheet". *Applied Physics Letters* 97.22 (2010), p. 223109.

[27] K. F. Mak, C. Lee, J. Hone, J. Shan, and T. F. Heinz. "Atomically thin MoS 2: a new direct-gap semiconductor". *Physical Review Letters* 105.13 (2010), p. 136805.

[28] I. Meric, M. Y. Han, A. F. Young, B. Ozyilmaz, P. Kim, and K. L. Shepard. "Current saturation in zero-bandgap, top-gated graphene field-effect transistors". *Nature nanotechnology* 3.11 (2008), pp. 654–659.

[29] A. A. Balandin, S. Ghosh, W. Bao, I. Calizo, D. Teweldebrhan, F. Miao, and C. N. Lau. "Superior thermal conductivity of single-layer graphene". *Nano letters* 8.3 (2008), pp. 902–907.

[30] G.-H. Lee, R. C. Cooper, S. J. An, S. Lee, A. van der Zande, N. Petrone, A. G. Hammerberg, C. Lee, B. Crawford, W. Oliver, J. W. Kysar, and J. Hone. "High-strength chemical-vapor–deposited graphene and grain boundaries". *Science* 340.6136 (2013), pp. 1073–1076.

[31] J.-H. Chen, C. Jang, S. Xiao, M. Ishigami, and M. S. Fuhrer. "Intrinsic and extrinsic performance limits of graphene devices on SiO2". *Nature nanotechnology* 3.4 (2008), pp. 206–209.

[32] K. S. Novoselov, V. Fal, L. Colombo, P. Gellert, M. Schwab, and K. Kim. "A roadmap for graphene". *Nature* 490.7419 (2012), pp. 192–200.

[33] J. Oostinga, H. Heersche, X. Liu, A. Morpurgo, and L. Vandersypen. "Gate-induced insulating state in bilayer graphene devices". *Nature Materials* 7 (2007), p. 151.

[34] M. Jang, H. Kim, Y.-W. Son, H. Atwater, and W. Goddard. "Graphene field effect transistor without an energy gap". *Proc. Natl. Acad. Sci. USA* 110 (2013), p. 8786.

[35] S. Lee, D. Duong, Q. Vu, Y. Jin, P. Kim, and Y. Lee. "Chemically modulated band gap in bilayer graphene memory transistors with high on/off ratio". *ACS Nano* 9 (2015), p. 9034.

[36] S. Berrada, V. Nguyen, D. Querlioz, J. Saint-Martin, A. Alarcon, C. Chassat, A. Bournel, and P. Dollfus. "Graphene nanomesh transistor with high on/off ratio and good saturation behavior". *Applied Physics Letters* 103 (2013), p. 183509.

[37] N. Khotkevych-Sanina, Y. A. Kolesnichenko, and J. van Ruitenbeek. "Fermi surface contours obtained from scanning tunneling microscope images around surface point defects". *New Journal of Physics* 15.12 (2013), p. 123013.

[38] J. Friedel. "Electronic structure of primary solid solutions in metals". *Advances in Physics* 3.12 (1954), pp. 446–507.

[39] Á. Bácsi and A. Virosztek. "Local density of states and Friedel oscillations in graphene". *Physical Review B* 82.19 (2010), p. 193405.

[40] A. Virosztek and Á. Bácsi. "Friedel Oscillations Around a Short Range Scatterer: The Case of Graphene". *Journal of superconductivity and novel magnetism* 25.3 (2012), pp. 691–697.

[41] V. V. Cheianov and V. I. Fal'ko. "Friedel oscillations, impurity scattering, and temperature dependence of resistivity in graphene". *Physical review letters* 97.22 (2006), p. 226801.

[42] C. Dutreix, L. Bilteanu, A. Jagannathan, and C. Bena. "Friedel oscillations at the Dirac cone merging point in anisotropic graphene and graphenelike materials". *Physical Review B* 87.24 (2013), p. 245413.

[43] Y. Tao and G. Bergmann. "Friedel oscillation about a Friedel-Anderson impurity". *The European Physical Journal B* 85.1 (2012), pp. 1–9.

[44] D. Khveshchenko. "Effects of long-range correlated disorder on Dirac fermions in graphene". *Physical Review B* 75.24 (2007), p. 241406.

[45] G. Gómez-Santos and T. Stauber. "Measurable lattice effects on the charge and magnetic response in graphene". *Physical review letters* 106.4 (2011), p. 045504.

[46] V. V. Cheianov. "Impurity scattering, Friedel oscillations and RKKY interaction in graphene". *The European Physical Journal Special Topics* 148.1 (2007), pp. 55–61.

[47] S. Power and M. Ferreira. "Electronic structure of graphene beyond the linear dispersion regime". *Physical Review B* 83.15 (2011), p. 155432.

[48] S. R. Power and M. S. Ferreira. "Indirect exchange and Ruderman–Kittel–Kasuya–Yosida (RKKY) interactions in magnetically-doped graphene". *Crystals* 3.1 (2013), pp. 49–78.

[49] F. Schwierz. "Graphene transistors". *Nature nanotechnology* 5.7 (2010), pp. 487–496.

[50] P. Avouris. "Graphene: electronic and photonic properties and devices". *Nano letters* 10.11 (2010), pp. 4285–4294.

[51] K. Kim, J.-Y. Choi, T. Kim, S.-H. Cho, and H.-J. Chung. "A role for graphene in silicon-based semiconductor devices". *Nature* 479.7373 (2011), pp. 338–344.

[52] X. Li, X. Wang, L. Zhang, S. Lee, and H. Dai. "Chemically derived, ultrasmooth graphene nanoribbon semiconductors". *Science* 319.5867 (2008), pp. 1229–1232.

[53] Y.-M. Lin, K. A. Jenkins, A. Valdes-Garcia, J. P. Small, D. B. Farmer, and P. Avouris. "Operation of graphene transistors at gigahertz frequencies". *Nano letters* 9.1 (2008), pp. 422–426.

[54] Y. Zhang, T.-T. Tang, C. Girit, Z. Hao, M. C. Martin, A. Zettl, M. F. Crommie, Y. R. Shen, and F. Wang. "Direct observation of a widely tunable bandgap in bilayer graphene". *Nature* 459.7248 (2009), pp. 820–823.

[55] I. Naumov and A. Bratkovsky. "Gap opening in graphene by simple periodic inhomogeneous strain". *Physical Review B* 84.24 (2011), p. 245444.

[56] K. Novoselov. "Graphene: Mind the gap". *Nature materials* 6.10 (2007), pp. 720–721.

[57] S. Zhou, G.-H. Gweon, A. Fedorov, P. First, W. De Heer, D.-H. Lee, F. Guinea, A. C. Neto, and A. Lanzara. "Substrate-induced bandgap opening in epitaxial graphene". *Nature materials* 6.10 (2007), pp. 770–775.

[58] C.-K. Chang, S. Kataria, C.-C. Kuo, A. Ganguly, B.-Y. Wang, J.-Y. Hwang, K.-J. Huang, W.-H. Yang, S.-B. Wang, and C.-H. Chuang. "Band gap engineering of chemical vapor deposited graphene by in situ BN doping". *ACS nano* 7.2 (2013), pp. 1333–1341.

[59] D. Usachov, O. Vilkov, A. Gruneis, D. Haberer, A. Fedorov, V. Adamchuk, A. Preobrajenski, P. Dudin, A. Barinov, and M. Oehzelt. "Nitrogen-doped graphene: efficient growth, structure, and electronic properties". *Nano letters* 11.12 (2011), pp. 5401–5407.

[60] L. Zhao, R. He, K. T. Rim, T. Schiros, K. S. Kim, H. Zhou, C. Gutierrez, S. Chockalingam, C. J. Arguello, and L. Palova. "Visualizing individual nitrogen dopants in monolayer graphene". *Science* 333.6045 (2011), pp. 999–1003.

[61] R. Lv, Q. Li, A. R. Botello-Mendez, T. Hayashi, B. Wang, A. Berkdemir, Q. Hao, A. L. Elias, R. Cruz-Silva, H. R. Gutierrez, Y. A. Kim, H. Muramatsu, J. Zhu, M. Endo, H. Terrones, J.-C. Charlier, M. Pan, and M.

Terrones. "Nitrogen-doped graphene: beyond single substitution and enhanced molecular sensing". *Scientific reports* 2 (2012).

[62] A. Zabet-Khosousi, L. Zhao, L. Pálová, M. S. Hybertsen, D. R. Reichman, A. N. Pasupathy, and G. W. Flynn. "Segregation of sublattice domains in nitrogen-doped graphene". *Journal of the American Chemical Society* 136.4 (2014), pp. 1391–1397.

[63] A. Lherbier, A. R. Botello-Mendez, and J.-C. Charlier. "Electronic and transport properties of unbalanced sublattice N-doping in graphene". *Nano letters* 13.4 (2013), pp. 1446–1450.

[64] A. R. Botello-Méndez, A. Lherbier, and J.-C. Charlier. "Modeling electronic properties and quantum transport in doped and defective graphene". *Solid State Communications* 175 (2013), pp. 90–100.

[65] T. Radchenko, V. Tatarenko, I. Y. Sagalianov, and Y. I. Prylutskyy. "Effects of nitrogen-doping configurations with vacancies on conductivity in graphene". *Physics Letters A* 378.30 (2014), pp. 2270–2274.

[66] W. Wan, H. Li, H. Huang, S. L. Wong, L. Lv, Y. Gao, and A. T. S. Wee. "Incorporating isolated molybdenum (mo) atoms into bilayer epitaxial graphene on 4h-sic (0001)". *ACS nano* 8.1 (2013), pp. 970–976.

[67] C. Lin, Y. Feng, Y. Xiao, M. Dürr, X. Huang, X. Xu, R. Zhao, E. Wang, X.-Z. Li, and Z. Hu. "Direct observation of ordered configurations of hydrogen adatoms on graphene". *Nano letters* 15.2 (2015), pp. 903–908.

[68] L. Zhao, M. Levendorf, S. Goncher, T. Schiros, L. Palova, A. Zabet-Khosousi, K. T. Rim, C. Gutierrez, D. Nordlund, and C. Jaye. "Local atomic and electronic structure of boron chemical doping in monolayer graphene". *Nano letters* 13.10 (2013), pp. 4659–4665.

[69] I. Deretzis and A. La Magna. "Origin and impact of sublattice symmetry breaking in nitrogen-doped graphene". *Physical Review B* 89.11 (2014), p. 115408.

[70] M. Telychko, P. Mutombo, M. Ondracek, P. Hapala, F. C. Bocquet, J. Kolorenc, M. Vondracek, P. Jelinek, and M. Svec. "Achieving high-quality single-atom nitrogen doping of graphene/sic (0001) by ion implantation and subsequent thermal stabilization". *ACS nano* 8.7 (2014), pp. 7318–7324.

[71] C. Rocha, A. Wall, A. Rocha, and M. Ferreira. "Modelling the effect of randomly dispersed adatoms on carbon nanotubes". *Journal of Physics: Condensed Matter* 19.34 (2007), p. 346201.

[72] C. Rocha, A. Wall, A. Rocha, and M. Ferreira. "Modeling the effect of dispersed doping agents in carbon nanotubes". *Journal of nanoscience and nanotechnology* 7.10 (2007), pp. 3446–3449.

[73] C. Rocha, A. Wall, and M. Ferreira. "Electronic properties of nanotube-based sensors: An inverse modeling approach". *EPL (Europhysics Letters)* 82.2 (2008), p. 27004.

[74] E. Economou. *Greenś Functions in Quantum Physics*. 3rd. Springer, 2006.

[75] D. Coppersmith and S. Winograd. "Matrix multiplication via arithmetic progressions". *Proceedings of the nineteenth annual ACM symposium on Theory of computing*. ACM. 1987, pp. 1–6.

[76] G. D. Mahan. *Many-particle physics*. Springer Science & Business Media, 2013.

[77] F. Banhart, J. Kotakoski, and A. V. Krasheninnikov. "Structural defects in graphene". *ACS nano* 5.1 (2010), pp. 26–41.

[78] P. W. Anderson. "Localized magnetic states in metals". *Physical Review* 124.1 (1961), p. 41.

[79] R. Zeller. "An elementary derivation of Lloyd's formula valid for full-potential multiple-scattering theory". *Journal of Physics: Condensed Matter* 16.36 (2004), p. 6453.

[80] P. Lloyd. "Wave propagation through an assembly of spheres: II. The density of single-particle eigenstates". *Proceedings of the Physical Society* 90.1 (1967), p. 207.

[81] C. H. Lewenkopf and E. R. Mucciolo. "The recursive Green's function method for graphene". *Journal of Computational Electronics* 12.2 (2013), pp. 203–231.

[82] S. Rotter, J.-Z. Tang, L. Wirtz, J. Trost, and J. Burgdoerfer. "Modular recursive Green's function method for ballistic quantum transport". *Physical Review B* 62.3 (2000), p. 1950.

[83] M. Sherafati and S. Satpathy. "RKKY interaction in graphene from the lattice Green's function". *Physical Review B* 83.16 (2011), p. 165425.

[84] M. L. Sancho, J. L. Sancho, J. L. Sancho, and J. Rubio. "Highly convergent schemes for the calculation of bulk and surface Green functions". *Journal of Physics F: Metal Physics* 15.4 (1985), p. 851.

[85] M. L. Sancho, J. L. Sancho, and J. Rubio. "Quick iterative scheme for the calculation of transfer matrices: application to Mo (100)". *Journal of Physics F: Metal Physics* 14.5 (1984), p. 1205.

[86] D. Greenwood. "The Boltzmann equation in the theory of electrical conduction in metals". *Proceedings of the Physical Society* 71.4 (1958), p. 585.

[87] R. Kubo. "Statistical-mechanical theory of irreversible processes. I. General theory and simple applications to magnetic and conduction problems". *Journal of the Physical Society of Japan* 12.6 (1957), pp. 570–586.

[88] S. Power, F. Guimaraes, A. Costa, R. Muniz, and M. Ferreira. "Dynamic RKKY interaction in graphene". *Physical Review B* 85.19 (2012), p. 195411.

[89] J. Klinovaja and D. Loss. "RKKY interaction in carbon nanotubes and graphene nanoribbons". *Physical Review B* 87.4 (2013), p. 045422.

[90] E. Kogan. "RKKY interaction in graphene". *Physical Review B* 84.11 (2011), p. 115119.

[91] J. A. Lawlor, S. R. Power, and M. S. Ferreira. "Friedel oscillations in graphene: Sublattice asymmetry in doping". *Physical Review B* 88.20 (2013), p. 205416.

[92] J. M. Arrieta. "Tight-Binding Description of Graphene Nanostructures". *Modelling of Plasmonic and Graphene Nanodevices*. Springer, 2014, pp. 13–23.

[93] C. Bena and G. Montambaux. "Remarks on the tight-binding model of graphene". *New Journal of Physics* 11.9 (2009), p. 095003.

[94] T. Wehling, A. Balatsky, M. Katsnelson, A. Lichtenstein, K. Scharnberg, and R. Wiesendanger. "Local electronic signatures of impurity states in graphene". *Physical Review B* 75.12 (2007), p. 125425.

[95] J. Rodrigues, N. Peres, and J. L. dos Santos. "Scattering by linear defects in graphene: a tight-binding approach". *Journal of Physics: Condensed Matter* 25.7 (2013), p. 075303.

[96] A. Lherbier, X. Blase, Y.-M. Niquet, F. Triozon, and S. Roche. "Charge transport in chemically doped 2D graphene". *Physical review letters* 101.3 (2008), p. 036808.

[97] S. Reich, J. Maultzsch, C. Thomsen, and P. Ordejon. "Tight-binding description of graphene". *Physical Review B* 66.3 (2002), p. 035412.

[98] Y. Wu and P. Childs. "Conductance of graphene nanoribbon junctions and the tight binding model". *Nanoscale Res Lett* 6.62 (2011), pp. 1–5.

[99] T. G. Pedersen and J. G. Pedersen. "Self-consistent tight-binding model of B and N doping in graphene". *Physical Review B* 87.15 (2013), p. 155433.

[100] F. Ducastelle. "Electronic structure of vacancy resonant states in graphene: A critical review of the single-vacancy case". *Physical Review B* 88.7 (2013), p. 075413.

[101] J. A. Lawlor and M. S. Ferreira. "Green functions of graphene: An analytic approach". *Physica B: Condensed Matter* 463 (2015), pp. 48–53.

[102] A. Carvalho, C. Bezerra, J. Lawlor, and M. Ferreira. "Density of states of helically symmetric boron carbon nitride nanotubes". *Journal of Physics: Condensed Matter* 26.1 (2014), p. 015303.

[103] R. Saito, G. Dresselhaus, and M. S. Dresselhaus. *Physical properties of carbon nanotubes*. Vol. 35. World Scientific, 1998.

[104] D. R. Cooper, B. D'Anjou, N. Ghattamaneni, B. Harack, M. Hilke, A. Horth, N. Majlis, M. Massicotte, L. Vandsburger, E. Whiteway, and V. Yu. "Experimental review of graphene". *ISRN Condensed Matter Physics* 2012 (2012).

[105] R. Kundu. "Tight-binding parameters for graphene". *Modern Physics Letters B* 25.03 (2011), pp. 163–173.

[106] A. C. Neto, F. Guinea, N. Peres, K. S. Novoselov, and A. K. Geim. "The electronic properties of graphene". *Reviews of modern physics* 81.1 (2009), p. 109.

[107] E. Saff, A. Snider, and L. Trefethen. *Fundamentals of Complex Analysis with Applications to Engineering and Science*. Prentice Hall, 2003. ISBN: 9780130179685.

[108] Y. Matsuda, J. Tahir-Kheli, and W. A. Goddard III. "Definitive band gaps for single-wall carbon nanotubes". *The Journal of Physical Chemistry Letters* 1.19 (2010), pp. 2946–2950.

[109] R. H. Baughman, A. A. Zakhidov, and W. A. de Heer. "Carbon nanotubes–the route toward applications". *Science* 297.5582 (2002), pp. 787–792.

[110] O. Stephan, P. Ajayan, C. Colliex, P. Redlich, J. Lambert, P. Bernier, and P. Lefin. "Doping Graphitic and Carbon Nanotube Structures with Boron and Nitrogen". *Science* 266.5191 (1994), pp. 1683–1685.

[111] M. Matos, S. Azevedo, and J. Kaschny. "On the structural properties of B–C–N nanotubes". *Solid State Communications* 149.5 (2009), pp. 222–226.

[112] K. Raidongia, D. Jagadeesan, M. Upadhyay-Kahaly, U. V. Waghmare, S. K. Pati, M. Eswaramoorthy, and C. Rao. "Synthesis, structure and properties of homogeneous BC 4 N nanotubes". *Journal of Materials Chemistry* 18.1 (2008), pp. 83–90.

[113] Z. Xu, W. Lu, W. Wang, C. Gu, K. Liu, X. Bai, E. Wang, and H. Dai. "Converting Metallic Single-Walled Carbon Nanotubes into Semiconductors by Boron/Nitrogen Co-Doping". *Advanced Materials* 20.19 (2008), pp. 3615–3619.

[114] S. Y. Kim, J. Park, H. C. Choi, J. P. Ahn, J. Q. Hou, and H. S. Kang. "X-ray photoelectron spectroscopy and first principles calculation of BCN nanotubes". *Journal of the American Chemical Society* 129.6 (2007), pp. 1705–1716.

[115] J. Garel, C. Zhao, R. Popovitz-Biro, D. Golberg, W. Wang, and E. Joselevich. "BCN nanotubes as highly sensitive torsional electromechanical transducers". *Nano letters* 14.11 (2014), pp. 6132–6137.

[116] H. M. Moghaddam. "The CNT/BCN/CNT structure (zigzag type) as a molecular switch". *Physica E: Low-dimensional Systems and Nanostructures* 42.2 (2009), pp. 167–171.

[117] R. d. L. Kronig and W. Penney. "Quantum mechanics of electrons in crystal lattices". *Proceedings of the Royal Society of London A: Mathematical, Physical and Engineering Sciences*. Vol. 130. 814. The Royal Society. 1931, pp. 499–513.

[118] D. Talwar and C. Ting. "Tight-binding calculations for the electronic structure of isolated vacancies and impurities in III-V compound semiconductors". *Physical Review B* 25.4 (1982), p. 2660.

[119] J. Robertson. "Electronic structure and core exciton of hexagonal boron nitride". *Physical Review B* 29.4 (1984), p. 2131.

[120] E. McCann and M. Koshino. "The electronic properties of bilayer graphene". *Reports on Progress in Physics* 76.5 (2013), p. 056503.

[121] R. Ribeiro and N. Peres. "Stability of boron nitride bilayers: Ground-state energies, interlayer distances, and tight-binding description". *Physical Review B* 83.23 (2011), p. 235312.

[122] M. Kohyama, S. Kose, M. Kinoshita, and R. Yamamoto. "The self-consistent tight-binding method: application to silicon and silicon carbide". *Journal of Physics: Condensed Matter* 2.38 (1990), p. 7791.

[123] K. Foyevtsova, H. O. Jeschke, I. Mazin, D. Khomskii, and R. Valenti. "Ab initio analysis of the tight-binding parameters and magnetic interactions in Na 2 IrO 3". *Physical Review B* 88.3 (2013), p. 035107.

[124] Y. Tan, M. Povolotskyi, T. Kubis, Y. He, Z. Jiang, G. Klimeck, and T. B. Boykin. "Empirical tight binding parameters for GaAs and MgO with explicit basis through DFT mapping". *Journal of Computational Electronics* 12.1 (2013), pp. 56–60.

[125] P. Rinke, A. Janotti, M. Scheffler, and C. G. Van de Walle. "Defect Formation Energies without the Band-Gap Problem: Combining Density-Functional Theory and the G W Approach for the Silicon Self-Interstitial". *Physical review letters* 102.2 (2009), p. 026402.

[126] N. Al-Aqtash, K. M. Al-Tarawneh, T. Tawalbeh, and I. Vasiliev. "Ab initio study of the interactions between boron and nitrogen dopants in graphene". *Journal of Applied Physics* 112.3 (2012), p. 034304.

[127] P. Lambin, H. Amara, F. Ducastelle, and L. Henrard. "Long-range interactions between substitutional nitrogen dopants in graphene: electronic properties calculations". *Physical Review B* 86.4 (2012), p. 045448.

[128] J. Vergés and P. De Andres. "Trapping of electrons near chemisorbed hydrogen on graphene". *Physical Review B* 81.7 (2010), p. 075423.

[129] V. Ivanovskaya, A. Zobelli, D. Teillet-Billy, N. Rougeau, V. Sidis, and P. Briddon. "Hydrogen adsorption on graphene: a first principles study". *The European Physical Journal B* 76.3 (2010), pp. 481–486.

[130] D. Boukhvalov, M. Katsnelson, and A. Lichtenstein. "Hydrogen on graphene: Electronic structure, total energy, structural distortions and magnetism from first-principles calculations". *Physical Review B* 77.3 (2008), p. 035427.

[131] C. Cab, R. Medina-Esquivel, C. Acosta, J. Mendez-Gamboa, F. Peñuñuri, and A. Tapia. "Influence of Electric Field in the Adsorption of Atomic Hydrogen on Graphene". *Advances in Condensed Matter Physics* 2015 (2015).

[132] T. Wehling, S. Yuan, A. Lichtenstein, A. Geim, and M. Katsnelson. "Resonant scattering by realistic impurities in graphene". *Physical review letters* 105.5 (2010), p. 056802.

[133] M. J. Schmidt and D. Loss. "Edge states and enhanced spin-orbit interaction at graphene/graphane interfaces". *Physical Review B* 81.16 (2010), p. 165439.

[134] J. Bang and K. Chang. "Localization and one-parameter scaling in hydrogenated graphene". *Physical Review B* 81.19 (2010), p. 193412.

[135] J. P. Robinson, H. Schomerus, L. Oroszlány, and V. I. Fal'ko. "Adsorbate-limited conductivity of graphene". *Physical review letters* 101.19 (2008), p. 196803.

[136] X. Liu, C.-Z. Wang, M. Hupalo, W.-C. Lu, P. A. Thiel, K.-M. Ho, and M. C. Tringides. "Fe-Fe adatom interaction and growth morphology on graphene". *Physical Review B* 84.23 (2011), p. 235446.

[137] M. Sherafati and S. Satpathy. "Analytical expression for the RKKY interaction in doped graphene". *Physical Review B* 84.12 (2011), p. 125416.

[138] S. Kopylov, V. Cheianov, B. L. Altshuler, and V. I. Fal'ko. "Transport anomaly at the ordering transition for adatoms on graphene". *Physical review b* 83.20 (2011), p. 201401.

[139] M. A. Ruderman and C. Kittel. "Indirect exchange coupling of nuclear magnetic moments by conduction electrons". *Physical Review* 96.1 (1954), p. 99.

[140] T. Kasuya. "Electrical resistance of ferromagnetic metals". *Progress of Theoretical Physics* 16.1 (1956), pp. 58–63.

[141] K. Yosida. "Magnetic properties of Cu-Mn alloys". *Physical Review* 106.5 (1957), p. 893.

[142] B. Nanda, M. Sherafati, Z. Popović, and S. Satpathy. "Electronic structure of the substitutional vacancy in graphene: density-functional and Green's function studies". *New Journal of Physics* 14.8 (2012), p. 083004.

[143] M. Sherafati and S. Satpathy. "Impurity states on the honeycomb and the triangular lattices using the Green's function method". *physica status solidi (b)* 248.9 (2011), pp. 2056–2063.

[144] V. M. Pereira, J. L. Dos Santos, and A. C. Neto. "Modeling disorder in graphene". *Physical Review B* 77.11 (2008), p. 115109.

[145] P. Brouwer, E. Racine, A. Furusaki, Y. Hatsugai, Y. Morita, and C. Mudry. "Zero modes in the random hopping model". *Physical review B* 66.1 (2002), p. 014204.

[146] V. Mkhitaryan and E. Mishchenko. "Resonant finite-size impurities in graphene, unitary limit, and Friedel oscillations". *Physical Review B* 86.11 (2012), p. 115442.

[147] C. Ataca, E. Aktürk, H. Şahin, and S. Ciraci. "Adsorption of carbon adatoms to graphene and its nanoribbons". *Journal of Applied Physics* 109.1 (2011), p. 013704.

[148] F. Schedin, A. Geim, S. Morozov, E. Hill, P. Blake, M. Katsnelson, and K. Novoselov. "Detection of individual gas molecules adsorbed on graphene". *Nature materials* 6.9 (2007), pp. 652–655.

[149] H. Amara, S. Latil, V. Meunier, P. Lambin, and J.-C. Charlier. "Scanning tunneling microscopy fingerprints of point defects in graphene: A theoretical prediction". *Physical Review B* 76.11 (2007), p. 115423.

[150] V. Meunier and P. Lambin. "Tight-binding computation of the STM image of carbon nanotubes". *Physical review letters* 81.25 (1998), p. 5588.

[151] J. Duffy, J. Lawlor, M. S. Ferreira, and C. Lewenkopf. "Impurity invisibility in graphene: Symmetry guidelines for the design of efficient sensors". *Under review, submitted to Physical Review B March 2016.* ().

[152] B. Uchoa, T. Rappoport, and A. C. Neto. "Kondo quantum criticality of magnetic adatoms in graphene". *Physical review letters* 106.1 (2011), p. 016801.

[153] V. M. Pereira, A. C. Neto, and N. Peres. "Tight-binding approach to uniaxial strain in graphene". *Physical Review B* 80.4 (2009), p. 045401.

[154] C. Lee, X. Wei, J. W. Kysar, and J. Hone. "Measurement of the elastic properties and intrinsic strength of monolayer graphene". *Science* 321.5887 (2008), pp. 385–388.

[155] S. Power, P. Gorman, J. Duffy, and M. Ferreira. "Strain-induced modulation of magnetic interactions in graphene". *Physical Review B* 86.19 (2012), p. 195423.

[156] J. H. Garcia, B. Uchoa, L. Covaci, and T. G. Rappoport. "Adatoms and Anderson localization in graphene". *Physical Review B* 90.8 (2014), p. 085425.

[157] A. D. K. Jones and T. Bekkedahl. "Storage of hydrogen in single-walled carbon nanotubes". *Nature* 386 (1997), p. 377.

[158] R. Oriňáková and A. Oriňák. "Recent applications of carbon nanotubes in hydrogen production and storage". *Fuel* 90.11 (2011), pp. 3123–3140.

[159] S. Dutta. "A review on production, storage of hydrogen and its utilization as an energy resource". *Journal of Industrial and Engineering Chemistry* 20.4 (2014), pp. 1148–1156.

[160] R. C. Bowman and B. Fultz. "Metallic hydrides I: hydrogen storage and other gas-phase applications". *MRS bulletin* 27.09 (2002), pp. 688–693.

[161] K. Gross, G. Thomas, and C. Jensen. "Catalyzed alanates for hydrogen storage". *Journal of Alloys and Compounds* 330 (2002), pp. 683–690.

[162] H. Chen and A. K. Ray. "Atomic hydrogen and oxygen adsorptions in single-walled zigzag silicon nanotubes". *Journal of nanoparticle research* 15.9 (2013), pp. 1–14.

[163] G. E. Froudakis. "Hydrogen storage in nanotubes & nanostructures". *Materials Today* 14.7 (2011), pp. 324–328.

[164] A. Nikitin, H. Ogasawara, D. Mann, R. Denecke, Z. Zhang, H. Dai, K. Cho, and A. Nilsson. "Hydrogenation of single-walled carbon nanotubes". *Physical review letters* 95.22 (2005), p. 225507.

[165] L. Schlapbach and A. Züttel. "Hydrogen-storage materials for mobile applications". *Nature* 414.6861 (2001), pp. 353–358.

[166] J. E. Johns and M. C. Hersam. "Atomic covalent functionalization of graphene". *Accounts of chemical research* 46.1 (2012), pp. 77–86.

[167] F. H. Yang and R. T. Yang. "Ab initio molecular orbital study of adsorption of atomic hydrogen on graphite:: Insight into hydrogen storage in carbon nanotubes". *Carbon* 40.3 (2002), pp. 437–444.

[168] Z. Zhang and K. Cho. "Ab initio study of hydrogen interaction with pure and nitrogen-doped carbon nanotubes". *Physical Review B* 75.7 (2007), p. 075420.

[169] T. Vehviläinen, M. Ganchenkova, V. Borodin, and R. Nieminen. "Multiscale Study of Hydrogen Diffusion and Clustering on Carbon Nanotube". *Journal of nanoscience and nanotechnology* 9.7 (2009), pp. 4246–4253.

[170] V. Borodin, T. Vehviläinen, M. Ganchenkova, and R. Nieminen. "Hydrogen transport on graphene: Competition of mobility and desorption". *Physical Review B* 84.7 (2011), p. 075486.

[171] Y. Tison, J. Lagoute, V. Repain, C. Chacon, Y. Girard, S. Rousset, F. Joucken, D. Sharma, L. Henrard, and H. Amara. "Electronic Interaction between Nitrogen Atoms in Doped Graphene". *ACS nano* (2015).

[172] P. Willke, J. Amani, S. Thakur, S. Weikert, T. Druga, K. Maiti, H. Hofsäss, and M. Wenderoth. "Short-range ordering of ion-implanted nitrogen atoms in SiC-graphene". *Applied Physics Letters* 105.11 (2014), p. 111605.

[173] F. Joucken, Y. Tison, J. Lagoute, J. Dumont, D. Cabosart, B. Zheng, V. Repain, C. Chacon, Y. Girard, A. R. Botello-Méndez, S. Rousset, R. Sporken, J.-C. Charlier, and L. Henrard. "Localized state and charge transfer in nitrogen-doped graphene". *Physical Review B* 85.16 (2012), p. 161408.

[174] H. Khalfoun, P. Lambin, and L. Henrard. "Long-range resonant effects on electronic transport of nitrogen-doped carbon nanotubes". *Physical Review B* 89.4 (2014), p. 045407.

[175] H. Khalfoun, A. Lherbier, P. Lambin, L. Henrard, and J.-C. Charlier. "Transport regimes in nitrogen-doped carbon nanotubes: Perfect order, semi-random, and random disorder cases". *Physical Review B* 91.3 (2015), p. 035428.

[176] D. Henwood and J. D. Carey. "Ab initio investigation of molecular hydrogen physisorption on graphene and carbon nanotubes". *Physical Review B* 75.24 (2007), p. 245413.

[177] J. S. Arellano, L. M. Molina, A. Rubio, M. López, and J. Alonso. "Interaction of molecular and atomic hydrogen with (5,5) and (6,6) single-wall carbon nanotubes". *The Journal of Chemical Physics* 117.5 (2002), pp. 2281–2288.

[178] G. Buchs, A. V. Krasheninnikov, P. Ruffieux, P. Gröning, A. S. Foster, R. M. Nieminen, and O. Gröning. "Creation of paired electron states in the gap of semiconducting carbon nanotubes by correlated hydrogen adsorption". *New Journal of Physics* 9.8 (2007), p. 275.

[179] X. Pei, X. Yang, and J. Dong. "Effects of different hydrogen distributions on the magnetic properties of hydrogenated single-walled carbon nanotubes". *Physical Review B* 73.19 (2006), p. 195417.

[180] T. Roman, W. A. Diño, H. Nakanishi, H. Kasai, T. Sugimoto, and K. Tange. "Hydrogen pairing on graphene". *Carbon* 45.1 (2007), pp. 218–220.

[181] V. Cheianov, O. Syljuåsen, B. Altshuler, and V. Fal'ko. "Sublattice ordering in a dilute ensemble of monovalent adatoms on graphene". *EPL (Europhysics Letters)* 89.5 (2010), p. 56003.

[182] N. A. Pike and D. Stroud. "Tight-binding model for adatoms on graphene: Analytical density of states, spectral function, and induced magnetic moment". *Physical Review B* 89.11 (2014), p. 115428.

[183] P. Gorman, J. Duffy, M. Ferreira, and S. Power. "RKKY interaction between adsorbed magnetic impurities in graphene: Symmetry and strain effects". *Physical Review B* 88.8 (2013), p. 085405.

[184] L. Hornekær, E. Rauls, W. Xu, Ž. Šljivančanin, R. Otero, I. Stensgaard, E. Lægsgaard, B. Hammer, and F. Besenbacher. "Clustering of chemisorbed H (D) atoms on the graphite (0001) surface due to preferential sticking". *Physical review letters* 97.18 (2006), p. 186102.

[185] Y. Tison, H. Lin, J. Lagoute, V. Repain, C. Chacon, Y. Girard, S. Rousset, L. Henrard, B. Zheng, and T. Susi. "Identification of nitrogen dopants in single-walled carbon nanotubes by scanning tunneling microscopy". *ACS nano* 7.8 (2013), pp. 7219–7226.

[186] R. Skomski, P. Dowben, M. Sky Driver, and J. Kelber. "Sublattice-induced symmetry breaking and band-gap formation in graphene". *Materials Horizons* 1 (2014), p. 563.

[187] Z. Ni, T. Yu, Y. Lu, Y. Wang, Y. Feng, and Z. Shen. "Uniaxial strain on graphene: Raman spectroscopy study and band-gap opening". *ACS Nano* 2 (2008), p. 2301.

[188] M. Schneider, D. Faria, S. Viola Kusminskiy, and N. Sandler. "Local sublattice symmetry breaking for graphene with a centrosymmetric deformation". *Physical Review B* 91 (2015), 161407(R).

[189] R. Carrillo-Bastos, D. Faria, A. Latgé, F. Mireles, and N. Sandler. "Gaussian deformations in graphene ribbons: Flowers and confinement". *Physical Review B* 90 (2014), 041411(R).

[190] M. Settnes, S. R. Power, J. Lin, D. H. Petersen, and A.-P. Jauho. "Patched Green's function techniques for two-dimensional systems: Electronic behavior of bubbles and perforations in graphene". *Physical Review B* 91.12 (2015), p. 125408.

[191] N. Levy, S. Burke, K. Meaker, M. Panlasigui, A. Zettl, F. Guinea, A. C. Neto, and M. Crommie. "Strain-induced pseudo–magnetic fields greater than 300 tesla in graphene nanobubbles". *Science* 329.5991 (2010), pp. 544–547.

[192] M. Vozmediano, F. de Juan, and A. Cortijo. "Gauge fields and curvature in graphene". *Journal of Physics: Conference Series* 129 (2008), p. 012001.

[193] M. Settnes, S. R. Power, J. Lin, D. H. Petersen, and A.-P. Jauho. "Bubbles in graphene-a computational study". *Journal of Physics: Conference Series*. Vol. 647. 1. IOP Publishing. 2015, p. 012022.

[194] D. Sánchez-Portal, P. Ordejón, E. Artacho, and J. Soler. "Density functional method for very large systems with LCAO basis sets". *Int. J. Quantum Chem.* 65 (1997), p. 453.

[195] P. Ordejón, E. Artacho, and J. M. Soler. "Self-consistent order-N density-functional calculations for very large systems". *Physical Review B* 53.16 (1996), R10441.

[196] F. de Juan, A. Cortijo, and M. A. Vozmediano. "Charge inhomogeneities due to smooth ripples in graphene sheets". *Physical Review B* 76.16 (2007), p. 165409.

[197] D. Faria, A. Latgé, S. E. Ulloa, and N. Sandler. "Currents and pseudomagnetic fields in strained graphene rings". *Physical Review B* 87.24 (2013), p. 241403.

[198] E. Cadelano, P. L. Palla, S. Giordano, and L. Colombo. "Nonlinear elasticity of monolayer graphene". *Physical Review Letters* 102.23 (2009), p. 235502.

[199] J. Perdew, K. Burke, and M. Ernzerhof. "Generalized gradient approximation made simple". *Physical Review Letters* 77 (1996), p. 3865.

[200] N. Troullier and J. Martins. "Efficient pseudopotentials for plane-wave calculations". *Physical Review B* 43 (1991), p. 1993.

[201] A. Kokalj. *Comp. Mater. Sci.* 28 (2003), p. 155.

[202] J. Lawlor and M. S. Ferreira. "Sublattice segregation of hydrogen adsorbates in carbon nanotubes". *Physical Review B* 92.11 (2015), p. 115405.

[203] J. A. Lawlor, P. D. Gorman, S. R. Power, C. G. Bezerra, and M. S. Ferreira. "Sublattice imbalance of substitutionally doped nitrogen in graphene". *Carbon* 77 (2014), pp. 645–650.

[204] J. A. Lawlor, C. G. Rocha, V. Torres, A. Latgé, and M. S. Ferreira. "The influence of Gaussian strain on sublattice selectivity of adsorbates in graphene". *Under review, submitted to Journal of Physics: Condensed Matter February 2016.* ().

[205] M. Chhowalla, Z. Liu, and H. Zhang. "Two-dimensional transition metal dichalcogenide (TMD) nanosheets". *Chemical Society Reviews* 44.9 (2015), pp. 2584–2586.

[206] M. M. Ugeda, I. Brihuega, F. Hiebel, P. Mallet, J.-Y. Veuillen, J. M. Gómez-Rodriguez, and F. Ynduráin. "Electronic and structural characterization of divacancies in irradiated graphene". *Physical Review B* 85.12 (2012), p. 121402.

[207] M. Saito, K. Yamashita, and T. Oda. "Magic numbers of graphene multivacancies". *Japanese Journal of Applied Physics* 46.12L (2007), p. L1185.

[208] M. Oubal, S. Picaud, M.-T. Rayez, and J.-C. Rayez. "Structure and reactivity of carbon multivacancies in graphene". *Computational and Theoretical Chemistry* 990 (2012), pp. 159–166.

[209] G.-D. Lee, C. Wang, E. Yoon, N.-M. Hwang, D.-Y. Kim, and K. Ho. "Diffusion, coalescence, and reconstruction of vacancy defects in graphene layers". *Physical review letters* 95.20 (2005), p. 205501.

[210] S. T. Skowron, I. V. Lebedeva, A. M. Popov, and E. Bichoutskaia. "Energetics of atomic scale structure changes in graphene". *Chemical Society Reviews* 44.10 (2015), pp. 3143–3176.

[211] R. Dettori, E. Cadelano, and L. Colombo. "Elastic fields and moduli in defected graphene". *Journal of Physics: Condensed Matter* 24.10 (2012), p. 104020.

[212] J. Duffy, P. Gorman, S. Power, and M. Ferreira. "Variable range of the RKKY interaction in edged graphene". *Journal of Physics: Condensed Matter* 26.5 (2014), p. 055007.

[213] B. Wunsch, T. Stauber, F. Sols, and F. Guinea. "Dynamical polarization of graphene at finite doping". *New Journal of Physics* 8.12 (2006), p. 318.

[214] E. J. Santos, D. Sánchez-Portal, and A. Ayuela. "Magnetism of substitutional Co impurities in graphene: Realization of single π vacancies". *Physical Review B* 81.12 (2010), p. 125433.

[215] Y. Mao, J. Yuan, and J. Zhong. "Density functional calculation of transition metal adatom adsorption on graphene". *Journal of Physics: Condensed Matter* 20.11 (2008), p. 115209.

[216] A. Rocha, M. Rossi, A. Fazzio, and A. J. da Silva. "Designing real nanotube-based gas sensors". *Physical review letters* 100.17 (2008), p. 176803.

[217] T. Aktor, A.-P. Jauho, and S. R. Power. "Electronic transport in graphene nanoribbons with sublattice-asymmetric doping". *Physical Review B* 93 (2016), p. 035446.

[218] Y. Lu and Y. P. Feng. "Adsorptions of hydrogen on graphene and other forms of carbon structures: First principle calculations". *Nanoscale* 3.6 (2011), pp. 2444–2453.

[219] E. J. Santos, D. Sánchez-Portal, and A. Ayuela. "Magnetism of covalently functionalized carbon nanotubes". *Applied Physics Letters* 99.6 (2011), p. 062503.

[220] E. H. Lieb. "Two theorems on the Hubbard model". *Condensed Matter Physics and Exactly Soluble Models*. Springer, 2004, pp. 55–58.

[221] J. Palacios, J. Fernández-Rossier, and L. Brey. "Vacancy-induced magnetism in graphene and graphene ribbons". *Physical Review B* 77.19 (2008), p. 195428.

[222] H. Kumazaki and D. Hirashima. "Tight-binding study of nonmagnetic-defect-induced magnetism in graphene". *Low Temperature Physics* 34.10 (2008), pp. 805–811.

[223] S. Casolo, O. M. Løvvik, R. Martinazzo, and G. F. Tantardini. "Understanding adsorption of hydrogen atoms on graphene". *The Journal of Chemical Physics* 130.5, 054704 (2009).

[224] H. González-Herrero, J. M. Gómez-Rodríguez, P. Mallet, M. Moaied, J. J. Palacios, C. Salgado, M. M. Ugeda, J.-Y. Veuillen, F. Yndurain, and I. Brihuega. "Atomic-scale control of graphene magnetism by using hydrogen atoms". *Science* 352.6284 (2016), pp. 437–441.

[225] S. Hollen and J. Gupta. "Painting magnetism on a canvas of graphene". *Science* 352.6284 (2016), pp. 415–416.

[226] M. I. Katsnelson. *Graphene: carbon in two dimensions*. Cambridge University Press, 2012.

[227] M. Craciun, S. Russo, M. Yamamoto, and S. Tarucha. "Tuneable electronic properties in graphene". *Nano Today* 6.1 (2011), pp. 42–60.

[228] Y. V. Skrypnyk and V. M. Loktev. "Electrical conductivity in graphene with point defects". *Physical Review B* 82.8 (2010), p. 085436.

[229] S. Ihnatsenka and G. Kirczenow. "Dirac point resonances due to atoms and molecules adsorbed on graphene and transport gaps and conductance quantization in graphene nanoribbons with covalently bonded adsorbates". *Physical Review B* 83.24 (2011), p. 245442.